XUV and VUV Photoabsorption and Emission Studies in Thorium and other High-Z Laser Plasmas

A thesis submitted for the degree of
Doctor of Philosophy
by

Oonagh Elizabeth Meighan B.Sc.

School of Physical Sciences

Research Supervisor
Dr. John T. Costello

August 2000

To Mam, Dad and Vincent

Declaration

I hereby certify that this material, which I now submit for assessment on the programme of study leading to the award of Doctor of Philosophy is entirely my own work and has not been taken from the work of others save and to the extent that such work has been cited and acknowledged within the text of my work.

Signed: Etuaga Mojeun *ID No.:* 9497102

Candidate

Date: 21/09/2000

Contents

Abstract

Fundamental investigations into the atomic structure of actinide atoms and ions provide a wealth of information on the physical and chemical behaviour of these elements. In this work, thorium, the second actinide element is investigated.

Inner shell photoabsorption features in the 6p and 5d spectra of the free thorium atom and thorium ions produced in a laser plasma plume have been recorded using the space and time resolved Dual Laser Plasma (DLP) spectroscopic technique. Studies focus, in particular, on the investigation of the 6p $\rightarrow$ 6d and the 5d $\rightarrow$ $\overline{5,\varepsilon}$f giant dipole resonance features residing in the VUV (15 to 40eV) and XUV (80 to 150eV) inner shell photoabsorption spectra of atomic and ionic thorium. The evolution of both giant dipole resonance profiles with increasing ionisation along the thorium isonuclear sequence Th to Th^{6+} has been studied. Results indicate that the 6d wavefunction is collapsed in neutral thorium, whereas the 5f wavefunction is to a large extent un-collapsed in neutral thorium but collapses with increasing ionisation along the thorium isonuclear sequence.

A picosecond XUV continuum laser plasma light source has been developed in this work and is characterised both spectrally and temporally using time integrated flat field spectroscopy and time resolved streak camera detection. XUV continuum emission pulsewidths of less than 200ps in the 100 to 200eV energy region were recorded from the high-Z metal plasmas of tungsten, gold, lead and samarium. When incorporated into the DLP technique, the picosecond XUV continuum source permits probing of the absorbing plasma plume with superior temporal resolution than previously achieved using XUV laser plasma sources produced using nanosecond laser pulses. The newly developed source was used to the study the collapse of the broad asymmetric 5d $\rightarrow$ $\overline{5,\varepsilon}$f giant dipole resonance feature to discrete Rydberg-like structure along the thorium isonuclear sequence.

Chapter One

Introduction and Theory

This chapter outlines current trends in atomic, nuclear and solid-state actinide research and describes the wavefunction collapse phenomenon that is responsible for filling the 5f subshell and thus the formation of the actinide series. The fundamental principles underlying the formation of giant dipole resonance features that occur prior to wavefunction collapse in the inner shell photoabsorption spectra of early actinide and lanthanide atoms and ions are described in detail.

1.1 The Actinide Series and Wavefunction Collapse

1.1.1 Background

In the 1940's it was suggested that elements of atomic number 89 to 103 formed a new series in the periodic table which was similar to the preceding lanthanide or rare earth series. Earlier members of the actinides: actinium, thorium, protactinium and uranium had been discovered as naturally occurring elements as early as 1913. It was not until the synthesis of the transuranium elements in the years 1940 to 1965 that the entire series was established (Seaborg 1995). The field of actinide research that has developed in the last half century is highly diverse, spanning a wide range of scientific disciplines. Fundamental investigations into the atomic structure of the actinide atom provide a wealth of information on the physical and chemical behaviour of these elements. In this work, thorium (Z=90), the second actinide element is investigated. Valence and inner shell photoabsorption and photoionisation features in the spectra of the free thorium atom and ions are studied and provide an increased understanding of the atomic structure of this element in atomic and lowly charged ionic states. Studies focus, in particular, on the variation in the spatial extent of the 5f and 6d wavefunctions along the thorium isonuclear sequence. Similar studies in the lanthanide series have served to increase our fundamental understanding of the atomic structure of these elements and have acted as a precursor to more recent studies in the actinides.

1.1.2 Trends in Actinide Research - Nuclear Physics and Technology

Experimental studies on the actinides present a serious challenge to research scientists due to the high levels of radioactivity and toxicity that occur across the series. Further limitations are imposed by the rarity and correspondingly high costs of obtaining quality samples for study and also the short half-lives of some actinide elements and isotopes. These constraints have resulted in the development of entirely new and specialised experimental techniques.

A major stimulus for actinide research in this century was prompted by the first nuclear fission experiment performed by Hahn and Strassmann in 1939. The recognition and investigation of actinide elements as fissile fuels began with particular emphasis on

thorium, uranium and plutonium. Thorium and uranium are the only actinide elements found in nature in significant abundance. Tons of plutonium are produced as an end product of the nuclear fission process. The remaining 'synthetic' actinide atoms are predominantly created via nuclear transmutation processes at large scale reactor and accelerator facilities (Seaborg 1995). Transuranium research is therefore more confined to large scale facilities (Seaborg 1989), located at the Argonne National Laboratory, the Lawrence Berkeley Laboratory, Los Alamos National Laboratory and Oak Ridge National Laboratory; in the United States, the Gesellschaft für Schwerionenforschung (GSI) in Germany, and in Russia, at the Joint Institute for Nuclear Research at Dubna. Specialised institutions dedicated solely to actinide research have also been established. These are the Institute for Transuranium Elements in Karlsruhe, Germany, and the Glenn T. Seaborg Institute for Transactinium Science located within the Lawrence Livermore National Laboratory. At Karlsruhe, research focuses on the production of high quality single crystal and polycrystalline intermetallic compounds (Spirlet 1989) for measurements of bulk physical properties such as electrical resistivity, magnetisation and the behaviour of high-pressure structures in order to investigate the electronic structure of actinide metals and compounds (see internet site: *http://itumagill.fzk.de*). At the Glenn T. Seaborg Institute, research interests are directed towards actinide waste management, environmental protection and determination and modelling of actinide nuclear, solid state and chemical properties (see internet site: *http://www-cms.llnl.gov/its/index.html*).

In the vast field of nuclear energy research much effort is expended on the study of the main fuel elements, thorium, uranium and plutonium. Research into the thorium fuel cycle is currently experiencing somewhat of a revival (Lung & Gremm 1998, Troyanov et al. 1998, Van Klinken 1998). Thorium was extensively studied prior to the 1970's as a fuel source (Kimura 1995) but ^{232}Th is not naturally fissile and cannot be used to produce a chain reaction by itself. It is only after neutron irradiation that ^{232}Th becomes the fissile fuel ^{233}U ($^{232}\mathrm{Th} + \mathrm{n} \rightarrow {}^{233}\mathrm{Th} - 2(\beta) \rightarrow {}^{233}\mathrm{U}$) which will undergo fission upon absorption of slow neutrons. ^{232}Th is therefore unsuitable for direct use in nuclear weapons that require a naturally fissile fuel material. Also, thorium does not breed large quantities of fissile plutonium (^{239}Pu) which is conventionally produced during neutron irradiation of ^{238}U. This non-proliferate nature of thorium coupled with the fact that it is not naturally fissile have until recently resulted in little thorium fuel and weapon research world-wide. India however has maintained an active interest in thorium

research. It possesses the world's largest known reserves of thorium and has designed and built reactors to operate on the thorium fuel cycle (Chidambaram et al. 1994).

Thorium can potentially serve as a fuel material in all types of nuclear reactor (Lung & Gremm 1998) and Radowsky and co-workers plan to begin testing thorium fuel rods in a conventional light water reactor in the year 2002 (Radowsky & Galperin 1998, Radowsky 1999). Energy is derived from the fission of ^{233}U that is produced within the conventional ^{232}Th – ^{233}U fuel cycle. Radowsky and co-workers have however employed a modified fuel composition and core assembly containing a series of *seed-blanket* units that are designed to improve the efficiency of the ^{232}Th – ^{233}U fuel cycle. The arrangement of a thorium oxide blanket around an enriched uranium core within each *seed-blanket* unit results in more efficient coupling of neutrons to the thorium fuel compared to the earlier homogenous distribution of enriched uranium within the thorium fuel. Also, the requirement in earlier thorium light water reactors to reprocess the ^{233}U in order to separate it from the thorium fuel before feeding it back into the reactor core is replaced by the more favourable and cost effective in situ burning of ^{233}U.

Another promising future application demonstrating the potential of thorium as a major nuclear fuel has emerged as a result of experiments at CERN, in Switzerland. These experiments, motivated by Carlo Rubbia and performed by Rubbia and co-workers (1994a,b) are investigating the use of thorium in an 'energy amplifier' type reactor. This reactor uses a high flux of fast neutrons produced by spallation when protons from a particle accelerator interact with a liquid lead target surrounding the thorium fuel. This reactor is capable of fully sustaining the ^{232}Th - ^{233}U fuel cycle. A very significant advantage of this concept reactor is its inherent safety since a fast shut down of the fission process occurs when the external proton beam is shut off. Also, the fact that the neutrons required for generation and fission of the fissile isotope ^{233}U are produced by the external proton source facilitates the use of sub-critical amounts of reactor fuel. Long lived radioactive daughter products produced during the ^{233}U fission process can be substituted in place of the thorium fuel rods and used as fuel while at the same time they are broken down into less potent radioactive isotopes. Also, large quantities of weapons grade ^{239}Pu can be incinerated in this way resulting in the reduction of world plutonium stockpiles. Only a small fraction of energy produced as a result of fission is required to drive the proton accelerator, hence the term 'energy amplifier'. Efficient use

of fuel can, according to Rubbia and co-workers (1994b), result in 780kg of thorium producing the same amount of energy as 200 tons of uranium used in a Pressurised Water Reactor (PWR). The use of thorium, uranium and plutonium as nuclear fuels in conventional fission reactors constitute the most significant industrial application of these actinide elements.

A novel interdisciplinary field of study linking both nuclear and atomic physics has emerged over the last decade. The actinide isotopes ^{229}Th and ^{235}U have low-lying nuclear energy levels (isomers) at 3.5eV and 76.8eV respectively. The proximity of these nuclear levels to the energy of electronic transitions within the atom has resulted in a series of theoretical studies in ^{235}U (Zon & Karpeshin 1990) and ^{229}Th (Karpeshin et al. 1992) designed to investigate the acceleration of nuclear decay from low-lying isomeric levels using the technique of *laser-induced resonant internal conversion.* ^{233}U decays via emission of an α-particle to form ^{229}Th with significant population of both the ground state and 3.5eV nuclear levels of the ^{229}Th isotope. A significant acceleration in the nuclear decay of the ^{229}Th 3.5eV isomeric level is achieved using the laser-induced resonant internal conversion technique, which results in the transfer of nuclear energy to an electron in the atomic shell (internal conversion). Absorption of a laser photon by the atomic shell or stimulated emission from the atomic shell using laser photons of suitably tuned frequency compensates for a small difference in energy that generally exists between a given nuclear transition and an atomic transition. This can result in the acceleration of the ^{229}Th decay rate by up to a few orders of magnitude.

Recently, Shaw and co-workers (1999) have identified ultra violet 'gamma ray' emission, which they suggest, may be due to the spontaneous decay of the ^{229}Th 3.5eV nuclear isomeric level which is the lowest known energy level of all nuclei. The possibility of nuclear excitation to the 3.5eV isomeric state in ^{229}Th using the inverse technique of nuclear excitation during non-radiative electronic transitions (NEET) has been explored both theoretically (1996) and experimentally (1998) by Karpeshin and co-workers at St. Petersburg University in Russia. In this technique, energy due to electronic de-excitation in the atomic shell is transferred directly to the nucleus without the emission of radiation and results in nuclear excitation.

1.1.3 Actinide Physics and Chemistry

The chemical and physical properties of an element, its alloys and compounds are largely determined by its electronic structure. The actinide series is similar to that of the lanthanide series in that the outer f subshell is progressively filled along both series. The 5f subshell is filled progressively in the case of the actinides and the 4f subshell in the case of the lanthanides. Despite this similarity in electronic configurations (excepting the difference in principal quantum number of unity) along both series, the physical and chemical properties of actinide solids are more complex (Haire 1995, Edelstein 1995). This is due to the participation of outer 5f electrons in chemical bonding in the solid state environment. 5f electrons in the 'light' actinides up to plutonium (Z=94) are delocalised (itinerant) and consequently participate in bonding whereas for the heavier elements, from americium (Z=95) to lawrencium (Z=103), 5f electrons are localised and therefore chemically inert (Johansson 1995). In contrast to the actinides, 4f electrons in the lanthanides are localised right across the series with the exception of the early element cerium (Z=58) and, consequently, 4f wavefunctions retain their atomic character. Research on actinide solids has greatly benefited from the vast body of knowledge accumulated on both the d-transition metals and the f-transition lanthanide series. This is due to the fact that early actinide members are 5f transition metals with bonding 5f electrons whereas heavier actinides behave as 6d transition metals due to the chemically inert 5f subshell (Brooks et al. 1995). Experimental evidence and consequently an increased understanding of the behaviour of 5f electrons can be obtained from investigation of actinide solid state properties.

The main actinide solid state research interests and current understanding of actinide solid state properties have been comprehensively compiled by Fournier and Manes (1985) and also in a series of review articles that were published in 1995 following a European actinide solid state workshop at Bühlerhöhe in Germany in 1994 (Journal of Alloys and Compounds, 1995). A systematic approach, such as that employed successfully in the study of lanthanide properties, is complicated in the actinides due to the varying localisation/delocalisation of 5f electrons across the series. This assertion is highlighted in a review by Gschneidner (1995) of crystal structures in both series. 5f delocalisation in the earlier actinides results in quite a number of possible bonding configurations involving 6s, 6d, 7s, and 5f orbitals which are nearly degenerate in energy. They give rise to a variety of low symmetry crystal structures that vary widely

with small changes in energy or pressure (Wills & Eriksson 1992, Haire 1995). Physical and chemical properties of the later actinides, characterised by localised 5f electrons, exhibit a higher degree of similarity to the preceding lanthanide series. Haire (1995) discusses the corresponding variations in atomic volumes (within the solid environment), melting behaviour, cohesive properties, bulk moduli and magnetism that occur across the actinide elements and the resulting information with reference to the behaviour of 5f electrons that can be obtained by studying some of the above properties. High-pressure experiments on the heavier actinides result in altered crystal structures caused by increased 5f valence occupancy. The corresponding induced 5f delocalisation provides valuable insights into actinide electronic structure (Benedict et al. 1989, Eriksson et al. 1993, Holzapfel 1995).

A rapidly expanding field of research linking both solid state and atomic physics is the investigation of atomic and ionic clusters. They provide a unique opportunity to study the variation in electron energy level distribution due to the changing environments encountered on moving between the free atom and clusters of various sizes. Actinide clusters, ranging from a few atoms to macroparticles (~10^6 atoms), have been produced for the first time by Gangrskii and co-workers (1997). High-power pulsed laser light was used to irradiate thorium and uranium metal targets with various on-target laser irradiances in the region of ~3×10^7 to ~3×10^9 W/cm^2. The number of atoms per cluster was determined using laser resonance fluorescence, time-of-flight measurements and counting of the number of tracks of fission fragments from the cluster nuclei. It was demonstrated that the yield of clusters (of a given size) depends on the temperature of the plasma formed and also on the target material under study.

1.1.4 Actinide Atomic Research

Studies of the actinide atom are challenging to both the theorist and the experimentalist. The heavy actinide atom represents a highly correlated electron system and much further work is required to truly elucidate its electronic structure (Baer 1984). The close proximity of 5f and 6d electron energies across the series resulted in an initial misinterpretation of many actinide ground state configurations whereby the importance of the 5f electrons was ignored and the actinide series was believed to form a 6d

transition series (Judd in Blaise & Wyart, 1992). The low lying configurations of the neutral actinide atom and lowly charged ions are characterised by several open subshells (5f, 6d and 7s) which give rise to a large number of terms within each configuration. Also the proximity in energy of the 5f, 6d and 7s subshell energies results in level crossing and a high density of energy levels close to the atomic/ionic ground state (Fournier & Manes 1985, Figure 1.9 Section 1.1.7). Actinide spectra are consequently very rich and complex. The interpretation of spectra and the determination of actinide electronic structure require advanced atomic structure codes. These codes must account for relativistic effects (which scale as Z^4) and the intermediate coupling schemes that dominate behaviour in heavy actinide atoms/ions (Fournier & Manes 1985).

A comprehensive energy level table has been compiled by Blaise and Wyart (1992) which details a series of atomic emission experiments and one absorption experiment (on uranium, Radziemski et al. 1971) performed on the elements actinium (Z=89) to fermium (Z=100) between 1936 and 1989. Neutral atoms and up to four times ionised ions were studied using electrodeless discharge tubes, hollow cathode tubes, sliding spark and arc sources, flash photolysis and flash discharge techniques. Emission lines from higher ions (Th^{7+} to Th^{15+}, U^{12+} and U^{14+}, Th^{10+} and Th^{12+}) created in a laser produced plasma (LPP) source have also been identified (Carroll & O'Sullivan 1981, Carroll et al. 1984, 1986). More recent laser plasma studies by McCormack and O'Sullivan (1993) have observed and identified emission lines in Th^{11+} and U^{13+}. The UV emission spectrum of a laser-produced uranium plasma in the 5 to 30eV range was recorded by Williams (1973). Such a *'non-fissioning'* laser plasma is similar to expected gas-core nuclear reactor conditions and provides valuable information on the behaviour of uranium atoms under such conditions. Lowly charged Th^- negative ions have been have been produced by Berkovits and co-workers (1991) in a negative ion sputter source. Measurements of the photodetachment cross sections of these ions were made when the ion beams interacted with a laser beam.

The study of very highly charged ions is of particular interest in the development of laser fusion (Cable et al. 1994) and also, in the particular case of actinide elements, to the investigation of relativistic and quantum electrodynamic (QED) effects (Marrs et al. 1994). Seely and co-workers (1986) have observed, measured and calculated the wavelengths of emission lines from Th^{60+} to Th^{63+} and U^{62+} to U^{65+} created in a laser produced plasma. The inclusion of QED effects in the Multi-Configurational Dirac-

Fock (MCDF) calculations performed by Seely and co-workers using the computer code of Grant and co-workers (1980) greatly improved the accuracy of the calculated wavelengths. Hydrogen-like high-Z ions are of particular interest for studies of the influence of relativistic and QED effects on atomic energy levels due to the absence of multielectron interactions. Studies at the Bevalac synchrotron at the Lawrence Berkeley Laboratory include measurements of lamb shifts in helium-like uranium (U^{90+}) (Munger & Gould 1986) and lithium-like uranium (U^{89+}) (Schweppe et al. 1991) and the observation and measurement of n=2 → n=1 transitions of U^{91+} and U^{90+} (Briand et al. 1990). All of these measurements were performed on ions travelling at near relativistic speeds produced by the beam foil technique. An electron beam ion trap (EBIT) has been developed at the Lawrence Livermore Laboratory where studies can be performed on near stationary ions that are relatively cold, having energies of just a few eV per ion. Experiments include measurements of the electron impact ionisation cross sections of U^{91+} and U^{90+} (Marrs et al. 1994), the n=2→2 transition energies in Th^{80+} to Th^{87+} and the isotope shift of the n=2→2 transitions energies between $^{233}U^{86+.....89+}$ and $^{238}U^{86+.....89+}$ (Widmann et al. 1997).

Atomic properties of the neutral actinide atom and lowly charged ion have been investigated using a range of atomic sources. The various sources used within the series of experiments compiled by Blaise and Wyart (1992) produce both neutral and ionic species. A number of other experimental techniques are suited to the vaporisation of actinide elements and also produce predominantly neutral and lowly charged atomic species. Evaporative techniques have been used to produce and study the motion of small numbers of Th^+ ions stored in an RF trap (Käbler et al. 1992). Measurement of the Doppler fluorescent linewidths obtained upon laser excitation of the Th^+ ions enabled Käbler and co-workers to study the motion of these stored ions. Evaporative heating techniques are particularly suited to the production of low-density neutral atomic beams which are suitable for Resonance Ionisation Mass Spectroscopy (RIMS) studies in order to determine trace elemental concentrations, isotopic concentrations and basic atomic properties such as ionisation potentials (Billen et al. 1993). ^{232}Th and ^{238}U have the longest actinide half-lives of 1.4×10^{10} years and 4.5×10^{9} years respectively and together with their various long-lived isotopes, are used for radio-dating in oceanography and environmental physics (Bard et al. 1990). Ionisation mass spectroscopic techniques provide more accurate and precise geological dating measurements than α-counting methods (Bard et al. 1990, Eichler et al. 1997). Billen and co-workers (1993) have

performed RIMS studies in order to investigate isotopically selective and non-selective schemes for ionising thorium. In subsequent studies they (Billen et al. 1995) combined both continuous thermal heating of a thorium metal sample and pulsed laser evaporation of the thorium surface with a low on-target laser irradiance of ~ 6×10^3 W/cm^2 in order to produce a thorium vapour. The use of a pulsed laser results in improved temporal and spatial overlap between the atoms produced and the ionising pulsed laser beams used in RIMS, thus resulting in an increased efficiency of the ionising process. RIMS has been employed by Köhler and co-workers (1995) to determine the ionisation potentials of thorium, neptunium and plutonium, and for the first time, americium and curium, using atomic beams produced by evaporation of the actinide sample from a hot filament. Eichler and co-workers (1997) have developed a more efficient actinide atomic beam source using a 'sandwich-type' filament with actinide oxides deposited between a series of metal layers. The resulting thermodynamic and kinetic behaviour of the actinide atoms in this layered structure results in low operating temperatures, reduced thermal ionisation and increased source stability and efficiency. Beams of plutonium, curium, berkelium and californium were produced in a tantalum – actinide oxide – titanium filament. Eichler suggests alternative filament configurations for the production of atomic beams of the lighter and more refractory actinide elements thorium and uranium. Their boiling points of 4788°C (Th) and 4131°C (U) are the highest of the known actinide boiling points (CRC handbook, 1998-99). The laser-produced plasma is particularly suited to the study of atomic photoabsorption in refractory and in some cases corrosive elements (Carroll & Costello 1986, 1987).

1.1.5 Recent Advances in Actinide Research at Large-Scale Synchrotron Facilities

Photoabsorption, photoionisation, photoelectron and photoion studies of actinides in the atomic, ionic, molecular and solid state phase have been limited, due in part to their radiotoxicity which has resulted in limited access to experimental large-scale synchrotron facilities. Recent efforts[1] have been made by several research institutions world-wide to address the problem of limited synchrotron access. Researchers working at the U8 beamline operating in the VUV to soft X-ray energy region of 20 to 300eV at

[1] A discussion of early actinide synchrotron experiments during the 1980's is deferred until the next section.

the Advanced Light Source at the Lawrence Berkeley Laboratory (Heimann et al. 1992) plan to perform photoelectron spectroscopy of gaseous atoms and molecules, spectroscopy of ions and actinide spectroscopy. Denlinger and co-workers (1995) have measured the 4d, 4f and valence electron energy levels in the energy range 100 to 1300eV of trace amounts of curium (< 1 microgram) deposited on a platinum disk using the 'ultraESCA' photoelectron spectrometer at another soft X-ray ALS beamline. Similar 'spectromicroscopy' studies were performed by Tonner and co-workers (1995) on trace amounts of plutonium oxide whereby a surface image was formed from the spatial dependence of the observed photoelectron spectral features. A specialised soft X-ray beamline dedicated solely to actinide studies has been built at the Photon Factory located at the National Laboratory for High Energy Physics in Japan (Yokoya et al. 1998). Here the combination of a variable polarising undulator and a vari-spaced plane grating monochromator produce circularly polarised light in the energy region 0.28 to 1.5keV. Proposed experimental investigations include photoemission studies of actinide compounds and magnetic circular dichroism measurements of ferromagnetic actinide compounds. The European Synchrotron Radiation Facility (ESRF) at Grenoble has completed an X-ray beamline that became operational in late 1998. Experiments include X-ray absorption spectroscopy (XAS) studies to investigate different physical and chemical forms of actinide elements that occur in solids and solutions in the energy region 5 to 35keV with particular application to radioecological research (Nitsche 1995). This beamline is operated by the Forschungszentrum Rossendorf (FZR) materials research centre, located in Dresden, Germany.

1.1.6 XUV and VUV Photoabsorption Studies of Thorium and Uranium

Extensive studies were carried out in the 1960's and 1970's to investigate the inner shell 4d $\rightarrow$ f photoabsorption and photoionisation spectra of the lanthanide elements (Zimkina et al. 1967, Haensel et al. 1970, Mansfield & Connerade 1976, Radtke 1979a,b). In particular, attention focused on the observation of a so-called Giant Dipole Resonance feature arising from the unusual behaviour in the spatial extent of the 4f wavefunction in the lanthanides. These results prompted similar investigations into 5d $\rightarrow$ f transitions in the two most accessible actinide elements (thorium and uranium) that began in the 1980's with the measurement of the XUV photoabsorption spectrum of

UF_4 and ThF_4 vapours by Connerade and co-workers (1980a,b) at the Bonn 500MeV synchrotron. These measurements were designed to study the effect, if any, of a fluorine cage on the spatial extent of the 5f wavefunction. The similarity between these results and photoabsorption spectra of thin solid thorium and uranium films obtained by Cukier and co-workers (1978) at the ACO storage ring in Paris provided evidence that the 5d $\rightarrow \overline{5,\varepsilon}$f giant dipole resonance was truly atomic in origin. Cukier and co-workers (1980) also measured the fast electron energy loss spectra (FEELS) of thorium and uranium metals and tetrafluoride molecular solids in the energy range of 2 to 160eV. Fuggle and co-workers (1974) have measured (and compiled previously known data on) the binding energies of the N-P shells of thorium and uranium metal and oxide films using X-ray photoelectron spectroscopy.

The first actinide atomic photoabsorption experiment was performed by Pantelouris and Connerade (1983). They measured the XUV photoabsorption spectrum of uranium vapour in the 100 to 140eV energy region at the Bonn 500MeV synchrotron. Subsequent XUV photoabsorption studies were performed by Carroll and Costello on neutral thorium (1986) and uranium (1987) atoms formed in a recombining laser-produced plasma. The synchrotron results on 5d subshell excitation in uranium showed a single, narrow, apparently autoionising feature in the 5d photoabsorption spectrum of atomic uranium. This is in conflict with the giant dipole resonance (described in detail in Section 1.2) observed by Carroll and Costello (1987) and predicted by Wendin (1984). XUV photoion studies of uranium vapour performed by Haase and co-workers at the BESSY synchrotron (1989) have recently been published in van Kampen and co-workers (2000). The latter paper reports the 5d $\rightarrow$ f photoabsorption spectrum of atomic uranium recorded at the Centre for Laser Plasma Research (CLPR) in Dublin City University (DCU). Both the new laser plasma results and the photoion data confirm the broad giant dipole resonance and call into question the earlier synchrotron data. Van Kampen and co-workers (2000) have also measured the 6p $\rightarrow$ d photoabsorption spectrum of the neutral uranium atom for the first time. The only other VUV measurement of the 6p$\rightarrow$d photoabsorption/ photoionisation cross section of an actinide atom to date was made on atomic thorium in the energy region 17 to 32eV (Meighan et al. 1999) as part of the current thesis. Also during the course of this work, inner shell photoabsorption experiments were performed along the thorium isonuclear sequence in order to study the collapse of the 5d $\rightarrow \overline{5,\varepsilon}$f Giant Dipole Resonance feature with

increasing ionicity (Meighan et al. 2000). All experimental investigations detailed in this thesis were performed at the CLPR in DCU and at the Lasers for Science Facility (LSF) in Rutherford Appleton Laboratory (RAL), UK.

1.1.7 5f and 6d Orbital/Wavefunction Collapse in Ground State and Low-Lying Configurations along the Actinide Series

The ground state electronic configurations of actinide atoms consist of a closed shell radon core ($1s^2 2s^2 2p^6 3s^2 3p^6 3d^{10} 4s^2 4p^6 4d^{10} 4f^{14} 5s^2 5p^6 5d^{10} 6s^2 6p^6$) to which electrons occupying the 5f, 6d and 7s subshells are added (see Table 1.1).

Table 1.1: Ground state electronic configurations of lanthanide and actinide atoms

Z	Lanthanide	Ground State	Z	Actinide	Ground State
57	Lanthanum	$5d6s^2$	89	Actinium	$6d7s^2$
58	Cerium	$4f5d6s^2$	90	Thorium	$6d^27s^2$
59	Praseodymium	$4f^36s^2$	91	Protactinium	$5f^26d7s^2$
60	Neodymium	$4f^46s^2$	92	Uranium	$5f^36d7s^2$
61	Promethium	$4f^56s^2$	93	Neptunium	$5f^46d7s^2$
62	Samarium	$4f^66s^2$	94	Plutonium	$5f^67s^2$
63	Europium	$4f^76s^2$	95	Americium	$5f^77s^2$
64	Gadolinium	$4f^75d6s^2$	96	Curium	$5f^76d7s^2$
65	Terbium	$4f^96s^2$	97	Berkelium	$5f^97s^2$
66	Dysprosium	$4f^{10}6s^2$	98	Californium	$5f^{10}7s^2$
67	Holmium	$4f^{11}6s^2$	99	Einsteinium	$5f^{11}7s^2$
68	Erbium	$4f^{12}6s^2$	100	Fermium	$5f^{12}7s^2$
69	Thulium	$4f^{13}6s^2$	101	Mendelevium	$5f^{13}7s^2$
70	Ytterbium	$4f^{14}6s^2$	102	Nobelium	$5f^{14}7s^2$
71	Lutetium	$4f^{14}5d6s^2$	103	Lawrencium	$5f^{14}6d7s^2$

Progressive filling of the outer 5f subshell along the actinide series follows a similar pattern to that of the 4f subshell along the lanthanide series resulting in similar ground state electronic configurations. As the atomic number Z increases along both series the

binding energy of 4f and 5f electrons increases more rapidly than that of the 5d and 6d electrons respectively. This increase in binding energy is due to a reduction in the spatial extension of the 4f and 5f orbitals resulting in the formation of the 4f and 5f transition series respectively. This is similar to the collapse of the 3d, 4d, 5d, and 6d orbitals[2], which gives rise to the various d-transition series in the periodic table. The 5d and 6d orbitals collapse at the start of the 4f and 5f transition series but the increased binding energies of the 4f and 5f electrons result in the preferential filling of these f subshells. However, it can be seen from Table 1.1 that it is sometimes energetically more favourable for electrons to occupy both f and d orbitals resulting in more complex ground state configurations having several open subshells. This is due to the fact that the binding energy of a given electron in an atom depends not only on the atomic number but also on the presence of electrons in other subshells with which it interacts via the Coulomb force (Section 4-13 Cowan, 1981).

Orbital collapse is a direct consequence of the interplay between the potential and kinetic energy contributions to the effective potential ($V_{eff}(r)$) for electrons occupying the 'higher' angular momentum orbitals such as d, f, g etc. The expression for $V_{eff}(r)$ is given by

$$V_{eff}(r) = V(r) + \frac{l(l+1)\hbar^2}{2m_e r^2} \tag{1.1}$$

where $\hbar$ is Plancks constant divided by 2π, m_e is the electron mass and r is the atomic radius. $V(r)$ represents the potential an electron experiences in the combined Coulomb field of the nucleus and all other N-1 electrons present in the N-electron atom/ion. The second term represents the kinetic energy of the electron during its centrifugal orbital motion about the nucleus. This $V_{kinetic}(r)$ term derives from the circular motion of the electron and is given by

$$V_{kinetic}(r) = \frac{1}{2} I\omega^2 \tag{1.2}$$

where I is the moment of inertia of the electron and ω is the electron angular velocity. Using the relation $L = I\omega$ for the electron orbital angular momentum, expression (1.2) becomes

$$V_{kinetic}(r) = \frac{1}{2}\left[\frac{L^2}{I}\right] \tag{1.3}$$

[2] The 'super-heavy' elements beyond lawrencium form a 6d transition series (Seaborg 1989).

For an orbiting electron, $I = m_e r^2$ and $L = \sqrt{l(l+1)}\hbar$. Substituting these relations into (1.3) the expression for $V_{kinetic}(r)$ given in (1.1) is obtained

$$V_{kinetic}(r) = \frac{l(l+1)\hbar^2}{2m_e r^2} \tag{1.4}$$

In the case of hydrogen, the electron potential energy $V(r)$ is solely determined by the electrostatic attraction of the nucleus and can be expressed simply as

$$V(\mathrm{r}) = -\frac{e^2}{4\pi\varepsilon_o r} \tag{1.5}$$

where e is the electronic charge and ε_o is the permittivity of free space. $V_{eff}(r)$ for hydrogen therefore becomes

$$V_{eff}(r) = -\frac{e^2}{4\pi\varepsilon_o r} + \frac{l(l+1)\hbar^2}{2m_e r^2} \tag{1.6}$$

Using (1.6), $V_{eff}(r)$ for an nl electron in hydrogen can be determined directly without the need for a more detailed atomic structure calculation. The profile of $V_{eff}(r)$ for nl electrons in hydrogen is shown in Figure 1.1 for l=0,1,2,3.

Figure 1.1: Effective potential energy $V_{eff}(r)$ for nl electrons in hydrogen for l=0,1,2,3

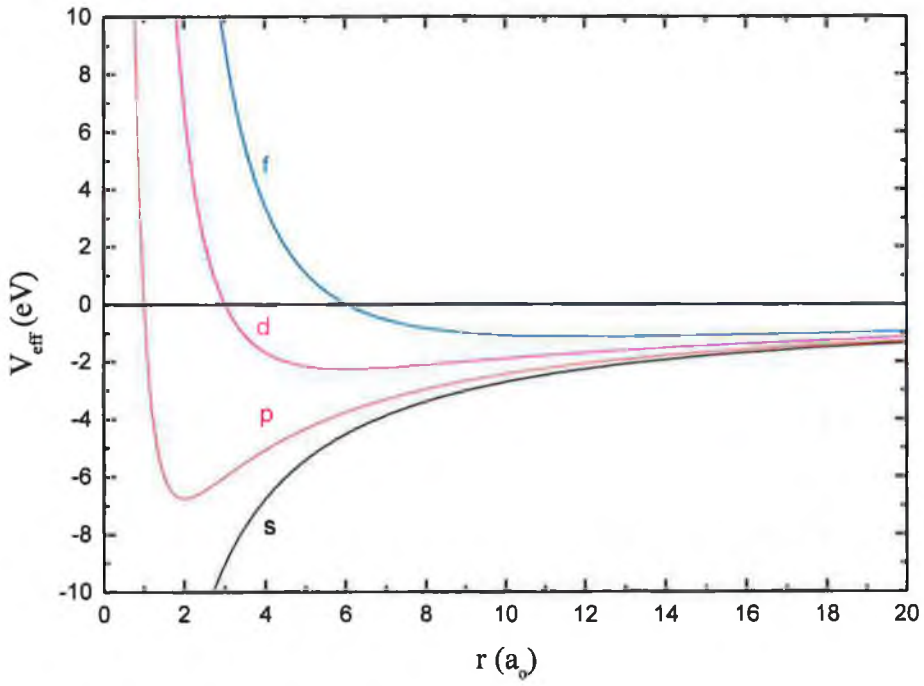

a_o, the unit used to express the atomic radius r, is the Bohr radius and is equal to

$$a_o = \frac{\hbar^2 4\pi\varepsilon_o}{m_e e^2} = 0.5292\,\text{Å} \tag{1.7}$$

For an s electron $V_{eff}(r)$ is just $V(r)$ and tends to -∞ at r = 0, thus allowing the s electron to penetrate the nuclear core. For p, d and f electrons l is no longer non-zero and because of the $1/r^2$ dependence of the centrifugal term it tends to +∞ more rapidly than $V(r)$ tends to -∞ as r→0. Consequently, p, d and f electrons experience a repulsive centrifugal force that increases with increasing l. This results in greater exclusion of higher angular momentum electrons from the atomic core region and their corresponding radial wavefunctions $P_{nl}(r)$ are to a large extent delocalised in the long-range Coulombic potential well that has formed.

In the case of a multielectron atom, $V_{eff}(r)$ is no longer accurately described by expression (1.6). The second term $V_{kinetic}(r)$ remains unchanged, but the first term, $V(r)$ must account for the combined effect of the electrostatic attraction of the nucleus and the inter-electron repulsion due to the other N-1 electrons present in the atom/ion. $V(r)$ now becomes

$$V(\bar{r}_1,\bar{r}_2....\bar{r}_N) = \sum_{i=1}^{N} -\frac{Ze^2}{4\pi\varepsilon_o \bar{r}_i} + \sum_{i<j=1}^{N} \frac{e^2}{4\pi\varepsilon_o \bar{r}_{ij}} \qquad (1.8)$$

where $\bar{r}_i$ is the relative vector co-ordinate of the i^{th} electron with respect to the nucleus and $\bar{r}_{ij} = |\bar{r}_i - \bar{r}_j|$ is the distance between each i and j electron pair. The first term in (1.8) represents the attractive force of the nucleus on all N electrons and the second term describes the inter-electron repulsion and is summed over all pairs of electrons. The exact nature of $V(r)$ can only be determined for hydrogen and a method known as the *central field approximation* was initially proposed by Hartree and Slater in order to obtain an approximation to $V(r)$ in a many-electron atomic system (Bransden & Joachain 1983). This method is based on the *independent particle model* whereby each electron moves in the spherically symmetric central field of the nucleus and the other N-1 electrons. All many-electron atomic structure computational codes are based on the *central field approximation.*

The effective potentials $V_{eff}(r)$ for s and p electrons in a many-electron atom are of similar shape to those in the case of hydrogen (see Figure 1.1). For d and f electrons however, the combined effect of the electron cloud and the strong influence of the centrifugal term ($V_{kinetic}$) for these high angular momentum electrons result in a dramatic change in the shape of the effective potential $V_{eff}(r)$ from the hydrogenic case. A schematic representation of $V_{eff}(r)$ for d and f electrons is shown in Figure 1.2. Unlike

the case of hydrogen, $V_{eff}(r)$ now assumes the form of a double well potential, where the inner and outer wells are separated by a finite centrifugal barrier. Goeppert-Mayer (1941) first used this idea of a double well potential to successfully explain the collapse of the 5f orbital at the onset of the actinide series. The outer well (region 1) is similar to the long range Coulombic potential well for d and f electrons in the case of the

Figure 1.2: Schematic representation of the double well effective potential $V_{eff}(r)$ for d and f electrons in a many-electron atomic system

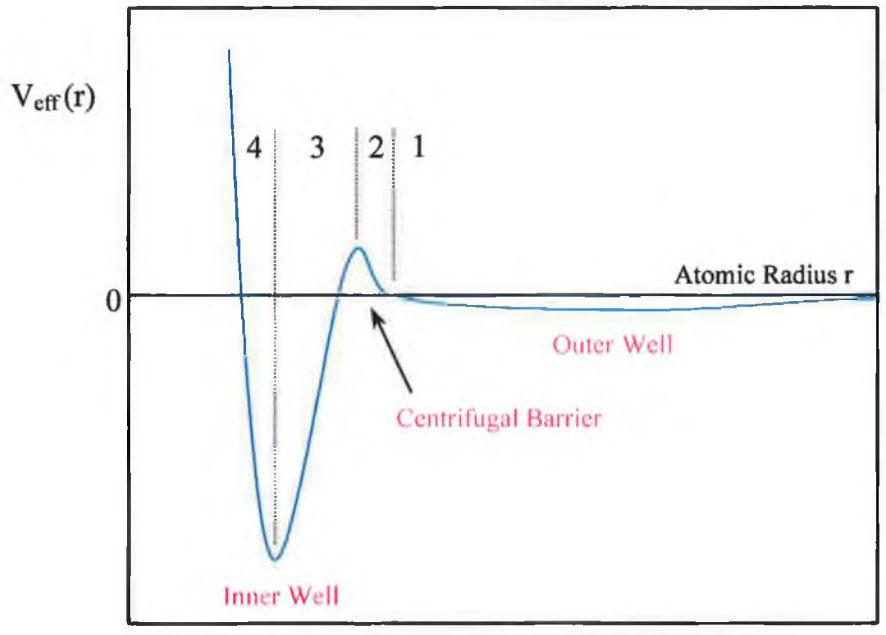

hydrogen atom (Figure 1.1). The significant contribution by the centrifugal term to $V_{eff}(r)$ excludes the d or f electron from the atomic core in much the same way as for hydrogen only now the centrifugal barrier is finite. An electron residing in this outer region is well screened from the attractive potential of the nucleus by the presence of inner shell electrons and therefore experiences a hydrogenic potential. The onset of the repulsive centrifugal barrier (region 2) occurs as r is reduced and the centrifugal term, which depends on $1/r^2$, becomes increasingly dominant at smaller atomic radii. This finite potential barrier is known as the *outer centrifugal rise* (Connerade 1978a). Moving from region 2, closer to the nucleus, the electron begins to penetrate the main electronic cloud and as a result, screening of the nuclear charge is significantly reduced. The attraction of the nucleus now exceeds centrifugal repulsion and results in a suppression of the centrifugal barrier and the formation of an inner short-range potential well (region 3). This inner well is referred to as a short range well due to the fact that its edges fall off faster than the 1/r fall off that occurs in the outer Coulombic well

(Connerade 1998). As r is decreased further the centrifugal term rapidly regains dominance resulting in the formation of an infinite centrifugal barrier known as the *inner centrifugal rise* (Connerade 1978a).

The formation of this double well potential for d and f electrons in a many-electron atom is essentially due to two factors: (i) the significance of the centrifugal term ($V_{kinetic}$) in the effective potential of high angular momentum electrons and (ii) the electronic cloud of inner shell electrons surrounding the atomic nucleus. The shape of this double well potential is extremely sensitive to local conditions existing within the atom such as atomic number Z, atomic ground and excited state configurations, ionicity, and the presence of inner shell holes due to electron excitation/ionisation. In atomic environments where a centrifugal barrier exists the d or f electron can reside predominantly in the outer well and so is delocalised. This situation is illustrated in Figure 1.3 where a configuration averaged relativistic Hartree with exchange (HXR) calculation was performed for a 5f electron in actinium (Z=89) using the Cowan suite of atomic structure codes (1981). These codes represent the main theoretical method of atomic structure calculation used throughout this work and details of these codes are given in Appendix I. The HXR method includes relativistic terms incorporated into the

Figure 1.3: Relativistic Hartree with exchange (HXR) calculation of $V_{eff}(r)$ and $P_{nl}^2(r)$ for a 5f electron in Actinium (7s6d5f)

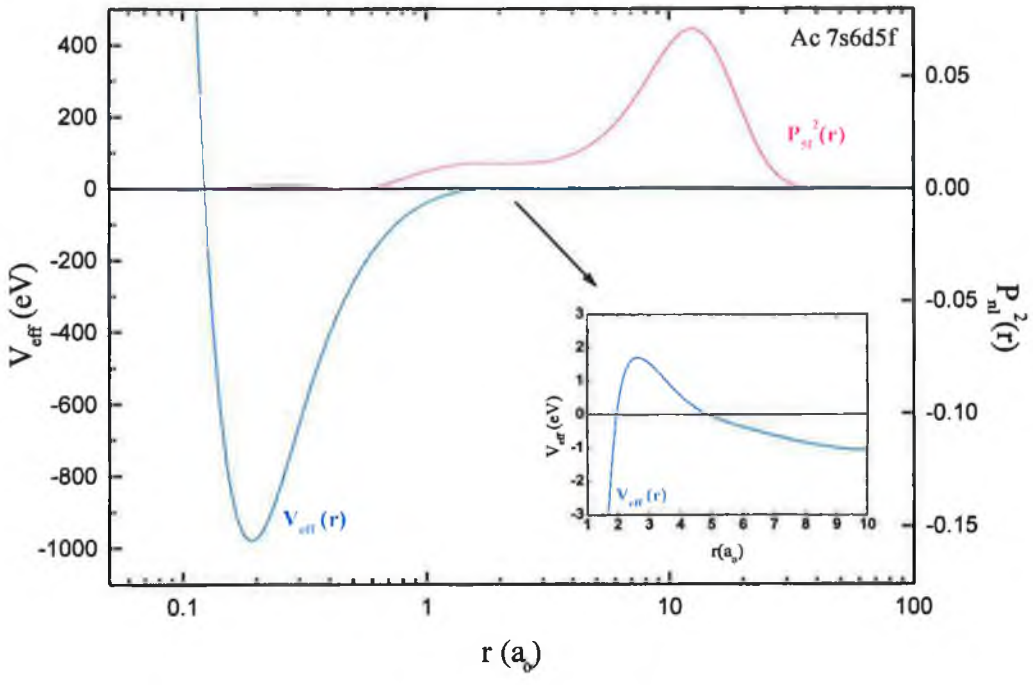

framework of a non-relativistic computational method. The ground state configuration of neutral atomic actinium is $7s^2 6d$. Following the method used by Griffin et al. (1969) a calculation of the effective potential $V_{eff}(r)$ for a 5f electron in actinium was performed using a 7s6d5f ground state. This serves to provide a good approximation to the shape of the 5f potential in this atom. The inset in Figure 1.3 provides an expanded view of the centrifugal barrier region and the presence of a positive centrifugal barrier in $V_{eff}(r)$ is evident. Also shown is $P_{nl}^2(r)$ for a 5f electron. This is the square of the one electron radial wavefunction ($P_{nl}(r)$) and is known as the *radial probability distribution function.* It represents the probability of finding an electron at a particular distance r from the nucleus. $P_{nl}(r)$ is a constituent of the one-electron wavefunction[3] $\psi_{n l m_l m_s}$ such that

$$\psi_{n l m_l m_s}(r, \vartheta, \phi, s_Z) = \frac{1}{r} P_{nl}(r) \cdot Y_{l m_l}(\vartheta, \phi) \cdot \sigma_{m_s}(s_Z) \qquad (1.9)$$

where $Y_{l m_l}$ and σ_{m_s} represent the spherical harmonic and spin functions respectively. $P_{5f}^2(r)$ peaks at $\sim 12 a_o$ with the result that the 5f electron is predominantly delocalised and resides in the outer Coulomb well. In Figure 1.4 a similar calculation is shown for thorium where a $7s^2 6d5f$ configuration, rather than the ThI $6d^2 7s^2$ thorium ground state configuration, was used. The unitary increase in Z upon the transition from actinium to thorium results in the collapse of the positive centrifugal barrier from a maximum value of 1.69eV in actinium to -0.87eV in thorium. Also, the depth of the inner potential well has increased from –981eV to –1046eV. This increased depth of the inner well increases the binding strength of this well and is due to the increased attraction of the nucleus with increasing Z. It is important to note that the centrifugal term is independent of Z and it is the additional nuclear attraction that results in the reduction of the centrifugal barrier (Clark & Lucatorto in Connerade et al. 1987). As a result, the inner potential well is capable of supporting a greater number of bound states. $P_{5f}^2(r)$ now peaks at $\sim 1 a_o$ due to the increased localisation of the 5f electron. This dramatic change in the spatial extent of the 5f wavefunction, resulting in the increased probability of finding the 5f electron in the inner rather than the outer well, is due to a reduction in the centrifugal barrier existing in the double well potential and is termed *wavefunction collapse*. It is important to note that it is not necessary for the centrifugal barrier to be positive in order to expel the electron from the core. In some cases, a centrifugal barrier having a negative maximum can still be sufficient to prevent significant core penetration. The

[3] With the inclusion of the $\sigma_{m_s}(s_Z)$ spin function by Fock and Slater to the original Hartree wavefunction, the one-electron wavefunction is more correctly termed a 'spin-orbital'. For further details refer to Appendix I.

Figure 1.4: Relativistic Hartree with exchange (HXR) calculation of $V_{eff}(r)$ and $P_{nl}^2(r)$ for a 5f electron in Thorium ($7s^2 6d5f$)

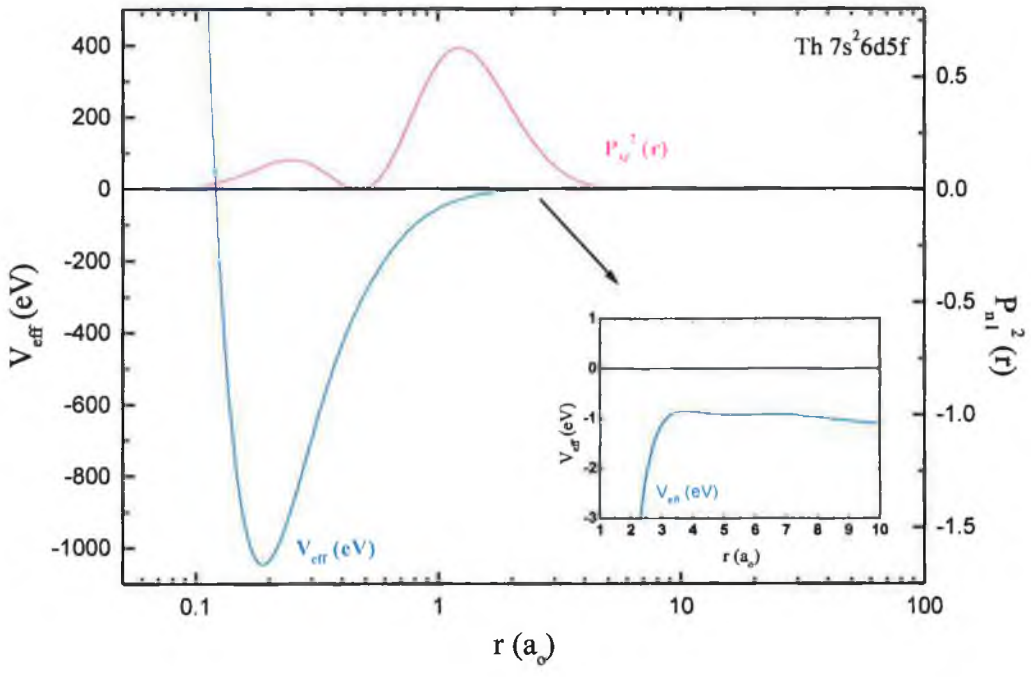

degree of localisation/delocalisation of the atomic wavefunction is extremely sensitive to the barrier height and the use of different computational atomic structure codes resulting in slightly different profiles for $V_{eff}(r)$ can lead to differing results. The occurrence of wavefunction collapse for d and f electrons results in the dramatic increase in electron binding energies mentioned earlier and, as a result, the filling of such collapsed orbitals represents the onset of the various d and f transition series.

The variation in the spatial extent of the various s, p, d, f and g orbitals along the periodic table, calculated by Cowan (1981), is shown in Figure 1.5. A more dramatic collapse is observed for the higher angular momentum subshells (d, f and g) compared to the more gradual contraction of s and p orbitals with increasing Z. The radial expectation value <r> for each n*l* orbital was calculated by Cowan using the relativistic Hartree with exchange (HXR) method (Sections 7.12 & 8.6 of Cowan, 1981). <r> is defined as the mean radial position of an electron in a given n*l* orbital and serves as a representation of the spatial extent of that particular orbital. The value <r> is obtained using

$$< r >= \int_0^\infty r P_{nl}^2(r) dr \qquad (1.10)$$

where $P_{nl}(r)$ is the normalised radial function such that

$$\int_0^\infty P_{nl}^2(r)dr = 1 \qquad (1.11)$$

where r, the distance from the centre of the nucleus, is expressed in Bohr radii. For the calculations shown in Figure 1.5, and for all following atomic structure calculations outlined in this section, $P_{nl}(r)$ is calculated numerically and then using (1.10) a value for <r> is obtained.

Figure 1.5: Radial expectation values <r> calculated by Cowan (1981) using the Hartree with exchange method including relativistic corrections (HXR) for the various orbitals of neutral atoms along the periodic table

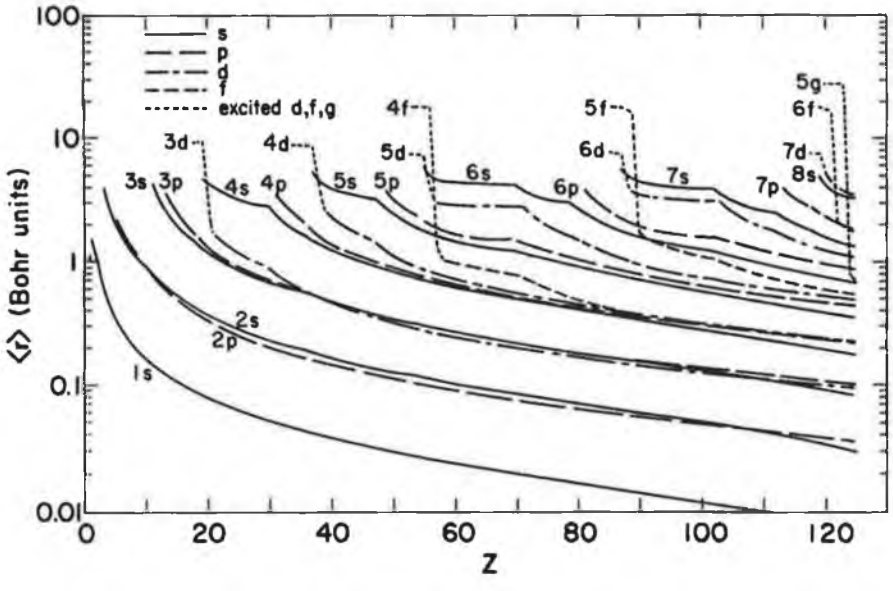

With particular reference to atomic thorium, the configuration averaged HXR calculation performed by Cowan (Section 7.12 Cowan, 1981) in Figure 1.5 shows a significant drop in the value of <r> for the 6d wavefunction at Z=88 (radium) before the start of the actinide series. The 5f wavefunction is calculated to collapse just after the start of the actinide series at Z=90 (thorium). The $6d^27s^2$ ground state of atomic thorium has no 5f occupancy and therefore a configuration of excited neutral thorium that has a 5f occupancy was used in order to obtain a value of <r>. Similarly, at the onset of each of the calculated d, f and g orbitals shown in Figure 1.5, excited atomic configurations in which these orbitals are occupied rather than the true atomic ground states were used in these calculations. Radial expectation values <r> for several valence and inner subshells across the lanthanide series calculated by Cowan (1973) using the non-relativistic HX method are shown in Figure 1.6. Desclaux has performed relativistic self-consistent Dirac-Fock (DF) calculations in order to obtain <r> values for atoms across the actinide series (Desclaux 1973, Chapter A in Fournier & Manes 1985). These

results are shown in Figure 1.7 and are in good general agreement with the HXR results of Cowan (Figure 1.5). Figures 1.6 and 1.7 clearly demonstrate the collapse of both the 4f and 5f wavefunctions from a maximum mean radial position of <r> ≅ $20a_o$ to values of <r> below $1a_o$. In both calculations performed by Cowan and Desclaux, the

Figure 1.6: Radial expectation values <r> for the outer orbitals of neutral atoms along the lanthanide series calculated by Cowan (1973) using the non-relativistic Hartree with exchange (HX) method

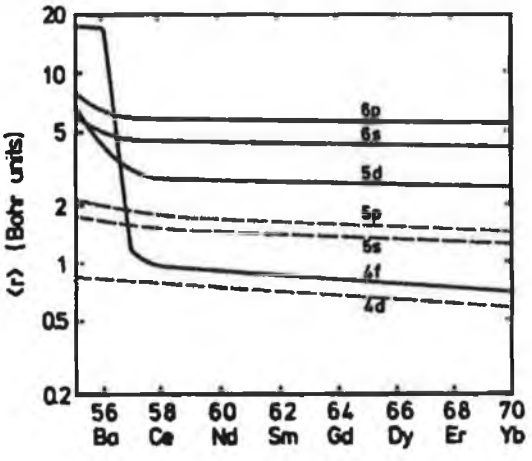

Figure 1.7: Radial expectation values <r> for the outer orbitals of neutral atoms along the actinide series calculated by Desclaux (in Fournier & Manes 1985) using the relativistic self-consistent Dirac-Fock method

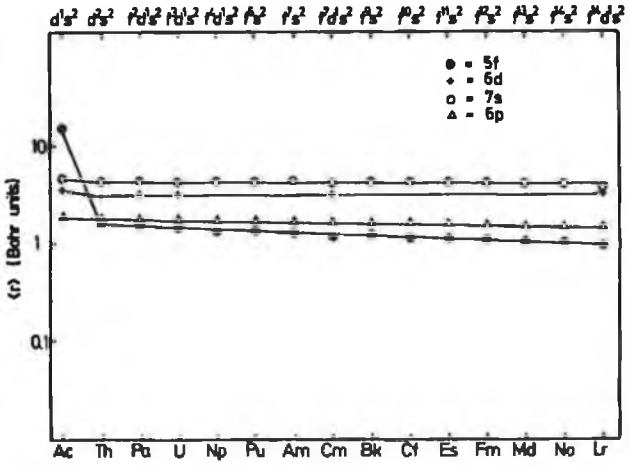

maximum value of <r> for the 5d and 6d wavefunctions in the lanthanides and actinides respectively lies below a value of $10a_o$. Both d orbitals are, as expected, initially more localised than f orbitals due to their lower orbital angular momentum l which reduces the dominance of the centrifugal term (and hence the repulsion from the nucleus).

Desclaux and Freeman (1984) stress the importance of relativistic atomic structure calculations in the treatment of both inner and outer shell electrons whose interaction with each other in heavy atomic systems is critical to their behaviour. Relativistic effects are more apparent for inner shell electrons in close proximity to the nucleus and travelling close to the speed of light. A *direct* manifestation of the relativistic speed of the inner shell electron is an increase in electronic mass and as a result, an increase in electron binding energy. This can be understood qualitatively in that the Bohr radius a_o of a hydrogenic orbital is inversely proportional to the electronic mass m_e (see 1.7). The electron binding energies (scaling as Z^2 and typically on the order of 0.1MeV for a thorium 1s electron) are therefore increased at smaller radii and the resultant contraction of inner shell orbitals towards the nucleus gives rise to improved screening of the nucleus by inner shell electrons. This latter *indirect* relativistic effect causes a reduction in the attractive force of the nuclear potential on outer shell electrons. Both *direct* and *indirect* relativistic effects influence the potential experienced by an electron in a given orbital and correspondingly the spatial extent of this orbital. Desclaux (1973) performed calculations using the self-consistent Dirac-Fock method in order to investigate the balance of both of these relativistic effects. The *indirect* effect was found to dominate for more weakly bound orbitals having a high orbital angular momentum (especially f orbitals) whereas *direct* effects dominated for more strongly bound orbitals of lower *l*.

The radial expectation value <r> calculated using the relativistic self-consistent Dirac-Fock method is shown across the actinide series for the outer orbitals 5f, 6p, 6d and 7s in Figure 1.8. These data were calculated in a similar manner to that shown in Figure 1.7 but were taken from tabulated results provided by Desclaux and Freeman (Table 3, 1984) and are shown overlapped with the results of Hartree-Fock calculations with relativistic corrections (HFR) performed as part of this thesis work using the Cowan suite of atomic structure codes.

The motivation behind the comparison of the HFR method with the relativistic DF method was to assess the performance of the former, which includes relativistic terms e.g., the spin-orbit interaction, as a perturbation. The Dirac-Fock <r> values shown in Figure 1.8 represent an average of the various spin orientations of a given subshell. Both calculations are based on a configuration-averaged atomic ground state. The trend in <r> across the series for a given subshell is very similar for both calculations with the

best agreement for the 5f subshell where HFR values differ from DF values by at most 0.2%. For the 6p, 6d and 7s subshells HFR values of <r> differ by a maximum of 3.3%,

Figure 1.8: Comparison of radial expectation values <r> for the 5f, 6p, 6d and 7s subshells computed using the relativistic Dirac-Fock (DF) method and Hartree-Fock (with relativistic corrections, HFR) method

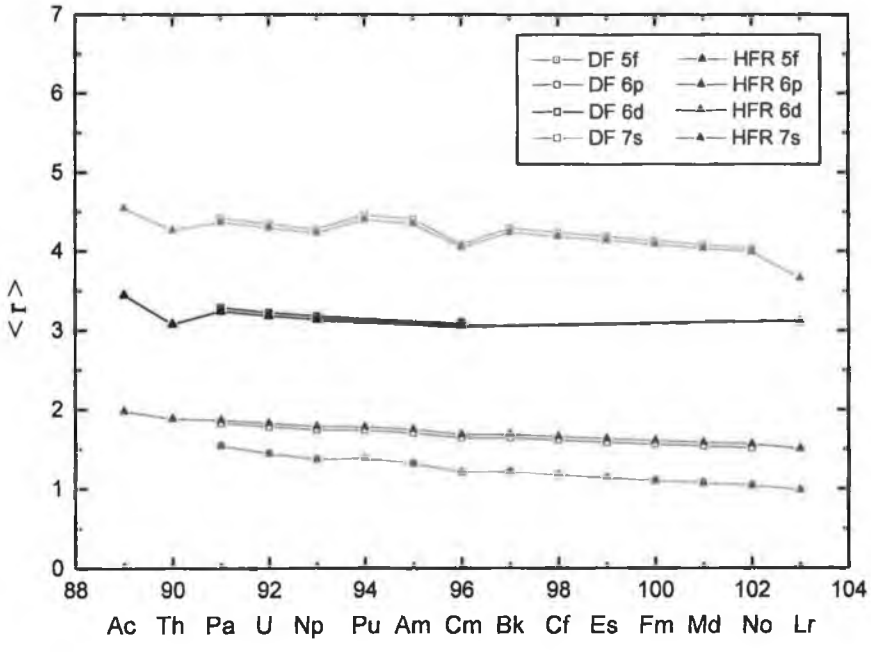

1.5% and 1.4% respectively. A comparison of the one-electron binding energies for the 5f, 6p, 6d and 7s valence subshells is shown in Figure 1.9 for both DF and HFR methods. As before, the DF results represent an average of the various spin orientations for a given subshell. The trend in binding energy across the series is very similar for both methods of calculation. The displacement between both sets of results for a given subshell is slightly higher than for Figure 1.8 with the HFR binding energies differing from the DF values by a maximum of 9.6%, 9.9%, 14.9% and 11.3% for the 5f, 6p, 6d and 7s subshells respectively. Both Figures 1.8 and 1.9 serve to demonstrate the good agreement between both the HFR method employed in this work and a fully relativistic treatment. The proximity of the binding energies of the 5f, 6d and 7s subshells is reflected in the competition for occupancy of these subshells in the various actinide atomic ground states (see Table 1.1). This results in level crossing and a high density of energy levels close to the lowest actinide ground state level. The dramatic collapse of the 5f wavefunction and the corresponding increase in 5f binding energy that occurs in the early actinides is not evident from the calculations shown in Figures 1.8 and 1.9. This is due to the fact that only ground state atomic configurations were used in both of

the calculations shown and there is no 5f occupancy in the atomic ground state for elements before protactinium (Z=91). The HXR calculations shown in Figures 1.3 and 1.4 serve to illustrate the dramatic nature of 5f wavefunction collapse with the unitary increase in Z upon transition from actinium to thorium.

Figure 1.9: *Comparison of the one-electron binding energies for the 5f, 6p, 6d and 7s subshells computed using the relativistic Dirac-Fock (DF) method and Hartree-Fock (with relativistic corrections, HFR) method*

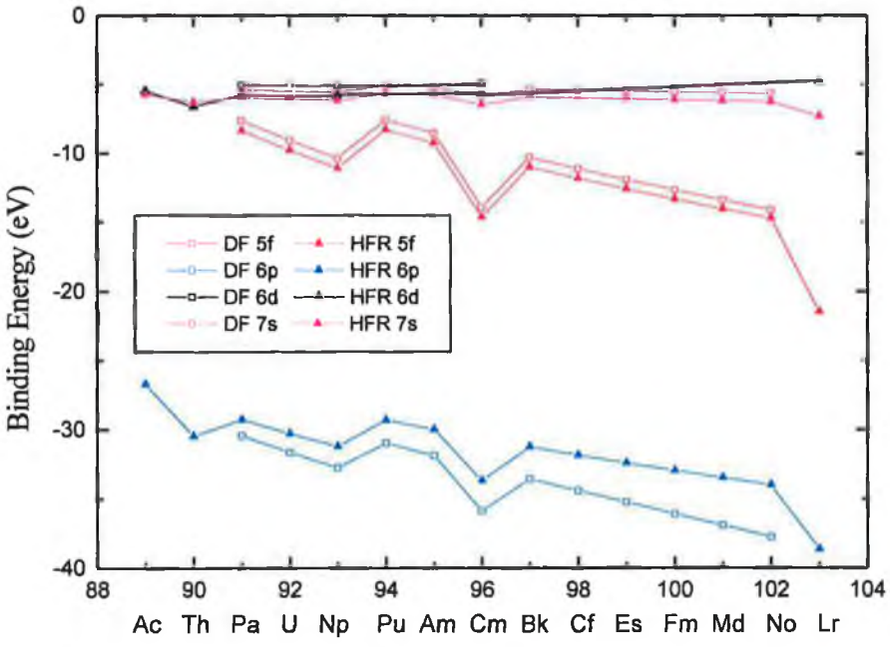

1.1.8 Investigation of Orbital Collapse along the Thorium Isonuclear Sequence

In this work, the collapse of the 5f and 6d atomic wavefunctions is studied in the single atomic/ionic system of thorium rather than along the isoperiodic sequence of the actinide series. Investigations focus on the change in the spatial extent of both wavefunctions with increasing ionicity (i.e. along the isonuclear sequence) and also in the presence of a core hole created in the inner shell XUV and VUV photoabsorption process. In the XUV region, 5d→f transitions are excited at a photon energy of ~100eV, whereas in the VUV, 6p→d transitions occur at ~25eV. The presence of a core hole created in the inner shell photoabsorption process results in reduced electron screening of the nuclear potential and alters $V_{eff}(r)$ resulting in a change in the spatial extent of the

d and f radial wavefunctions. Promotion of a core electron can, in some cases, result in a collapse of the outer d or f wavefunction in an excited configuration where initially the wavefunction was un-collapsed in the ground state atomic configuration. This is termed *configuration-dependent* wavefunction collapse (Connerade 1978a).

Photoabsorption, photoelectron and photoion studies have been performed in the lanthanides and preceding elements along isonuclear (Lucatorto et al. 1981, O'Sullivan et al. 1996, Koizumi et al. 1997, Murphy et al. 1999, Cummings et al. 2000, D'Arcy et al. 2000), isoperiodic (Fomichev et al. 1967, Zimkina et al. 1967, Haensel et al. 1970, Radtke 1979a,b, Richter et al. 1989a,b, Baier et al. 1993), isoelectronic (Hansen et al. 1989, Köble et al. 1995) and isoionic (Koizumi et al. 1996) sequences. The most gradual form of wavefunction collapse occurs along an isoperiodic sequence. As Z is increased progressively along such a sequence so too is the number of electrons. The screening of the nucleus by inner shell electrons also increases but not as efficiently as the attraction of the nucleus and hence a collapse of an outer orbital (where $l > 1$) will eventually occur. Along isoionic sequences the initial ionisation results in an already contracted wavefunction and hence accelerated collapse as one proceeds up the sequence. Along isoelectronic sequences, the simultaneous increase in Z and decrease in the number of electrons results in highly ineffective screening of the nuclear charge and hence a more rapid onset of wavefunction collapse is observed. Along an isonuclear sequence the entire wavefunction collapse is observed in a single atomic/ ionic system. However, since Z remains fixed, the contraction is more gradual than along an isoelectronic sequence.

As mentioned earlier, in the HXR, DF and HFR calculations presented in Section 1.1.7 only a configuration-averaged ground state of the neutral atom was considered. It is well know that wavefunction collapse is a term dependent effect (Hansen 1972, Connerade 1978a) and the effective potential V_{eff} for each individual term of a given configuration must be determined before calculating term dependent radial wavefunctions which can differ quite significantly from each other. Term dependent Hartree-Fock (HFR) calculations were performed using the Cowan code (1981) for the ^1S, ^1D, ^1G, ^3P and ^3F terms of the ground state of neutral thorium, ThI $[Rn]6d^27s^2$. For the 6d subshell, the variations in $\langle r \rangle$ and in the profile of the effective potential $V_{eff}(r)$ were investigated for each ground state term. These results, coupled with experimental data serve to indicate

(within the scope of our atomic calculations) that the 6d wavefunction is collapsed in atomic thorium (see Section 5.2.3, Chapter 5).

Kucas and Karazija (1998) have stated however that the use of the same radial orbital for all electrons occupying a given n*l* subshell (for a given term) is insufficient for elucidating the true nature of wavefunction collapse. They have performed *spin-polarised* calculations that involve the calculation of a one-electron radial orbital for each electron within a given n*l* subshell. Using this method for $4d^{10}4f^{N} \rightarrow 4d^{9}4f^{N+1}$ transitions in lanthanide atoms, they observed that the complete collapse of 4f orbitals does not occur for $4d^{9}4f$ configurations until the middle of the series at the transition from europium (Z=63) to gadolinium (Z=64). They also note that LS dependent Hartree-Fock calculations performed for the same $4d^{9}4f^{N+1}$ configurations having more than one 4f electron result in complete 4f wavefunction collapse at the start of the lanthanide series. In addition, Kucas and Karazija (1998) have been able to interpret the shift from predominantly photoionisation to photoexcitation processes that occurs in the experimental photoabsorption spectra of atoms at the centre of the lanthanide series (see Richter et al. 1989b for a compilation of these experimental results). An important note sounded by Kucas and Karazija (1998) is that the true nature of the experimentally observed photoabsorption features (Giant Dipole Resonances) can be understood by studying their position with respect to ionisation limits. This fact has been employed in the interpretation of both the 6p (Meighan et al. 1999) and 5d (Meighan et al. 2000) photoabsorption spectra of atomic/ionic thorium for which, at present, no spin polarised calculations have been performed.

In summary, the specific nature of 5f and 6d electrons in the actinides depends critically on the effective potential $V_{eff}(r)$ in which they move and also on indirect relativistic effects due to their interaction with inner shell electrons. These factors combine to dramatically influence the observed actinide photoabsorption spectra. A direct manifestation of the 5f and 6d electronic behaviour in atomic/ionic thorium is the appearance of a strong broad asymmetric resonance in the vicinity of 5d ionisation limits and also in the 6p photoexcitation spectrum. This profile is termed a Giant Dipole Resonance (GDR) and changes appearance radically with increased ionicity due to the collapse of the 5f wavefunction[4] that occurs along the thorium isonuclear sequence.

[4] HFR calculations performed during the course of this work (Section 5.2.3 Chapter 5) indicate that the 6d wavefunction is collapsed in neutral thorium and therefore in ionic thorium.

1.2 The Atomic Giant Dipole Resonance

1.2.1 Background

The term *Giant Resonance* has been employed within several scientific disciplines to describe resonance profiles that occur over a broad range of physical environments spanning from the atomic nucleus to the solid. Consequently, such resonance features are excited over a vast energy range from typically a few eV to tens of MeV. Giant resonance features observed experimentally in nuclear, atomic, molecular, cluster and solid state environments have been the subject of much inter-disciplinary research efforts (Connerade et al. 1987, Bréchignac & Connerade 1994, Kaplan et al. 1996, Kaplan 1997). The *collective* nature of such resonance profiles has also prompted theorists to explore the many-body effects contributing to their formation (Connerade 1992, 1998). The central physical scenario unifying all types of giant resonance is the existence of fermion particles (protons, neutrons or electrons) within a short-range confining potential that results in the coherent, collective motion, of such particles. The resulting giant resonances possess similar physical attributes and their strong, broad and asymmetric profiles dominate, and in some cases, eliminate other spectral features.

Giant resonances were first observed in the atomic nucleus where they were termed *Giant Dipole Resonances* due to the fact that their origin lies in the collective oscillation of neutrons and protons relative to each other, thus resulting in a large electric dipole moment (Baldwin & Kleiber 1947, 1948, DeShalit & Feshbach 1974). This new term was then adopted by the many-body atomic theorist, Göran Wendin (1973), and applied to atomic features, the formation of which could also be attributed to collective effects. In addition, the observed atomic resonances exhibit profiles similar to nuclear resonances. Atomic giant dipole resonances occur in the VUV to soft X-ray inner shell electronic photoabsorption spectra of many atomic and ionic species located along the transition regions of the periodic table (Clark & Lucatorto in Connerade et al. 1987). The atomic giant dipole resonance originates deep within the atom, close to the atomic nucleus, involving the excitation of inner shell (localised) electrons. Consequently this resonance survives in molecular, cluster and solid state environments and modulations in its profile serve as a probe of the local environmental conditions within which the atom is located (Connerade et al. 1987, Bréchignac & Connerade 1994, Luberek & Wendin 1996). In fact this atomic feature was first observed in the photoabsorption spectra of thin solid lanthanide films by Zimkina and co-workers (1967) who realised

the atomic origin of such resonances despite popular belief at the time that they originated from band structure within the solid state environment (see overview by Connerade 1998).

Another form of giant resonance occurs in the solid state environment and also in clusters of sufficient size (possessing at least 8 to 10 valence electrons that are involved in binding the atoms together). It is known as a *plasmon* resonance and is caused by the collective oscillation of the outer (delocalised) valence electrons. The long range atomic Coulomb potential is modulated in the solid/cluster environment by an exponentially decaying factor which results in a 'screened' Coulomb potential that is of sufficiently short range so as to induce coherent electron oscillations (Bréchignac & Connerade 1994). Such plasmon resonances were first observed in sodium clusters (DeHeer et al. 1987, Hoheisel et al. 1988) and the investigation of these resonances in the VUV photoionisation spectra of the fullerene molecules C_{60} and C_{70} has also been performed (Hertel et al. 1992). The plasmon resonance, like the atomic giant dipole resonance, provides an excellent means to study the cluster/solid environment and in particular the changes occurring upon transition from an atomic-like cluster system to the solid state medium. This form of collective resonance enables the study of more global properties due to the fact that its origins lie in the oscillation of delocalised valence electrons. Information on the shape of different clusters (spherical or deformed) is determined by the number of valence electrons and can be obtained from an analysis of the differing resonance profiles observed (Kaplan et al. 1996).

The following sections detail the properties and origin of the atomic giant dipole resonance with particular emphasis on the evolution of such resonances in the changing local environment existing within an atom whose ionicity is progressively increased along an isonuclear sequence.

1.2.2 Properties of an Atomic Giant Dipole Resonance

The general profile of an atomic giant dipole resonance is illustrated in Figure 1.10. The curves shown represent the experimental photoabsorption cross sections of uranium from Connerade et al. 1980a) in the inner shell 5d→f excitation energy region of 70 to

Figure 1.10: $5d \rightarrow \overline{5,\varepsilon f}$ giant dipole resonances in the XUV photoabsorption cross sections of metallic uranium and uranium tetrafluoride (UF_4) vapour (from Connerade et al. 1980a)

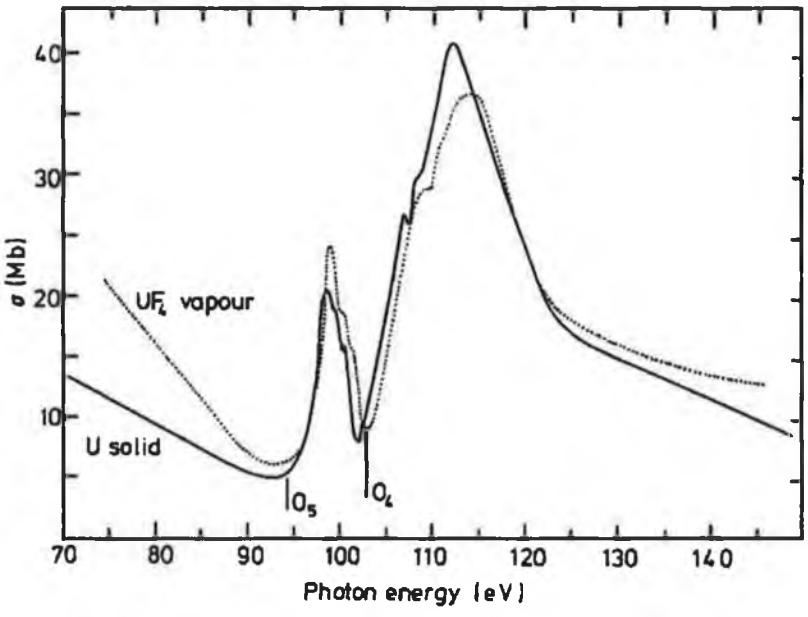

150eV. The striking similarity in the general shape of the resonance in both the solid and molecular environments and also their similarity to the XUV photoabsorption cross section of the free uranium atom (Carroll & Costello 1987, van Kampen et al. 2000) provides evidence of the highly localised nature of this kind of resonance. The use of the term 'giant' is particularly appropriate in describing these resonance features whose peak values are typically on the order of 10's to ~100 Mb (1 Mb = 10^{-18}cm^2), exhausting all of the available oscillator strength for the total number of electrons in a given inner subshell. Their 'non-Rydberg' nature is evidenced by their dominance of atomic inner shell photoexcitation/ photoionisation spectra resulting in a complete or sometimes partial suppression of the conventional discrete Rydberg series expected (Connerade 1978a). The spin-orbit interaction splits the resonance into a series of peaks located either above or below their associated inner subshell ionisation limits depending on whether the final state/s contributing to a given peak lie/s in the photoionisation or discrete photoexcitation spectrum respectively. A combination of the exchange interaction and the extent of wavefunction collapse determines the energy of these final state/s and therefore the location of the resonance peaks. These processes are explored further in the following section. The resonance peaks shown in Figure 1.10 lie above the solid state ionisation limits, O_5 and O_4, of the 5d subshell ($5d_{5/2}$ and $5d_{3/2}$ limits). In some cases however a resonance peak can actually straddle both the photoexcitation and photoionisation spectra. The main resonance has a broad asymmetric profile with a long

'tail' towards higher energies. Its width is typically on the order of a few to several tens of eV and the corresponding lifetimes of $\sim 10^{-17}$ seconds are on the order of two to three times shorter than that of the autoionising Fano-Beutler resonance (Connerade in Connerade et al. 1987). The width of the resonance increases linearly with increasing distance from its associated inner subshell ionisation threshold as a consequence of the uncertainty principle (see Section 1.2.3). Also, above threshold, the giant dipole resonance is more specifically termed a giant continuum resonance (Connerade in Connerade et al. 1987). It is understood to originate from the direct promotion of an inner shell electron to the continuum, unlike the case of the autoionising Fano-Beutler resonance whose formation involves excitation to a discrete excited state, embedded in the continuum of another channel, before ionisation occurs. Giant dipole resonances located below threshold in the discrete photoexcitation spectrum more closely resemble a Fano-Beutler resonance and will autoionise into available continuum channels.

The atomic giant dipole resonance has been described by Wendin (1973) to originate from the collective oscillation of all electrons within the inner subshell subject to excitation. Connerade (1992), however has stated that the resonance lifetimes ($\sim 10^{-17}$ seconds) are shorter than the period of oscillation of these electrons at a given peak resonance energy (E_{res}) resulting in an over-damping of such collective oscillations (Connerade 1992). Also, higher harmonics of the resonance frequency have not been observed. Therefore the analogy between the three types of resonance (atomic, nuclear giant dipole resonance and plasmon resonance) mentioned in Section 1.2.1 does not necessitate the collective oscillation of series of particles. The overriding physical phenomenon is the confinement of a fermion particle in a short-range potential.

The photoabsorption process permits the observation of *dipole allowed* transitions such as the atomic giant *dipole* resonance due to the $\Delta l = \pm 1$ selection rule. This feature is observed for resonant (ground state) $np \rightarrow nd$ (for $n = 3,4,5,6$) and $n'd \rightarrow n'f$ (for $n' = 4,5$) transitions (where $\Delta n = 0$ and $\Delta n' = 0$) for medium and high-Z elements located in the transition regions of the periodic table. The conditions necessary for the formation of the atomic giant dipole resonance are detailed in Section 1.2.3 and those resulting in its collapse are described with reference to the first observation of such behaviour in the case of the barium isonuclear sequence (Lucatorto et al. 1981) in Section 1.2.5.

1.2.3 The Origin of an Atomic Giant Dipole Resonance

The following list outlines the specific physical conditions required within the atomic environment for the formation of an atomic giant dipole resonance. The profile of the resonance for a given atom/ion is a direct result of the combination of these physical conditions that have been discussed in detail by Connerade (1978a, 1987, and 1998).

(i) Inner shell excitation must be to a high angular momentum subshell such as d or f, where the effective potential $V_{eff}(r)$ for d and f electrons has a double well profile similar to that illustrated in Figure 1.2 of Section 1.1.7. Non-Coulombic effects (e.g. the centrifugal term in equation (1.1)) contributing to the effective potential form a short-range inner well giving rise to non-Rydberg spectral features. These features would not be observed in the case of a long range Coulombic well, which results in the formation of a conventional Rydberg series.

(ii) The inner well must be of sufficient binding strength so as to confine the escaping electron (in a resonantly localised continuum state) for a finite period of time on the order of 10^{-17} seconds. This results in the broad width of the giant continuum resonance observed above threshold.

(iii) A high degree of spatial overlap between the initial and final state radial wavefunctions is required in order to devote a large portion of available oscillator strength into a single channel e.g. 5d→5f. The photoionisation cross section σ is proportional to the degree of overlap between the initial and final (continuum) radial wavefunctions, which is expressed using the radial overlap integral $R_{\varepsilon,l\pm1}$ given by

$$R_{\varepsilon,l\pm1} = \int_0^\infty P_{nl}(r) r P_{\varepsilon,l\pm1}(r) dr \tag{1.12}$$

where $P_{nl}(r)/r$ and $P_{\varepsilon,l\pm1}(r)/r$ are the radial parts of the single-particle wave functions of the initial (discrete) and final (continuum) states respectively. ε is the kinetic energy of the escaping electron (in Rydbergs). $\sigma(\varepsilon)$ for a particular nl subshell is

$$\sigma_{nl}(\varepsilon) = \frac{4}{3}\pi^2 \alpha a_o^2 \left[\frac{N_{nl}(\varepsilon - \varepsilon_{nl})}{(2l+1)}\right] \times \left[l R^2_{\varepsilon,l-1} + (l+1) R^2_{\varepsilon,l+1}\right] \tag{1.13}$$

where α is the fine structure constant (~1/137), a_o is the Bohr radius (0.5292Å), N_{nl} is the number of electrons in the nl subshell, ε_{nl} (in Rydbergs) is the binding energy of an

electron in the n*l* shell and *l* is the orbital angular momentum quantum number (Kennedy & Manson, 1972).

(iv) All higher Rydberg levels are excluded from the inner potential well by the centrifugal barrier in the double well effective potential. For example, in the case of 5d→5f inner shell excitation this means that all nf levels where n>5 reside in the outer Coulombic potential well which is capable of supporting an infinite number of bound states. The centrifugal barrier prevents the penetration of higher nf radial wavefunctions into the core region and therefore their overlap with the initial 5d wavefunction is so small that Rydberg structure is suppressed.

As previously mentioned, the 5f wavefunction collapses into the inner well at the start of the actinide series. The extent of this collapse however is strongly *term dependent* (Connerade 1978a) and the nature of $V_{eff}(r)$ can differ radically for different terms of the final state configuration resulting in term dependent radial wavefunctions. The exchange interaction pushes states with anti-parallel spins (singlet states) to higher energies than states with parallel spins (triplet states). Discrete giant dipole resonance structure below the 5d ionisation limits is predominantly due to 5d→5f excitations where the final state terms contributing to the resonance peak are bound states of the inner well that autoionise into available continuum channels. This situation is illustrated in Figure 1.11 where the collapsed 5f terms reside in the inner potential well.

In the case of the $4d^{10}\rightarrow 4d^9 4f$ giant dipole resonance in atomic barium (Z=56) the $4d^9 4f\ ^3P$ and $4d^9 4f\ ^3D$ levels are bound states and their corresponding peaks lie in the discrete 4d spectrum. The $4d^9 4f\ ^1P$ however lies in the photoionisation spectrum of the 4d subshell and was proposed by Ederer et al. (1975) to be pushed into the εf continuum by the exchange interaction where it subsequently autoionises. Mansfield & Connerade (1976) and Wendin (1976) argued that the inner potential well is too shallow to support the $4d^9 4f\ ^1P$ state and it consequently resides in the outer well. However, a $4d^9 \varepsilon f\ ^1P$ continuum state possessing an energy slightly higher than the $4d^9 4f\ ^1P$ state can surmount the centrifugal barrier and penetrate the atomic core. There its wavefunction (free electron travelling wave) can assume the character of the $4d^9 4f\ ^1P$ wavefunction in the vicinity of the inner potential well just as if the $4d^9 4f\ ^1P$ state was a *bound* state of the inner well. States such as this $4d^9 \varepsilon f\ ^1P$ state have been labelled $\overline{4,\varepsilon f}$ (Mansfield &

Connerade, 1976) due to their hybrid nature. As a result of their resonant 4f-like behaviour in the inner well, coupled with a free electron travelling wave nature outside this well these states are known as *resonantly localised continuum states* (Wendin 1976). Similarly in the case of actinide atoms/ions a $\overline{5,\varepsilon}f$ state can form in the vicinity of the inner well (see Figure 1.11).

Figure 1.11 illustrates the main physical processes underpinning the formation of the giant dipole resonance in an actinide atom/ion. All nf Rydberg levels (where n>5) reside in the outer Coulombic potential well. The 4f wavefunction collapses at the start of the

Figure 1.11: Schematic representation of the double well effective potential $V_{eff}(r)$ for an nf electron which can support a $\overline{5,\varepsilon}f$ resonantly localised continuum state in an actinide atom/ion

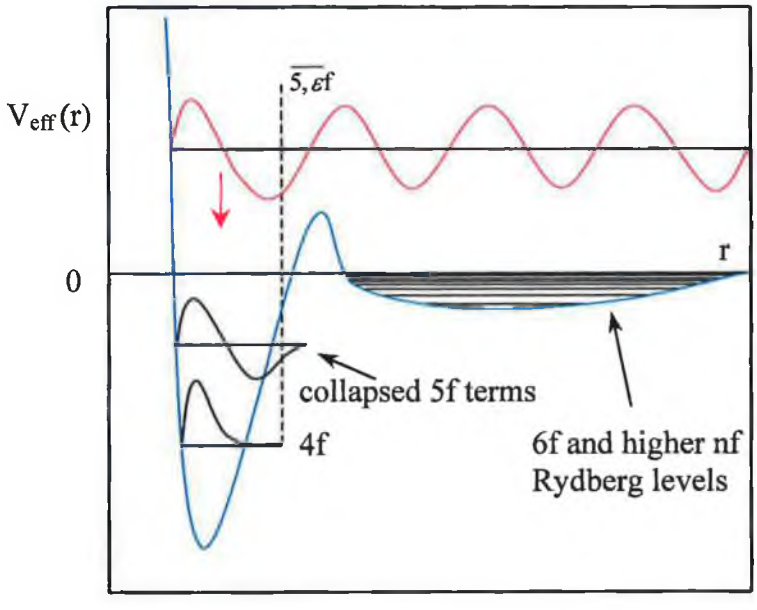

lanthanide series and is shown as a bound state of the inner potential well. This narrow well is only capable of supporting a finite number of widely spaced energy levels. As the depth of the inner well is increased it's binding strength increases and so too is its ability to support an increased number of states. The depth of this well increases with increasing Z along an isoperiodic sequence and also with reduced nuclear screening along an isonuclear sequence. A combination of both increased Z and reduced nuclear screening contribute to its depth along isoelectronic and isoionic sequences. The ultimate profile of an atomic giant dipole resonance is independent of the shape of this inner potential well. This is a consequence of Schwinger's theorem, which states that

only the binding strength of the inner well influences the resonance profile (Connerade 1978a, 1998). A direct result of this theorem is that the shape of the inner well cannot be determined from investigations of the giant dipole resonance profile.

As the binding energy of the inner well is increased the energy of the resonance sweeps downwards toward threshold as the $\overline{5,\varepsilon}$f resonantly localised continuum state is drawn closer to the inner well. The lifetime Δt of this state increases as it nears the inner shell ionisation threshold (located at $V_{eff}(r)=0$ in Figure 1.11). The width of the giant continuum resonance ΔE is related to the lifetime of the resonantly localised continuum state Δt by Heisenberg's Uncertainty Principle,

$$\Delta E \Delta t \approx \hbar \tag{1.14}$$

and as a result, ΔE decreases as Δt increases with increasing proximity to threshold. This linear relationship is illustrated in Figure 1.12 for experimentally determined widths of the 4d $\rightarrow$ $\overline{4,\varepsilon}$f giant dipole resonance in the lanthanide and preceeding elements. The $\overline{4,\varepsilon}$f resonantly localised continuum state becomes a bound state of the inner well once it has reached the critical binding strength to support the 4f state.

Figure 1.12: Linear variation in the width of the 4d→$\overline{4,\varepsilon}$f giant dipole resonance with energy above the 4d threshold as the depth of the inner potential well varies with Z (experimental data from Connerade in Connerade et al. 1987)

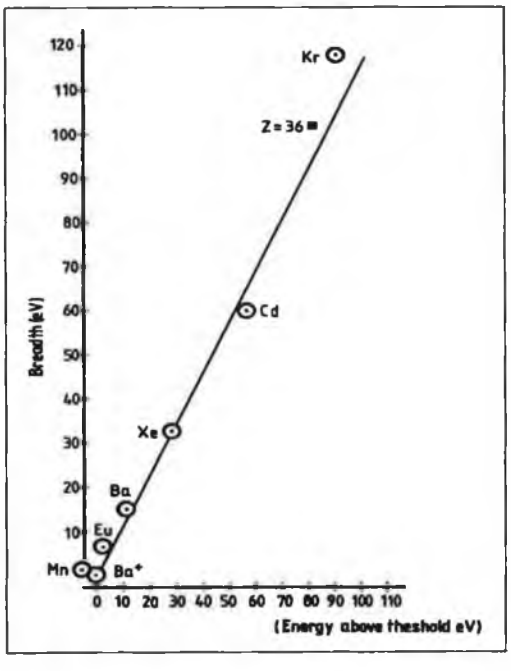

In the case of the actinides, at high enough Z, the $\overline{5,\varepsilon}$f state collapses into the inner well which can now support both a 4f and a 5f bound state. At this point the collapse of all terms of the final state wavefunction is complete. As the depth of the inner well is increased further the 5f level falls below the higher nf levels located in the vicinity of the outer potential well. The first peak of each of the higher nf (n>5) wavefunctions now moves to the inner well so that orthonormality with the collapsed 5f wavefunction is retained. The first node of these higher nf wavefunctions occurs in the centrifugal barrier region between both wells where the wavefunction has a very small amplitude. As a result of 4f wavefunction collapse in the lanthanides, higher nf (n>4) wavefunctions in the outer well now assume the character of an (n-1)f wavefunction (see Figure 1.13) due to the location of their first node in the inner well (Section 8.6 Cowan 1981, Cheng & Froese-Fischer 1983). It is important to note that because the 4f wavefunction is already collapsed in the case of the actinides that nf (n>5) wavefunctions actually behave as (n-2)f wavefunctions after 5f wavefunction collapse (see Figure 1.13). This value of 1 or 2 that is subtracted from the principal quantum number n, is known as the quantum defect (δ) and the result of this subtraction is an effective principal quantum number n*,

$$n^* = n-\delta \tag{1.15}$$

The variation in n* for f wavefunctions calculated using the HX method (Griffin et al. 1969) is shown in Figure 1.13 for elements belonging to the second half of the periodic table. The quantum defect (δ) is ultimately an expression of the degree of screening of the electrons in a given subshell by electrons in inner subshells and it is dependent on l and to lesser extent n. δ increases as the degree of screening of the atomic nucleus is reduced and consequently the departure from a hydrogenic-like system increases. As Z is increased along the periodic table nf (and nd) wavefunctions collapse. As a result, the screening of these nf (and nd) wavefunctions is significantly reduced as they now lie closer to the atomic core, within the main electron cloud. Consequently, δ increases, resulting in a decrease in n* (see Figure 1.13). In the case where the 4f wavefunction collapses at $Z \cong 56$, δ for the unoccupied 5f, 6f, 7f,...nf Rydberg levels has a value of one and the effective quantum number n* is therefore reduced by one. Similarly, the effect of 5f wavefunction collapse on higher nf Rydberg states is also clearly demonstrated in Figure 1.13.

Figure 1.13: HX calculation of the variation in the effective quantum number n with Z for f electrons along the second half of the periodic table (Griffin et al. 1969)*

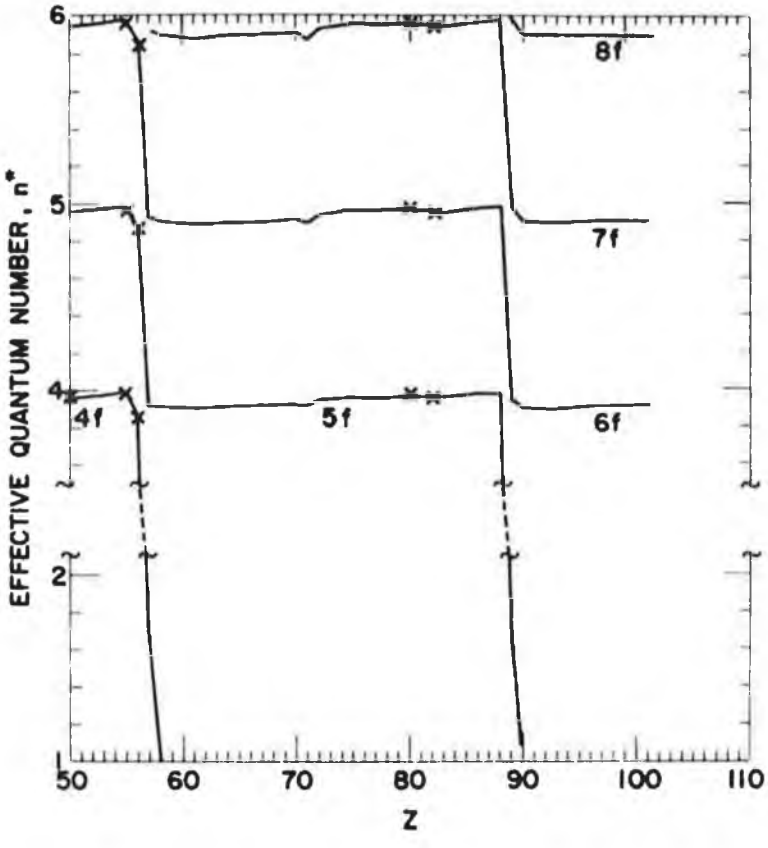

In the case of 4f wavefunction collapse, a unique situation occurs along the barium isonuclear sequence whereby the 4f wavefunction in Ba^{2+} is partially collapsed. Observations by Lucatorto and co-workers (1981) provide the first experimental evidence of a partially collapsed wavefunction also known as a hybridised wavefunction due to its comparable amplitude in both inner and outer potential wells. This phenomenon manifests itself upon transition from Ba^{+} to Ba^{2+} where a series of strong resonance lines below the 4d thresholds that are not present in the Ba^{+} spectrum suddenly appear in the Ba^{2+} spectrum. This situation is explored further in Section 1.2.5 where the collapse of an nf wavefuction along an isonuclear sequence is discussed.

The essential physical processes associated with wavefunction collapse have been described in the case of nf wavefunctions but it is important to note that they also pertain in the case of nd wavefunction collapse. The collapse of an nd wavefunction is more gradual however and not as dramatic as that for an nf wavefunction (Connerade 1978a, Griffin et al. 1969). This is because of the centrifugal term contributing to the

effective potential $V_{eff}(r)$ for nd electrons (see equation (1.1)) is smaller than that for nf electrons. Consequently the centrifugal barrier is less pronounced and in some cases is non-existent. nf wavefunctions can collapse very suddenly with a unitary increase in Z upon the transition between two neighbouring elements whereas nd wavefunction collapse is more gradual, occurring (with just a few exceptions) over two to three elements along an isoperiodic sequence (Griffin et al. 1969). In the case where $V_{eff}(r)$ is in the form of a double well potential, delocalised nd electrons in the outer potential well reside at smaller atomic radii than nf electrons due also to the reduced centrifugal term. The outer nd potential well predominantly overlaps the main electron cloud, which for a typical many-electron neutral atom (of any Z) extends to ~ 5 to $6a_o$ (Griffin et al. 1969). As a result nd wavefunction collapse is less dramatic as both delocalised and localised nd electrons (before and after wavefunction collapse) reside close to the inner atomic region. Also, the close proximity of delocalised nd electrons to other electrons within the atomic core results in less effective screening of the nuclear charge than for delocalised nf electrons and this, coupled with reduced centrifugal repulsion, results in the relatively low potential barrier in the effective potential for d electrons. Delocalised nf electrons in the outer potential well reside outside the main electron cloud where screening of the nuclear charge by core electrons is more efficient and therefore changes in the core potential result in a more dramatic collapse of nf wavefunctions.

The excitation and decay mechanisms responsible for the formation of a typical giant dipole resonance profile residing in either the discrete spectrum or photoionisation spectrum of an inner subshell are explored further in Sections 1.2.4.1 and 1.2.4.2.

1.2.4 Atomic Excitation and Decay Processes Contributing to the Formation of a Giant Dipole Resonance

The following outline of excitation and decay processes is presented with particular reference to the 5d $\rightarrow$ $\overline{5,\varepsilon f}$ giant dipole resonance in atomic thorium. However the underlying physical processes apply to similar resonances across the actinide and lanthanide series.

1.2.4.1 Excitation processes: Photoionisation and Photoexcitation

The two main inner shell excitation processes contributing to typical giant dipole resonance features are shown in Figure 1.14. The first of these excitation processes is labelled 'a' in Figure 1.14 and results in photoionisation of the 5d subshell by an incoming XUV photon of sufficient energy. This process involves excitation to a $\overline{5,\varepsilon f}$ resonantly localised continuum state located above the uppermost 5d ionisation threshold. The excited state has a very short lifetime as the 5f electron tunnels though the centrifugal barrier to become a free εf electron. This is known as continuum enhancement (Becker in Connerade et al. 1987). In the case of neutral atomic thorium this processes is described by,

$$(\mathrm{Th})\ 5d^{10}(^1S_0)\,6d^2 7s^2 + h\upsilon \rightarrow (\mathrm{Th}^*)\ 5d^9\,\overline{5,\varepsilon f}\ (^1P)\,6d^2 7s^2 \qquad \text{(a)}$$

The resulting spectral feature is a broad asymmetric giant continuum resonance located at ~100eV, close to the uppermost thorium 5d threshold ($5d_{3/2}$). The calculated profile of the 5d atomic total photoionisation cross section obtained by Wendin (1984) using the Local Density based Random Phase Approximation (LDRPA) method is shown in Figure 1.15 (solid curve). To date, the 5d ionisation limits for atomic thorium have not

Figure 1.14: Schematic representation of the excitation and decay processes contributing to the formation of a 5d →$\overline{5,\varepsilon f}$ giant dipole resonance in an actinide atom/ion

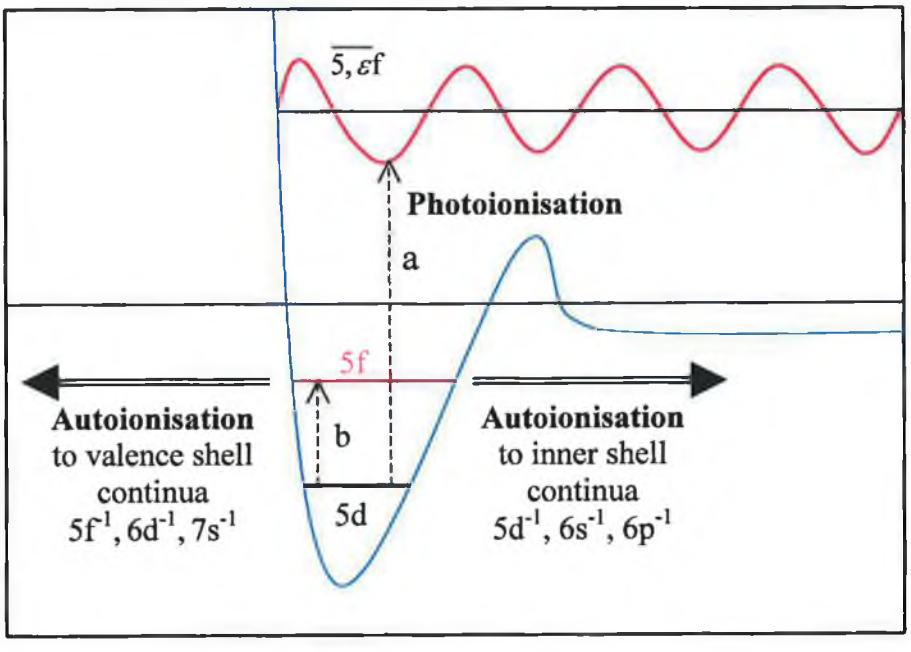

been determined experimentally and those shown in Figure 1.15 have been calculated. Also shown is the 5d photoionisation cross section for solid state thorium (Cukier et al. 1978) whose location and overall profile closely resembles the atomic 5d spectrum measured by Carroll and Costello (1986). In the case of the thorium 5d $\rightarrow \overline{5,\varepsilon f}$ giant dipole resonance, the photoionisation process involves a transition to a singlet state (^{1}P). This state resides close to the higher energy 5d ionisation threshold ($5d_{3/2}$) and at higher energies than triplet terms due to the increased exchange interaction energy for singlet terms.

The second inner shell excitation process is that of photoexcitation and is labelled 'b' in Figure 1.14. In this process, lower energy XUV photons promote a 5d electron to a discrete 5f state whose energy lies below one ($5d_{3/2}$) or both ($5d_{5/2}$ & $5d_{3/2}$) of the 5d thresholds. In the case of neutral atomic thorium this process is given by,

$$(\mathrm{Th})\ 5d^{10}(^1S_0)\,6d^27s^2 + h\upsilon \rightarrow (\mathrm{Th}^*)\ 5d^95f\,(^3P,\ ^3D)\,6d^27s^2 \qquad (b)$$

where the final state term is a triplet (^{3}P,^{3}D). Both triplet terms appear to be collapsed in

Figure 1.15 *Total LDRPA photoionisation cross section of atomic thorium (solid curve) and thorium metal (dashed curve) in the 5d inner shell XUV region displaying the 5d $\rightarrow \overline{5,\varepsilon f}$ giant dipole resonance*

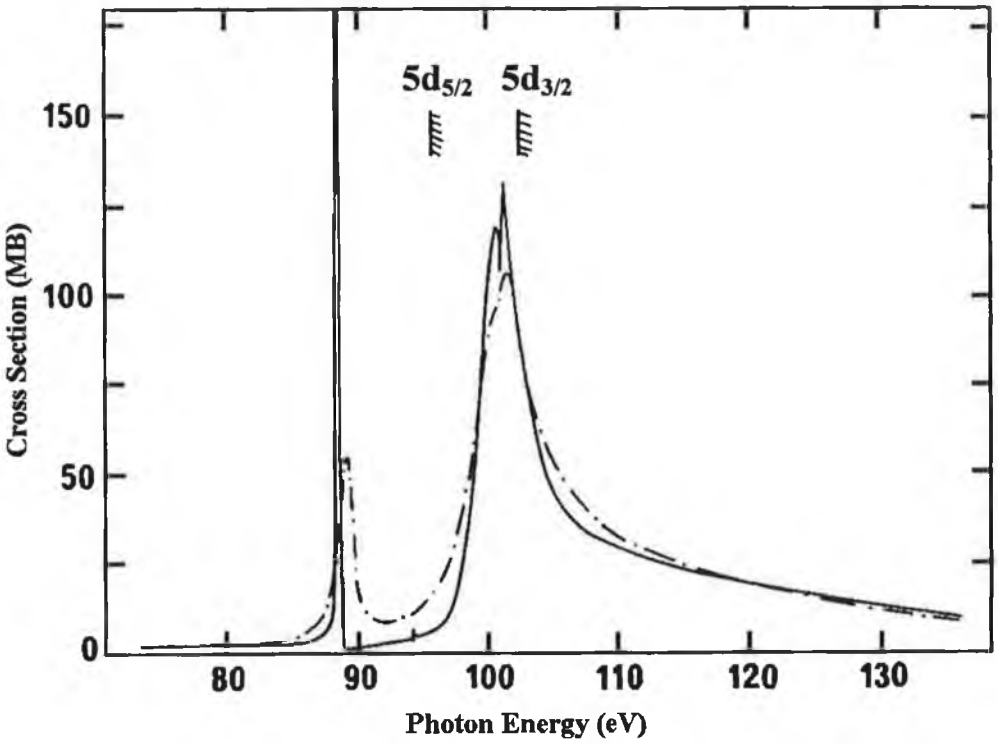

neutral atomic thorium and reside in the discrete photoexcitation spectrum. The spectral properties of the 5d → $\overline{5,\varepsilon}$f giant dipole resonance in atomic thorium are explored further in Section 5.3.2 Chapter 5.

It is important to note that in spectral regions lying between both the lower and higher energy inner shell ionisation limits that both *photoionisation* above the lower energy limit and *photoexcitation* below the higher energy limit contribute to the total cross section. An example of such a region is that extending from ~ 97 to 103eV located between both $5d_{5/2}$ and $5d_{3/2}$ limits in Figure 1.15.

1.2.4.2 Decay Processes: The Auger Effect and Autoionisation

Both forms of inner shell excitation discussed above result in an intermediate excited atomic/ionic state that possesses a 5d core hole or vacancy. This state will subsequently decay, thus filling the 5d hole. The decay channel of an intermediate state produced by photoionisation (process 'a' Figure 1.14) is shown in Figure 1.16. This decay pathway

Figure 1.16: Photoionisation to an excited ionic state (Th^{+*}) followed by a subsequent Auger decay into adjacent valence or inner shell continua to produce a doubly charged ion (Th^{2+})

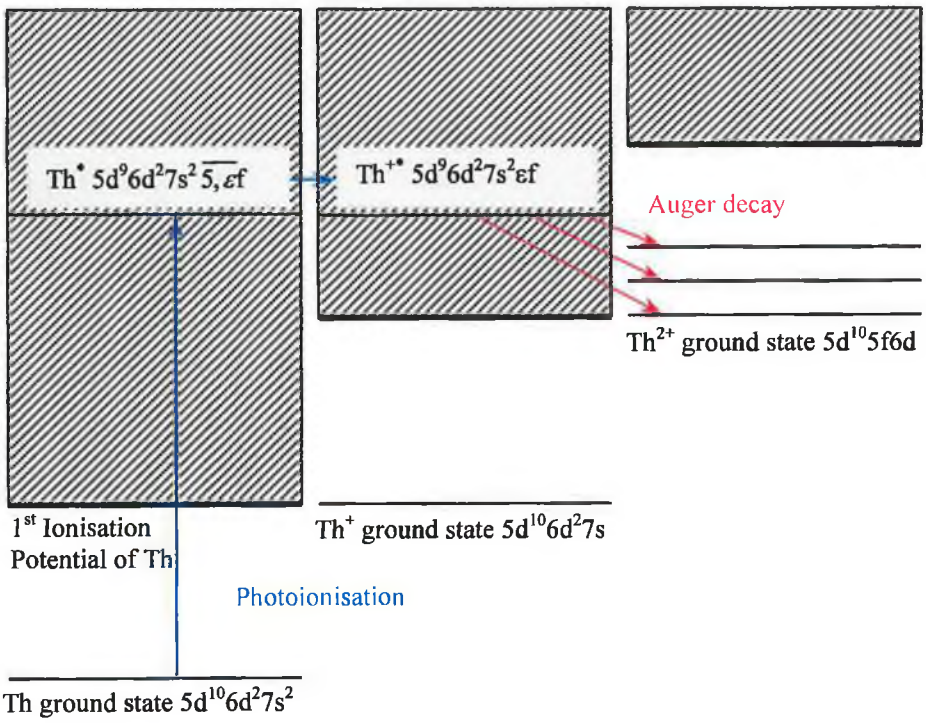

is known as resonant Auger decay. Initially, photoionisation produces a Th^{+*} intermediate state which decays via resonant Auger decay to produce a Th^{2+} final state. The total excitation and decay pathway above all 5d thresholds is therefore,

$$(Th)\ 5d^{10}6d^27s^2 + h\upsilon \rightarrow (Th^*)\ 5d^96d^27s^2\overline{5,\varepsilon f} \rightarrow (Th^{+*})\ 5d^96d^27s^2\varepsilon f \rightarrow (Th^{2+})\ 5d^{10}V^{-1} + \varepsilon f + \varepsilon l$$

where V represents the combined valence (7s and 6d) and inner (6s, 6p) subshells and εl is the Auger electron. Auger decay is a general term used to describe the entire range of radiationless transitions to inner subshell vacancies (Section 5.1 Crasemann, 1985) and is an autoionising process. During the autoionisation process an electron from an outer subshell fills the 5d hole in a radiation-less transition and the excess energy is carried off in the ionisation of another outer shell electron. This free electron, unlike a photoelectron, has a fixed kinetic energy that is independent of photon energy and is equal to the difference in energy between the excited intermediate state and the final ionic ground state. The process of Auger decay (resonant and non-resonant) results in a doubly charged ion, a photoelectron (εf) and a fixed energy Auger electron (εl). Autoionisation, on the other hand, involves inner shell excitation to a discrete state of the neutral atom followed by a radiation-less decay that results in the production of a singly charged ion and a fixed energy electron (similar to an Auger electron). This is represented schematically in Figure 1.17 and is the predominant form of decay for the

Figure 1.17: Photoexcitation to an excited neutral state (Th^*) followed by autoionisation into available valence or inner shell continua to produce a singly charged ion (Th^+)

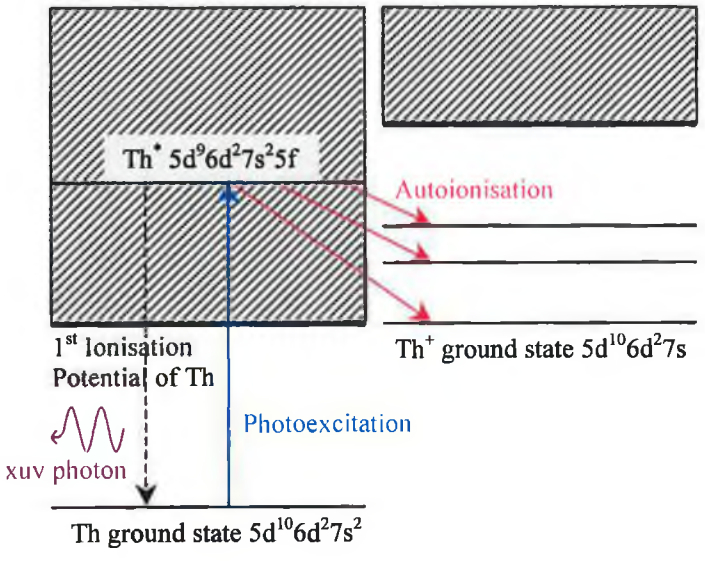

second type of excitation process mentioned, inner shell photoexcitation (process 'b' Figure 1.14). The alternative process of decay via the return of the excited 5d electron to fill its initial position in the 5d subshell thus emitting an XUV photon is indicated with a dashed line in Figure 1.17 but has a very small probability of occurrence. This decay channel is also possible but autoionisation into available valence and inner shell continua is more likely to occur. Radiative decay processes have lifetimes of typically 10^{-9} seconds compared with much shorter non-radiative autoionising lifetimes lying in the region of 10^{-13} to 10^{-18} seconds.

The autoionising pathways into *valence* subshell continua that are available for decay of the (Th^*) $5d^96d^27s^25f$ excited state in neutral atomic thorium are:

$$(Th)\ 5d^{10}6d^27s^2 + h\upsilon \xrightarrow[\text{excitation}]{} (Th^*)\ 5d^96d^27s^25f \xrightarrow{\text{autoionisation}} (Th^+)\ 5d^{10}5f^{-1}$$
$$(Th^*)\ 5d^96d^27s^25f \xrightarrow{\text{autoionisation}} (Th^+)\ 5d^{10}7s^{-1}$$
$$(Th^*)\ 5d^96d^27s^25f \xrightarrow{\text{autoionisation}} (Th^+)\ 5d^{10}6d^{-1}$$

The autoionising pathways into *inner* subshell continua for decay of the same excited state in neutral atomic thorium are:

$$(Th)\ 5d^{10}6d^27s^2 + h\upsilon \xrightarrow[\text{excitation}]{} (Th^*)\ 5d^96d^27s^25f \xrightarrow{\text{autoionisation}} (Th^+)\ 5d^{10}6p^{-1}$$
$$(Th^*)\ 5d^96d^27s^25f \xrightarrow{\text{autoionisation}} (Th^+)\ 5d^{10}6s^{-1}$$
$$(Th^*)\ 5d^96d^27s^25f \xrightarrow{\text{autoionisation}} (Th^+)\ 5d^{-1}$$

The final autoionising decay channel shown above, is only possible for excited states $5d^9{}_{3/2}6d^27s^25f$ lying above the $5d_{5/2}$ ionisation limit and below the $5d_{3/2}$ limit. These states can autoionise into the $5d_{5/2}$ inner shell continuum via a 'spin-flip' process whereby the spin orientation of the 5d core hole changes. This process is as follows

$$(Th)\ 5d^{10}6d^27s^2 + h\upsilon \rightarrow (Th^*)\ 5d^{-1}_{3/2}6d^27s^25f \rightarrow (Th^+)\ 5d^{-1}_{5/2}6d^27s^2 + \varepsilon p, \varepsilon f$$

where the final Th^+ state is similar to that achieved via the process of direct photoionisation of the 5d subshell above the $5d_{5/2}$ ionisation limit.

The process of autoionisation can be subdivided into three main types of transitions depending on the initial and final subshell vacancies that have been created following the photoexcitation and autoionisation processes respectively. This sub-division applies

to both the Auger double ionisation and single autoionisation processes mentioned (Section 5.1 Crasemann, 1985).

(i) *Auger transitions* occur when neither of the two final subshell vacancies (produced when one electron fills the initial core hole and the second electron is emitted) are located in the principal shell where the initial core vacancy was produced during photoexcitation.

(ii) *Coster-Kronig transitions* occur when one of the two final subshell vacancies is located outside the principal shell where the initial core vacancy was produced.

(iii) *Super-Coster-Kronig transitions* occur when both of the final subshell vacancies occur in the same principal shell as the initial core hole. In this case all three vacancies have the same principal quantum number n.

A number of experimental spectroscopic techniques facilitate the study of inner shell excitation and subsequent de-excitation processes. The absorption of VUV $\rightarrow$ soft X-ray photons in the photoabsorption/photoionisation process permits the investigation of dipole allowed excitation transitions. The use of broad-band continuum emitting sources (e.g. the laser produced plasma) permit the determination of total photoionisation cross sections whereas photoelectron studies utilising highly monochromatic synchrotron light permit the measurement of partial as well as total photoionisation cross sections. The use of synchrotron radiation thus enables the investigation of possible enhancement of underlying continuum channels in the vicinity of the giant resonance (Connerade in Connerade et al. 1987). The technique of electron energy loss spectroscopy (EELS), in which variable quantities of momentum can be exchanged between the exciting electrons and bound atomic electrons during the inelastic scattering process, permits the observation of both dipole allowed and dipole forbidden excitation transitions (Matthew in Connerade et al. 1987). Matthew and co-workers (1987) have demonstrated the existence of a 4p$\rightarrow$4f giant quadrupole resonance in the 200 to 230eV X-ray spectrum of cerium in a comparison of EELS and X-ray photoabsorption spectra.

Both photoelectron spectroscopy and photoion spectroscopy investigate the de-excitation channels that ultimately result in ionisation of the atom/ion following initial photoexcitation. The study of the range of direct photoelectron and Auger/autoionising

electron energies permits the determination of decay pathways and subsequent final ionic states. Photoion spectroscopy enables the determination of the dominant ionisation processes and final ionic states. Comparison of relative cross sections for different ion stages produced as a result of photoionisation enables the determination of the relative importance of single and multiple ionisation processes.

1.2.5 Observation of the Collapse of a Giant Dipole Resonance along an Isonuclear Sequence

The profile of the giant dipole resonance occurring in the inner shell photoabsorption spectrum of neutral atoms lying in (or close to) d and f transition sequences in the periodic table changes as the effective potential experienced by d and f electrons changes. Extensive observations of the 4d $\rightarrow \overline{4,\varepsilon}$f giant dipole resonance along lanthanide isoperiodic sequences have revealed the extent of the changes to the giant dipole resonance profile which is seen to narrow in width and shift below the ionisation limits of the inner subshell undergoing excitation as Z increases (Richter et al. 1989b). These changes to the resonance profile are as a direct result of the gradual wavefunction collapse that occurs with increasing Z across an isoperiodic sequence. It is however possible to induce a more rapid wavefunction collapse within a single element by changing factors such as (i) inner shell occupation, (ii) valence shell occupation or by (iii) the formation of a molecular bond (Clark & Lucatorto in Connerade et al. 1987). Connerade (1978b) first performed a theoretical investigation into the feasibility of an experimental method for inducing the collapse of an atomic nf wavefunction. Such an experiment would in effect constitute a form of *controlled* wavefunction collapse whereby the potential in the outer regions of the atom where the un-collapsed nf wavefunctions reside is externally modified, thus producing conditions favourable for collapse of such nf wavefunctions. He proposed to excite a valence 6s electron in neutral caesium to higher ns, np, nd, or nf levels by two step laser excitation and then probe the 4d $\rightarrow \overline{4,\varepsilon}$f giant dipole resonance in the 100eV energy region using synchrotron radiation. Neutral atomic caesium was chosen as a suitable candidate because of the very low potential barrier between the inner and outer potential wells in the effective potential for nf electrons. This barrier is easily lowered with the increased attraction of the nucleus due to reduced nuclear screeing in the valence excited atom. To

date, this novel experiment has not yet been performed in order to study the effects on the giant dipole resonance profile (Connerade 1998). The basic concept underpinning this proposal has however been implemented experimentally in order to investigate the photoionisation cross section of excited atoms for the first time by Bizau and co-workers (1986). A tuneable dye laser was used to produce valence excited barium atoms and the 5d photoionisation cross section in the 15 to 150eV photon energy region was recorded. The effect of valence excitation on the $4d \rightarrow \overline{4,\varepsilon f}$ giant dipole resonance was however not investigated.

Apart from the method of valence excitation proposed by Connerade (1978b), the removal of valence electrons upon successive ionisation of an element along an isonuclear sequence has been successfully implemented in order to induce wavefunction collapse. The first such experiment was performed by Lucatorto and co-workers (1981) on the barium isonuclear sequence. Subsequent studies of 4f wavefunction collapse have been performed on the iodine (O'Sullivan et al. 1996), antinomy (D'Arcy et al. 2000) and caesium (Cummings et al. 2000) isonuclear sequences using the DLP photoabsorption technique. Similar DLP photoabsorption studies in Th to Th^{6+}, performed as part of this thesis work, represent the first study of 5f wavefunction collapse along an actinide isonuclear sequence (Meighan et al. 2000).

In the experiment of Lucatorto and co-workers, barium ions were produced using the technique of resonant laser driven ionisation (RLDI) whereby barium atoms produced in a resistively heated furnace were ionised using suitably tuned dye laser light thus resulting in the production of Ba ($4d^{10}5s^25p^66s^2$ ground state), Ba^+ ($4d^{10}5s^25p^66s$) and Ba^{2+} ($4d^{10}5s^25p^6$) ions. A uranium anode spark was then used to provide pulsed XUV continuum light suitable for recording inner shell 4d photoionisation spectra. The results obtained are shown in Figure 1.18 and serve to illustrate the dramatic transfer of oscillator strength from the main $4d \rightarrow \overline{4,\varepsilon f}$ giant dipole resonance feature in the 4d photoionisation spectrum of Ba and Ba^+ to the nf (n>4) Rydberg transitions in the discrete 4d spectrum of Ba^{2+}.

In general, the radical spectral changes along an isonuclear sequence are indicative of wavefunction collapse. The giant dipole resonance profile that dominates the photoionisation cross section changes to a series of discrete peaks corresponding to

Figure 1.18 *Photoabsorption cross sections of (a) Ba, (b) Ba^+ and (c) Ba^{2+} in the region of the 4d $\rightarrow \overline{4,\varepsilon f}$ giant dipole resonance (from Lucatorto et al. 1981)*

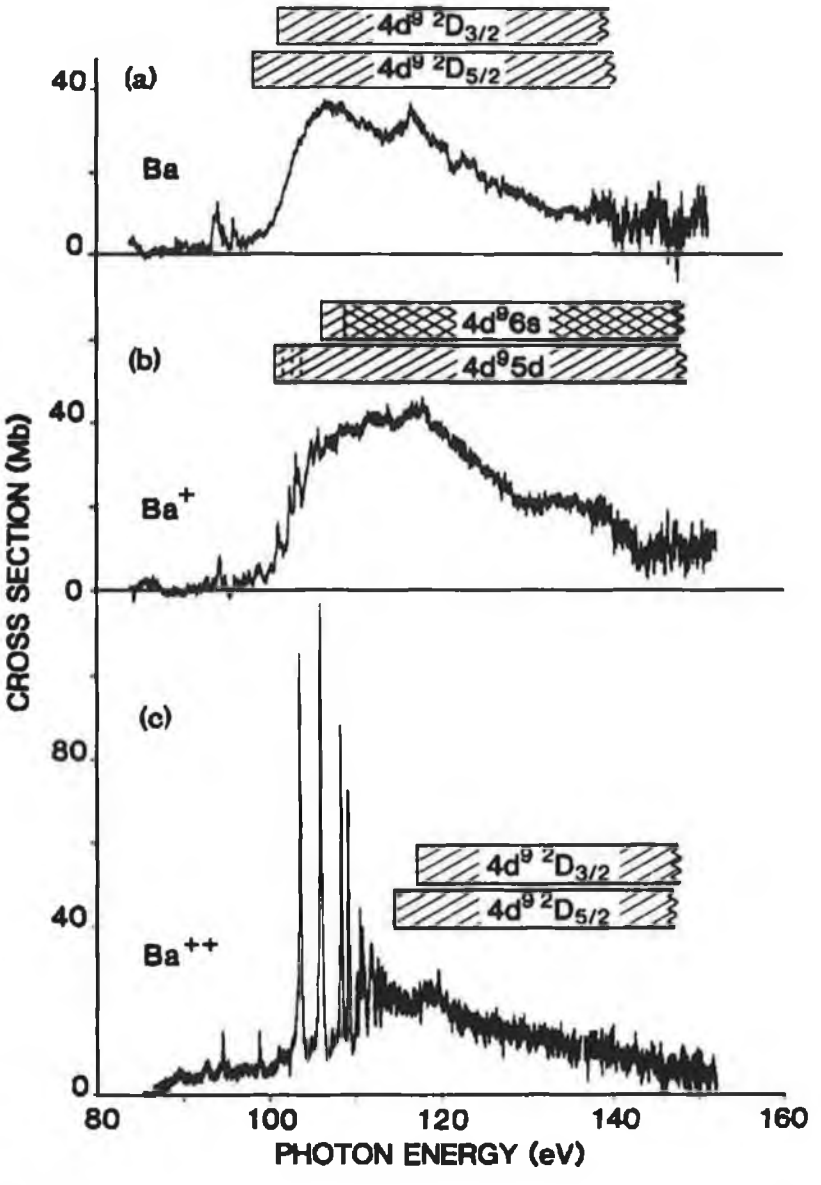

Rydberg excitations to higher nf states that have now collapsed into the inner well of the effective nf potential. nf wavefunction collapse along an isonuclear sequence results from the lowering of the potential barrier which is caused by the increasing dominance of the nuclear coulombic attraction over the constant centrifugal repulsion that occurs when valence electrons are removed. This results in the deepening of the inner potential well which now supports an increased number of bound states. Excitation to these states appears as a series of sharp peaks in the discrete inner shell photoexcitation spectrum.

The situation whereby higher nf (n>4) wavefunctions collapse into the inner well is not entirely true in the case of the Ba^{2+} spectrum which is physically unique. Lucatorto and

co-workers (1981) used term dependent Hartree-Fock calculations to interpret the observed features in the Ba^{2+} photoabsorption spectrum as being due to a partially collapsed or hybridised 4f wavefunction. Connerade and Mansfield (1975) had previously postulated the phenomenon of partial wavefunction collapse in order to interpret 5d→nf transitions observed in the photoabsorption spectrum of Ba^{+*}. In the case of the Ba^{2+} 4d photoabsorption cross section recorded by Lucatorto and co-workers, the 4f wavefunction has a comparable amplitude in both inner and outer potential wells of the effective potential for nf electrons. Consequently it causes a resonant enhancement of higher nf Rydberg states in the region of the inner well and so their overlap with the 4d wavefunction is significantly increased (Cheng & Froese-Fischer 1983). Transitions to these Rydberg levels, even though the nf wavefunctions have *not* actually collapsed into the inner well, are observed as sharp lines in the discrete 4d photoexcitation spectrum of Ba^{2+} (Figure 1.18 (c)). Since the experimental observation by Lucatorto and co-workers (1981), the phenomenon of partial 4f wavefunction collapse has been observed in Sb^{+} to Sb^{3+}, I^{2+}, Xe^{+}, Xe^{2+} and Cs^{+} (Cummings et al. 2000). The nature of the 4f wavefunction collapse phenomenon along the isonuclear sequences of elements preceding xenon (Z=54) differs quite significantly to that which occurs along the isonuclear sequences of the heavier elements with Z>54. For elements lighter than xenon, a 4d→εf giant continuum resonance appears approximately 20 to 30eV above the 4d threshold in the photoabsorption spectrum of the neutral atom. This 'delayed onset' in photoionisation is essentially due to the high degree of exclusion of εf wavefunctions from the atomic core due to the presence of a centrifugal barrier in the double well effective potential for f electrons (Cooper 1964). As the kinetic energy of an outgoing photo-excited electron (εf) increases, so too does its ability to tunnel through the centrifugal barrier. As a result, higher εf wavefunctions can penetrate deeper into the core region and the extent of their overlap with the 4d wavefunction is increased, thus increasing the oscillator strength of higher 4d→εf transitions. As the ionicity increases along the isonuclear sequence of an element with atomic number less than 54, the inner well of the double well f potential deepens slowly, thus lowering the centrifugal barrier and causing a gradual contraction of 4f and higher nf states into the core region. This process manifests itself as a gradual transfer of oscillator strength from the 4d→εf continuum resonance to the discrete features in the 4d photoexcitation spectrum. In the discrete 4d photoexcitation spectra of ions such as Sb^{+} to Sb^{3+}, I^{2+}, Xe^{+}, Xe^{2+} and Cs^{+}, where the 4f wavefunction is partially collapsed, features remain narrow due to the small degree of spatial overlap between the 4d and 4f

radial wavefunctions and the corresponding reduced non-radiative decay rates of inner shell excited $4d^9 4f$ states. As the degree of ionisation increases, the 4f wavefunction collapses further into the inner well, its spatial overlap with the 4d wavefunction increases resulting in an increased transfer of oscillator strength from 4d→nf, εf transitions to 4d→4f transitions.

As mentioned, the physical scenario of 4f wavefunction collapse in the elements following xenon (Z>54) is different. Here the effective double well f potential in the neutral atom is capable of supporting a 'quasi-discrete' or 'resonantly localised' 4f state. With increased ionicity along an isonuclear sequence (e.g. Ba to Ba^{2+}, Lucatorto et al. 1981), 4f wavefunction collapse is more dramatic and more 'sudden', in that it occurs over less ion stages in these heavier elements. The result is a radical and sudden collapse of the profile of the $4d \rightarrow \overline{4, \varepsilon f}$ giant dipole resonance feature to discrete, predominantly 4d→4f transitions, below the 4d limits. The dominance of 4d→4f transitions, as before, increases with increasing collapse of the 4f wavefunction and the corresponding increase in the spatial overlap of the 4d and 4f wavefunctions.

The latter physical scenario of wavefunction collapse appears, on the basis of experimental atomic and ionic photoabsorption spectra recorded during the course of this work, to be the most accurate description of 5f wavefunction collapse along the thorium isonuclear sequence. The evolution of the $5d \rightarrow \overline{5, \varepsilon f}$ giant dipole resonance in atomic and ionic thorium has been recorded along the thorium isonuclear sequence Th→Th^{6+} (see Chapter 5). Also, the 6p→6d giant dipole resonance, which appears to be collapsed in atomic thorium, has been studied for the first time. Thorium atomic and ionic species were generated within a nanosecond laser produced plasma. A second laser plasma acted as a VUV→XUV continuum source and its generation was suitably delayed with respect to that of the thorium plasma in order to probe different atomic/ ionic species. The production of continuum emission from both nanosecond and picosecond laser produced plasmas and the implementation of the dual laser plasma (DLP) technique, which is particularly suited to time resolved (ps and ns) photoabsorption studies along an isonuclear sequence, are discussed in detail in Chapter 2. The various different experimental regimes used in the VUV and XUV energy regions for recording inner shell atomic/ionic time resolved photoabsorption spectra are described in detail in Chapter 3. In Chapter 4, the spectral and temporal emission

characteristics of a picosecond XUV continuum laser plasma source (developed at RAL) are investigated using time-integrated XUV dispersive spectroscopy and time-resolved streak camera measurements. Measurements of the 6p (VUV) and 5d (XUV) inner shell relative photoabsorption cross sections of atomic and ionic thorium recorded using both picosecond and nanosecond XUV continuum source plasmas are presented in Chapter 5. The results of atomic calculations, of the 6p and 5d inner shell photoabsorption cross sections of atomic and ionic thorium, using different theoretical models are also presented in Chapter 5 and compared with experimental results.

Chapter Two

The Laser Plasma Light Source and the Dual Laser Plasma Technique

In this chapter the generation, evolution, fundamental physical properties and primary applications of a laser produced plasma are discussed. The atomic processes occurring within a laser plasma plume are described in detail, with particular reference to the mechanisms responsible for generating continuum emission. The physical characteristics of short pulse (<1ns) laser produced plasmas are discussed and recent advances in ultra-short, ultra-intense laser matter interactions are presented. The origins and implementation of the Dual Laser Plasma (DLP) space and time resolved spectroscopic technique used to record valence and inner shell relative photoabsorption cross sections of atoms and ions are reviewed.

2.1 The Laser Produced Plasma (LPP)

2.1.1 Introduction

The laser produced plasma, created during the interaction of a high-power laser pulse with a solid surface, serves as a rich and highly dynamic source of atoms and low, medium and highly charged ions emitting radiation across a broad spectrum ranging from the infra-red to the X-ray region. Applications utilising the plasma as both a source of atomic/ionic species and as an intense light source are highly diverse and wide-ranging, spanning both engineering and fundamental scientific research. The laser produced plasma serves as a source of both line and continuum emission, the latter being well suited to photoabsorption studies of the low, medium and highly charged ions produced in a second laser plasma plume (Carroll & Kennedy 1977, Costello et al. 1991, Nicolosi et al. 1991, Kennedy et al. 1995).

2.1.2 Fundamental Physical Properties of a Laser Produced Plasma

A short-lived, high density, high temperature plasma is formed when a pulse from a Q-switched laser is focused onto the surface of a solid with an on-target irradiance in excess of $10^9 W/cm^2$. The high temperatures and high densities attained within the plasma plume are a direct result of the high irradiance which in turn yields an extremely high rate of material ablation, heating and ionisation (Carroll & Kennedy 1981, Kim in Radziemski & Cremers, 1989). The resulting plasma is an ionised gas which will expand outwards from the focal zone, cooling and emitting radiation as it does so. Within the plasma plume a variety of atomic and ionic species (in ground and excited states) and free electrons are present at any one time. The populations of these three constituents vary continually throughout the duration of the plasma. Initial populations of atoms, ions and electrons and their subsequent dynamics vary considerably with laser pulse duration and laser energy, wavelength and irradiance. The type of target material and the variation of its optical, thermal and mechanical properties with temperature and pressure greatly influence the generation and subsequent evolution of the plasma plume (Hughes 1975). Also, the ambient atmosphere, or lack of it, within a vacuum environment plays a significant role in the resulting hydrodynamic expansion of the plasma plume (Root in Radziemski & Cremers, 1989).

The predominant laser-matter interaction of interest in this work is that which occurs when laser light is incident on an opaque metal surface. Several physical processes occur at the metal surface as the irradiance is increased within the range 10^6 to 10^9 W/cm^2. Initially at an irradiance of ~10^6 W/cm^2 surface heating without a phase change predominates (Ready 1971). As the laser irradiance is increased melting and vaporisation occur, until at irradiances $\geq 10^9$ W/cm^2, vaporised material becomes increasingly ionised thus producing a plasma. Typical electron densities (n_e) within the laser plasma plume lie in the range of 10^{23} to 10^{28} m^{-3} with typical electron temperatures (T_e) of 10 to10^5 eV corresponding to 10^5 to 10^9 degrees Kelvin (Carroll & Kennedy 1981).

Throughout the duration of the plasma, overall electrical neutrality is maintained whereby the electron density, n_e equates with the sum over the total number of ions in all charge states existing within the plasma

$$n_e = \sum_z n_z z \tag{2.1}$$

where n_z is the ion density of charge state z. Charged particles within the plasma plume interact via the long-range Coulomb force. A quantity known as the Debye length (λ_D) is used as a measure of the spatial extent over which this force acts. Effectively it is a measure of the distance over which the electric field emanating from a single charged particle acts before being screened by oppositely charged particles within the plasma plume. The Debye length is therefore inversely proportional to the electron density n_e and is consequently reduced in dense plasma regions where charge screening is highly effective. λ_D is given by

$$\lambda_D = \left(\frac{\varepsilon_o k T_e}{n_e e^2} \right)^{1/2} \tag{2.2}$$

where ε_o is the permittivity of free space, k is Boltzmann's constant, T_e (in units of Kelvin) is the electron temperature and e is the electronic charge. Charged particles within the plasma will respond collectively to external perturbing fields via the long-range Coulomb force when the dimensions of the plasma exceed that of λ_D. In plasmas where this condition holds and in the presence of a driving field, electrons will become displaced with respect to positive ions, thus polarising the charge cloud (Carroll & Kennedy 1981). This results in the establishment of a restoring force that causes the electrons to oscillate against the positive ionic charge. The frequency at which they oscillate is known as the plasma frequency ω_p and is given by

$$\omega_p = \left(\frac{n_e e^2}{m_e \varepsilon_o} \right)^{1/2} \tag{2.3}$$

where m_e is the electron mass. Similarly ion oscillations occur at frequencies characteristic of the ion charge. Such frequencies can be calculated by simply replacing m_e with the ion mass, m_{ion}, in equation 2.3.

Propagation of external electromagnetic waves in the plasma medium is governed by the frequency dependent refractive index of the plasma. The propagation of an external electromagnetic wave (of frequency $\omega = 2\pi f$) within the plasma plume is described by the dispersion relationship

$$\omega^2 = \omega_p^2 + c^2 k^2 \tag{2.4}$$

where k ($= 2\pi / \lambda$) is known as the propagation constant. Because an electron density gradient exists within the plasma plume, ω_p varies accordingly. When $\omega > \omega_p$, k is real and the incoming wave propagates through the plasma medium. In the situation where $\omega < \omega_p$, k is imaginary and the wave is attenuated. The incoming wave is reflected at an electron density for which $\omega = \omega_p$. This is known as the *critical density* (n_c) and is given by

$$n_c = \left(\frac{\varepsilon_o m_e \omega^2}{e^2} \right) \tag{2.5}$$

As a consequence of this result, short wavelength lasers such as a KrF excimer laser producing pulses at 248nm are ideally suited to heating denser plasma regions compared to Nd:YAG lasers at 1064nm (Offenberger & Fedosejevs 1989).

2.1.3 Generation and Evolution of a Laser Produced Plasma

Plasma formation is initiated when, as previously mentioned, the on-target laser irradiance equals to or exceeds ~10^9 W/cm^2. For typical laser pulse durations of a few nanoseconds, heating, melting, vaporisation and ionisation of surface material occurs so rapidly that accurate modelling of plasma initiation is highly complex (Hughes 1975). Incident laser light is strongly attenuated within the metal and therefore only penetrates a thin layer of the opaque metallic surface known as the *skin depth* (δ). The extent of

this penetration is dependent on the frequency of the laser light (ω) and also the metal type,

$$\delta = \sqrt{\frac{2}{\omega\mu\sigma}} \tag{2.6}$$

where σ is the conductivity of the metal and μ its magnetic permeability. Skin depth values are comparable to typical laser wavelengths in the range 1064nm (Nd:YAG) to 248nm (KrF excimer). Within this region, the large electric field associated with the laser pulse results in rapid ionisation of surface atoms. The rms value of this electric field is determined by the irradiance (ϕ in W/cm^2) and is given by,

$$E_{rms} \cong 19.4\phi^{1/2} \tag{2.7}$$

For an irradiance $\geq 10^9$ W/cm^2, E_{rms} is $\geq 6\times10^5 Vm^{-1}$ resulting in the stripping of large numbers of electrons from their associated atoms. In the case of a thorium target, electrons in the valence and inner shells 7s, 6d, 6p and 6s, with binding energies ranging from 6 to 60eV, are ionised by an electric field of $6\times10^5 Vm^{-1}$. An rms electric field of $\sim1\times10^9 Vm^{-1}$ (3×10^{15} W/cm^2) would be required to ionise a 1s electron in thorium.

Two methods of ionisation predominate. Firstly, direct photoionisation occurs when an incoming photon has sufficient energy to directly ionise an atom. Electrons produced in this way may then proceed to ionise further atoms during collision events, thus resulting in a cascade effect (Weyl in Radziemski & Cremers, 1989). The second method, known as Multi-Photon Ionisation (MPI), occurs when a number of laser photons are absorbed simultaneously permitting a rather tightly bound electron (as in an insulating material) to be liberated. This latter process occurs very rapidly (within a few cycles of the laser electric field, Hughes 1975) and predominates at shorter laser wavelengths where the probability of its occurrence is greatly increased. For example, at longer wavelengths such as that of a CO_2 laser (10.6μm), the simultaneous absorption of 100 laser photons each of energy 0.1eV would be required to overcome a 10eV ionisation potential – compared to ~10 photons for an Nd:YAG laser (Weyl in Radziemski & Cremers, 1989). It should of course be stated that a 100 photon absorption event is highly improbable except at extreme irradiances ($\geq 10^{16} W/cm^2$, Svanberg et al. 1997). The rapid ionisation of surface atoms provides a large free electron population and this results in the increased efficiency of absorption of laser photons via the process of Inverse Bremsstrahlung. This is a process whereby a free electron in the electric field of an ion

Figure 2.1: A Q-switched laser pulse focused to an irradiance of ~10^9W/cm^2 on a metal surface produces a short lived, high density, high temperature plasma plume

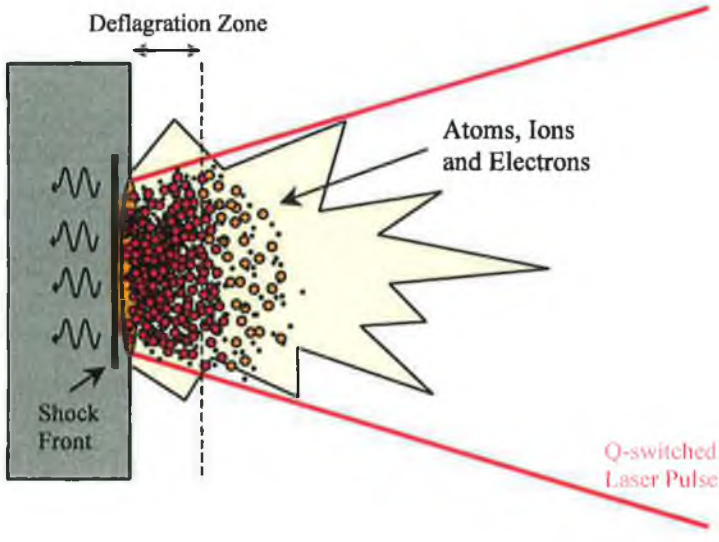

absorbs a laser photon, thus increasing its kinetic energy. Collisions with atoms/ions in the solid result in rapid melting and vaporisation of the metallic surface. The change in phase that occurs upon melting results in a decrease in the reflectivity of the target surface and consequently increased coupling of laser light onto the target (Ready 1971). The hot, dense vaporised plume that now forms at the target surface does not have time to expand by any significant amount throughout the very short laser pulse duration and so remains close to the surface. Most of the incident laser light is absorbed in this dense plasma region where $n_e \approx n_c$. This is termed the *deflagration zone* and is illustrated in Figure 2.1. The momentum recoil of matter ablating from the target surface, coupled with the radiation pressure of the laser light, result in the transmission of a compressive shock wave that propagates into the metal (Ready 1971). The increase in pressure at the target surface results in an increase in the surface vaporisation temperature due to its pressure dependency (Ready 1971).

After initial plasma formation, the coupling of laser light to the target surface is reduced due to the fact that it is reflected in the dense plasma region where $n_e = n_c$. As a result, heating and subsequent ablation of surface material is reduced. As the plasma begins to expand, n_e decreases and laser light once again reaches the target surface. This behaviour is termed *self-regulation* and occurs throughout the duration of the laser pulse (Hughes 1975). Upon termination of the laser pulse, the plasma continues to expand away from the target surface. Early time resolved spectroscopy and mass spectroscopy

experiments have yielded important information as to the energy distribution, velocity distribution, trajectories (angular distribution) and relative populations of various ionic/atomic species within the plasma plume (Boland et al. 1968, Bykovskii et al. 1971, Irons et al.1972). Higher ion stages, heated to higher temperatures and travelling at greater velocities than neutral and lowly charged ions, lead the expanding plasma plume. Such highly charged ions are distributed within a narrow angular region about the normal to the target surface and the radii of such distributions increase with decreasing charge state. Analysis of spectral lines emitted by the plasma plume permits the determination of n_e, T_e and atom/ion velocities (Bekefi et al. in Bekefi 1976, Tondello et al. 1977). The absolute intensity and/or relative intensity of spectral lines permits the determination of T_e. The width of the spectral line that is subject to two main types of broadening, Doppler and Stark, permits the determination of n_e, T_e and atom/ion velocities. Doppler broadening is attributed to the velocity of the atoms/ions within the plasma plume. Stark broadening results from the influence of the electric field emanating from charged particles in the vicinity of the emitting atom/ion and greatly exceeds Doppler broadening in dense, hot regions of the plasma formed near the target surface just after plasma initiation. Such highly ionised regions emit predominantly continuum emission. As the plasma cools and expands, the continuum intensity falls and line emission increases. The atomic processes occurring within the plasma plume are detailed further in Section 2.1.4 and the nature and origin of continuum emission particularly suited to photoabsorption type studies are detailed in Section 2.1.5.

2.1.4 Atomic Processes occurring within a Laser Produced Plasma

Energy derived by the plasma from the heating laser pulse is absorbed and consequently re-radiated via a number of different atomic processes. The relative importance of these processes varies with target material and the degree of ionisation, which in turn is determined by conditions such as plasma temperature and density. It is important to determine the contribution of each process to the net energy gain and corresponding losses within the plasma medium in order to improve our understanding of plasma behaviour. Various theoretical models are used to compute the behaviour of different types of laboratory plasmas. Such models are based on the assumption that some form

of equilibrium balance exists between the principal atomic gain and loss processes. A number of standard models exist and details of these are given in Section 2.1.4.4.

There are three main types of atomic process occurring within the plasma plume. These are (i) bound-bound transitions, (ii) bound-free transitions and (iii) free-free transitions. For each of these three processes, excitation or ionisation and the inverse processes, de-excitation or recombination can occur. All of these processes can be broadly classified as either a collisional or radiative events. The main atomic processes occurring within a laser produced plasma are summarised in Table 2.1.

Table 2.1 *Collisional and radiative events associated with the three main atomic processes occurring within a laser produced plasma*

Process	Collisional		Radiative	
	Excitation	De-Excitation	Excitation	De-Excitation
Bound ↔ Bound	Collisional Excitation	Collisional De-Excitation	Photoexcitation	Photo De-excitation
Bound ↔ Free	Collisional Ionisation	Recombination	Photoionisation	Recombination
Free ↔ Free		Bremsstrahlung (photon emitted)	Inverse Bremsstrahlung	

2.1.4.1 Bound ↔ Bound Transitions

A bound-bound excitation transition occurs when an atom/ion occupying a discrete atomic/ionic level is promoted to a higher energy level by the absorption of a finite quantum of energy. Collision of the atom/ion with other atoms, ions or electrons within the plasma plume can result in a bound-bound excitation occurring (Collisional Excitation). It is important to note that collisions with electrons are much more efficient than those with heavier particles due to higher electron velocities (Colombant & Tonon 1973) and so only electron collisions will be considered here. The reverse process can also occur whereby an atom/ion in an excited state losses energy to an electron during a collision event resulting in a transition to a lower energy discrete state (Collisional De-

excitation). Both processes are described by 2.8 where X is the initial atom/ion and e is the electron involved in the collision event.

$$X + e\,(T_1) \rightleftharpoons X^* + e\,(T_2) \quad (T_1 > T_2) \qquad (2.8)$$

In radiative bound-bound excitation transitions an atom/ion absorbs a photon of fixed energy and is thus promoted to a higher discrete state (Photoexcitation). In the reverse process, a photon of light is emitted as the atom/ion returns to lower energy state (Photo De-excitation). These processes are outlined in 2.9.

$$X + h\nu \rightleftharpoons X^* \qquad (2.9)$$

Spectroscopic investigations of light emitted as a result of the bound-bound photo de-excitation process reveal discrete line emission. The width of such spectral lines is determined by the lifetime of the upper excited atomic/ionic state. Superimposed on this are the effects due to Doppler and Stark broadening. Also, collisions with other plasma particles while the atom/ion is emitting (pressure broadening) contribute to the overall linewidth. Line emission from cool partially ionised plasmas for which $T_e \approx 1$eV emit predominantly in the infra red to visible spectral regions. As T_e is increased, atoms/ions occupy higher energy states and so, upon photo de-excitation, emit radiation at increasingly shorter wavelengths. Also, as many-electron atoms become increasingly ionised, discrete transitions shift to shorter wavelengths due to reduced nuclear screening.

2.1.4.2 Bound ↔ Free Transitions

A bound–free excitation occurs when an n (n=0,1,2…) times ionised atom gains energy in excess of one of its associated ionisation potentials, thus promoting an electron from a bound energy level to a 'free' continuum energy level. The result is a free electron (e_1) and an (n+1) times ionised atom (X^{n+1}). Collisions with other electrons within the plasma plume can result in such transitions (Collisional Ionisation). The reverse collisional process occurs when a free electron (e_1), during a collision with an (n+1) times ionised atom[1], loses energy and reverts to a bound discrete level. A third particle (e_2) involved in the collision process absorbs the excess energy (Three-Body Recombination). Both collisional processes are outlined in 2.10.

$$X^n + e_2\,(T_1) \rightleftharpoons X^{n+1} + e_1 + e_2\,(T_2) \quad (T_1 > T_2) \qquad (2.10)$$

[1] The electron (e_1) can also recombine with a neutral atom to produce a negative ion.

A bound-free radiative excitation transition occurs when a photon having sufficient energy to directly ionise an atom/ion is absorbed (Photoionisation). The inverse process occurs when a free electron drops from a continuum level to a discrete atomic/ionic energy level with the emission of a photon (Recombination). Both radiative processes are outlined in 2.11.

$$X^n + h\nu \rightleftharpoons X^{n+1} + e \qquad (2.11)$$

Collisional and radiative recombination result in the emission of continuum radiation rather than line radiation. For each atomic/ionic bound state formed after recombination of the free electron, continuum radiation is emitted over a broad energy range with a low-energy cut-off known as the *recombination limit* (Hughes 1975). This limit corresponds to the minimum energy required to remove an electron from the final atomic/ionic bound state. As a result, spectrally observed continuum emission is an integration of the various different recombination continua each of differing intensity and originating from numerous atomic/ionic bound states.

2.1.4.3 Free ↔ Free Transitions

Free-free radiative absorption occurs when a free electron that is travelling in the field of an ion absorbs a fixed energy photon. This process results in an increase in the electron's kinetic energy and is termed Inverse Bremsstrahlung. This process is one of the most important methods of plasma heating by laser light of all wavelengths (Hughes 1975). The process of Inverse Bremsstrahlung is particularly important in high-density plasma regions where $\omega >> \omega_p$ due to the fact that the absorption rate for this process scales as n_e^2. This process is outlined in 2.12 where n, the charge state of the ion is greater than zero,

$$X^n + e\,(T_1) + h\nu \rightleftharpoons X^n + e\,(T_2) \qquad (T_2 > T_1) \qquad (2.12)$$

The inverse process (i.e. Bremsstrahlung) occurs when a free electron collides with another particle resulting in the emission of a photon. Such emission is continuous in nature. Electron-ion and electron-atom collisions result in Bremsstrahlung emission where the former of these collision events is more efficient. Electron-electron collisions only produce radiation when travelling at relativistic speeds (Hughes 1975). The Bremsstrahlung emission process is outlined in 2.12, where X^n is an atom or ion of charge n.

2.1.4.4 Standard Plasma Models

Three standard plasma models have been developed in order to theoretically model and therefore correctly interpret the plasma conditions and observed emission spectra from a laser produced plasma (McWhirter 1965). The need for a range of differing models has arisen from the highly diverse nature of laboratory produced laser plasmas. The main criterion distinguishing such models is the value of the electron density n_e, which greatly influences the relative importance of the various atomic excitation and de-excitation processes. The laser plasma plume can reside in a steady state where ionisation equilibrium will exist if either rapid ionisation or rapid recombination does not occur. The three standard models describing different forms of ionisation equilibrium are,

(i) Local Thermal Equilibrium (LTE)
(ii) Coronal Equilibrium (CE)
(iii) Collisional-Radiative Equilibrium (CR)

and detailed descriptions of each are given by McWhirter (1965). Within each model the determination of the fractional ionisation density (2.13) for an ion of charge state z during steady-state is determined,

$$n_z \Big/ \sum_{i=1}^{z} n_i \tag{2.13}$$

where n_z is the ion density of charge state z and $\sum_{i=1}^{z} n_i$ is the total ion density in the plasma plume.

If the laser plasma behaved as an ideal black body radiator then its emission spectrum would be described by the Planck radiation distribution function. Its kinetic energy, excitation energy and ionisation energy would be described by the Maxwell, Boltzmann and Saha distribution equations respectively (Carroll & Kennedy 1981). A state of thermodynamic equilibrium would exist in the plasma and a single value of plasma temperature can then be used to determine all of the above energy distributions. Every atomic process occurring within the plasma is directly balanced by its opposite process. For example the rate of spontaneous radiative emission equals that of photoexcitation. The three standard plasma models attempt to describe departures from this ideal case, which is never realised in practice.

(i) Local Thermodynamic Equilibrium (LTE)

A high density, collisionally dominated plasma is said to be in a state of LTE when collisional excitation and collisional ionisation processes are balanced by the inverse processes of collisional de-excitation and three-body recombination. In order for the LTE model to apply, the probability of collisional de-excitation occurring should exceed that of radiative decay by a factor of at least ten for all transitions (Hughes 1975). The plasma temperature is, in general, not uniform throughout the plasma, but it is assumed that a temperature exists that will satisfy the Maxwell, Boltzmann and Saha energy distribution equations locally. Due to the dominance of collisional events, radiation from the plasma is significantly reduced and so is ignored. The lower electron density limit, above which LTE applies, is given by McWhirter (1965) as,

$$n_e \geq 1.6 \times 10^{12} T_e^{1/2} \chi^3 \mathrm{cm}^{-3} \qquad (2.14)$$

where T_e is in Kelvin and χ is the largest energy difference (in eV) between terms of the ion under consideration.

(ii) Coronal Equilibrium (CE)

As the electron density of the laser plasma is reduced the probability of radiative de-excitation transitions occurring becomes comparable to that of collisional de-excitation and even exceeds it for low densities comparable to that of the Sun's corona ($n_e \approx 10^8 \mathrm{cm}^{-3}$). In this low density regime plasma conditions are best described using the coronal equilibrium model. Here excitation/ionisation occurs via electron collisions due to the fact that the plasma, at such low electron densities is optically thin and radiation escapes without being absorbed. The main processes of de-excitation are spontaneous radiative decay and radiative recombination as the atom/ion has time to emit before suffering a collision (Hughes 1975). The differing importance of atomic processes and also the fact that each process is not balanced by the direct inverse process results in a different type of equilibrium being established in the coronal equilibrium model (Colombant & Tonon 1973).

(iii) Collisional-Radiative Equilibrium (CR)

This model applies in intermediate electron density regimes and is an adaptation of the coronal model in order to account for the addition of collisional de-excitation and

recombination (three-body) processes that are important for upper (high principal quantum number) energy levels at intermediate densities (McWhirter 1965, Colombant and Tonon 1973). Spontaneous radiative decay and radiative recombination remain important for lower energy levels. The CR model is best suited to electron densities in the region where n_e=10^{19}cm^{-3} to 10^{21}cm^{-3}. The electron densities of 10^{19}cm^{-3} and 10^{21}cm^{-3} are the critical densities for plasmas produced using CO_2 and Nd:YAG (or Nd:Glass) laser wavelengths of 10.6μm and 1.06μm respectively (Colombant and Tonon 1973). In steady state relative ion densities can be determined using

$$\frac{n_{z+1}}{n_z} = \frac{S(z,T_e)}{[\alpha_r(z+1,T_e) + n_e\alpha_{3b}(z+1,T_e)]} \tag{2.15}$$

where $S(z, T_e)$ is the collisional ionisation rate, $\alpha_r(z+1, T_e)$ is the radiative recombination rate and $\alpha_{3b}(z+1, T_e)$ is the three-body recombination rate, all of which apply to a charge state z and electron temperature T_e . These quantities are determined using the following relations (Colombant and Tonon 1973),

$$S = \frac{9\times10^{-6}\xi_z(T_e/\chi_z)^{1/2}}{\chi_z^{3/2}(4.88+T_e/\chi_z)} exp(-\chi_z/T_e)\text{cm}^3\text{s}^{-1} \tag{2.16}$$

$$\alpha_r = 5.2\times10^{-14}(\chi_z/T_e)^{1/2} z\left[0.429+\tfrac{1}{2}log(\chi_z/T_e)+0.469(T_e/\chi_e)^{1/2}\right]\text{cm}^3\text{s}^{-1} \tag{2.17}$$

$$\alpha_{3b} = 2.97\times10^{-27}\xi_z/T_e\chi_z^2(4.88+T_e/\chi_z)\text{s}^{-1} \tag{2.18}$$

where T_e is in units of eV, χ_z (eV) is the ionisation potential of an ion of charge state z and ξ_z is the number of electrons occupying the outer subshell of an ion of charge state z. Using 2.15 the fractional ion density for a given element can be computed and its evolution as a function of electron temperature T_e can be determined. In the case of thorium, as is the case for many rare earth and actinide elements, very few of its 90 ionisation potentials are known and so only an estimation of fractional ionic charge densities can be calculated. Colombant and Tonon (1973) obtained an approximation to expression 2.15. By removing the three-body recombination term from 2.15, the dependency on electron density n_e is removed. This approximation expresses the average ionic charge state z in terms of T_e (eV) only

$$z \approx \frac{2}{3}[ZT_e]^{1/3} \tag{2.19}$$

where Z is the element atomic number. This simplification is valid only for $T_e \geq 30$eV and $n_e \sim 10^{21}$cm^{-3} and also applies better in the case of high-Z ions such as in the case of uranium ions (modelled by Colombant and Tonon 1973). Using a hydrodynamic expansion model Colombant and Tonon (1973) have related T_e (eV), which is assumed to equal the ion temperature T_{ion}, to the incident laser power density ϕ (W/cm^2) such that

$$T_e \approx 5.2 \times 10^{-6} Z^{1/5} \left[\lambda^2 \phi\right]^{3/5} \tag{2.20}$$

where Z is the atomic number, λ (μm) is the wavelength of the laser light and ϕ is the on-target irradiance in W/cm^2. Equation 2.19 can therefore be applied with reasonable confidence in the case of the thorium laser plasmas produced using an Nd:YAG laser during the course of this work (see Figure 2.2). This permits an initial estimate of the average ionic charge state (z) residing in the plasma at a given electron temperature T_e. The laser characteristics, ϕ and λ, permit an estimation of T_e using 2.20. When the power density (ϕ) of the incident laser light is known, a corresponding value of T_e can be determined, thus enabling an estimate of the average ionic state for a given power density to be determined from plots such as Figure 2.2. The on-target irradiance can therefore be selected in order to optimise the density of a particular ionic charge state within the plasma plume. Using the DLP technique, the time synchronisation achievable between the source and absorbing plasmas permits probing of the latter at different times during its evolution. This facilitates the selection and optimisation of particular ionic species under investigation as higher ions can be studied early in the evolution of the absorbing plasma, whereas lower ion stages appear later on.

Typical on-target irradiances used in the production of thorium plasmas during the course of this work lay in the region of ~10^9 to 10^{12} W/cm^2 and were produced when 300mJ to 800mJ Nd:YAG laser pulses 15 to 30 ns in duration were focused to spot sizes of ~0.1 to 1mm diameter on planar targets.

Figure 2.2: Plot of average ionic charge state z vs. electron temperature T_e for a thorium laser plasma produced over a range of on-target irradiance values $\phi \approx 6\times10^9$ to 1×10^{12} W/cm^2 with 1.06μm Nd:YAG laser light

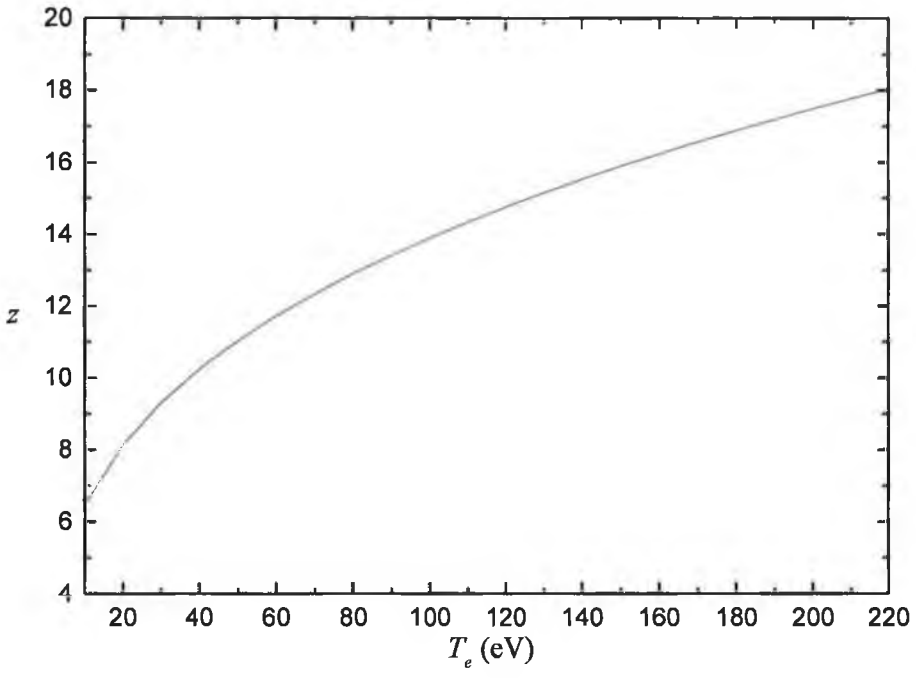

2.1.5 Origins and Characteristics of VUV/XUV Continuum Emission from a Laser Produced Plasma

The development of the synchrotron as a source of XUV continuum radiation in the 1960's resulted in the rapid growth of research interests in the fields of atomic, molecular and solid state physics utilising the high-energy continuous nature of this radiation. In particular, XUV continuum radiation permitted the investigation of inner shell excitation and decay dynamics and the extent of electron correlation effects on such excitations in atomic/ionic and molecular species using photoabsorption and photoionisation techniques. In parallel with the development of the synchrotron as a continuum source, the development of the ruby solid state laser in 1960 (Maiman) initiated a new field of study involving the interaction of intense laser light with matter. The massive on-target irradiances achievable with such high-power lasers facilitate the production of sufficiently high ion stages required for generation of continuum emission. As a result, laser produced plasmas (where $\phi \geq 10^9$W/cm^2) emit both line and

continuum radiation, the relative contributions of each depending on the choice of target material, distribution of ionisation stages achieved within the plasma, and spectral regions of observation. In 1966 continuum emission from a laser plasma was first observed by Ehler and Weissler in the VUV spectral region extending from 35 to 400nm. The target materials of beryllium (Z=4), aluminium (Z=13), nickel (Z=28), tantalum (Z=73), tungsten (Z=74) and platinum (Z=78) used in this study illustrated the transition from predominantly line emission, in low-Z elements, to continuum emission in the higher Z elements. In this same year, XUV continuum emission was observed at ~7nm by Fawcett and co-workers (1966) for a series of targets ranging from carbon (Z=6) to zinc (Z=30). Breton and Papoular (1973) studied VUV continuum emission from laser-irradiated tantalum and tungsten targets in the 100 to 200nm region. A primary motivation for this study was to develop a high radiance VUV source in order to determine the density distribution of hydrogen atoms in thermonuclear devices. The laser plasma source was chosen by Breton and Papoular over conventional continuum-emitting spark sources due to its higher VUV spectral radiance and the relative ease with which the source can be located within an experimental system. Before the development of synchrotron and laser plasma sources, discharge systems were used to produce continuum emission in the VUV to XUV regions (Ballofet et al. 1961). However, such sources suffered from limited spectral coverage and were contaminated with undesirable line emission, thus reducing their attractiveness to photoabsorption studies in particular (Carroll & O'Sullivan 1991). Carroll and co-workers (1978, 1980) observed broad, essentially 'line-free' bands of continuum within the VUV to XUV spectral region of 4 to 200nm in a systematic study of laser plasma emission from samarium (Z=62) to tungsten (Z=74). The broad-band continuum emitted by typically ten to sixteen times ionised species within the plasma plume of high-Z elements makes them ideal background sources and consequently they have been utilised extensively in time and space resolved photoabsorption/photoionisation experiments (Costello et al. 1991, Nicolosi et al. 1991, O'Sullivan et al. 1994, Kennedy et al. 1999). Soft X-ray continuum emitted from highly ionised hydrogen-like and helium-like carbon and beryllium plasmas (2 to 4.2nm region) and moderately ionised copper and uranium plasmas (3 to 8nm region) was observed by Nicolosi and co-workers (1981). Again, essentially 'line-free' continuum dominated the higher Z plasmas, whereas resonance transitions of hydrogen-like and helium-like ions were superimposed on the soft X-ray continuum observed in the lower Z elements of carbon and beryllium. X-ray spectra in the 0.8 to 1.6nm region emitted by hydrogen-like oxygen ions produced in a laser

plasma and recorded using a crystal spectrometer also displayed strong emission lines superimposed on the underlying x-ray continuum (Korukhov & Troshin 1990).

Three different types of radiative atomic transition contribute to the formation of continuum emission. These are Bremsstrahlung emission (free-free transitions), recombination emission (free-bound transitions) and unresolved transition arrays (UTA, bound-bound transitions). The processes of recombination emission (2.11) and Bremsstrahlung emission (2.12) have been discussed in Sections 2.1.4.2 and 2.1.4.3 and always occur together in an ionised plasma plume despite different relative contributions for diverse laser (and hence plasma) conditions. UTA's, on the other hand, are a direct result of the wavefunction collapse phenomenon and consequently only contribute to the continuum in the emission spectra of highly ionised high atomic number atoms and will be discussed in detail later in this section. Suffice to say here that they are arrays of many hundreds of thousands of lines, which are narrowly spaced over a photon energy interval of typically <10eV.

The intensity of recombination continuum emission depends on ξ_{av}^4, whereas Bremsstrahlung continuum intensity depends on ξ_{av}^2 (where ξ_{av} is the average ionic charge state in the plasma plume). As Z is increased along the periodic table, ξ_{av} increases due to the fact that ionisation potentials on average decrease for a given charge state with increasing Z and as a result higher values of ξ_{av} are achieved (O'Sullivan et al. 1999). Also the heavier mass of high-Z atoms/ions means that they spend more time in the high density heating region (deflagration zone) and this factor also contributes to higher values of ξ_{av} (O'Sullivan et al. 1999). In low-Z materials the intensity of recombination radiation varies in a step-like manner with energy due to the sharp recombination limits present for each final bound atomic/ionic state. Such features become more smoothed in appearance in the spectra of high-Z elements due to the presence of a greater range of ion stages resulting in the significant overlap of recombination continuum channels. The intensity of Bremsstrahlung radiation varies smoothly with energy for all elements. The intensity of Bremsstrahlung emission will dominate over that for recombination in a fully ionised system when the following condition holds,

$$kT_e > 3\chi_o Z^2 \tag{2.21}$$

where kT_e is the plasma temperature, χ_o is the ionisation potential for hydrogen and Z is

the atomic number. Consequently, Bremsstrahlung emission dominates in low-Z plasmas where T_e is high as a result of a high on-target laser irradiance (Carroll & Kennedy 1981). Conversely, recombination emission dominates in situations where conditions opposite to those above prevail.

As previously mentioned, line emission is superimposed on underlying continuum, particularly in low-Z elements. As the atomic number (Z) of the target material is increased higher electron and ion densities can be achieved due to the increased degree of ionisation and the reduced mass flow rate (O'Sullivan 1983). Line emission consequently decreases in high-Z materials due to the fact that self-absorption (by the plasma) of line radiation occurs at lower ion densities than that for continuum radiation. The condition for self-absorption or line radiation trapping within Doppler broadened lines is

$$\int_0^R n_\xi(r)dr > \frac{9.28\times10^{15}(kT_e^{1/2}/Z)}{f\lambda} \tag{2.22}$$

where $n_\xi(r)$ is the number density (in cm^{-3}) of absorbing ions of charge state ξ, r is a radial co-ordinate (cm), R is the absorbing path length (cm), kT_e is the plasma temperature (eV), f is the oscillator strength of a given transition and λ (Å) is the transition wavelength. f values for continuum radiation are relatively weak and consequently continuum radiation can propagate unattenuated through the plasma at higher ion densities than individual line transitions having higher f values (Carroll & O'Sullivan 1982). This effect, known as plasma opacity, is not entirely responsible for the extensive VUV and XUV regions of essentially 'line-free' continuum in the 4 to 200nm spectra of elements in the region $62 \leq Z \leq 74$ studied by Carroll and co-workers (1978, 1980). Strong line emission that occurs in elements before these elements reappears again in elements beyond them. The lack of strong line emission in these elements is essentially due to the formation of UTA's that contribute to the underlying recombination and Bremsstrahlung continua. Regions of 'line-free' continuum emission and regions of line emission superimposed on underlying continuum measured in elements $62 \leq Z \leq 74$ by Carroll and co-workers (1978, 1980) are shown in Figure 2.3. All plasmas were produced by a 25ns Q-switched ruby laser pulse focused to an on-target irradiance in the region of 10^{11} to 10^{12} W/cm^2. Most of the strong line emission originates from low ion stages up to six times ionised and can be eliminated by increasing the plasma temperature (O'Sullivan 1983). Also, in similar experimental studies, it was observed that careful focusing of the hot dense plasma core onto the

entrance slit of the spectrograph results in a reduction in the intensity of line emission that originates from lowly charged ions outside the dense core region (Breton & Papoular 1973, Orth et al. 1986).

The UTA is a major process contributing to the flattening out of line emission for ions of the elements in the region $62 \leq Z \leq 74$ and is formed as a result of 4f wavefunction collapse. For lowly charged ions of such elements, the 5s and 5p subshells are filled whereas the 4f contains a variable number of electrons across the series. As the ion charge state is increased the binding energy of 4f electrons increases more rapidly than that of 5s and 5p so that for approximately six times ionised species it exceeds that of the 5p (Carroll & O'Sullivan 1982). 4f collapse continues with increased ionisation until

Figure 2.3: *VUV/XUV emission spectra of elements in the region $62 \leq Z \leq 74$ exhibiting bands of 'line-free' continuum and line emission superimposed on underlying continuum for an on-target irradiance of ~2 $\times 10^{11}$ W/cm^2 (from O'Sullivan 1983)*

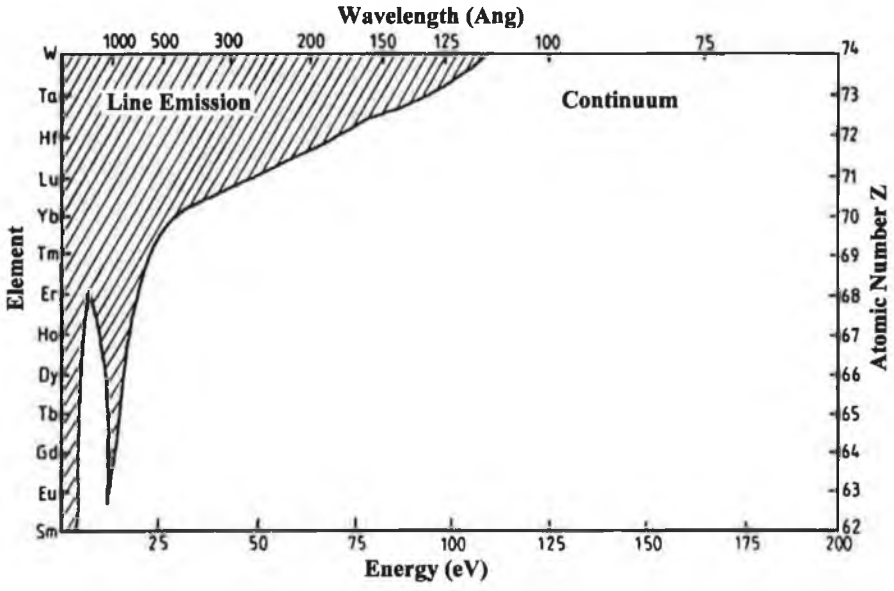

at approximately the thirteenth ionisation stage the 4f binding energy exceeds that of the 5s. In the plasmas produced by Carroll and co-workers (1978, 1980), ion stages up to and including sixteen times ionised were estimated to reside in the plasma plume using the collisional-radiative model of Colombant and Tonon (Carroll et al. 1983). These ions will therefore contain 4f electrons in their ground state configurations resulting in a large number of associated terms. Also, the close proximity of the 4f, 5s and 5p binding

energies results in many excited configurations lying close to the ionic ground state, making the exact ionic ground state uncertain and it is therefore best described as $(4f5s5p)^q$, where q is the total number of electrons occupying the 4f, 5s and 5p subshells (O'Sullivan 1983). Transitions among the many terms of such closely lying states can amount to hundreds of thousands of closely spaced lines that are weakened due to the fact that the available oscillator strength is spread over such a huge number of transitions. Doppler or other broadening mechanisms within the plasma plume result in these closely spaced lines merging together to form an emission band (Bauche et al. 1988). The strongest transition series observed in the region $62 \leq Z \leq 74$ is the 4d→4f UTA which occurs in approximately the same spectral region for adjacent ion stages of a given element which is in turn characteristic of $\Delta n=0$ transitions (Carroll & O'Sullivan 1982). The superposition of 4d→4f transitions originating from seven to fifteen times ionised species results in the formation of UTA spanning 30eV (Carroll et al. 1983). This range of ion stages are believed to contribute to the observed emission in the 70nm spectral region where the 4d→4f transitions are located. The huge number of possible lines calculated for $4d^{10}4f^{n} \rightarrow 4d^{9}4f^{n+1}$ transitions within an LS coupling scheme for n=0 to 13 are shown in Table 2.2. In fact it has been shown by O'Sullivan and co-workers (1999) that strong configuration interaction between $(4f5s5p)^q$ configurations leads to a redistribution of oscillator strength from stronger transitions leading to further smoothing of the spectrum. Of course, the number of transitions also increases as LS

Table 2.2: *Number of possible lines within the $4d^{10}4f^{n} \rightarrow 4d^{9}4f^{n+1}$ transition array calculated within an LS coupling scheme for ground/excited states of lanthanide and neighbouring ions where n=0 to 13 (from Carroll & O'Sullivan 1982)*

$4d^{10}$-$4d^{9}4f$	1	$4d^{10}4f^{7}$-$4d^{9}4f^{8}$	75 997
$4d^{10}4f$-$4d^{9}4f^{2}$	51	$4d^{10}4f^{8}$-$4d^{9}4f^{9}$	48 151
$4d^{10}4f^{2}$-$4d^{9}4f^{3}$	636	$4d^{10}4f^{9}$-$4d^{9}4f^{10}$	19 483
$4d^{10}4f^{3}$-$4d^{9}4f^{4}$	4 574	$4d^{10}4f^{10}$-$4d^{9}4f^{11}$	4 317
$4d^{10}4f^{4}$-$4d^{9}4f^{5}$	19 013	$4d^{10}4f^{11}$-$4d^{9}4f^{12}$	638
$4d^{10}4f^{5}$-$4d^{9}4f^{6}$	45 334	$4d^{10}4f^{12}$-$4d^{9}4f^{13}$	53
$4d^{10}4f^{6}$-$4d^{9}4f^{7}$	83 024	$4d^{10}4f^{13}$-$4d^{9}4f^{14}$	3

coupling begins to break down thereby further enhancing the continuum-like appearance of rare earth plasma spectra. Other series of UTA's occur across the 4 to 200nm VUV/ XUV region in lanthanide and neighbouring elements but are not as prominent as that of the 4d→4f UTA and consequently are more submerged into the background continuum.

2.1.5.1 Spectral Characteristics of Tungsten XUV and VUV Continuum Emission

Throughout the course of this work, tungsten was primarily used as a backlighting continuum source in the XUV (5 to 50nm) and VUV (20 to 220nm) regions as defined by the spectral ranges of a 2.2m grazing incidence spectrometer and a 1m normal incidence spectrometer. The profile of tungsten emission in the XUV region of 8 to 40nm is shown in Figure 2.4. This spectrum, measured by Bridges and co-workers (1986), was emitted from a tungsten plasma produced when a 500mJ Nd:YAG laser pulse, having a FWHM of 25ns, was focused to an irradiance in the region of 10^{11} to 10^{12} W/cm^2 on the surface of a cylindrical tungsten rod target. Such conditions are very similar to those used in the Centre for Laser Plasma Research laboratory where Nd:YAG lasers produce pulses ranging from 300 to 800mJ with pulse-widths in the region of 15ns FWHM yielding on-target irradiances of 10^9 to 10^{12} W/cm^2. The

Figure 2.4: *XUV emission from a tungsten plasma produced when a 500mJ Nd:YAG laser pulse, having a FWHM of 25ns, was focused to an irradiance in the region of 10^{11} to 10^{12} W/cm^2 on the surface of a cylindrical tungsten rod target in the 8 to 40nm region (from Bridges et al. 1986)*

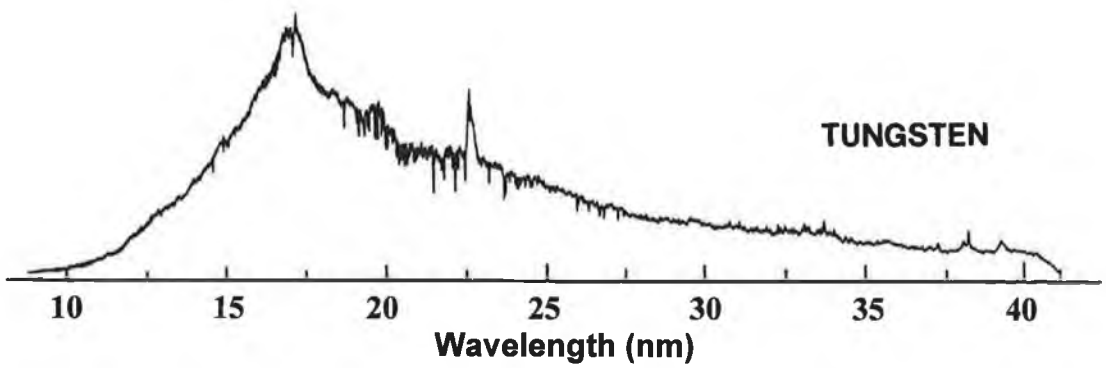

spectrum in Figure 2.4 was recorded using a 1.5m grazing incidence spectrometer and represents an average of 20 laser shots. In this XUV region tungsten emits predominantly smooth continuum with some line structure in the 17 to 25nm region.

Tungsten emission measured in the VUV region of 20 to 220nm during the course of this work is shown in Figure 2.5. This spectrum was obtained using a 1m normal incidence spectrometer and represents an average of 10 laser shots. The tungsten plasma was produced when a 700mJ Nd:YAG laser pulse, having a FWHM of ~15ns was

Figure 2.5: *VUV emission from a tungsten plasma produced when a 700mJ Nd:YAG laser pulse, having a FWHM of ~15ns, was focused to an irradiance of ~5×10^{11} W/cm^2 on the surface of a cylindrical tungsten rod target in the 20 to 220nm region*

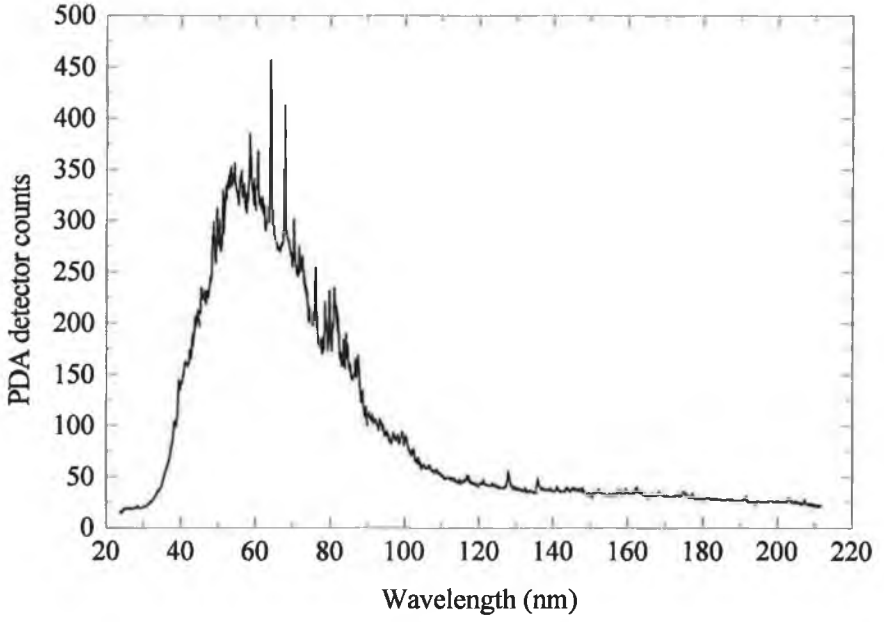

focused to an irradiance of ~5×10^{11} W/cm^2 on a cylindrical tungsten rod target. Again the spectrum exhibits extensive regions of featureless continuum with some line structure in the 30 to 90nm region. Both spectra in Figures 2.4 and 2.5 are shown uncorrected for the respective grating efficiencies of the two spectrometer instruments, which are known peak at 19nm (XUV) and 80nm (VUV)[2] respectively. Consequently the true intensity profile of the XUV and VUV continua is modulated by the varying

[2] Although the 1m normal incidence grating is blazed for 80nm, the peak of emission intensity in tungsten is located in the 50-60nm region. This apparent shift in system peak response is due to the brightness of the tungsten plasma in this region (Doyle, 1995).

spectral efficiencies of the spectrometer system components such as gratings, optical components and detectors.

2.1.5.2 Temporal Characteristics of XUV and VUV Continuum Emission

The focus of a major portion of this work was on the production and subsequent spectral and temporal characterisation of the XUV continuum emission from high-Z plasmas produced using a 7ps 248nm KrF excimer laser system at the Rutherford Appleton Laboratory (Meighan et al. 1997). Of particular interest was the study of the temporal evolution of XUV continuum emission in the 100 to 200eV (12 to 6nm) region from copper (Z=29), samarium (Z=62), tungsten (Z=74), gold (Z=79) and lead (Z=82) plasmas.

Breton and Papoular (1973) measured the duration of VUV continuum emission in the wavelength region from 60 to 240nm for the high-Z metals, tungsten and tantalum, upon irradiation with a 30ns 1J Nd laser pulse. The emission rise time (from zero to maximum) ranged from ~55ns at 60nm to ~60ns at 240nm. The decay time (from maximum to 20% of maximum) was observed to increase and become more exponential with increasing wavelength and varied from ~60ns at 60nm to ~160ns at 240nm. Similar emission profiles were observed by Carroll and co-workers (1980), who recorded VUV and XUV continuum emission from high-Z plasmas produced using 1J ruby laser pulses of 25ns FWHM. At 220nm, VUV emission pulses having a FWHM of ~100ns were recorded, with a long exponential fall time resulting in appreciable amplitude 300ns after the rising edge of the exciting ruby laser pulse. At 8nm, XUV emission durations significantly shorter than those in the VUV and having a FWHM of 20 to 25ns, which is comparable to that of the laser pulse, were measured. Nicolosi and co-workers (1981) measured the duration of soft X-ray continuum emission from a carbon laser plasma produced using 10J 14ns ruby laser pulses. Measurements of ~30ns at 3nm were again of similar duration to that of the laser pulse. Mosnier and co-workers (1996) observed XUV pulse durations of ~20ns FWHM (at 10nm) for a series of high-Z plasmas produced using 0.5J, 15ns, FWHM Nd:YAG laser pulses.

With the choice of suitable target material, the laser plasma provides an excellent back-lighting source of UV to soft X-ray continuum emission which is particularly suited to probing a second (sample) laser plasma in DLP-type photoabsorption studies. The temporal resolution of such studies is defined by the duration of the source continuum emission and increases with decreasing wavelength. The use of short pulse lasers (ps, fs) to produce the back-lighting continuum laser plasma source results in a mainly laser-matter interaction rather than the predominantly laser-plasma interaction that occurs throughout the duration of a nanosecond laser pulse. The short pulse picosecond XUV continuum produced during this work using a picosecond laser pulse provides increased temporal resolution when probing the dynamics of the absorbing plasma. This is particularly important at times soon after the creation of the absorbing plasma (0→50ns) when the usual ~20ns XUV continuum pulse integrates over the early history of the plasma. The evolution of higher ionic charge states, occurring at the start of plasma evolution, can therefore be investigated in greater detail using a picosecond XUV continuum pulse. The characteristics of plasmas produced using picosecond laser pulses are outlined in Section 2.1.7. Details of experimental set-ups used in the production and characterisation of the picosecond XUV continuum laser plasma source are given in Section 3.2.3 and Section 3.2.4 Chapter 3. The spectral and temporal characteristics of the source are discussed in Chapter 4.

2.1.6 Recent Advances in Ultra-Short, Ultra-Intense Laser-Matter Interactions

Recent developments in laser technology now permit the study of laser-matter interaction at ultra-high irradiances never before attained. State of the art high-power, short-pulse lasers at large-scale research facilities are now capable of generating on-target irradiances in excess of 10^{21} W/cm^2, which is equivalent to focusing the entire sunlight incident on the surface of the earth down to the size of a pinhead for less than a picosecond (Backus et al. 1998). International Inertial Confinement Fusion (ICF) research efforts have prompted rapid developments in laser science and technology and have permitted the study of laser-solid and laser-plasma interactions in new and previously unexplored regimes. High power lasers used in direct- and indirect-drive fusion research produce pulses with typical durations of 0.5 to 1ps and with energies of several hundred joules (Kruer 1991, Backus et al. 1998). Short wavelength laser light in

the visible and near UV regions, produced by converting 1.06μm Nd:Glass laser light to the second (0.53μm), third (0.35μm) and fourth (0.26μm) harmonic, is best suited to ICF studies (Campbell 1992). An example of a current state of the art high power laser is the *petawatt* (1 petawatt = 10^{15}W) beamline at the Nova laser fusion facility at the Lawrence Livermore National Laboratory. 527nm pulses approximately 500fs (1 femtosecond = 10^{-15}s) in duration are amplified to energies of ~600J, resulting in a peak pulse power of up to 1.25 petawatts and on-target irradiances in excess of 10^{21}W/cm^2 (Backus et al. 1998). For intensities in excess of 10^{18} W/cm^2 the coupling of laser light to the near solid-density plasma plume becomes increasingly non-linear. Effects such as Stimulated Brilluoin Scattering (SBS), Stimulated Raman Scattering (SRS), parametric instabilities, laser self-focusing (filamentation) and plasma hole-boring gain increasing significance (Campbell 1992).

The generation and subsequent amplification of laser pulses as short as a few femtoseconds has been achieved using the self mode-locking, broad band width Ti:sapphire crystal amplifier (Spence et al. 1991). Coupled with the use of the Chirped Pulse Amplification (CPA) technique (Strickland & Mourou 1985) these new developments have revolutionised both large-scale and table-top laser systems. Table Top Terawatt (T^3, 1 terawatt = 10^{12}W) lasers can run at high repetition rates (up to kHz) producing pulses 10 to 100's of femtoseconds in duration with energies up to 10's of mJ's. Such systems, producing on-target irradiances in the region of 10^{15} to 10^{18} W/cm^2, have permitted the observation of high-order harmonic generation (Macklin et al. 1993), laser-wake field acceleration with accompanying MeV X-ray emission and MeV electron generation (Kmetec 1992, Hamster et al. 1993) and short pulse subpicosecond incoherent X-ray emission (Murnane et al. 1989a).

Of particular interest here is the generation of short pulse incoherent soft X-ray/XUV emission when a short pulse (fs, ps) laser produces a hot, high density, short-lived plasma. Such plasmas, in particular those produced using femtosecond pulses, differ greatly from conventional plasmas produced using 'long-pulse' nanosecond lasers.

2.1.7 Physical Characteristics of Laser Plasmas Produced using Short Pulse (<1ns) Lasers

When an intense femtosecond laser pulse is focused onto a solid material, electrons within a skin depth (δ) of the surface are stripped from their parent atoms/ions by the intense electric field of the laser pulse and undergo rapid heating. If the duration of the laser pulse (τ) is less than the time (t) required for the target material to expand by an amount equal to the skin depth δ, then laser energy is absorbed at solid density where $n_e \approx 10^{24}\text{cm}^{-3}$ (Murnane et al. 1991a,b). This condition is expressed as

$$\tau < t \approx \frac{\delta}{v} \approx \frac{\delta}{\sqrt{k\xi T_e / M_i}} \tag{2.23}$$

where v is the plasma expansion velocity, k is Boltzmann's constant, ξ the ion stage, T_e the electron temperature and M_i the ionic mass. When laser energy is absorbed at solid density, the density scale length (L) is very small. This quantity is used to characterise the spatial extent of the plasma and is inversely proportional to the electron density gradient (Kruer 1988)

$$-\frac{1}{L} = \frac{1}{n_e}\frac{dn_e}{dx} \tag{2.24}$$

where the electron density profile $n_e(x)$ falls off exponentially from a maximum value n_o to $0.1n_o$ over the plasma scale length L

$$n_e(x) = n_o \exp\left(\frac{-x}{L}\right) \tag{2.25}$$

Laser energy is efficiently absorbed via the process of inverse Bremsstrahlung in a collisionally dominated short scale length plasma. High electron temperatures are consequently achieved resulting in the formation of a short lived, high density X-ray emitting plasma plume at the target surface. Subpicosecond incoherent keV X-rays are emitted from such a plasma due to (i) rapid thermal conduction into the target material, (ii) rapid expansion of the plasma plume into the vacuum environment due to the high pressure gradient existing in a short scale length plasma and (iii) a rapid decrease in electron temperatures caused by frequent inelastic collisions with atoms/ions at high densities (Murnane et al. 1989b, 1991a).

Plasma expansion occurs at speeds of typically 0.1nm fs^{-1} and for laser pulsewidths in excess of 1ps (7ps pulsewidth used in RAL studies), plasma expansion during the laser pulse results in laser energy being absorbed at the critical density (n_c), which is orders

of magnitude below solid density[3] (Murnane et al. 1991b, Leng et al. 1995). Rapid expansion and cooling of such a plasma having a relatively long density scale length does not occur and consequently X-ray emission durations increase with increased cooling times (Murnane et al. 1991b).

The presence of a pedestal (often due to a nanosecond duration amplified spontaneous emission (ASE) pulse) of sufficient intensity (i.e.$\phi \geq 10^9$ W/cm^2 when focused) on the leading edge of a short laser pulse (< 10ps) will result in the ablation of material from the target surface. This results in the formation of a long scale length plasma in which most of the laser energy is deposited at the critical density (rather than at higher densities close to solid density). This results in increased X-ray emission durations, which are again due to reduced cooling rates in a lower density plasma plume. A similar effect on X-ray emission durations is observed when a pre-pulse arrives at the target surface, creating a pre-formed plasma before the arrival of the main laser pulse. If the pre-pulse is sufficiently close to the main pulse, then energy from the main pulse will be deposited in the pre-formed plasma (Murnane et al. 1991a,b). Also, the presence of such a pre-pulse beneficially results in increased X-ray emission intensities (Dunne et al. 2000, Ahn et al. 1996, Steingruber et al. 1996). Amplified spontaneous emission, originating in the laser amplifier and with pulsewidths equal to the laser pump cycle (ns), can also generate a pre-formed plasma when it is of sufficient intensity. The presence of an ASE pedestal results in changes to X-ray pulsewidths and intensities similar to those observed with pre-pulses (Murnane et al. 1989b, Kyrala et al. 1994, Kieffer et al. 1994). A high contrast ratio between the main laser pulse energy and the ASE-pedestal or pre-pulse energy ensures that the energy of the latter processes is insufficient to generate a pre-formed plasma before the arrival of the main pulse (Gamaly 1994).

2.1.8 Advantages of Laser Produced Plasma Sources

The laser produced plasma ultimately serves as both a particle (electron, positive ion) and a light source. Laser plasmas produced using both Q-switched (ns) and self-modelocked/modelocked (fs/ps) laser systems possess many favourable characteristics,

[3] n_c is highest for short wavelength laser light. For example $n_c = 10^{22}$cm^{-3} for UV 248nm KrF laser light.

thus making them applicable to numerous and diverse experimental regimes. The main attributes of the LPP are as follows:

(i) Set-up and operation of an LPP source are highly cost effective when compared with large-scale synchrotron storage rings. Experimental equipment required is limited to a laser system, vacuum system and suitable target material (solid/liquid/gas). Consequently an LPP source can be established relatively easily in a small scale-laboratory.

(ii) An LPP source can be accurately positioned within an experimental set-up by simply adjusting reflecting and focusing optical components.

(iii) The spatial extent of VUV to X-ray emitting regions within an LPP is so small (typically less than a few hundred microns) that the LPP source is effectively point-like, thus permitting spatially resolved studies.

(iv) Target materials of differing atomic number Z and variations in the laser intensity (for a given target material) result in the emission of varying degrees of line and continuum emission. Line emitting plasmas are particularly suited to the wavelength calibration of spectroscopic detectors, whereas continuum emitting plasmas serve as ideal backlighting sources in pump-probe type studies.

(v) Light emitted from a 'table-top' LPP covers a wide spectral region, ranging from several tenths to hundreds of nanometers.

(vi) The various atomic processes occurring within an LPP source remain unaffected by ambient pressures up to several Torr (see results obtained by Carroll et al. 1980). This eliminates the need for differential pumping and strict UHV environments such as those required at synchrotron sources. This inherent feature of the LPP source also permits photoabsorption/photoionisation studies of gases using the LPP as a backlighting source.

(vii) The LPP serves as a source of both electrons (Van Wonterghem & Rentzepis 1990) and positively charged ions (Sellmair & Korschinek 1988) which can be

extracted and collimated to form charged particle beams using electric and magnetic fields.

(viii) Light pulses emitted from an LPP source have durations ranging from 100's of nanoseconds in the VUV to 100's of femtoseconds in the X-ray spectral region depending on the choice of target material, laser pulsewidth and laser energy. LPPs are therefore highly suited to a wide range of temporal studies that probe the dynamics of transient species with different temporal resolution in different spectral regions.

(ix) Light emitted from an LPP is to a large extent incoherent and unpolarised. However, coherence lengths of ~10μm have been observed in the 2.3 to 4.4 nm 'water window' spectral region (Daido et al. 1992). Reflection off focusing and collimating mirrors at VUV photon energies and multi-layered structures at XUV/soft X-ray photon energies (Bijkerk & Shevelko 1991) yield laser plasma light with a reasonable degree of polarisation. High order harmonic generation of the laser frequency at high laser intensities ($\phi \geq 10^{15}$ W/cm^2) yields coherent XUV light pulses from both laser plasma (L'Huillier & Balcou 1993) and gaseous media (Macklin et al. 1993).

(x) The LPP is a high brightness light source with peak photon fluxes in the XUV/X-ray region. The peak (single pulse) spectral brilliance of the LPP source in the 1 to 10nm photon energy range can be as high as ~5×10^{17} photons/ s.mm^2.mrad^2.0.1% bandwidth (exceeding that of second-generation synchrotron sources). The introduction of insertion devices into third generation synchrotron sources has resulted in increased spectral brilliance, with average values ranging from 5×10^{18} to 1×10^{19} photons/s.mm^2.mrad^2.0.1% bandwidth over the X-ray region of 1 to 10nm (U5 undulator at the Advanced Light Source). The spectral brilliance of the laser plasma based X-ray laser sources developed at Princeton and the Lawrence Livermore National Laboratory (LLNL) in the mid 1980's have typical peak values of 1×10^{20} photons/s.mm^2.mrad^2.0.1% bandwidth and 3×10^{23} photons/ s.mm^2.mrad^2.0.1% bandwidth at ~20nm. The proposed peak spectral brilliance of the TTF Free Electron Laser (FEL) at the HasyLab in Germany is 2.2×10^{30} photons/s.mm^2.mrad^2.0.1% bandwidth at 6.4nm, with that of the HasyLab TESLA FEL proposed to be 9.7×10^{33} photons/

s.mm^2.mrad^2.0.1% bandwidth at 0.1nm. For applications requiring moderate XUV/X-ray photon fluxes, the laser plasma is an attractive source option due to its extreme versatility and low-cost. Advances in laser technology resulting in increased repetition rates, e.g. duty cycles of kHz for the Ti:sapphire laser (Backus et al. 1998), have resulted in an increase in the average spectral brilliance of the laser plasma source relative to that of synchrotron devices.

(xi) The spectral radiance of a laser plasma source in the 115 to 220nm range has been demonstrated by O'Sullivan and co-workers (1982) to be reproducible to within ±10% from laser shot-to-shot. Fischer and co-workers (1984) measured a peak spectral radiance of ~10^{14} photons/nm/sr (at 10nm) emitted from a tungsten plasma produced using 1064nm, 800mJ, 15ns (FWHM) laser pulses very similar to those used in this work (SL803). They found the spectral radiance to be reproducible to within ±10%, with a large portion of this uncertainty attributed to the measuring instrumentation.

2.1.9 Primary Applications of the Laser Produced Plasma

As mentioned previously, the LPP source has numerous diverse applications due to the very high degree of versatility it displays. The following is a brief outline of the primary areas where the LPP finds application.

The utilisation of X-ray light and super-heated electrons emitted from an LPP to initiate indirect-drive and direct-drive (see for example Kilkenny et al. 1999) ICF experiments has been a major driving force behind laser plasma research and development. The requirement of the international ICF community for ever-increasing on-target laser irradiances has resulted in tremendous advancements in laser technology (Kruer 1991, Backus et al. 1998) and permits the study of matter in previously unexplored regimes (Campbell 1992). The LPP source can also be used as a diagnostic X-ray backlighting source, whose short wavelength emission is particularly suited to imaging high-density imploding ICF fuel pellets (Failor et al. 1990). The technique of point projection absorption spectroscopy (PPAS), whereby X-ray emission from a laser plasma source is used to probe matter, has been employed to image laser-irradiated spherical imploding

targets (Lewis & McGlinchey 1985). More recently, the point projection technique has been used to study plasmas used in X-ray laser research in order to determine the spatial and temporal dependence of atomic/ionic level populations and also the density and temperature of the absorbing plasma plume (O'Neill et al. 1991).

The LPP serves as an ideal lasing medium and is utilised in XUV/Soft X-ray laser research to produce high brightness coherent light pulses in the 10 to 30nm spectral region (Matthews & Rosen 1988). The first demonstration of an X-ray laser was performed by Matthews and co-workers (1985) at the Lawrence Livermore National Laboratory. Population inversion was achieved in a neon-like selenium plasma via an electron-ion collisional excitation scheme and spontaneous emission at 20.63nm and 20.96nm was amplified by up to 700 times. X-ray laser schemes based on rapid recombination to upper laser levels of highly charged low-Z ions during rapid cooling and expansion of the plasma plume have achieved increasing levels of gain at lower wavelengths such as 18.2nm (Suckewer et al. 1985, Zhang et al. 1995). Novel schemes have been presented to efficiently pump the lasing plasma medium. One such scheme entailed pumping metastable Be^{2+} ions (populated by recombination processes in the laser plasma plume) using a dye laser at 614.2nm in order to populate an upper laser level resonant with the Be^{2+} ground state. This resulted in population inversion and subsequent lasing at 10.03nm to the Be^{2+} ground state level (Simanovskii et al. 1996). Norreys and co-workers (1993) have utilised resonant nickel-like line radiation from a samarium 'pump' plasma to populate upper laser levels in a second lasing samarium plasma and thus achieve lasing action at 6.46nm, 6.92nm and 9.85nm. In 1994, Rocca and co-workers extended the realm of the X-ray laser from large-scale laser facilities to a small-scale laboratory environment. They built a 'table-top' soft X-ray laser using a 12cm discharge-induced argon plasma column lasing at 46.9nm. Recent advances in fast capillary discharges and ultrafast terawatt laser systems (both of which can be used to produce the lasing plasma medium in different 'table-top' X-ray laser schemes) have resulted in accelerated research and development of 'table-top' systems capable of lasing at wavelengths as low as 14nm (see review by Rocca 1999). Potential applications utilising the short wavelength, coherence, monochromaticity, and short duration of the X-ray laser include, high resolution imaging of transient (living) biological specimens, X-ray microsurgery, X-ray microscopy, X-ray micro-machining of nano-structures, X-ray lithography, plasma diagnostics (particularly in ICF studies), probing deep inner shells of atomic, ionic and molecular species, and the production of

ultra-high density and ultra-high temperature LPPs (Matthews & Rosen 1988, Matthews 1996).

Current commercial projection lithographic techniques are based on the use of 248nm UV laser light to expose semiconductor wafers, producing sub 0.2μm track features. XUV/soft X-ray radiation from laser plasma and synchrotron sources provide alternative short wavelength light sources capable of producing sub 0.1μm features on the wafer surface using projection lithography (Tichenor et al. 1995). Research efforts into the feasibility of utilising an LPP soft X-ray source in the techniques of projection and proximity lithography focus on the suitable choice of target material and laser wavelength, pulse duration and energy in order to optimise X-ray conversion efficiencies (Chaker et al. 1992, 1993). Also, methods to reduce plasma debris in order to protect XUV multilayer optical components and methods to improve laser and LPP source stability are under investigation (Bijkerk et al. 1995).

The feasibility of using a laser plasma source for medical imaging purposes has been investigated. Grätz and co-workers (1996) demonstrated the applicability of an LPP X-ray source (produced using 150fs 792nm laser light) to magnification radiography (with 1ps exposure times) and differential absorption imaging. The LPP source is also ideally suited to the observation of live, untreated biological specimens using the techniques of soft X-ray contact microscopy and scanning X-ray microscopy in the 2.3 to 4.4 nm 'water window' spectral region (Stead et al. 1995, Michette et al. 1993). Short-pulse soft X-rays emitted from an LPP source reduce blurring due to motion within the specimen and permit imaging of the specimen before significant propagation of radiation damage occurs.

2.2 The Dual Laser Plasma (DLP) Technique

2.2.1 Implementation of the Dual Laser Plasma Technique

The DLP technique is a highly versatile experimental procedure that permits both time and space resolved studies of a diverse range of atomic and ionic species. In essence, it is a 'pump-probe' technique and its application to photoabsorption/ photoionisation studies has proven highly successful. The essential elements of a DLP experimental configuration are shown in Figure 2.6. A Q-switched laser pulse, focused onto one

Figure 2.6 *Essential elements of the DLP experimental regime used to perform time and space resolved photoabsorption / photoionisation studies of atomic and ionic species*

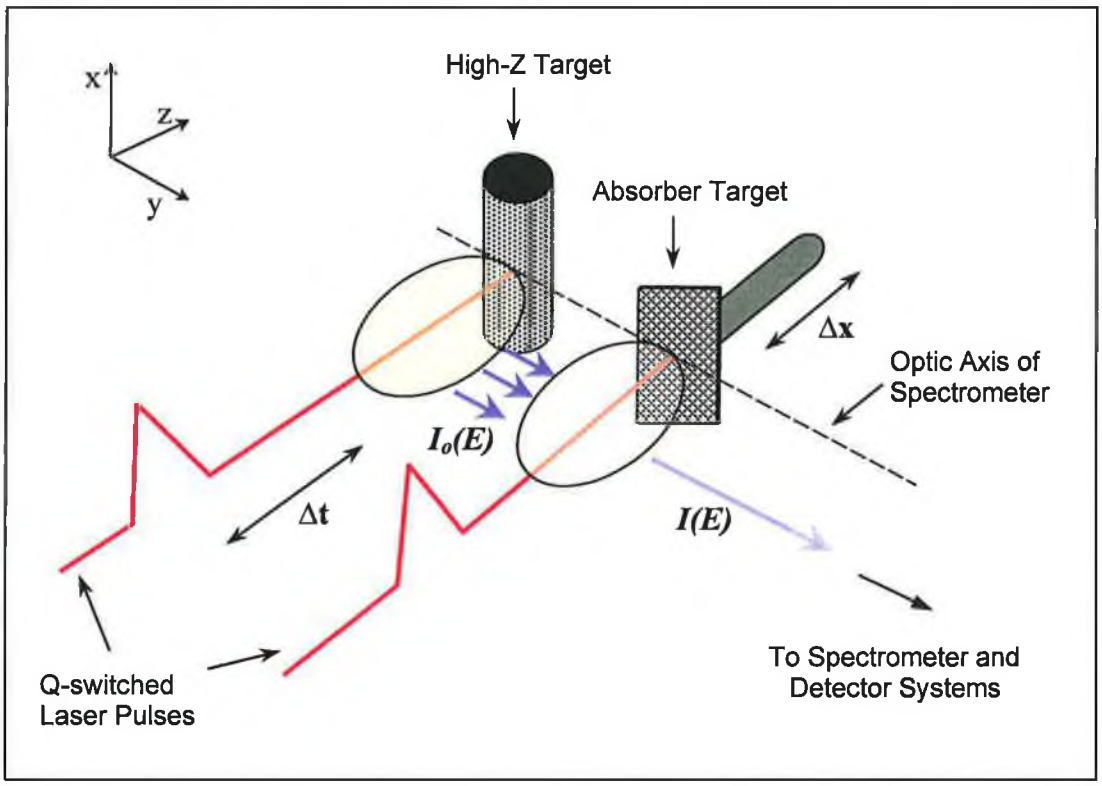

target material produces the absorbing plasma plume. A second laser pulse, incident at high irradiance on a high-Z target surface, produces the continuum source plasma at a time Δt after the first laser pulse. Time resolved studies are performed by varying Δt and thus probing the absorbing plasma at different stages during its evolution. In this way, different ionic species with different temporal distributions can be studied. Also, the position of the absorbing plasma with respect to the spectrometer optic axis can be varied (Δx) by translation of the absorber target along the horizontal z direction. This

facilitates the study of the spatial distribution of atomic/ionic species in the absorbing plasma plume.

Light emitted from the backlighting source plasma, $I_o(E)$, is attenuated as it propagates through the absorbing plasma under study. The relationship between the light signal transmitted through the absorbing plasma, $I(E)$, and the unattenuated light signal from the source plasma, $I_o(E)$, is described by the Beer-Lambert Law,

$$I(E) = I_o(E)e^{(-\sigma(E)\overline{nl})} \tag{2.26}$$

where $\sigma(E)$ is the absorption cross section of the atomic/ionic species at a given photon energy E. $\sigma(E)$ is a measure of the effective cross-sectional area that the absorbing species presents to light propagating through the absorbing plasma plume at a given energy E and is expressed in units of cm^2. n (cm^{-3}) is the number density of absorbing atoms/ions in the light path and l (cm) is the length of this light path in the plasma under study. The product $\overline{nl}$ gives the integrated column density and its value must be ascertained in order to calculate an absolute value for the absorption cross section. Total relative photoabsorption cross sections of numerous atomic/ionic species in ground and excited states that are populated within the plasma plume at any one space and time are recorded. In studies where $\overline{nl}$ is unknown, relative total cross sections are measured,

$$\sigma(E)\overline{nl} = Log\left(\frac{I_o(E)}{I(E) - I_f(E)}\right) \tag{2.27}$$

where the unitless ratio $Log\left(I_o(E)/I(E) - I_f(E)\right)$ is a measure of absorbance. The additional term $I_f(E)$ in (2.27) represents the intensity of emission from the front absorbing plasma. This must be subtracted from the transmitted signal $I(E)$ in order to determine the true absorption signal. In experimental regimes where an electronically gated light detector is used, integration of $I_f(E)$ can be reduced. Since $I_f(E)$ occurs early and usually lasts <100ns, gating the detector to coincide with the XUV source reduces $I_f(E)$ (or after ~100ns, eliminates it completely). In this way only $I(E)$ is recorded. In the absence of a gated detector critical angular alignment of the absorber target occludes the hot (absorbing) plasma core from direct view of the spectrometer optic axis and so significantly reduces the contribution from front plasma emission. Further details of this procedure are outlined in Chapter 5, Section 5.2.1.

To date, the DLP technique has played a significant role in the determination of relative, and in some cases absolute (see for e.g. Jannitti et al. 1984), photoabsorption /

photoionisation cross sections of atomic and ionic species. In particular its ability to produce ionic species in sufficient densities has enabled important investigations of ionic photoabsorption / photoionisation processes. Merged synchrotron radiation – ion beam experiments (e.g. Kjeldsen et al. 2000 and references within) still require much development and at present the DLP technique provides a supportive role to such studies (Kennedy et al. 1995). Determination of energy positions and strengths of discrete transitions using laser plasma based studies provides an important map from which to direct future experimental investigations with monochromatic synchrotron radiation. Ultimately, the most detailed information on ground and excited state atoms and ions will emerge from synchrotron based experiments (Kennedy et al. 1995).

2.2.2 Origins and Development of the Dual Laser Plasma Technique

The first experimental investigation using the DLP technique was performed by Carillon and co-workers in 1970 where they observed absorption of light produced in an aluminium source plasma by an second absorbing aluminium plasma. Both plasmas were produced using a single Q-switched Nd:Glass laser pulse (1J, 40ns FWHM) which was split into two pulses. The first pulse produced the aluminium absorbing plasma and the second, delayed with respect to the first by use of an optical delay line, produced the source. Aluminium emission is dominated by line emission with narrow bands (≤1nm) of featureless continuum and therefore use of such a source permits observation of the absorbing plasma at a limited number of narrow wavelength bands. Time and space resolved studies of the absorbing plasma at 9.8nm permitted the investigation of the relative contribution due to various absorption mechanisms in different regions and at different times during the evolution of the absorbing aluminium plasma.

Jaeglé and co-workers (1974) also used two aluminium plasmas created from a single Q-switched Nd-laser pulse (20J, 40ns) to study the intensity of emission of three Al^{3+} lines $2p^5 4d(^1P_1, ^3P_1, ^1D_1) \rightarrow 2p^6(^1S_0)$ from the front (absorbing) aluminium plasma. It was observed that for the $2p^5 4d(^3P_1) \rightarrow 2p^6(^1S_0)$ transition at 11.741nm, temperature and particle density conditions in the absorbing plasma enabled population inversion between these two Al^{3+} levels to be attained when the absorbing plasma was pumped by the aluminium source plasma. This line is termed 'superradiant' as it exhibits gain along

the length of the absorbing plasma plume and appears as a negative signal in the absorption spectrum obtained. This experimental result provided the first demonstration of population inversion in a laser plasma medium and prompted vast research efforts into the development of the x-ray laser (Elton, 1990).

In 1977 Carroll and Kennedy used a high-Z tungsten plasma emitting broad band XUV continuum in the 5 to 20nm region to probe a lithium plasma. A single laser pulse from a Q-switched ruby laser (1J, 30-40ns) was again used to create both plasmas. The absorption spectrum of the principal series $1s^2\ ^1S \rightarrow 1snp\ ^1P$ (up to n=7) of Li^+ was observed. Also, the first three doubly excited autoionising resonances in the series $1s^2\ ^1S \rightarrow 2snp\ ^1P$ (first observed in helium by Madden and Codling (1965) using a synchrotron source) were observed in helium-like Li^+ for the first time. The energy position (E_o), width (Γ) and q-value of the n=2 member of the doubly excited series were measured.

Carroll and Costello recorded the profile of the 5d → f giant dipole resonance in atomic thorium (1986) and uranium (1987) using an improved version of the DLP technique whereby plasmas were created using two independent time-synchronised laser pulses. This extension of the DLP technique permitted increased on-target irradiances due to the increased energy per laser pulse. A small fraction of the first Q-switched laser pulse was directed to a fast photodiode that triggered an electronic delay generator. After the duration of a pre-set delay, the delay generator sent an electronic pulse to trigger the Pockels cell of the second Q-switched laser. In this way the inter-laser time delay (Δt) could be varied very effectively over a broad range of 0.25μs to 100μs with an inter-laser jitter of <0.1% of the full range. The experiments performed by Carroll and Costello (1986, 1987) served to demonstrate the suitability of the DLP technique to studies of refractory and corrosive elements such as thorium and uranium.

The inclusion of a photoelectric detection system and an XUV toroidal mirror to focus source plasma light into the absorbing plasma plume of the DLP grazing incidence spectrometer system of Jannitti and co-workers (1987) provided a significant improvement in the quality of data obtained using the DLP technique. The detector consisted of a scintillator-coated faceplate located tangentially to the Rowland circle of a 2m grazing incidence spectrometer. The scintillator converted XUV photons to visible photons, which were then relayed to an image intensified 512-pixel linear photodiode

array via a fibre optic bundle. An Optical Multi-channel Analyser (OMA) coupled to the photodiode array then produced an electronic video output signal. Photoelectric detection is superior to photographic detection due to the fact that the linear response of the photoelectric detector with incident photon energy enables direct measurement of relative cross sections. Also, photoelectric data can be displayed and analysed in almost real time. The addition of a toroidal mirror to the spectrometer system serves to increase the XUV flux incident on the grating and also to reduce the astigmatism introduced by the need for small (grazing) angles of incidence on the grating in the XUV spectral region (Rense & Violett, 1959). The research group of Jannitti, Nicolosi and Tondello at the University of Padua in Italy has used this improved DLP experimental regime to measure, in particular, the photoabsorption spectra of low-Z ions in both grazing incidence and normal incidence spectroscopic regimes (Nicolosi et al. 1991). More recently, their research interests focus on the study of ions of astrophysical interest such as those of the carbon isonuclear sequence (Nicolosi & Villoresi 1998, Villoresi & Nicolosi 1998).

A chronological summary of VUV/XUV DLP experimental investigations performed since 1977 by three research groups located at the University of Padua, Dublin City University and University College Dublin is provided in Appendix II. Also, for further details on the origin and development of the DLP technique and also a discussion on the use of the point projection technique in X-ray absorption studies, the reader is referred to the comprehensive review paper on this subject by Costello et al. (1991).

Chapter Three

VUV and XUV Experimental Spectroscopic Regimes

This chapter describes the 1m normal incidence VUV spectrometer system and the 2.2m grazing incidence XUV spectrometer system used to perform time and space resolved DLP photoabsorption studies at the Centre for Laser Plasma Research (DCU). A 5.6m flat field XUV spectrometer system used to perform DLP photoabsorption studies and to characterise continuum emission from high-Z picosecond laser plasma sources at the Central Laser Facility (RAL) is described. An XUV streak camera system (RAL) used in time-resolved studies of continuum emission from high-Z picosecond laser plasma sources is detailed. The design and operation of the individual components within each experimental system and their contribution to the overall system performance are described in detail.

3.1 Nanosecond Experimental Facility

3.1.1 Introduction

The Centre for Laser Plasma Research (CLPR) at DCU houses two multi-laser, multi-channel spectrometer systems. Atomic/ionic photoabsorption and emission spectra are recorded photoelectrically using CEMA/PDA[1] detectors coupled to a 1m normal incidence VUV spectrometer covering the 30 to 220nm spectral range and a 2.2m grazing incidence XUV spectrometer covering the 5 to 50nm spectral range. Dual laser plasma experiments are performed using two of the four laser systems available within the laboratory. These laser systems are: two Q-switched Nd:YAG lasers, a Q-switched ruby laser and a tuneable dye laser. Synchronisation of laser pulses is achieved electronically rather than through the use of optical delay lines, thus enabling synchronisation of lasers having flashlamp pump cycles of differing durations. The use of an inter-laser time delay permits temporally resolved studies of the absorbing laser plasma species over a wide-ranging nanosecond time scale (0 to 10μs) with a delay jitter of $< \pm 5$ns. Target materials for the VUV/XUV source and absorbing laser plasmas are placed in specially designed target chambers attached to the front end of each spectrometer system. X-Y-Z micrometer translation mounts, to which the absorbing target materials are attached, permit accurate alignment of each plasma with respect to the spectrometer axis and also permit spatially resolved studies of the absorbing plasma plume. Both spectrometer/detector systems permit the recording of single shot photoabsorption and emission spectra.

3.1.2 Nd:YAG Nanosecond Laser Systems

In all DLP experimental studies performed in DCU as part of the work reported in this thesis, both the backlighting source and absorbing plasmas were produced using two Q-switched Nd:YAG laser systems operating at the fundamental wavelength of 1064nm. Both lasers were manufactured by Spectron Laser Systems (UK). One laser is a two stage amplifier-oscillator system (Model No: SL803) and the second is an oscillator-only system (Model No: SL404). A schematic diagram of the SL803 laser head is shown in Figure 3.1. The laser cavity is defined by the 100% reflecting rear coupler

[1] A Channel Electron Multiplier Array (CEMA) is butt coupled to a PhotoDiode Array (PDA).

Figure 3.1: Schematic outline of the optical components in the SL803 Nd:YAG two stage amplifier-oscillator laser head

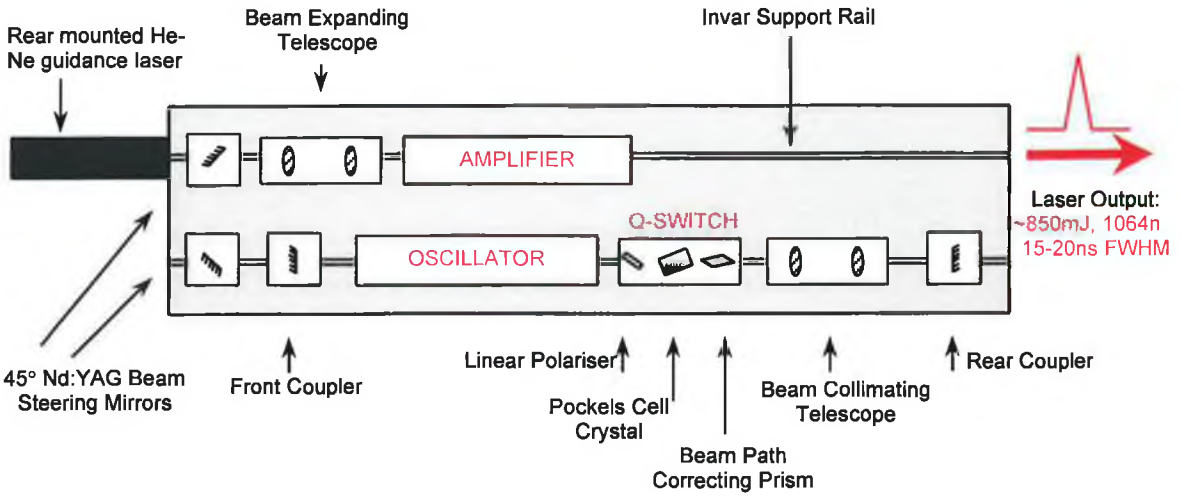

(mirror) and the partially transmitting front coupler. The active lasing medium is a 103mm long, 6.35mm diameter yttrium aluminium garnet (Y_2 Al_5 O_{12}) crystal rod doped with neodymium ions (Nd^{3+}). Population inversion in the lasing medium is achieved when sufficient light emitted during a ~200μs flashlamp pump cycle has been absorbed by the Nd:YAG rod. The flashlamp is located in the oscillator chamber above the Nd:YAG rod and is separated from it by a glass filter plate. This serves to protect the rod from damage caused by UV light emitted from the flashlamp. A telescope located within the laser cavity serves to collimate the laser beam, thus reducing beam divergence. The final beam divergence, following traversal through all optical components within the laser head, lies in the region of 0.8 to 2 mrad. The telescope also compensates for lensing action that can occur in the laser rod when it heats up during operation. The inter-lens distance in the telescope is adjusted according to the laser repetition rate required in order to achieve optimum laser performance. The combination of linear polariser and Pockels cell crystal within the Q-switch unit are used to inhibit oscillations within the laser cavity until a sufficient level of population inversion has been attained. A 915V signal applied to the Pockels cell crystal at the start of the flashlamp pump cycle induces birefringence and causes the crystal to behave as a quarter wave plate. The position of the two optic axes of the Pockels cell crystal are at 45° with respect to the horizontal plane of polarisation of light transmitted by the linear polariser. This polarised light is resolved into two mutually perpendicular components one of which is shifted 90° out of phase with respect to the other upon traversal of the Pockels cell crystal. After reflection from the rear coupler, a further 90° phase shift

occurs in the Pockels cell crystal, resulting in vertically polarised light, which is then prevented from re-entering the laser oscillator by the linear polariser. When the high voltage signal is removed, oscillation within the laser cavity occurs and the Nd:YAG gain medium is depleted in several tens of nanoseconds. A second telescope located before the flashlamp-pumped amplifier expands the beam before it traverses the 103mm long, 8mm diameter Nd:YAG amplifier crystal. The final output pulse at 1064nm has a Gaussian intensity profile, a FWHM of 15-20ns and an energy in the region of 700 to 800mJ.

The SL404 Nd:YAG laser is of similar design and component specification to the SL803. In this oscillator-only system however, the beam expanding telescope, the amplifier and the 45° Nd:YAG beam steering mirrors have been omitted. The final laser pulse is extracted at the front coupler following amplification in the oscillator crystal. Output pulses, at 1064nm, have a Gaussian intensity profile, a FWHM of 15-20ns and an energy in the region of 200 to 300mJ. A third Nd:YAG laser (SL404G), with similar output pulse characteristics to that of the SL404, was used prior to the introduction of the SL404 laser into the DLP system at the CLPR.

The total energy per laser pulse was recorded during experimental procedures using a Radiant Dyes Chemie™ thermopile-based energy monitor. Depending on the sensitivity scale chosen, a voltage output with a conversion ratio of 0.65V or 1.15V per Joule of incident laser energy was measured. Both the flashlamps and the Pockels cells of the SL803 and SL404 lasers were triggered externally using suitably timed electronic signals derived from a Stanford Research Systems™ digital delay generator. In Section 3.1.5 further details are provided on the timing sequence used to trigger both laser systems, with a variable delay between output laser pulses that is suited to DLP-type studies.

3.1.3 1m Normal Incidence VUV Experimental Regime

3.1.3.1 System Overview

The 1 metre normal incidence spectrometer system developed at the CLPR is suited to time and space resolved DLP photoabsorption studies and single-plasma emission

Figure 3.2: *1 metre normal incidence spectrometer-based system for recording of VUV DLP photoabsorption and single-plasma emission spectra of atomic and ionic species*

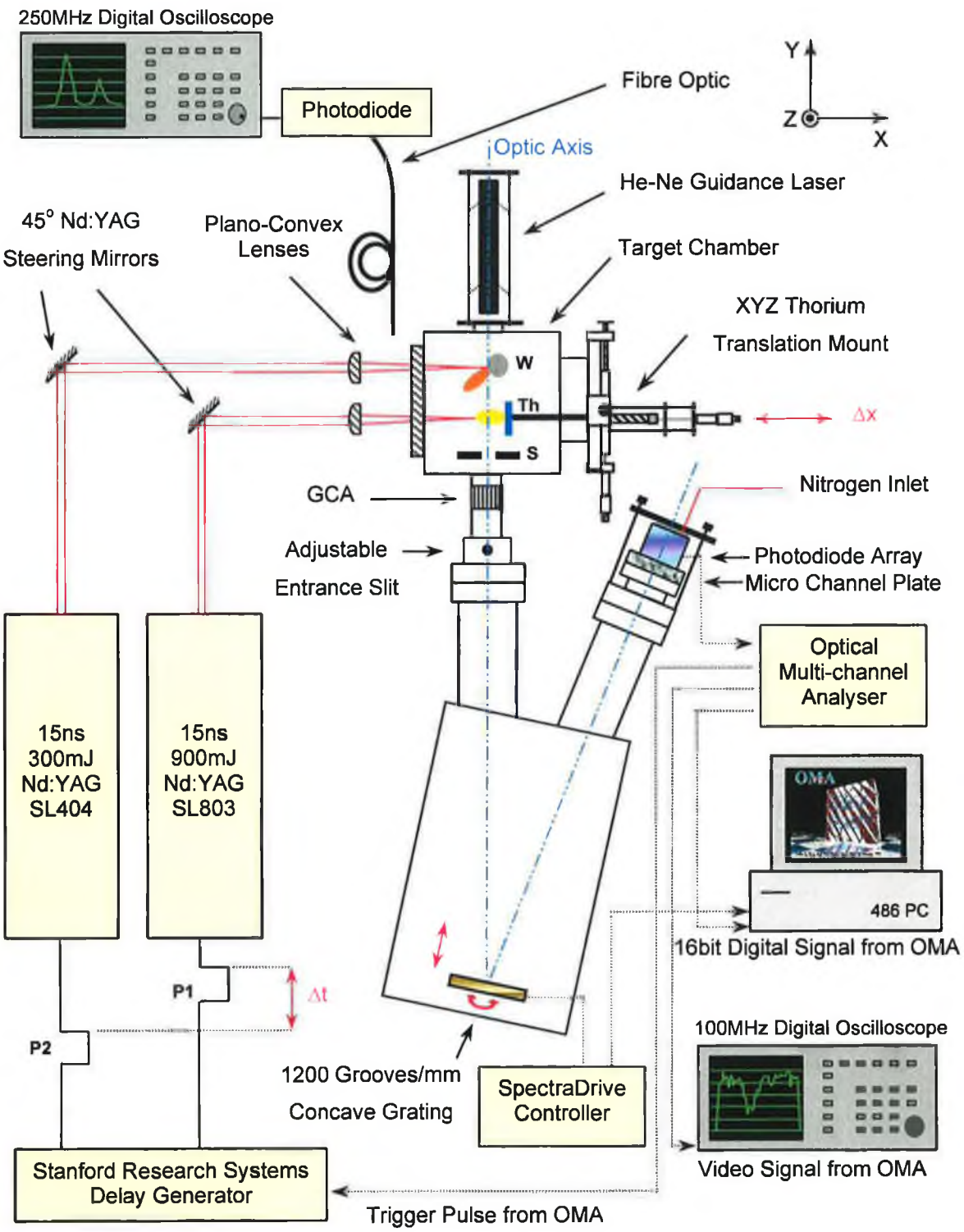

studies of atomic and ionic species. A schematic overview of the essential system components required to carry out such experimental studies is shown in Figure 3.2 for a tungsten (W) backlighting plasma and a thorium (Th) absorbing/emitting plasma.

Central to this system is an Acton Research Corporation™ 1m *near* normal incidence spectrometer with fixed entrance and exit arms. Light incident on an entrance slit of adjustable width (5 to 3000μm) fixed to one arm of the spectrometer is dispersed and focused onto a fixed position linear (or 2-D) detector array attached to the spectrometer exit arm. A 1200 grooves/mm Bausch & Lomb™ spherical concave holographic grating mounted within the spectrometer chamber is operated in an off-Rowland circle type configuration. In this configuration, scanning of dispersed radiation across the detector plane is achieved through rotation of the grating, while focusing is maintained by linear translation of the grating. Either a Galileo™ Channel Electron Multiplier Array (CEMA) coupled to an EG&G™ linear PhotoDiode Array (PDA) detector or a 2-D Photometrics™ back-thinned CCD detector permitted photoelectric recording of multichannel absorption and emission spectra.

Both VUV continuum and absorbing plasmas in DLP-type photoabsorption studies and emitting plasmas in single-plasma emission studies were produced in a custom built target chamber (Doyle 1995) coupled to the entrance arm of the spectrometer via a vacuum sealed Galileo™ Glass Capillary Array (GCA). The porous glass structure of the GCA serves to reduce the amount of plasma debris entering the spectrometer system and also permits differential pumping of the spectrometer and target chambers. This latter feature permits photoabsorption studies of gases filling the target chamber at up to 0.01mbar while a pressure of less than 10^{-6}mbar is maintained in the spectrometer chamber. In this work only solid target materials were used. For studies with the 1m spectrometer, cylindrical tungsten, aluminium and beryllium oxide targets were attached to micrometer driven (z-direction) target holders mounted on top of the target chamber (Dardis 1998) whereas planar thorium targets were attached to an X-Y-Z micrometer driven target holder mounted on the side of the target chamber (Moloney 1998). Spatially resolved studies of thorium laser produced plasmas were performed by translating the thorium target in the x-direction, perpendicular to the path of the spectrometer optic axis. During the course of this work a secondary 500μm vertical slit (S) was placed between the thorium plasma and the entrance slit of the spectrometer, resulting in an improved spatial resolution (~500μm) along the x-direction (see Figure 3.2) at the thorium plasma plume.

Plano-convex lenses with typical focal lengths in the region of 90 to 120mm focused Q-switched Nd:YAG laser pulses to a spot size approximately 100μm in diameter

resulting in on-target irradiances of up to 10^{12} W/cm^2. In Figure 3.2 the 300mJ SL404 laser is used to produce the tungsten backlighting plasma whereas the 900mJ SL803 laser produces the thorium absorbing plasma. For different experimental procedures the laser output pulses were directed onto any of the two target surfaces by simply translating the 45° Nd:YAG beam steering mirrors along optical rails external to the lasers. Choice of laser system for production of the *backlighting source plasma* was based on the on-target irradiance required and the spectral brightness of plasma emission in the energy region of study. The laser system used to produce the *absorbing plasma* in DLP studies and the emitting plasma in single-plasma emission studies was selected on the basis of the on-target irradiance required to produce sufficient densities of the atomic/ionic species under study. The energy per pulse from each Nd:YAG laser system could be reduced by lowering the oscillator voltage below its optimum value of 790V for maximum energy output. In the case of the SL803, this has little effect as the amplifier is generally saturated. Instead the amplifier voltage was reduced to a voltage below which the laser output energy began to fluctuate.

Laser light reflected from the glass entrance window of the target chamber was detected using a fibre optic cable (600μm core diameter, 660μm cladding diameter) coupled to a BPX-65 fast photodiode. The peak-to-peak laser pulse separation (Δt) and also the duration and relative intensities of each laser pulse were monitored on the display of a Hewlett Packard™ HP54510A (250MHz, 1G sample/second) digital oscilloscope to which the photodiode was connected via a BNC cable. In this way, an inter-pulse jitter of approximately ±5ns was measured.

Initiation of spectral data acquisition, set-up of detector integration times, triggering of the Stanford Research Systems™ digital delay generator to fire both Nd:YAG laser systems and recording/display of spectral data are controlled via the interaction of the PC-based software packages *Omasoft* (written by Shaw (1996) and Doyle (1995)) and *Lightview* (from Photometrics™) with the electronic controllers of the CEMA/PDA and CCD detector systems respectively. The operation and resolution capabilities of the CCD camera used in VUV studies (1m) and the CEMA/PDA system used in XUV studies (2.2m) are detailed in Section 3.1.3.4.1 & 3.1.3.5.1 (1m) and Section 3.1.4.3 & 3.1.4.4.1 (2.2m). Under the control of the 486 PC, the CCD camera controller (1m) (or the optical multichannel analyser (2.2m)) and the Stanford™ delay generator synchronise firing of both lasers with the acquisition of spectral data (Section 3.1.5).

3.1.3.2 Acton Research Corporation™ 1m Normal Incidence Spectrometer

The Acton Research Corporation™ VM-521 1m normal incidence spectrometer, when equipped with a 1200 grooves/mm spherical concave grating can, in theory, disperse light over the VUV energy region of 30 to 325nm. The overall system (spectrometer and detector) wavelength region covered is determined by the combination of the reflection efficiency of the grating and also the limited wavelength sensitivity of the CEMA and CCD detectors. The reflection efficiency of the iridium coated Bausch & Lomb™ grating falls off gradually in the long wavelength region whereas the detection efficiency of the Galileo™ CEMA is low (<10%) outside the 20 to 180nm wavelength region. The quantum efficiency of the silicon-based back-thinned Photometrics™ CCD ranges from ~40% to 15% over the wavelength region dispersed by the grating (Figure 3.11). The advantage of using the CCD rather than the CEMA/PDA arrangement is that it permits experimental investigations with improved spatial (and hence spectral) resolution and also two-dimensional recording of spectra. The efficiency of the grating is low for wavelengths less than ~35nm (see tungsten emission spectrum, Chapter 2 Figure 2.5) and so the region from ~35nm to ~70nm is largely free from second order light. This region is ideally suited to photoabsorption studies, where the first order absorption spectrum is not altered by the absorption signature of higher order light.

The spectrometer set-up is shown in Figure 3.3 and Figure 3.4. In the original spectrometer design, an exit slit permitted observation of monochromatic VUV light. This slit was subsequently removed by Doyle (1995) and a custom built vacuum flange, to which the Galileo™ MCP was attached, was used to locate the front face of the MCP at the spectrometer focal plane (see Figure 3.4). As a result of this modification, the VM-521 now operates as a multichannel spectrometer rather than a monochromator, where a wavelength interval of ~21nm incident on the ~25mm active diameter of the MCP is recorded. The spectrometer operates at near normal incidence and the angle subtended by the entrance slit and the centre of the detector at the grating is 7.5°, hence the deviation angle $D_v = 15°$ (see Figure 3.3).

Figure 3.3 *Position of the spherical concave diffraction grating, the entrance slit and the exit plane on a Rowland circle whose diameter (ϕ=995.4mm) equals the radius of curvature (R) of the grating in the VM-521 spectrometer system (all dimensions in mm, scale 1:10)*

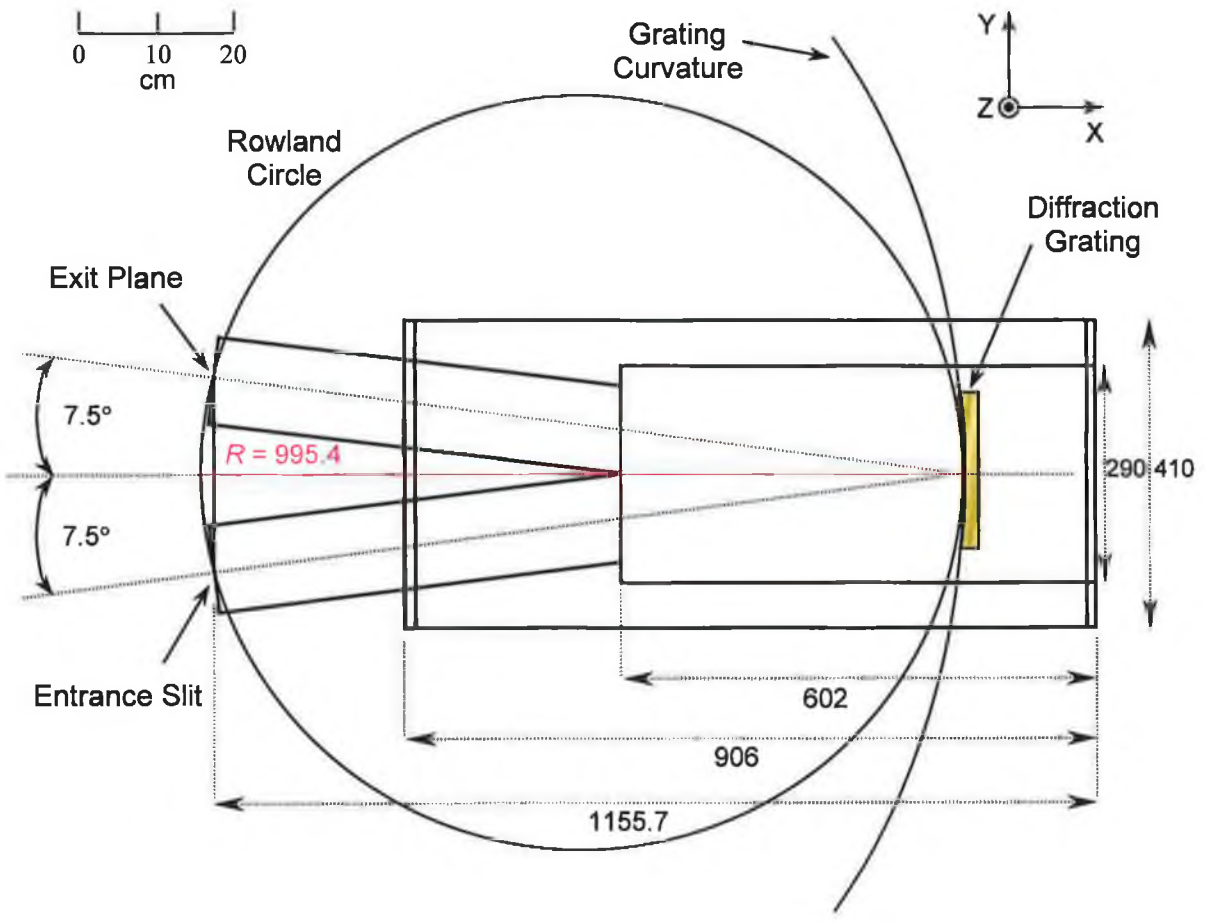

Figure 3.4 *Acton Research Corporation™ VM-521 1 metre normal incidence spectrometer*

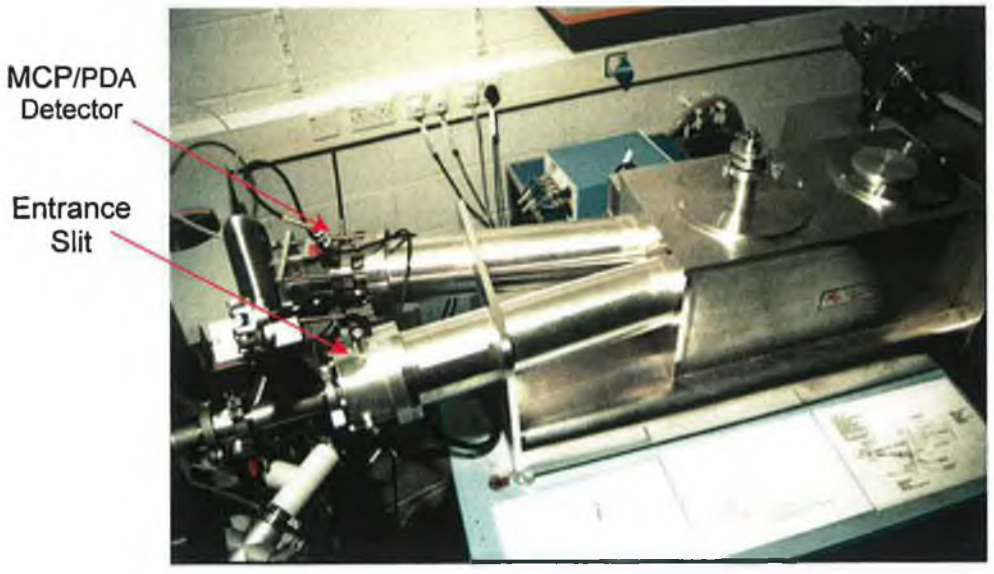

3.1.3.2.1 Bausch & Lomb™ Diffraction Grating

The Bausch & Lomb™ spherical concave diffraction grating is held in a kinematic mount in the VM-521 spectrometer chamber. This mount type permits the removal of the grating and its subsequent return or replacement without the need for re-alignment. The grating is 96mm wide and 56mm high (direction of groove ruling) and its iridium-coated surface is holographically ruled at 1200 grooves/mm. The rulings of the grating are blazed at an angle of 2.75°, resulting in a maximum conversion efficiency of incident radiant flux to first order light at 80nm. The radius of curvature (R) of the spherical concave profile of the gratings front face is 995.4mm (~1m).

3.1.3.2.2 Off-Rowland Circle Concave Diffraction Grating Mount

The concave diffraction grating, first developed by H. A. Rowland in 1882, combines the dispersive properties of a ruled grating surface with the focusing ability of a concave mirror (Samson 1967). VUV/XUV light emerging from a point source lying on a circle, known as the Rowland circle, is dispersed and focused by the grating so that the resultant spectral distribution is brought to a focus along the Rowland circle (see Figure 3.5). The centre of the concave diffraction grating lies tangential to the Rowland circle, the diameter (ϕ) of which equals the radius of curvature (R) of the grating. The positions of the horizontal (primary) and vertical (secondary) foci of the concave spherical grating differ and their relative position changes quite dramatically according to the regime in which the grating is operated. In the near normal incidence regime, the angles of incidence (α) and diffraction (β) are small ($\alpha = \beta = 7.5°$ in zero order for the VM-521) and the concave grating produces an almost stigmatic focus. In such a quasi-stigmatic imaging system a point source is focused to a point image on the focal plane. This is a consequence of the fact that the position of both the vertical focus (which lies on a tangent to the Rowland circle perpendicular to the grating normal) and the horizontal focus (which lies on the Rowland circle) begin to coincide for small angles of incidence and diffraction. As α is increased light impinges on the grating at a decreasing grazing incidence angle δ ($\delta = 90° - \alpha$). For an increasing angle of diffraction (β), the horizontal focus moves upwards along the Rowland circle towards the grating whereas the vertical focus moves outward along the tangent to the Rowland circle perpendicular to the

Figure 3.5 *Diffraction and focusing (horizontal and vertical) of the constituent wavelengths (λ_1, λ_2, λ_3, ...) of light emerging from an entrance slit located on the Rowland circle of a concave grating to form the outside spectrum, central image (α=β) and inside spectrum also located on the Rowland circle*

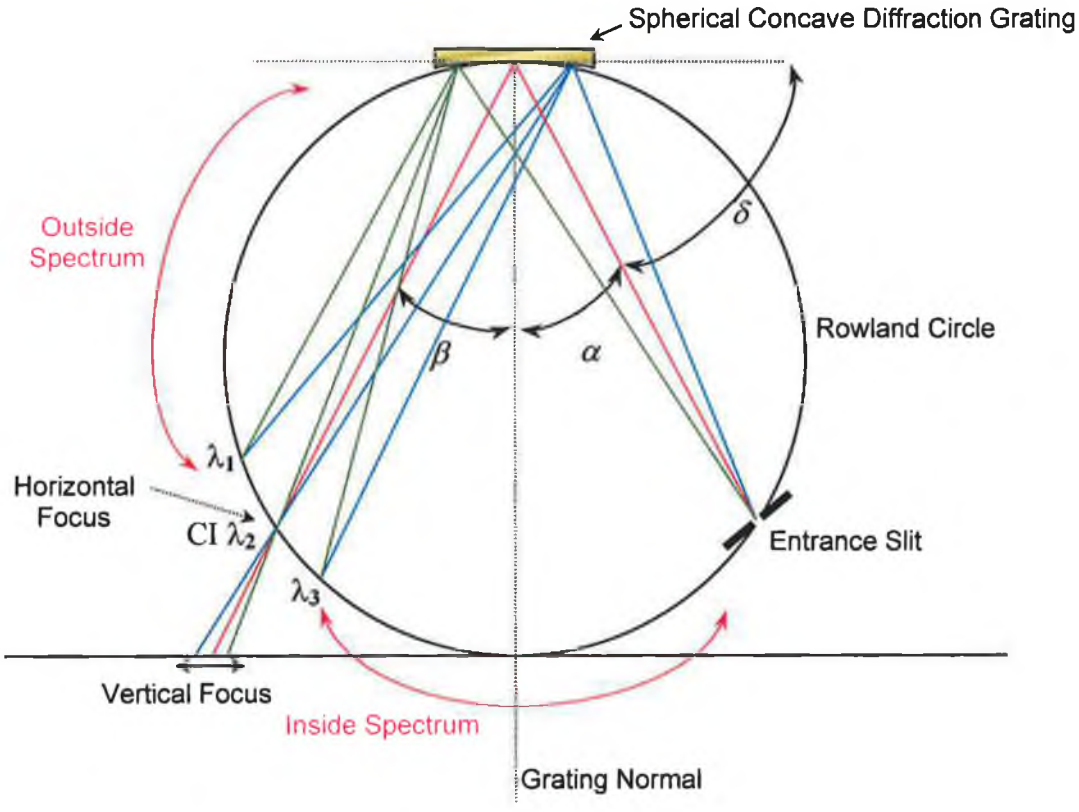

grating normal (see Figure 3.5). A direct result of this increasing separation between both foci is more severe astigmatism whereby a point source at the entrance slit is focused to a vertical line on a detector located on the Rowland circle. A grazing incidence configuration is employed in the 2.2m XUV spectrometer also used in this work. Details of the grating mount and toroidal optics used to reduce the inherent astigmatism associated with this mount are provided in Section 3.1.4.2.

Diffraction by the spherical concave grating of the constituent wavelengths of light emerging from the entrance slit is described by the same grating equation as that used for a plane grating,

$$\pm m\lambda = d(\sin\alpha + \sin\beta) \qquad (3.1a)$$

where m (=1, 2, 3...) is the spectral order, λ is the wavelength of light and d is the inter-groove separation (d = $8{\cdot}33\times10^{-7}$m for the 1200 grooves/mm Bausch & Lomb™ grating). The negative sign in (3.1a) describes the outside spectrum that lies along the

Rowland circle between the zero order position or the central image (CI) and the tangent to the grating. The positive sign describes the inside spectrum located along the Rowland circle between the central image and the entrance slit. In the VM-521 spectrometer system the inside spectrum only is recorded and so (3.1a) becomes,

$$m\lambda = d(\sin\alpha - \sin\beta) \qquad (3.1b)$$

where α and β lie on opposite sides of the grating normal and consequently have an opposite sign. As previously mentioned, the region from ~35 to 70nm is predominantly first order light. Outside this region higher orders, of wavelength λ/m that satisfy (3.1b), overlap first order spectral light. The presence of up to 3rd order light was observed in a study of oxygen lines emitted from a beryllium oxide plasma used in this work for the calibration[2] of VUV spectral energy regions. Fourth order carbon spectral lines have been observed in emission from a polyethylene (C_4H_8) plasma by Dardis (1998) in the 180 to 200nm wavelength region.

When the angles of incidence and diffraction are equal ($\alpha = \beta$), the grating is in its zero order position and specular reflection results in the formation of a 'white light' image known as the central image or zero order image (see Figure 3.5). For this grating position, equation (3.1b) is satisfied for all wavelengths and m, the spectral order, is zero. When the grating is rotated through an angle ϑ about an axis lying in the z-direction that passes through the centre of the gratings front face, α and β change accordingly and thus dispersed light is scanned across the fixed detector array (Figure 3.6). In order to maintain good focus for each angle of rotation (ϑ) the grating is translated a certain distance l in the y-direction along the bisector of the angle subtended by the entrance slit and the centre of the detector at the centre of the grating. The need for this linear translation (l) arises as a consequence of the fixed positions of both the entrance slit and the detector. Upon rotation of the grating, both the entrance slit and the detector no longer lie on the circumference of the Rowland circle, which has also undergone rotation. The entrance slit is located a distance s beyond the newly rotated Rowland circle and the centre of the detector plane a distance s' inside it. Translation of the grating by an amount determined by the angle of rotation ϑ re-establishes focusing of diffracted spectral light onto the detector, which is now lying in an *off-Rowland circle* position. For near normal incidence, $s' \approx s$ and s is related to ϑ as in equation

[2] The wavelengths of emission lines observed in this work were determined using the atomic and ionic spectral reference tables compiled by Kelly (1987).

Figure 3.6: *Rotational and translational motion of the spherical concave grating within an off-Rowland circle type mount in order to achieve scanning and focusing of spectral light at the detector array*

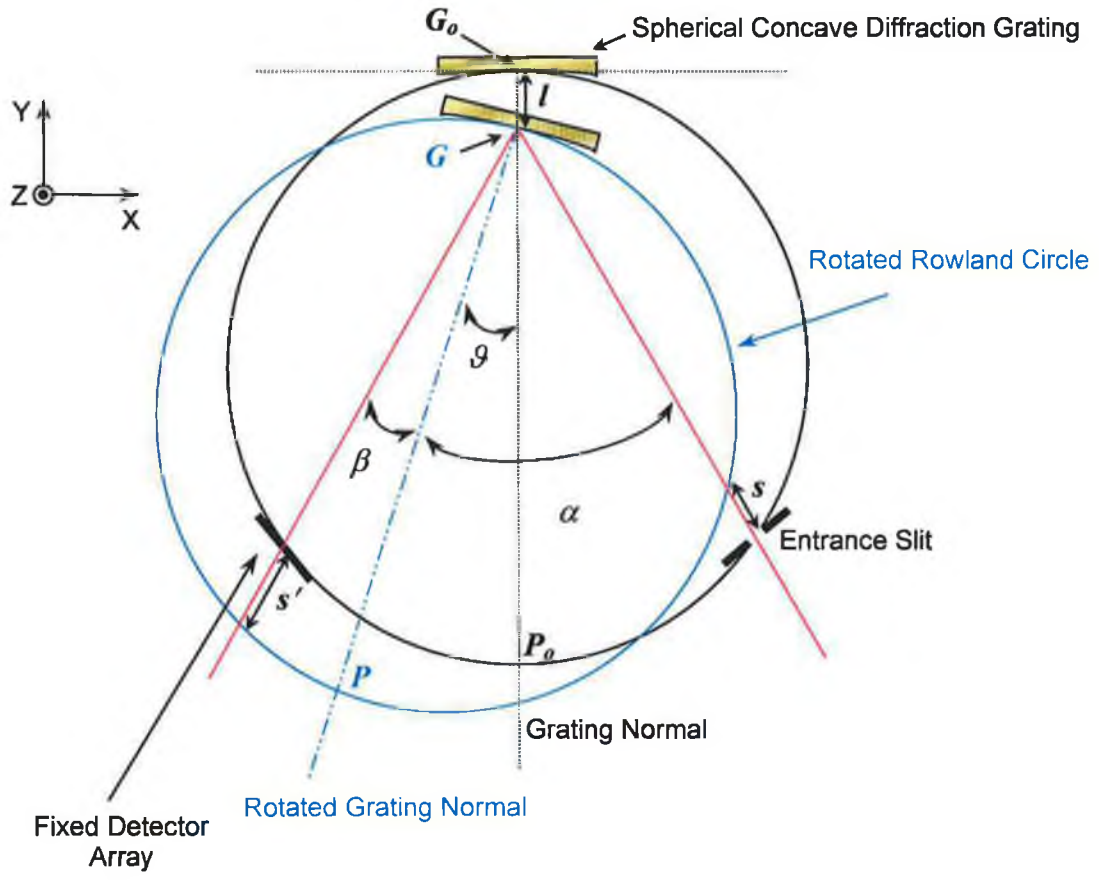

$$s = R \sin \alpha_o \sin \vartheta \tag{3.2}$$

(3.2) from Samson (1967), where α_o is the angle of incidence before the grating is rotated and R is the radius of curvature of the grating. An expression relating the translation of the grating (l) to ϑ can be obtained using the following construction from Figure 3.6,

$$l + GP_o = R$$

$$\Rightarrow l + R\cos\vartheta \cong R \quad (\text{as } GP_o \cong R\cos\vartheta)$$

$$l \cong R(1 - \cos\vartheta) \tag{3.3}$$

During operation in the VM-521 spectrometer, the Bausch & Lomb grating is rotated through an angle ϑ ranging from 0° to 20° in order to scan the 30 to 325nm wavelength range over which the grating disperses light. Using (3.3), the resultant linear translation of the grating is calculated to range from 0 to 20mm. The grating equation can now be rewritten using $\alpha = 7.5° + \vartheta$ and $\beta = 7.5° - \vartheta$ (see Figure 3.6) such that

$$m\lambda = 2d\cos(D_v / 2)\sin\vartheta \qquad (3.4)$$

where D_v is the angle of deviation.

Accurate positioning of the grating is achieved via a cam driven stage that is machined to give the correct combination of movements for each wavelength setting. A precision lead screw located outside the VM-521 vacuum chamber rotates the cam. The screw is connected to a stepper motor and this, in turn, is connected to an electronic SpectraDrive™ controller that permits manual or computer control (via an electronic interface) of the gratings position. A single revolution of the stepper motor changes the central wavelength on the detector by 1nm when a 1200 grooves/mm grating is used.

3.1.3.3 1m Target Chamber

The 1m target chamber assembly shown in Figure 3.7 was designed by Doyle (1995) and consists of a 127×127×127mm aluminium cube with 70mm diameter entrance holes (which connect to form a hollow central area) drilled into each of its six faces. Custom built flanges, attached to one side of the target chamber cube and to the entrance slit

Figure 3.7: Target chamber assembly coupled to the entrance arm of the Acton Research Corporation™ VM-521 1m spectrometer chamber

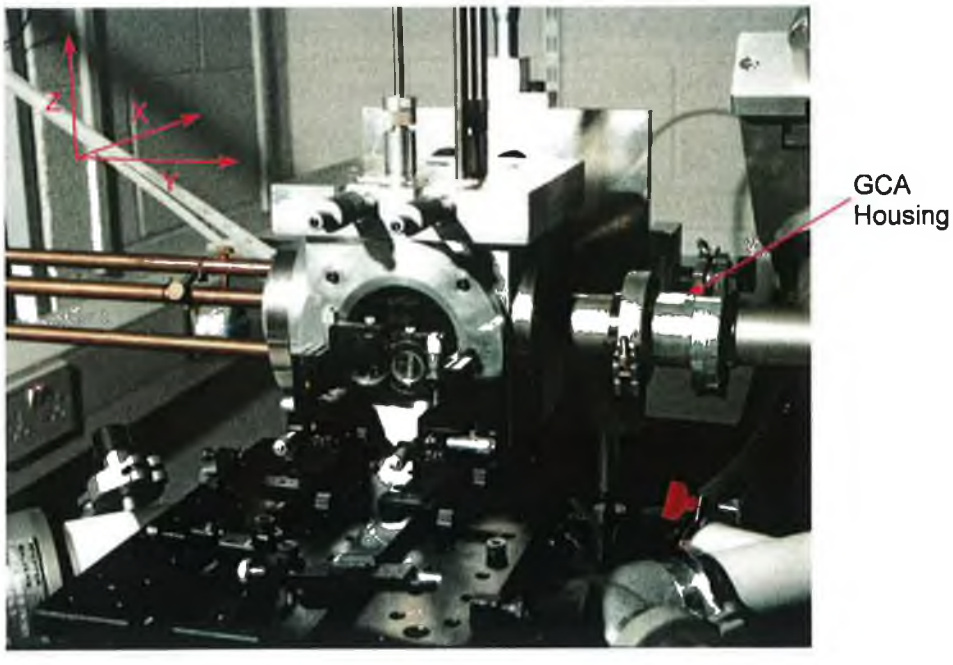

housing located on the entrance arm of the VM-521 spectrometer chamber, facilitate vacuum coupling of both chambers. The target chamber cube is supported independently of the spectrometer entrance arm by a cylindrical mount with a vacuum port to which a turbo/rotary pumping system is attached. A Galileo™ glass capillary array (GCA), mounted within its own housing, is inserted into the vacuum line between the target and spectrometer chambers (see Figure 3.7). The GCA is circular with a diameter of 25mm, a thickness of 3mm, and a pore diameter of 50μm. An aluminium disk with a 6mm diameter hole drilled off-centre covers the end of the GCA that is facing towards the target chamber and hence most likely to be coated by target debris. Rotation of this disk permits the exposure of a fresh area of the GCA surface, which is free from a coating of plasma material that accumulates during repeated plasma generation. The effect of the GCA in limiting the maximum acceptance angle of the spectrometer system is discussed in detail in Section 3.1.3.5.

A slit isolation valve on the entrance arm of the VM-521 spectrometer permits the isolation of the spectrometer and target chamber vacuum systems. This permits venting of the target chamber without altering the vacuum environment in the spectrometer chamber, thus reducing the turn around time for replacement of target materials.

3.1.3.3.1 1m Target Holders

The 1m target chamber has three target holders, two of which are mounted on the top of the chamber (Figure 3.7 and Figure 3.8) and a third on the side (Figure 3.9). Both target holders mounted on the top of the target chamber consist of a stainless steel rod (20mm long, 6mm diameter) passing through a Wilson vacuum seal that is fixed to an aluminium supporting block. Both aluminium blocks are then inserted into specially machined grooves in a custom built flange (Dardis 1998) attached to the top of the target chamber. Sitting on o-ring seals these blocks are free to move in one dimension while still holding good vacuum. Translation of the target holders in the horizontal x-direction (perpendicular to the optic axis) is achieved using two micrometers attached to the side of the flange (see Figure 3.8). The 90mm length of the grooves, coupled with the 70mm length of the aluminium blocks, confine the motion of the target to a maximum displacement of 20mm in the x-direction. Motion in the vertical z-direction is

Figure 3.8: Front view of 1m target chamber assembly (all dimensions in mm, scale 1:1.25)

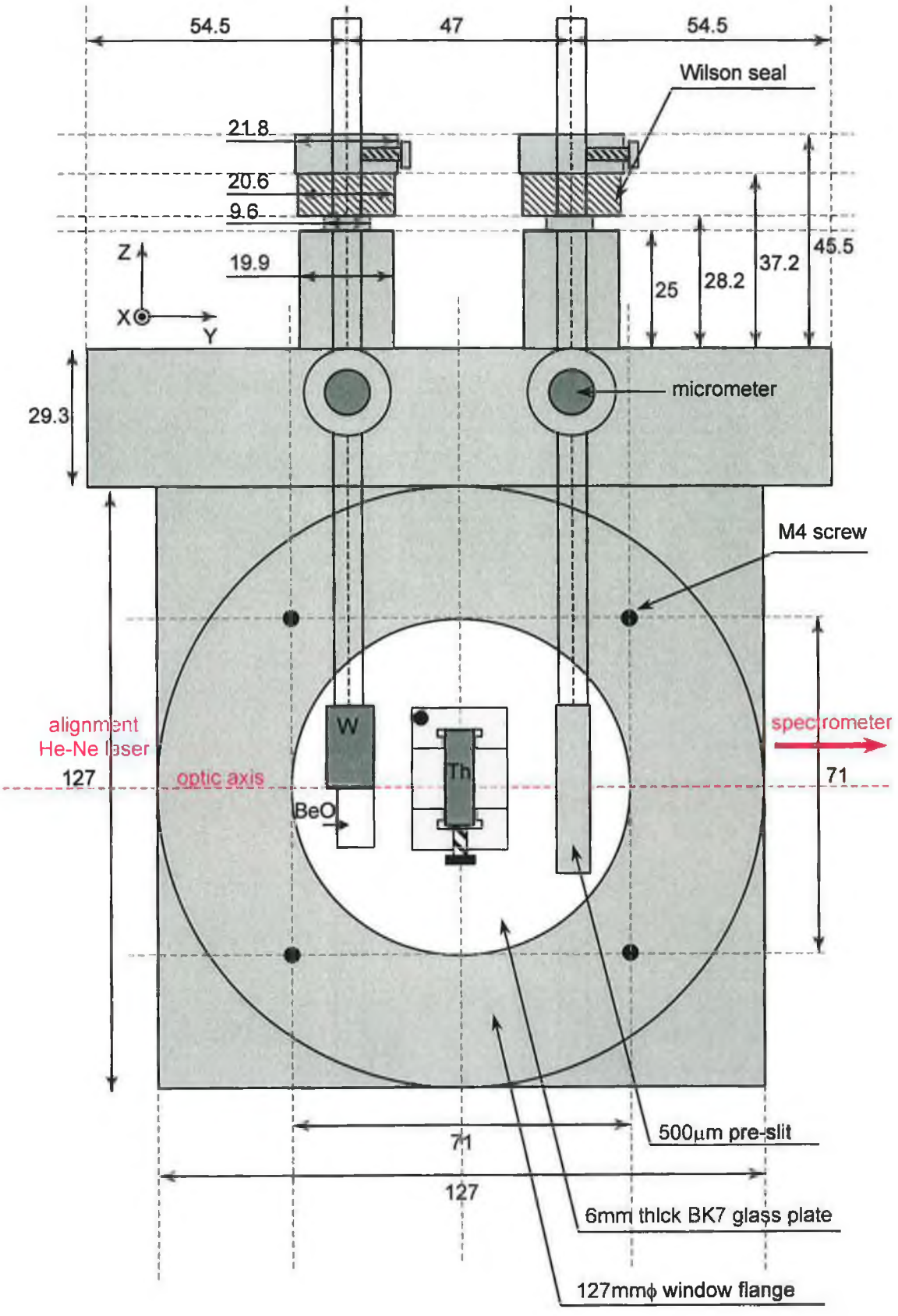

achieved through extension and retraction of the stainless steel rod through the Wilson seal. The rod can also be rotated (about the z-axis) in order to expose a fresh surface of the target to the laser focal spot. The ends of both rods are threaded (M6) and target materials that have an M6 tapped hole can be attached directly to each rod. For a DLP experiment, the target holder on the left in Figure 3.8 is used to hold backlighting, (VUV continuum emitting) target materials whereas the target holder on the right holds the absorbing (target) material. For single plasma emission studies either holder may be used. In all 1m DLP and emission studies performed as part of this thesis work a 500μm pre-slit was used to improve the system spatial resolution at the absorbing/emitting plasma plume. The pre-slit housing was attached to the absorbing target holder as in Figure 3.8 and so a third target holder, mounted on the side of the target chamber cube, was used to hold the absorbing target material (thorium) between both the pre-slit and the backlighting target material (tungsten). This side mounted target holder, designed and constructed by Moloney (1998), is shown in Figure 3.9 and permits x-y-z translation of the target material with rotation about the x-axis. Again, the target material is attached to a 6mm stainless steel rod that is extended into and retracted from the target chamber via a Wilson seal. A bracket mounted on top of the Wilson seal supports a micrometer that translates the rod in the x-direction. The Wilson seal/

Figure 3.9: *Micrometer driven X-Y-Z target holder/manipulator mounted on the side of the 1m target chamber cube*

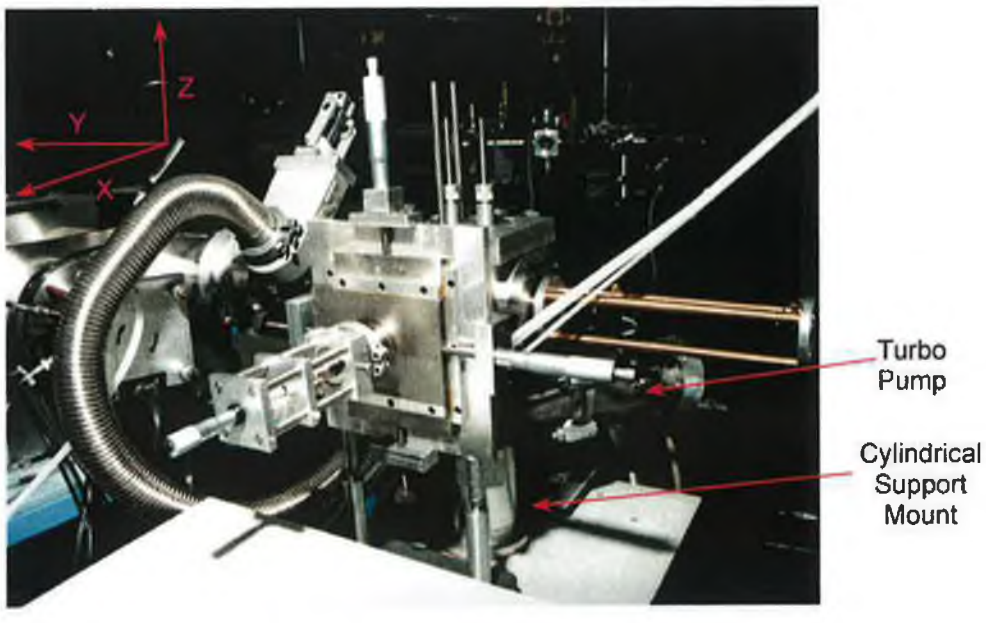

micrometer arrangement is centred on a stainless steel plate, which is in turn driven by two additional micrometers (y- and z- directions), thus permitting motion over a distance of 50mm in 5μm increments in all three dimensions.

3.1.3.3.2 Preparation and Mounting of Target Materials

A 10mm diameter cylindrical tungsten rod was used as a VUV continuum target material for all 1m (and 2.2m) DLP investigations performed during this work. A 7.8mm diameter beryllium oxide cylindrical target was attached to the base of the tungsten rod (as in Figure 3.8) using Araldite™ glue. An M6 tapped chuck and locking nut were used to secure the untapped tungsten target to the leftmost target holder rod. By translating the target holder rod in the z-direction (vertically) the target material under study could be interchanged. This permitted the recording of tungsten continuum spectra and beryllium oxide line-dominated calibration spectra without the need for adjustment of the laser focal spot position.

Thorium metal foils measuring 20mm × 6mm and of 1mm thickness were mounted in a custom built target holder (Figure 3.8 and Figure 3.10) tapped with an M6 hole and secured onto the end of the stainless steel rod of the X-Y-Z target holder/manipulator using an M6 nut and bolt. An M4 screw passing through a spring located between both front and back sections of the target holder was used to rotate the front face section with respect to the stationary back section. The ability to rotate thorium planar targets about the vertical z-axis was incorporated into the design of the target holder in order to reduce front plasma emission from the thorium laser plasma. Upon rotation, one edge of the thorium target approaches the optic axis, while the opposite edge is driven further away from the axis. The resulting occlusion of the hottest (brightest) region of the thorium plasma by the edge closest to (or on) the optic axis results in the reduction of plasma light entering the spectrometer. The angular range through which the target holder can rotate the thorium target is 0° (target parallel to the optic axis) to 13°. The angle chosen is determined experimentally by recording the intensity of front plasma emission in a given spectral region and then establishing the degree of occlusion required to eliminate it.

Figure 3.10: Target holder designed to rotate a planar target material secured to its front face about the vertical (z-axis). The target holder is pivoted on one side while adjustment of an M4 screw on the other side effects the angular action through rotation of the front section about a pivot joint (all dimensions in mm, scale 1:1)

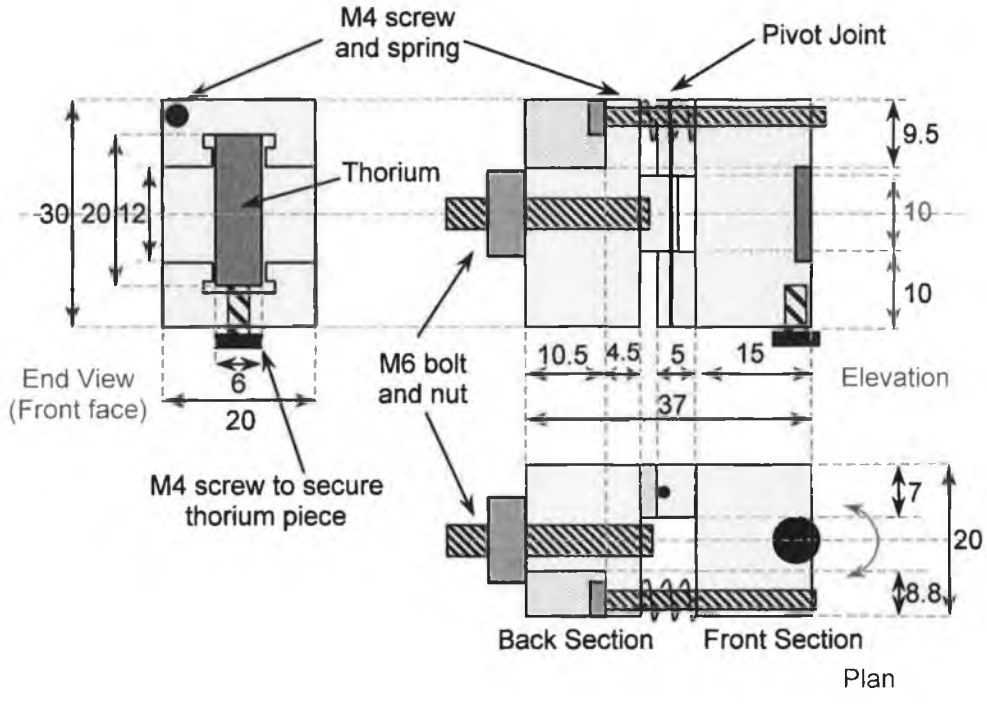

3.1.3.3.3 Handling Thorium – Precautions Required

Several precautions were necessary when performing experimental procedures involving the production of thorium plasmas. Thorium ($^{232}_{90}$Th) is both a toxic and a radioactive material. It has a half-life of 1.4×10^{10} years and decays via six α and four β emitting steps before becoming the stable lead isotope, $^{208}_{82}$Pb. During its decay series thorium produces an α-emitting radioactive gas 'thoron' ($^{220}_{86}$Rn) thus posing the need for the preparation of samples in a well-ventilated area. The 7.3g (25mm×25mm×1mm) sample used in this work had a total activity of 0.6μCi and was cut into five smaller pieces by the supplier, Goodfellow™ (specified purity of 99.5%).

Two specially designed hollow cylindrical collars made from aluminium (inside diameter ϕ=62mm, outside diameter ϕ=67mm) and stainless steel (inside ϕ=63mm,

outside ϕ=69mm) were constructed for insertion into the target chambers of both 1m and 2.2m spectrometers respectively. These served to collect thorium plasma debris and thus prevented contamination of the chamber walls. A series of holes were machined into each collar in order to permit evacuation of the target chambers via pumping lines attached to the cylindrical pillars supporting both the 1m and 2.2m target chamber cubes (see Figure 3.9 for example). Also, holes in the collar, aligned with the BK7 glass windows at the front end of both target chamber cubes, permitted laser beam access to target materials. Contaminated glass windows were removed after use. No attempt was made to clean and re-use them. Instead, they were stored with other contaminated materials. Two further holes were drilled in each collar in order to permit the passage of the alignment He-Ne lasers defining the optic axis through both target chambers and also to enable plasma light to enter the spectrometer.

All five pieces of thorium metal were stored in a radiation safe when not in use. All personnel involved in experiments wore a thermoluminescent detector badge, which was returned to the Radiological Protection Institute of Ireland (RPII) for development and assessment of dosages received. Gloves and a facemask were worn when mounting thorium targets in the target holder. Once in the target chamber (1m and 2.2m), any small amounts of thoron gas produced by the thorium sample were evacuated through a sealed venting conduit connected to a turbo/rotary pumping arrangement (1m and 2.2m). A Geiger-Müller tube, located beside the target chamber, was used to monitor radiation levels within the laboratory before, during and after experimental procedures involving the use of thorium. Once the thorium target was placed in the target chamber, radiation counts in the laboratory remained at a background level.

3.1.3.3.4 Target Chamber Laser Focusing Optics

Q-switched Nd:YAG laser pulses were focused onto target materials using a series of plano convex lenses with diameters in the range 17 to 30mm and focal lengths ranging from 90 to 130mm for all experiments reported here. A lens holder system, shown in Figure 3.7, was designed by Pattison (1997) for mounting and accurate positioning of two lenses (DLP experiment) using X-Y-Z micrometer driven holders. This optical system has subsequently been replicated and both systems are attached to the target

chambers of the 1m and 2.2m spectrometers. All lens holder micrometers permit translation of lenses over a distance of 6mm with an accuracy of ±5μm, thus allowing accurate three-dimensional positioning of the laser focal spot. He-Ne alignment lasers mounted to the rear of both the SL404 and SL803 laser heads serve to indicate the beam path of infra red Nd:YAG laser light (see Figure 3.1).

Each lens holder is mounted on an optical rail (250mm long) attached to an optical breadboard (250mm × 200mm). The optical rails permit coarse adjustment of each lens holder in order to set the lens at a distance approximately equal to its focal length from the target. A locking screw at the base of each lens holder is used to secure it to the optical rail. A telescope focused at infinity is then independently mounted in a retort stand and used to optimise the lens focus by viewing craters on the target surface. All such optimisation is achieved by fine adjustment of micrometer driven stages onto which the lens holders are bolted. When focusing on a continuum target, the x-direction micrometer is adjusted during firing of the laser in order to optimise continuum counts recorded by the CEMA/PDA detector (2.2m) or the CCD detector (1m).

3.1.3.4 Photoelectric Detectors

The multi-channel CEMA/PDA detector arrangement attached to the exit arm of the 1m spectrometer was replaced by a back-thinned CCD camera during VUV spectral studies performed as part of this thesis work. This permitted recording of the VUV photoabsorption spectra of atomic and ionic thorium in the vicinity of 6p subshell excitation, ~15 to 35eV with superior spectral resolution and dynamic range to that of the CEMA/PDA system. One of the major advantages of photoelectric spectral recording over that of photographic techniques is its linear response, thus enabling direct comparison and determination of the relative cross sections of spectral features.

3.1.3.4.1 Photometrics™ CCD

The back-thinned Photometrics™ SI003AB CCD camera (on loan from the DESY synchrotron in Hamburg) consisted of a two-dimensional array, 1024 pixels high × 1024 pixels wide, with a pixel size of 24×24μm corresponding to an active imaging area of 24.6×24.6mm. The CCD (charge coupled device) is essentially a device designed for charge accumulation and transfer and the architecture of the CCD chip is based on a two-dimensional array of metal-oxide-semiconductor (MOS) capacitors. A bias voltage applied to the gate electrode of each MOS capacitor induces a depletion region in the bulk silicon semiconductor material. Photons, incident on the CCD array, will create electron-hole pairs within the depletion region if their energy exceeds 1.1eV (1127nm), the band-gap of silicon. Depending on whether the semiconductor is n- or p-type either holes or electrons will be stored within the potential well under each electrode. As with a PDA, the CCD response is linear at all wavelengths (i.e., the number of charge carriers produced is proportional to the incident light intensity).

The SI003AB (SITe™ – Scientific Imaging Technologies™) CCD chip is a three-phase device, having three separate clocking signals to shift accumulated charge packets from one pixel to the next at the 200kHz readout frequency of the CCD array. Clock signals are both serial and parallel. The 1024 rows of pixels are divided into two groups of 512 rows (upper and lower sections). A parallel clocking signal transfers the signal charge collected in the imaging array along the columns to two serial registers located beside the upper and lower array sections. Further subdivision of the serial registers into two sections permits the division of the entire array into four quadrants thus maximising the speed of data transfer. A serial clocking signal transfers charge from the four serial registers to four amplifiers before the arrival of the next row of accumulated charge. Analog video signals are then digitised in a 16bit analog-to-digital converter in the camera control unit before being relayed to the computer for display as a two-dimensional image. With the SI003AB CCD chip it is possible to shift more than one row of charge into the serial register. This process, known as 'binning', permits summing of the total charge accumulated in each column of the array and gives a one-dimensional readout. Binning reduces the spectral resolution if the detector is tilted in any way, but it also improves the signal-to-noise ratio in energy regions of low light intensity.

The upper wavelength detection limit of silicon and polysilicon based detectors is defined by the requirement that incident photons must have an energy in excess of 1.1eV and therefore a wavelength below 1127nm. The lower wavelength limit is 400nm for front illuminated CCDs due to the fact that polysilicon gate electrodes become opaque to radiation of wavelength < 400nm. By etching the silicon substrate of the CCD chip (back-thinning) to a thickness of ~10μm (SI003AB) and illuminating the back rather than the front of the CCD, its wavelength detection interval is extended from beyond 400nm down to ~0.1nm in the soft X-ray region (Poletto et al. 1999). The absorption coefficient (α) of silicon increases with decreasing wavelength and so short wavelength light is absorbed (producing electron-hole pairs) close to the surface of the illuminated area (Holst 1996). By thinning the silicon substrate, the distance for electrons (or holes) to travel to the depletion region is reduced, thus reducing the probability of recombination/capture before arrival and subsequent storage in the depletion region. Poletto and co-workers (1999) have measured the quantum efficiency from the infra red to the x-ray region (1100nm to 0.14nm) of a similar 512 ×512 SITe™ CCD chip using the spectral response of calibrated photodiodes. The results they obtained (see Figure 3.11) were recorded using a Czerny-Turner monochromator in the

Figure 3.11 Effective quantum efficiency of a thinned, back-illuminated SITe ™ CCD chip in the 0.14 to 1100nm range (from Poletto et al. 1999)

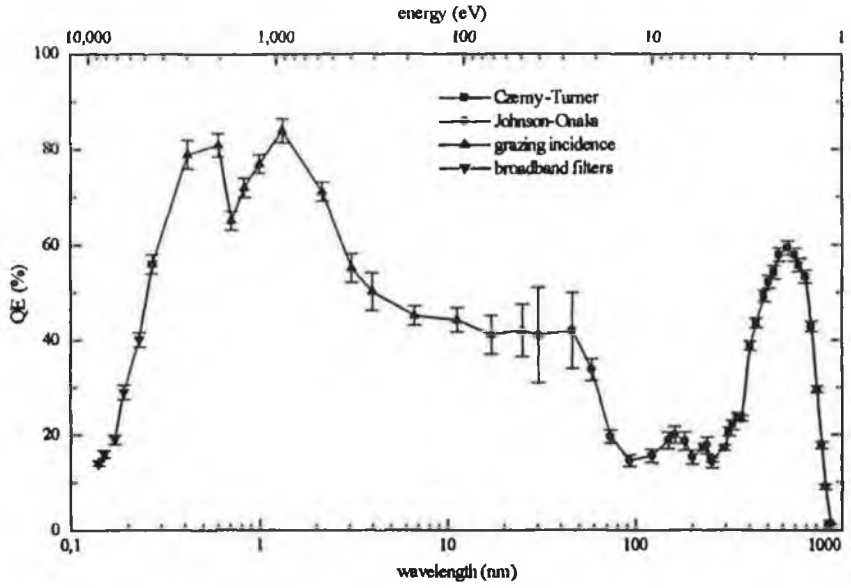

1100-250nm region, a normal incidence Johnson-Onaka monochromator in the 250-30nm region, a grazing incidence Rowland monochromator in the 30-0.27nm region, and broadband filters in the 0.27-0.14nm region. The quantum efficiency (~40% to

15%) over the 20 to 220nm operating range of the VM-521 1m spectrometer was found here to be sufficient for recording of spectral data of high signal to noise ratio.

Various UV and visible enhancement coatings can also be applied to both types of CCD structure to improve quantum efficiency in these regions. The SI003AB chip was un-coated due to the fact that UV and visible coatings absorb VUV radiation. The backside of the CCD was placed tangential to the Rowland circle of the VM-521 spectrometer, thus directly exposing the silicon substrate to dispersed VUV radiation.

The CCD array is thermoelectrically cooled in order to reduce thermally generated dark currents that are independent of photon flux. The CCD was cooled to a temperature of -35°C using a Peltier cooler. Heat generated by the cooler is removed by a mixture of 50% ethylene glycol (anti-freeze) and 50% distilled water that is circulated in a heat exchanger. The dark current at -35°C (as measured by the manufacturer) is 0.5 electrons/pixel/second.

3.1.3.5 1m Normal Incidence Spectrometer System: Performance

Because of its position as the first optical component in the path of light emitted from the plasma plume, the length (l = 3mm) to diameter (ϕ = 50μm) ratio ($\alpha = l/\phi$) of the pores within the GCA glass structure ultimately determines the solid angle over which the spectrometer can collect light. The maximum acceptance angle ϑ shown in Figure 3.12 is,

$$\vartheta = \mathrm{Tan}^{-1}\left(\frac{50}{3000}\right) = 17\mathrm{mrads} \qquad (3.5)$$

VUV radiation from the laser plasma source that is incident on the GCA at an angle in excess of 17mrads will be attenuated as it undergoes multiple reflections along each GCA channel. Consequently, the GCA (in conjunction with the GCA-slit-grating separation) will determine the dimensions of the footprint image of the source on the grating surface. The GCA-slit separation is 212mm and the slit-grating separation is ~1000mm resulting in the illumination of ~33mm (W) of the gratings 96mm width. The theoretical resolving power ($\Re$) of the grating is dependent on W (in m), the width of the

Figure 3.12 *Maximum acceptance angle (ϑ) for light transmitted through a pore within the Galileo™ GCA structure*

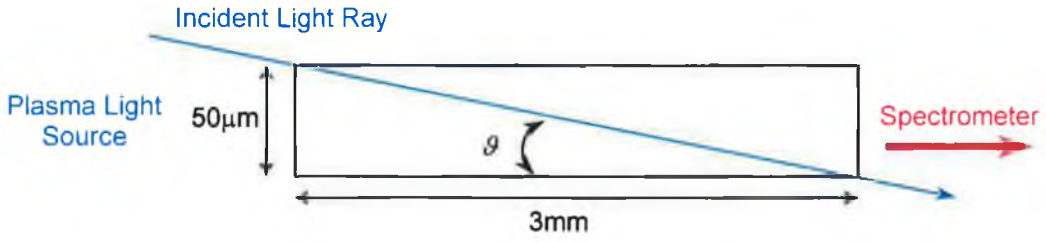

grating that is illuminated. For a concave grating, the resolution ($\Re$) at a particular wavelength (λ) is optimum when $W=W_{opt}$. An expression for W_{opt} has been derived by Namioka (1961) using geometrical optics

$$W_{opt} = 2.38\left[R^3\lambda\frac{\cos\alpha\cos\beta}{(\sin^2\alpha\cos\beta+\sin^2\beta\cos\alpha)}\right]^{1/4} \tag{3.6}$$

where R is the radius of curvature of the grating and α and β are the angles of incidence and diffraction respectively. Expression (3.6) was derived on the basis of a modified version of Rayleigh's criterion whereby two lines of equal intensity will be resolved if the separation between them is such that the minimum total intensity of both lines is 0.8106 ($8/\pi^2$) times that of the total intensity of both at the central maximum of either line. $\Re(\lambda)$ can then be determined from table 3.1 depending on the value of W with

Table 3.1 *Resolving power ($\Re$) of the concave grating as a function of the illuminated width (W) (from Samson 1967)*

Width of Grating Illuminated W	**Resolving Power** $\Re$
$W \leq 0.85W_{opt}$	mN or $W(m/d)$
$W=W_{opt}$	$0.92W_{opt}(m/d)$
$W \gg W_{opt}$	$0.75W_{opt}(m/d)$

respect to $W_{opt}(\lambda)$. For the VM-521 1m spectrometer W_{opt} lies between 55mm and 95mm across the wavelength region of 20 to 300nm. As W is limited by the GCA

aperture to ≅ 33mm, W is always less than $0.85W_{opt}$ and so the theoretical resolution $\Re$ of the grating is 39,616 (from Table 3.1). In practice this value is reduced by factors such as the quality of the grating surface, entrance slit width and more importantly the size of the spatial sampling interval (pixel size) of the detector at the spectrometer focal plane. Acton Research Corporation™ quote a value of $\Re$=5,700 at 80nm for a 10μm entrance slit width.

The reciprocal linear dispersion of the grating describes the spatial separation between two adjacent wavelengths and is given by

$$\frac{d\lambda}{dl} = \frac{d\cos(D_v/2)\cos\vartheta}{mR} \tag{3.7}$$

where l is distance along the Rowland circle, d is the inter groove separation (8.33×10^{-7} m), D_v is the angle of deviation (15° for the VM-521), ϑ is the angle of rotation of the grating, m is the spectral order and R is the radius of curvature of the grating. For a given wavelength, the value of ϑ can be determined using the grating equation (3.4). For the VM-521 1m spectrometer the reciprocal linear dispersion varies from 0.830nm/mm at 20nm to 0.816nm/mm at 300nm. The 25.5mm diameter of the MCP and the 24.6×24.6mm dimensions of the CCD array result in the coverage of a ~20nm wavelength interval along the Rowland circle. For an entrance slit of width W_s, the corresponding image on the focal curve of a concave grating in a Rowland mount has a width corresponding to a wavelength interval Δλ, determined by Mack et al. (1932) using

$$\Delta\lambda = \frac{W_s d}{R} \tag{3.8}$$

In all 1m studies performed as part of this work a 50μm slit width was used, resulting in a spectrometer instrumental line width Δλ of 0.042nm. Section 3.1.3.5.1 details the spatial resolution capabilities of the CCD detector system and its effect in determining the system resolution for a given entrance slit width.

3.1.3.5.1 Spectral Resolution with CCD Detector

The Photometrics™ SI003AB CCD records VUV light directly on its 24.6 × 24.6mm back surface, the centre of which is mounted tangentially to the Rowland circle of the Acton™ 1m spectrometer. The absence of a front-end channel electron multiplier array CEMA for conversion of VUV photons to visible light (MCP) prevents associated broadening of the system instrument function inherent in CEMA systems (Cromer et al. 1985), thus providing superior spatial and hence spectral resolution. A beryllium oxide emission spectrum, recorded using the CCD system, is shown in Figure 3.13. The beryllium oxide plasma was produced when a 300mJ, 15ns Nd:YAG laser pulse was focused onto a cylindrical target using a 110mm focal length plano-convex lens. The laser repetition rate was 5Hz and plasma light from 100 laser shots accumulated on the detector (cooled to –35°C) during a 20s integration time.

The two-dimensional CCD image, shown in Figure 3.13, is a section of the total 1024 × 1024 image size. A 1024(x) × 200(y) pixel area of the image has been vertically binned

Figure 3.13 100 shot beryllium oxide VUV emission spectrum (~70 to 90nm) recorded using a back-thinned CCD detector system

Line	Wavelength (nm)	
1	83.5096	O III
2	83.3332	O II
2a	83.2927	O III
3	80.2200	O IV
4	79.6661	O II
5	79.0199	O IV
6	78.7711	O IV
7	77.9821	O IV
8	77.4518	O V
8a	76.2003	O V
8b	76.1128	O V
9	76.0445	O V
9a	75.9441	O V
9b	75.8678	O V
10	72.8733	O V
11	72.4932	O I
12	71.8484	O II

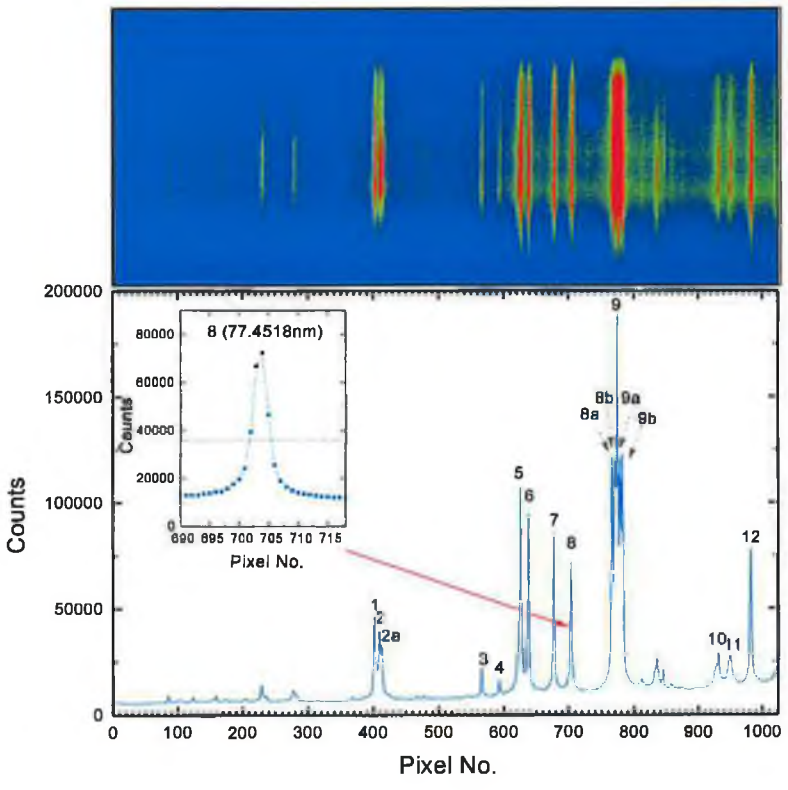

(y-direction) in order to produce the spectrum shown underneath. For a slit width of 50μm, and using an OV emission line at 77.4518nm, the system instrument function was measured to be ~3.5 pixels FWHM (or 0.07nm). This compares well to a calculated value of 3 pixels for a dispersion of 0.02nm/pixel at 75nm and a 24μm CCD pixel size. Investigations of the FWHM of the 77.4518nm OV line were performed by viewing single 1024(y) × 1(x) pixel lines through the image which yielded values in the region of ~3 to 3.5 pixels, thus indicating accurate detector alignment. As a consequence of this, vertical binning of photoabsorption and emission spectra recorded as part of this work in order to improve the CCD signal-to-noise ratio, did not result in any significant deterioration of system resolution. The system spectral resolution ($\lambda/\Delta\lambda$) varies from ~500 to ~1150 over the 35 to 80nm (35 to 15eV) energy region.

The near-stigmatic imaging properties of the near-normal incidence 1m spectrometer are evident in Figure 3.13. The vertical length of the 50μm spectrometer entrance slit was ~7mm and is imaged as a series of straight spectral lines ~7mm high (300 y pixels) at the spectrometer focal plane. Because plasma light is not collected and focused onto the grating, spectral lines do not yield spatial information about the plasma plume.

3.1.4 2.2m Grazing Incidence XUV Experimental Regime

3.1.4.1 System Overview

The design and operation of the 2.2m grazing incidence spectrometer-based DLP system (Figure 3.14) is similar to that of the 1m normal incidence system and also permits time and space resolved DLP photoabsorption studies and single-plasma emission studies of atomic and ionic species. However, the utilisation of grazing incidence optics to focus and diffract XUV wavelengths permits deeper inner shell photoabsorption/photoionisation investigations than in the 1m normal incidence regime. Also, the shorter continuum pulse duration in the XUV region permits probing of the absorbing plasma with improved temporal resolution.

Central to the XUV-DLP system is a McPherson Instrument Corporation™ 2.2m grazing incidence monochromator (Model 247M8) which has been converted to a spectrometer by the removal of the exit slit and the addition of a photoelectric detector array (Kiernan 1994). XUV radiation in the 5 to 50nm (248 to 25eV) region is diffracted and focused along a 2.2176m diameter Rowland circle by a 1200 grooves/mm McPherson™ concave diffraction grating. The addition of a toroidal mirror located between the plasma source and the fixed position entrance slit of the spectrometer serves to reduce the inherent astigmatism associated with a concave grating operating in the grazing incidence regime, thus permitting *quasi-stigmatic* imaging. The toroidal mirror, also operating at grazing incidence, increases the light flux incident on the spectrometer entrance slit and ultimately dispersed along the Rowland circle. Dispersed radiation is recorded using a Galileo™ channel electron multiplier array (CEMA) coupled to an EG&G™ photodiode array (PDA). The detector arrangement is attached to a UHV detector chamber such that the front face of the microchannel plate (MCP) within the CEMA lies tangential to the Rowland circle. Scanning of the 5 to 50nm wavelength range is achieved by manually turning a precision screw resulting in the translation of the detector along the circumference of the Rowland circle. The entire detector chamber is mounted on a carriage assembly designed to traverse a stainless steel track attached to a granite base and machined to the diameter of the Rowland circle. A flexible metal bellows connecting the grating chamber to the detector chamber extends and contracts (while maintaining vacuum) in order to permit free movement of the detector chamber. The analog video signal, integrated by the PDA during an exposure, is digitised by a 12bit (11 bits + 1 signed bit) analog-to-digital converter (0 to

Figure 3.14 *2.2 metre grazing incidence spectrometer-based system for recording of XUV DLP photoabsorption and single-plasma emission spectra of atomic and ionic species*

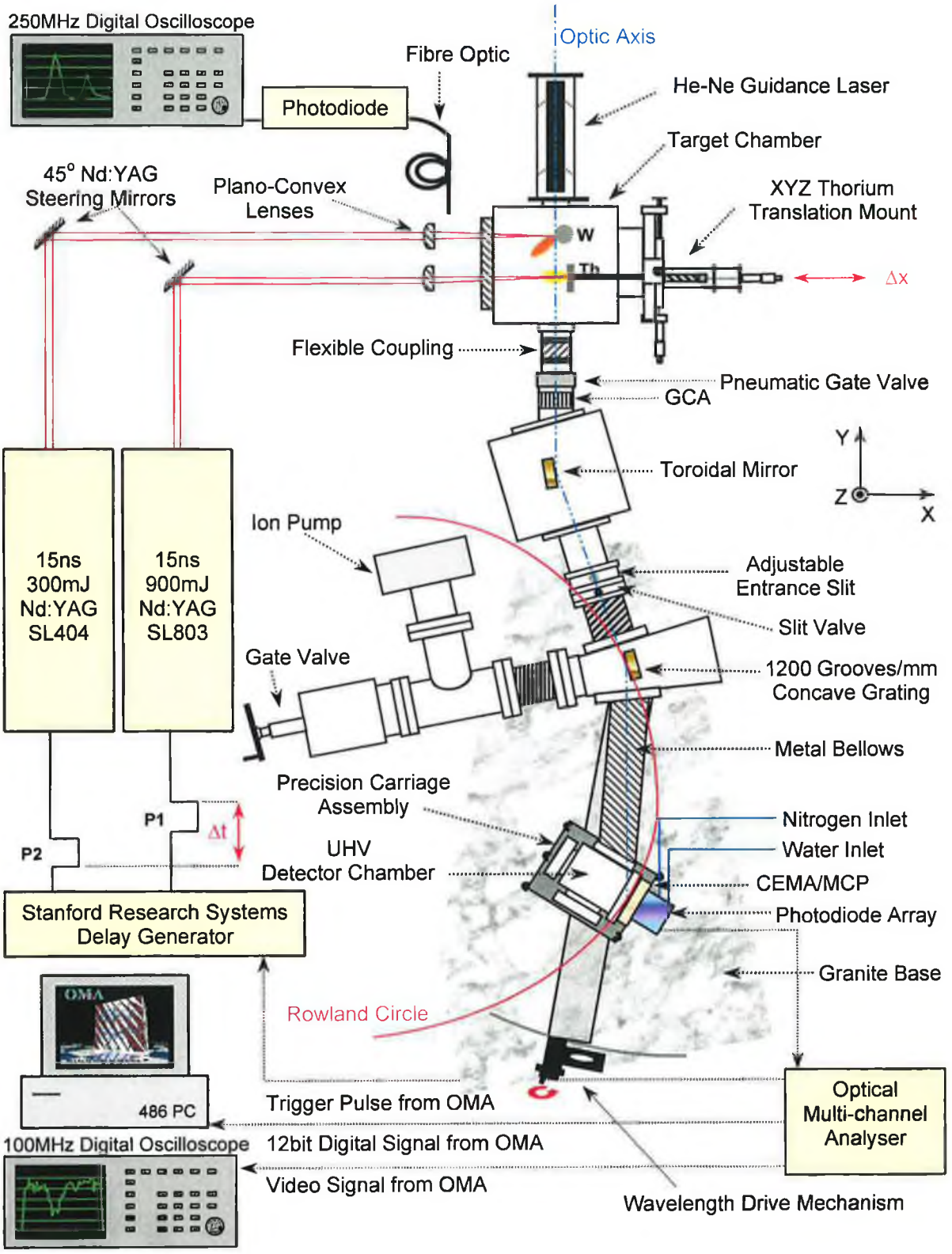

2048 dynamic range) within an optical multichannel analyser (OMA Model 1461). In both VUV and XUV regimes the video signal from the OMA is fed to a HP54510A

100MHz digital oscilloscope for shot-to-shot monitoring of the absorption/ emission signal recorded by the PDA detector. The digitised signal is sent to a 486 PC via a GPIB (General Purpose Interface Bus) card for display and manipulation within the *Omasoft* software package. As with the 1m system a second HP54510A 250MHz digital oscilloscope is used for monitoring the characteristics of both laser pulses.

The combination of a turbo/rotary pumping system and a getter type ion pump results in vacuum pressures of ~2×10^{-7}mbar in the detector chamber. Once this pressure is reached a gate valve is used to close off the turbo and rotary pumps thus allowing the ion pump, which operates without the need for a backing line, to maintain good vacuum in the detector chamber. The spectrometer and detector housing pressures attained are well below the maximum 2×10^{-6}mbar required for operation of the CEMA. A slit valve located between the grating and the entrance slit isolates the detector chamber from the toroidal mirror chamber. The custom-built stainless steel mirror chamber (127mm × 127mm × 127mm) is evacuated by a turbo/rotary pumping system which maintains a pressure of ~1×10^{-6}mbar. It is isolated from a similarly designed stainless steel target chamber (127mm × 127mm × 127mm) by a pneumatically controlled gate valve (Kiernan 1994). This vacuum isolation between mirror and target chambers again permits fast pumping times following venting of the target chamber for replacement of target materials. A Galileo™ GCA, 25mm in diameter, 2mm thick and with a 50μm pore size serves a similar purpose to that of the 1m system (i.e. helps maintain a differential pressure between the target chamber and spectrometer system) and is mounted in the vacuum line between the gate valve and the entrance port to the mirror chamber cube.

As in the normal incidence regime, both absorbing and emitting plasmas studied in this work were produced when two Q-switched Nd:YAG lasers (SL404 and SL803) were focused onto metal targets mounted within the target chamber cube. Spherical and cylindrical lenses were mounted on a similarly designed optical breadboard to that coupled to the 1m target chamber and focused laser light to a point- or line-type geometry. Target materials were attached to custom-built target holders mounted on top of (continuum target) and to the side of (absorbing target) the target chamber. The X-Y-Z translation holder used in 1m VUV studies (Section 3.1.3.3.1) was adapted for coupling to both 1m and 2.2m target chambers and so was used for mounting and accurate positioning of thorium targets here also. Cylindrical tungsten and aluminium

rod targets were attached via a chuck and an M6 locking nut to the end of a 6mm diameter stainless steel rod passing through the top of the target chamber via a Wilson vacuum seal attached to a 108mm × 108mm micrometer driven X-Y translation plate. This system permitted translation of tungsten/aluminium targets over a distance of 15mm in the x- and y-directions in increments of 5μm.

3.1.4.2 McPherson™ 2.2m Grazing Incidence Spectrometer

3.1.4.2.1 McPherson™ Spherical Concave Diffraction Grating

The focusing and diffracting properties of the spherical concave diffraction grating, which is central to the operation of the McPherson™ 2.2m spectrometer, have been discussed in Section 3.1.3.2.2. In the XUV region, below 30nm, the grating reflectivity becomes so poor at near-normal incidence that it becomes necessary to operate in grazing incidence geometry. The McPherson™ diffraction grating is held in a kinematic mount located in the main spectrometer chamber. The grating is 50mm wide and 30mm high along the direction of the groove ruling and its gold-coated surface is holographically ruled at 1200 grooves/mm. The surface of the grating is blazed at an angle of 2°4′, resulting in a maximum conversion efficiency of incident radiant flux to first order light at 8.43nm. The radius of curvature (R) of the spherical concave profile of the gratings front face is 2217.6mm (~2.2m). The location of a fixed position entrance slit (15mm high, 10μm and 20μm width settings), which lies on the circumference of the 2217.6mm diameter Rowland circle and is 231.8mm from the grating centre (also located on the Rowland circle), defines an angle of incidence (α) of 84° with respect to the grating normal (Figure 3.15). The corresponding grazing incidence angle δ is 6° (where $\delta = 90° - \alpha$) and consequently the minimum reflected wavelength from the gold coated surface of the grating is calculated to be approximately 1.6nm using (3.9) from Samson (1967),

$$\lambda = \sin\delta \left(\frac{e^2 N}{mc^2 \pi} \right)^{-1/2} \tag{3.9}$$

where λ(Å) is wavelength, δ is the grazing angle of incidence, e is the electronic charge, m is the electronic mass, c is the speed of light and N is the number of electrons per unit volume of the surface material coating on the grating and equals 4.66×10^{24} electrons for

Figure 3.15 *Schematic overview of the position of the spherical concave diffraction grating in the McPherson™ 247M8 spectrometer with respect to the fixed position entrance slit, the translating MCP front face and the toroidal coupling mirror (all dimensions in mm)*

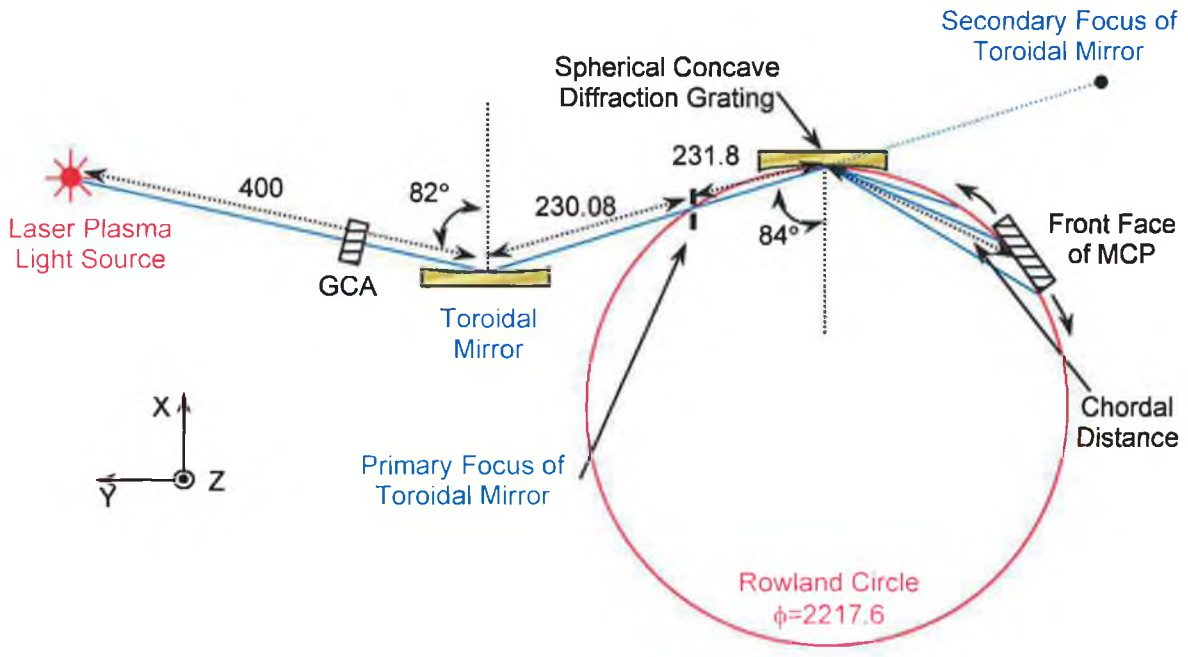

gold. The reflectivity of the grating, the angle of incidence α and the optical properties of the toroidal mirror (to be discussed in Section 3.1.4.2.2) combine to define the accessible wavelength range of the 2.2m spectrometer system as 5 to 50nm. The chordal distance, defined as the distance from the centre of the grating to close to the centre of the front face of the MCP, is displayed in inches on a dial on the manual wavelength driver and varies from 37.5cm (5nm) to 77.5cm (50nm).

3.1.4.2.2 Toroidal Coupling/Focusing Optic

At grazing angles of incidence the most significant aberration of a concave mirror is that of astigmatism and this aberration is consequently inherited by the concave grating because of its similar focusing properties. Astigmatism manifests itself as a reduction in the vertical focusing ability of the grating for light emerging from a point source on the entrance slit and diffracted along the Rowland circle. This results in the formation of vertical spectral lines rather than points (stigmatic imaging) due to light rays converging

in the meridional plane (x-y) at the horizontal focus (primary focus) along the Rowland circle. As previously mentioned the vertical focus (secondary focus) forms due to the convergence of light rays in the sagittal plane (y-z) beyond the Rowland circle along a tangent to the grating normal, producing a horizontal line (see Figure 3.5). In general, the diffracted spectral lines along the Rowland circle are curved and their vertical length increases with increasing angles of incidence and diffraction (α and β), with the illuminated vertical length of the rulings on the grating (L) and the vertical length of the entrance slit (l). The horizontal focusing achieved along the Rowland circle is sufficient for wavelength separation, thus permitting spectroscopic measurements. The intensity per unit area at the focal plane and the spatial resolution at the laser plasma source are significantly reduced however due to the spreading out of light in the vertical direction. The introduction of a toroidal mirror between the laser plasma light source and the entrance slit (Figure 3.15) is in fact the most efficient method for reducing astigmatism (and thus increasing the intensity per unit area at the focal plane) over a wide wavelength range in the grazing incidence regime (Samson 1967).

Rense and Violett (1959) discuss the addition of a toroidal mirror to a grazing incidence spectrograph resulting in reduced astigmatism, improved light intensity per unit area along the Rowland circle and a corresponding decrease by a factor of four in the time required to expose photographic plates. Jannitti and co-workers (1979) built a stigmatic spectrograph consisting of a toroidal mirror and a concave grating for application to the study of light emitted from laser produced plasmas in the 1 to 30nm XUV/soft X-ray region. The optical parameters of the toroidal mirror chosen determined the acceptance angle of the spectrographic system and the corresponding field of view at the laser plasma source. Also, movement of the mirror in order to alter the source-mirror (p) and mirror-slit (p') distances for a fixed source position, permitted variation of the stigmatic wavelength interval over the detectable wavelength range. The reduction in astigmatism achieved upon addition of the toroidal mirror to the spectrograph yielded a spatial resolution of 20 to 30μm over a distance of 1mm at the expanding plasma plume along the direction parallel to the entrance slit.

The addition of a concave toroidal mirror to a grazing incidence spectrometer provides several significant improvements to the overall system performance. There is a reduction in astigmatism by improving vertical focusing at the horizontal (primary) focus along the Rowland circle of the concave grating. This results in *stigmatic* or *near-*

stigmatic imaging, depending on the optical properties of the mirror selected, with a consequent improvement in *spatial resolution* at the laser plasma source. Further consequential benefits include an increase in the *intensity per unit area* along the Rowland circle due to a reduction in the vertical height of spectral lines and also due to the ability of the mirror to collect and focus more laser plasma light onto the spectrometer entrance slit. Also, an increase in the system *spectral resolution* is achieved when the width of the mirror is chosen so as to utilise the full aperture of the grating, or at least to fill the optimum width (W_{opt}) in a given wavelength region (see equation 3.7 and table 3.1).

The concave toroidal mirror, mounted in a kinematic holder in the McPherson™ 2.2m spectrometer, is 30mm high and 30mm wide with a gold surface coating. The front surface of the mirror is a segment from a torus having a major radius of curvature, R_m=2099mm and a minor radius of curvature, r_m=111.34mm. The source-mirror distance (p) is set at 400mm and in conjunction with the GCA is chosen to reduce the possibility of contamination of the mirror surface by laser plasma blow-off material. Like the concave grating, the toroidal mirror is operated at grazing incidence and light from the laser plasma source is incident on the mirror at an angle (ϕ) of 82° with respect to the mirror normal (Figure 3.15). Again, like the concave grating, the toroidal mirror produces two spatially separated images, known as the primary and secondary images. The primary image is formed at the horizontal focus where light rays converge in the meridional plane (x-y) to produce a vertical line. The secondary image is formed at the vertical focus where light rays converge in the sagittal plane (y-z) to produce a horizontal line. The values of R_m and r_m chosen will determine the positions of the primary and secondary images respectively. The source-mirror distance (p) and the angle of incidence (ϕ) will also determine the positions of the primary and secondary images. The mirror-slit distance (p') is 230.1mm and coincides with that of the primary (horizontal) focus. Whereas the mirror-secondary focus distance (p'') is set at infinity and because of the location of the grating (see Figure 3.15) a virtual image is formed behind the grating.

When operating in the grazing incidence regime, both the horizontal (primary) and vertical (secondary) foci of the concave grating will coincide along the Rowland circle if light emerging from the entrance slit onto the grating is diverging in the horizontal (meridional) plane and converging in the vertical (sagittal) plane towards a virtual

source behind the grating. The position of the virtual source, behind the grating, is unique for each wavelength and so for a given compound optical configuration a stigmatic image on the Rowland circle will be produced for one wavelength only. This can result in the recording of a 'hot spot' using an image intensified detector system (Kiernan 1994) and is avoided by setting the position of the secondary focus of the toroidal mirror at infinity ($p'' = \infty$) thus producing *quasi-stigmatic* imaging over a wavelength band. The result is a series of spectral 'lines' along the Rowland circle that have a shorter vertical length than would be attainable in a grating-only spectrometer system.

3.1.4.3 Galileo™ Channel Electron Multiplier Array (CEMA) and EG&G™ PhotoDiode Array (PDA)

As previously mentioned, the entire photoelectric detector arrangement (CEMA/PDA) is attached to the detector vacuum chamber which traverses an arc section of the 2.2m Rowland circle of the McPherson™ spectrometer. A schematic diagram illustrating the operation of the CEMA/PDA detector arrangement is shown in Figure 3.16. The CEMA is in essence an image intensifier consisting of a micro-channel plate (MCP) and a phosphor- coated fibre optic faceplate. The MCP, from Galileo Electro-Optics Corporation™, utilises both fibre optic and photomultiplier technologies to convert charged particles or energetic photons to an electron signal, which it subsequently amplifies. The MCP finds application in the sensing of VUV/XUV radiation, soft X-rays, neutrons and charged particles in scanning electron microscopes, residual gas analysers, image tubes and time-of-flight mass spectrometers. Its sensitivity and dynamic range at VUV, XUV and soft X-ray wavelengths make it an ideal candidate for multi-channel detection of dispersed radiation.

The MCP consists of an array of lead glass fibre optic bundles that are fused together and chemically etched to form a porous array. Each glass pore has a diameter of 12μm and a centre-to-centre spacing between pores of 15μm. The total MCP structure has a diameter of 40mm with an active area of 12.57cm^2. The open area ratio, determined by the number of pores and the pore diameter, is 55%. The quantum efficiency (QE) of a standard MCP lies in the region of 10% to 20% for normal incidence photons having an

Figure 3.16 Schematic representation of the operation of the Galileo™ CEMA image intensifier incorporating an MCP and phosphor-coated fibre optic face plate butt coupled to a 1024 pixel linear photodiode array

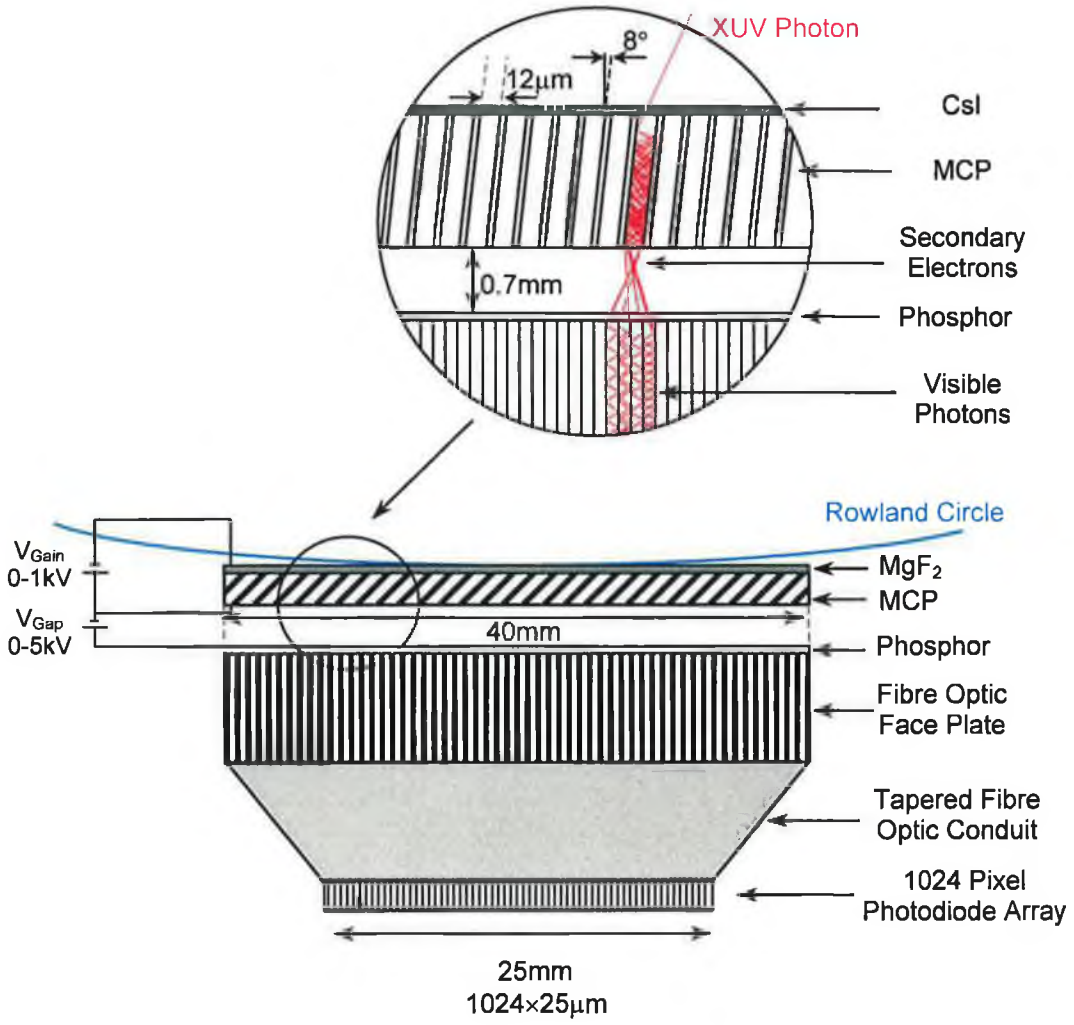

energy in excess of 15eV. The MCP front face is located tangentially on the Rowland circle of the 2.2m grazing incidence spectrometer system.

The internal walls of each pore within the MCP structure are firstly coated with a semi-conducting layer followed by a silicon dioxide-rich secondary electron emissive coating. XUV photons incident on the MCP front face stimulate the production of electrons in the CsI coating. Thin metallic layers vacuum deposited on both the front and back faces of the MCP structure serve as electrodes across which a negative bias V_{Gain} (0 to –1kV) is applied. V_{Gain} is typically set at a value in the region of –800V to –1000V and because of its bias, electrons are accelerated into the pores. Collisions with the electron emissive coating on the pore walls stimulate secondary electron emission and this process continues, amplifying the electron signal with repeated collisions down

the continuous dynode structure of the pore walls. The pores within the MCP are set at an angle of 8° with respect to the MCP surface normal in order to prevent ion feedback within the pore channels. Following traversal of the pore length, an initial primary electron is amplified to produce ~10^4 secondary electrons. Such a high gain permits sensing of very low intensity XUV light.

The electron bunch at the output of each pore within the MCP structure is then accelerated across a 0.7mm vacuum gap by a positive potential V_{Gap} = +4.2kV, where it strikes a phosphor (P20) coated fibre optic faceplate. The phosphor fluoresces in the visible region (with a decay time of 60μs) causing visible photons to propagate down a tapered fibre optic conduit which de-magnifies the initial 40mm image by a factor of 1.6 in order to fill the 25mm length of the EG&G Princeton Applied Research™ photodiode array (Model 1453). The fibre optic conduit is butt coupled to the PDA, which is capable of detecting light in the wavelength region of 180 to 1100nm. The PDA consists of a linear array of 1024 reversed-biased photodiodes (pixels). Light incident on the depletion region of the diode p-n junction is absorbed, resulting in the production of electron-hole pairs, and thus reducing the capacitance of the depletion region. An EG&G™ optical multichannel analyser (OMA - Model 1461) controls the PDA readout and triggering and is connected to a PC via a GPIB interface (Shaw 1996). During readout each photodiode is successively connected to the input of an amplifier using a shift register and an FET switch. The potential across each p-n junction is determined by the integrated photon flux incident on that pixel. Following buffering and amplification, an ADC in the OMA converts the PDA analog video signal, which is directly proportional to the incident photon flux, to a 12 bit digital signal. One bit of this signal is allocated as a signed bit and so the detector dynamic range is 0 to 2048.

A Peltier cooler, thermally bonded to the PDA, is used to reduce thermally generated noise within the detector, thus reducing the dark current signal. Water is circulated through the PDA head in order to assist the thermoelectric cooler to bring it down to a temperature of 5°C. Nitrogen gas is also circulated through the detector head in order to prevent the formation of condensation on the detector when operating at temperatures below room temperature. Vacuum pressure in the 2.2m detector chamber was maintained at $< 2 \times 10^{-7}$ mbar (using a rotary/turbo/ion pumping arrangement) in order to prevent arcing of the CEMA. The performance of the CEMA/PDA detector system is

discussed in Section 3.1.4.4.1 with reference to its role in ultimately determining the spectral resolution of the 2.2m grazing incidence spectrometer system.

3.1.4.4 Performance and Resolution Capabilities of the McPherson™ 2.2m Grazing Incidence Spectrometer System

Vertical and horizontal knife-edge experiments performed by Moloney (1998) permitted the determination of the spatial dimensions of an XUV laser plasma source as imaged on the focal plane of the 2.2m spectrometer system at energies of 50, 75, 100, 125 and 150eV (25, 17, 12, 10 and 8nm). The XUV ray-tracing software *Shadow™* (see *Shadow™* reference) was then used to perform simulated knife-edge experiments using a range of different source sizes in order to obtain the best approximation to the real physical laser plasma source size. Using this information, the 'footprint' of the source on the toroidal mirror, entrance slit, grating and detector can then be computed using *Shadow™* for a range of XUV wavelengths across the operating range of the spectrometer. Of particular interest to this thesis work is the 100eV (12nm) region where the $5d \rightarrow \overline{5,\varepsilon f}$ giant dipole resonance in atomic/ionic thorium occurs. The size of the XUV region of the laser plasma source that emits radiation at 100eV has been measured and calculated (using *Shadow™*) to have an approximate area of 400μm × 400μm at a distance of 350μm along an axis at 45° with respect the spectrometer optic axis (Moloney 1998). The laser plasma source used in *Shadow™* calculations simulated one produced using a cylindrical target with the laser focus and the spectrometer optic axis both at 45° with respect to the target surface normal. Calculations yielded an effective source height of 400μm (z) and an effective source width of 530μm (x), at a distance of 350μm from the target surface along the optic axis (y). The experimental laser plasma source was produced at a distance of 400mm from the toroidal mirror when Nd:YAG laser light was focused to a ~100μm diameter spot size on a cylindrical target surface using a plano-convex lens.

Details of the light 'footprint' on each of the components within the McPherson™ 2.2m spectrometer system, obtained by ray tracing the system at 100eV using *Shadow™* with a 10μm entrance slit width, are as follows. The footprint on the toroidal mirror is 30mm

wide (y) and 10mm high (z), centred about a horizontal axis through the mirror centre. The primary image of the toroidal mirror is a curved line (13mm high (z), 0.48mm wide (x)) and fills approximately 10.5mm of the 15mm high entrance slit. The footprint on the grating is approximately 10.5mm high (z) along the direction of ruling and 42mm wide (y). Finally, the footprint at the Rowland circle for a wavelength of 100eV is approximately 10.25mm high (z) and 0.0315mm wide (x). Similar final image sizes along the Rowland circle were obtained at 50, 75, 125 and 150eV (Moloney 1998).

W_{opt}, the optimum width of the grating illuminated increases from 20 to 42mm over the 5 to 50nm wavelength range of the spectrometer and so the theoretical resolving power $\Re$ of the grating can be determined from Table 3.1. The width of the grating illuminated at 12nm (100eV) is 42mm and so $W = W_{opt}$. The theoretical resolving power $\Re$ at 12nm is 46,387 in first order (m=1) and is determined using equation (3.10) from Table 3.1.

$$0.92W_{opt}(m/d) \tag{3.10}$$

The reciprocal linear dispersion is calculated using

$$\frac{d\lambda}{dl} = \frac{d\cos\beta}{mR} \tag{3.11}$$

where l is distance, d is the inter-groove separation (8.33×10^{-7}m), β is the angle of diffraction at a given wavelength λ, m is the spectral order and R is the radius of curvature of the grating. For the McPherson™ grating the reciprocal linear dispersion varies from 0.0601nm/mm at 5nm to 0.1360nm/mm at 50nm. The 40mm diameter of the MCP front face results in coverage of a 2.4nm wavelength interval at 5nm and a 5.4nm wavelength interval at 50nm. For entrance slit widths (W_s) of 10μm and 20μm, the corresponding image on the focal curve has a width $\Delta\lambda$ (determined using equation 3.8) of 0.0038nm and 0.0076nm respectively. Throughout this thesis work both 10μm and 20μm entrance slit widths were used. A 20μm slit width was predominantly used, in particular when thorium ions were investigated. In such experimental situations the higher power Nd:YAG (SL803) laser was required to produce sufficient thorium ion densities and consequently the lower power Nd:YAG (SL404) laser was used to generate the backlighting continuum. In order to maintain a good signal to noise ratio, resolution was sacrificed for a higher continuum flux on the detector, and so a 20μm slit width was used. The following section details the resolution capabilities of the CEMA/PDA detector system, which ultimately determines the 2.2m grazing incidence spectrometer system resolution.

3.1.4.4.1 Spectral Resolution of CEMA/PDA Detector System

Due to the presence of the tapered fibre optic reducer in the CEMA/PDA detection system, the 25μm size of each PDA pixel records light accumulated over a 40μm interval at the front face of the MCP, and so the effective spatial sampling interval at the Rowland circle is 40μm. As mentioned earlier, thorium 5d studies (emission and photoabsorption) were performed in a 60eV photon energy interval centred on 100eV (~12nm). At 12nm the reciprocal linear dispersion is 0.0773nm/mm and therefore two and a half 40μm (1.6 × 25μm) 'pixels' (0.0031nm/pixel) are required to resolve the 0.0076nm spectrometer instrument function for an entrance slit width of 20μm[3]. In practice however, the system instrument function has a FWHM of five pixels (or 0.0155nm) and this is demonstrated in Figure 3.17 using two aluminium emission lines at 12.6068nm (Al V) and 12.5529nm (Al V). The corresponding system resolution ($\lambda/\Delta\lambda$) is ~800 at 12nm.

Figure 3.17: 20 shot (averaged) aluminium XUV emission spectrum recorded using the CEMA/PDA detector system for an entrance slit width of 20μm

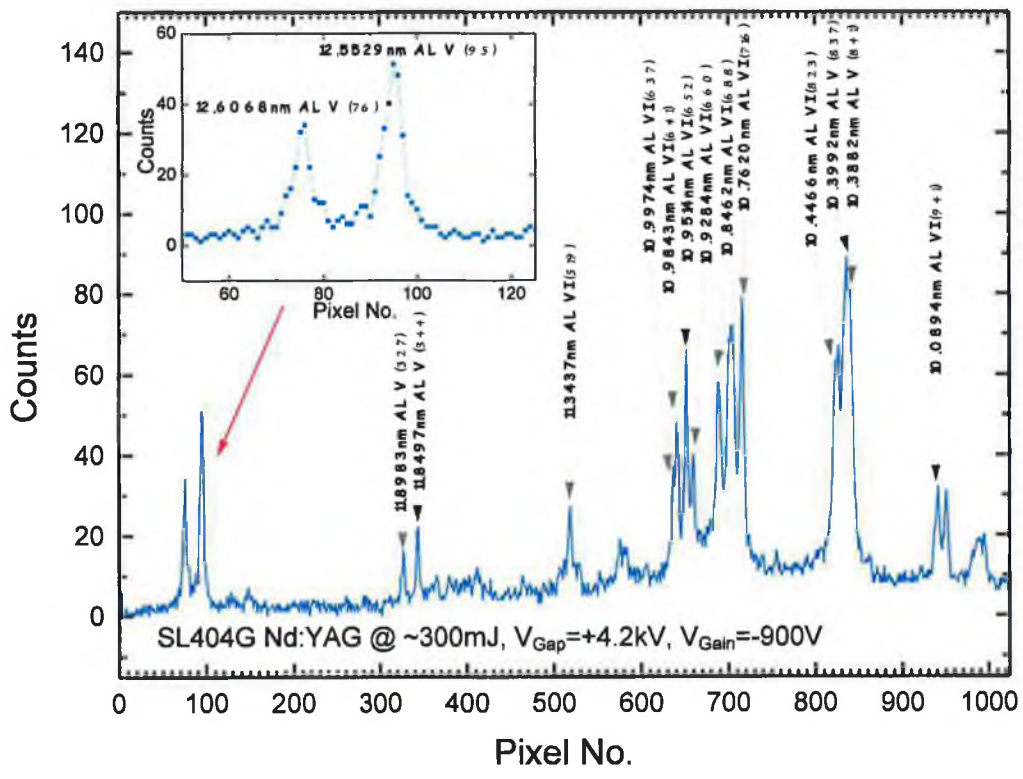

[3] For an entrance slit width of 10μm, just one 40μm 'pixel' is required to resolve the 0.0038nm instrument function (0.0031nm/pixel) at 100eV. *Shadow™* calculations at 100eV yielded a spectral line width of 31.5μm, within one 'pixel' width (Moloney 1998).

Factors contributing to the broadening of the spectrometer instrument function are the actual size of the electron bunch on the phosphor coated fibre optic conduit, shear distortion of the fibre optic conduit, and defocusing of spectral lines dispersed along a curved focal surface and then recorded using a linear detector. For an entrance slit width of 10μm the instrument function recorded on the detector reduces to ~4 pixels FWHM. The resolution ($\lambda/\Delta\lambda$) for a 10μm slit width is approximately 1400 at 32nm (the central wavelength of the system), corresponding to a wavelength resolution of approximately 0.023nm.

3.1.5 Laser Synchronisation and Procedure for Spectral Data Acquisition

Accurate synchronisation and control of the firing of both Nd:YAG laser systems in order to generate two laser produced plasmas separated in time by an amount Δt is essential in DLP-type experiments. Also, laser firing and subsequent plasma production must be accurately timed so as to coincide with detector integration periods. The interaction of the 486 PC, optical multichannel analyser and Stanford™ digital delay generator (see Figure 3.2 or Figure 3.14) via inter-communicating electronic signals orchestrates the sequence of events required to achieve the above criteria.

Experimental parameters such as the number of laser shots fired, the duration over which the detector integrates (exposure time) at each laser shot, and the delay between laser shots are entered and stored on the PC via the *Omasoft* software package. Any number of laser shots ranging from a single shot to hundreds of shots can be selected. The read/reset time of each pixel in the PDA (Model 1453) is 28μs and so an exposure time of 30ms is required to read all 1024 pixels. Multiples of 30ms can therefore be selected as suitable exposure times. In practice a value of 30ms is selected, as the typical duration of laser plasma emission is less than 1μs and exposure times longer than 30ms result in a build up of dark current and a subsequent decrease in the dynamic range (Shaw 1996). The delay between laser shots is generally set at 1 to 3s in order to permit complete cooling of the laser heads during repeated firing. Both lasers can however run efficiently at repetition rates of up to 10Hz. The inter-lens separation in the intra-cavity telescopes of both lasers was optimised for firing at lower repetition rates

Figure 3.18 *Sequence of electronic signals used to synchronise firing of both Nd:YAG laser systems with a programmable delay Δt between both laser pulses*

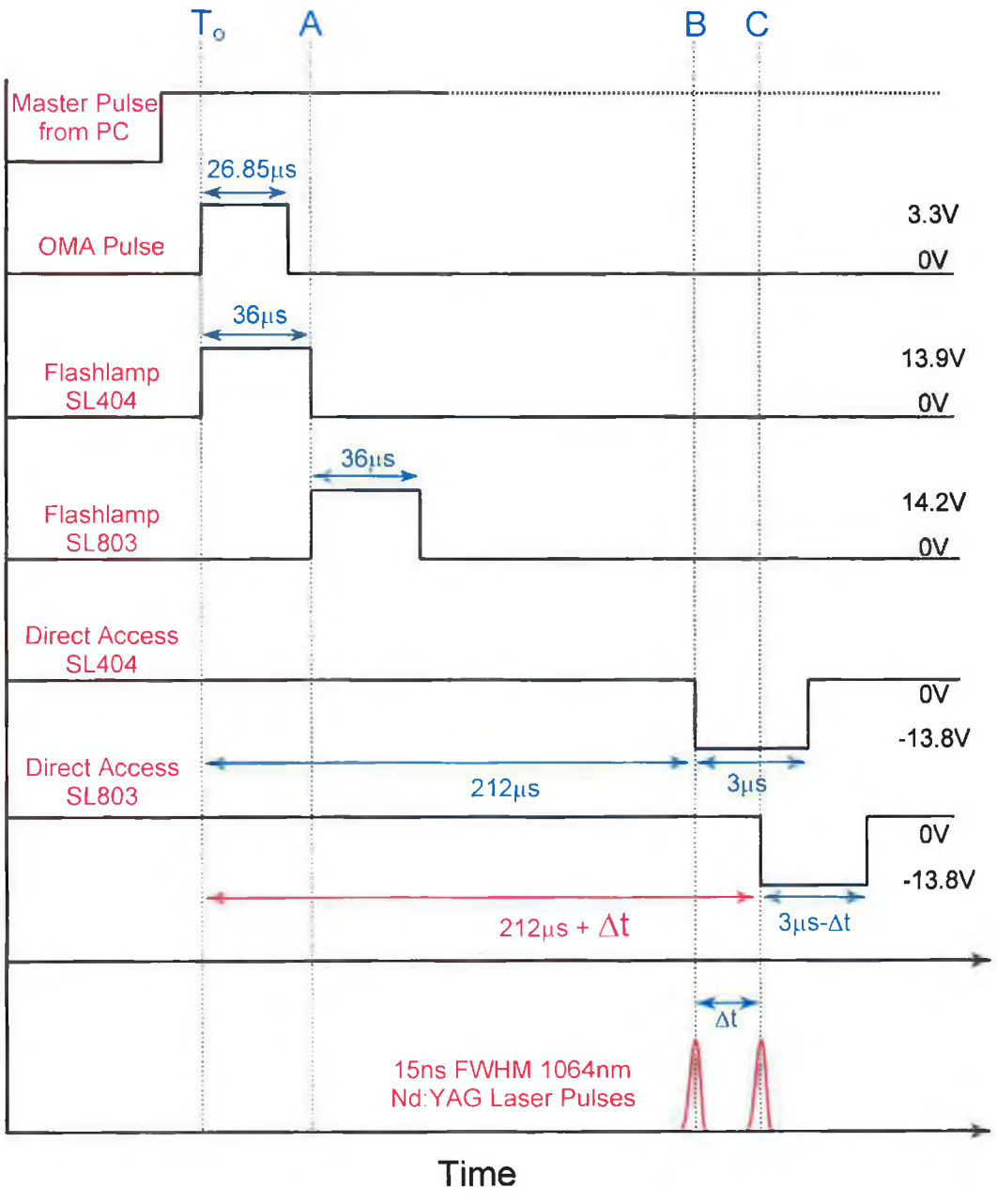

(~2Hz), and so the optimum laser energy per pulse was delivered at these lower frequencies.

Experiments are initiated by selecting the appropriate option within the *Omasoft* package. A master TTL pulse is sent from the PC to the OMA controller (Model 1461) via a GPIB parallel interface (see Figure 3.18). The OMA controller in turn generates a TTL pulse, which it sends to the BNC input channel of the Stanford™ digital delay

generator upon initiation of detector integration. This pulse is 26.85μs in duration and its rising edge is defined as time 'T_o' (see Figure 3.18). The Stanford™ digital delay generator has a single input channel and five output channels T_o, A, B, C and D. The delay on each of the four BNC terminated output channels is programmable with respect to T_o and can be varied from 0 to 1000s with a minimum 5ps increment. The amplitude of each output (TTL) pulse from the Stanford™ delay generator is insufficient to trigger the flashlamp or Q-switch circuitry (direct access) of both Spectron™ Nd:YAG laser systems. The laser flashlamp triggers on the rising edge of a 0→15V pulse and the Q-switch triggers on the falling edge of a 15→0V or a 0→ –15V pulse. The output pulses from the four output channels of the Stanford™ delay generator are amplified to ~ +/-14V (Figure 3.18) using custom built amplifier circuitry. These voltage levels are sufficient to initiate triggering of both flashlamp and Q-switch circuitry of both SL404 and SL803 laser systems.

Upon arrival of the OMA TTL pulse, the Stanford™ delay generator instantly sends a pulse from T_o to trigger the flashlamps of the SL404 before those of the SL803. This is due to the fact that the SL404 should be Q-switched 212μs after flashlamp triggering, compared with 177μs for the SL803. The SL803 flashlamp is triggered by a pulse from channel A, which is appropriately delayed by 36μs with respect to T_o. The duration of both flashlamp trigger pulses leaving the custom built amplifier circuitry is fixed at 36μs and falls within the 10 to 100μs pulse duration requirement for the Spectron™ flashlamp circuitry. Channels B and C are used to trigger the direct access circuitry of the SL404 and SL803 Pockels cells respectively. By altering the delay between channels B and C, one can produce two optical pulses within a defined time interval; i.e., the Pockels cells act as 'optical gates'. Channel B is delayed by 212μs with respect to T_o and Δt is altered by changing the delay on channel C (212μs + Δt), where Δt is defined as the peak-to-peak separation between both laser pulses (see Figure 3.18). The duration of each of the electronic pulses from channels T_o, A, B and C is determined by subtracting a value programmed into a fifth channel (channel D) from each of their programmed values. Channel D was set at 215μs and the 3μs and 3μs-Δt duration of pulses from channels B and C (the duration of which were unchanged by the amplifier circuitry) were sufficient to trigger the SL404 and SL803 Q-switch circuitry, which required a pulse 2 to 100μs in duration. The inter-laser jitter of ±5ns is recorded using a

photodiode connected to a digital oscilloscope and is due to the jitter in the Q-switch circuitry and the buffer circuit used to convert the TTL pulses to ±14V pulses.

3.2 Picosecond Experimental Facility

3.2.1 System Overview

The laser plasma X-ray laboratory, located within the Lasers for Science Facility (LSF) at the Rutherford Appleton Laboratory (RAL), is a user-facility providing a picosecond soft X-ray laser plasma light source for multi-disciplinary UK and EU scientific research. The high brightness and picosecond duration of soft X-rays emitted from the laser plasma source find application in a wide range of areas such as biochemistry, radiobiology, X-ray microscopy, X-ray microlithography, holography and spectroscopy (Daido et al. 1992, Turcu et al. 1994).

A high density, high temperature X-ray emitting laser plasma is produced using picosecond UV laser pulses generated and amplified in an excimer-based multi-laser system. Synchronisation of each laser within the system, in order to ultimately produce a UV picosecond pulse, is achieved both optically and electronically. A series of fibre optic cables pick up stray laser light following the firing of each laser. Optical signals are converted to electronic signals before feedback to a programmable digital delay generator, which synchronises laser firing. Tape and cylindrical source target materials are mounted in a custom-built target chamber that has a number of access ports to which user experimental equipment is attached. For experiments performed as part of this thesis work, a series of additional vacuum chambers housing a Flat Field Spectrometer (FFS) operating in the XUV/soft X-ray region of 5 to 20nm (240 to 60eV) and a soft X-ray streak camera were attached to the main target chamber. Dispersed line and broadband XUV[4] continuum radiation were recorded photoelectrically using a series of CCD detectors (front-illuminated (image intensified), back illuminated) coupled to a flat field spectrometer. An additional Q-switched nanosecond Nd:YAG laser was integrated into the RAL laser system, and with appropriate electronic synchronisation, permitted temporally resolved DLP 'pump-probe' type experimental investigations of nanosecond plasma species using a picosecond XUV laser plasma continuum source.

[4] XUV is used to refer to the XUV/soft X-ray energy region from 100 to 200eV where RAL emission and photoabsorption studies were performed.

3.2.2 Picosecond Laser System

The RAL picosecond laser system, shown in Figure 3.19, consists of a series of laser and optical components, the combined operation of which ultimately produces a train of UV (248nm) pulses at a repetition rate variable from 0 to 100Hz with a pulse duration of 7ps and a typical pulse energy of ~15 to 20mJ. Three distinct functions are performed within the laser system. These are (i) generation of picosecond laser pulses, (ii) wavelength conversion of picosecond laser light to 248nm and (iii) amplification of picosecond UV laser pulses. The laser system configuration shown in Figure 3.19 and

Figure 3.19 Schematic outline of the laser and optical components comprising the RAL picosecond KrF excimer-based UV laser system

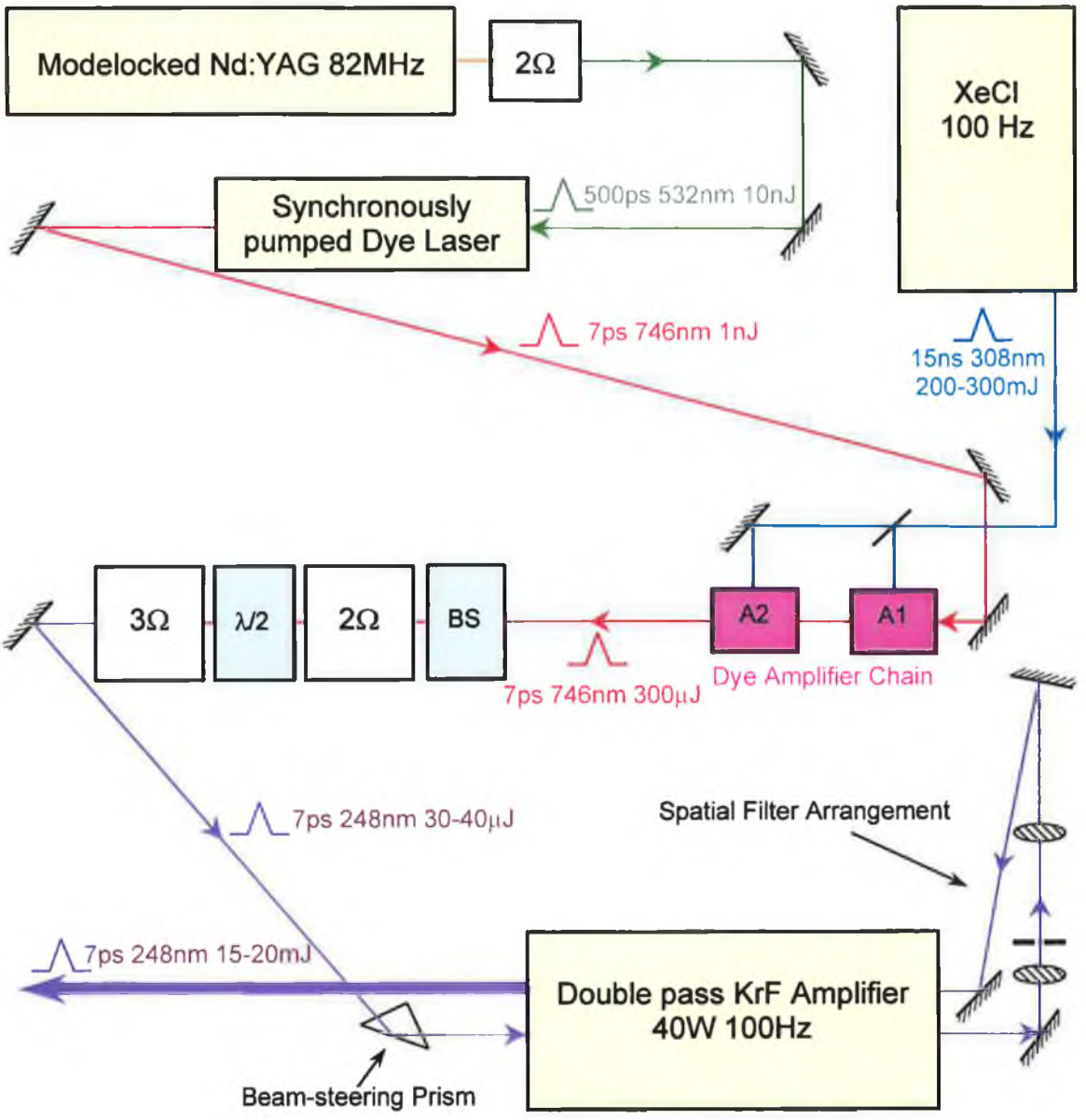

outlined in this section was used in experimental work performed at RAL in 1997. The arrangement and number of excimer lasers used in experimental work in 1995 differs slightly and details of this difference are outlined where appropriate.

A periodic train of 1064nm pulses, each 500ps in duration with an inter-pulse separation of 12ns, is derived from a modelocked Spectra Physics™ Nd:YAG laser operating at a repetition rate of 82MHz. After frequency doubling to 532nm, these pulses are then amplified and converted to 746nm in a synchronously pumped Spectra Physics™-375 dye laser circulating Pyridine 2 to produce shorter 7ps pulses with a pulse energy of ~1nJ. The pulse train is then directed via a series of beam-steering mirrors through two dye amplifiers (A1 and A2) containing the organic dyes Pyridine 2 (A1) and Rhodamine 700 (A2). A Lumonics™ XeCl excimer laser[5] operating at the same repetition frequency as the final KrF excimer amplifier(s) (10Hz in work performed in 1995 & 12Hz in 1997) simultaneously pumps both dye cells with 15ns optical pulses at 308nm (200 to 300mJ per pulse) in order to achieve population inversion within the dye media. The 746nm picosecond pulse train is then input into the dye chain resulting in the amplification of the pulse energy by a factor of 300,000 to ~300μJ per pulse. Only 12 pulses per second of the 82 million produced per second are amplified at this stage. A beam splitter directs a portion of the 746nm beam through a non-linear β Barium Borate Oxide (BBO) crystal where it is of sufficiently high intensity to generate light at 373nm via the second order non-linear process of second harmonic generation. As a result of this process, light at 373nm is 180° out of phase with respect to 746nm light, and is consequently passed through a half wave plate in order to phase match both frequencies. 746nm light (ω) and 373nm light (2ω) then interact in a second BBO crystal via the second order non-linear process of sum frequency mixing (ω + 2ω) to produce UV light at 248nm with a typical pulse energy of 30 to 40μJ. Final pulse amplification is achieved using a single 40W KrF excimer amplifier (Lambda Physik™) in a double pass configuration (1997) or two 40W KrF excimer amplifiers (Lumonic™ and Lambda Physik™) in a single pass configuration (1995). Due to the manifold of upper excited states of the KrF molecule, the broad optical bandwidth of the KrF excimer is ideally suited to short pulse amplification. Two 7ps pulses (separated by 12ns) initially amplified in the dye chain during the 15ns KrF (1995) or XeCl (1997) laser pump cycle, were further amplified during the 20ns KrF excimer pump cycle (running at 10 or

[5] A Questec™ KrF excimer laser at 248nm was used in 1995 to pump the dye amplifier chain.

12Hz), resulting in a final output energy of ~15 to 20mJ per pulse. A spatial filtering arrangement at the back end of the KrF excimer was incorporated into the laser system during 1997 experimental work. Incorporation of pinholes of varying diameter between the plano-convex lenses permitted control of the relative levels of incoherent Amplified Spontaneous Emission (ASE) and picosecond pulse energy coupled to the source target in the final output beam (see Section 4.3.3, Chapter 4). Also, as mentioned earlier, a Quanta Ray™ GCR series Q-switched nanosecond Nd:YAG laser was incorporated into the RAL laser system, thus permitting DLP type studies (1997). The output Nd:YAG pulse at 1064nm had a FWHM of ~10ns with an energy of ~300mJ and was similar to that of the SL404 Nd:YAG laser in DCU.

3.2.2.1 Laser Synchronisation and Timing

As with the nanosecond laser system at the CLPR in DCU, a Stanford Research Systems™ programmable digital delay generator is central to the synchronisation of the RAL picosecond multi-laser system. Firstly, a radio frequency (RF) generator running at 41MHz is used to mode-lock the Spectra Physics™ Nd:YAG laser which, after frequency doubling, is used to pump the Spectra Physics™ dye oscillator. The resulting 746nm pulse train has a repetition frequency of 82MHz, which is twice the RF frequency. This is due to the fact that a 41MHz acoustic standing wave, established (by the RF signal) in an acousto-optic crystal in the Nd:YAG laser cavity, diffracts laser light within the cavity twice during its oscillation period. As a result, modelocked pulses transmitted by the acousto-optic 'shutter' and emerging from the Nd:YAG laser are at 82MHz, twice the frequency of the RF signal. The 41MHz RF signal, which is accurately synchronised to the 746nm pulses, is sent to a divide-down circuit in order to produce a synchronised electronic signal at typically 10 or 12 Hz. This signal constitutes the system master clock and is sent to a Stanford™ digital delay generator. All excimer lasers (XeCl and KrF) within the system run at 10 or 12Hz and are triggered using suitably delayed pulses from the digital delay generator. A series of fibre optic cables pick-up laser light after the firing of each excimer laser. These signals are converted to electronic signals via fast photodiodes and returned to the delay generator, permitting accurate synchronisation of each excimer laser by accounting for possible drift in the internal firing of these lasers. The propagation speeds of light in air (~0.3m/ns) and in

the glass core of a fibre (~0.2m/ns) are accounted for when deciding on suitable inter-pulse delays to be chosen for each output channel of the Stanford™ delay generator. The final KrF excimer laser (or lasers) fires 30 to 40ns after the XeCl laser, depending on the optical path length through air between the laser heads. For DLP experimental studies (1997), the Quanta Ray™ Nd:YAG laser was fired at a repetition rate of 12Hz using a signal from the Stanford™ delay generator. Δt, the inter pulse delay between the KrF and Nd:YAG laser pulses, was varied by simply changing the programmable delay on the relevant output channel of the Stanford™ delay generator.

3.2.3 5.6m Grazing Incidence (XUV) Flat Field Spectrometer Experiment

3.2.3.1 System Overview

3.2.3.1.1 Picosecond XUV Emission Studies

XUV spectroscopic emission studies of low to high-Z picosecond laser plasma sources were performed at RAL (1995) using the grazing incidence spectrometer-based system shown in Figure 3.20. A 5.6m grazing incidence flat field spectrometer (from the Queens University of Belfast) was vacuum coupled to a cylindrical RAL target chamber (see Figure 3.28) in order to view plasma light at 45° with respect to the target normal. The flat focal plane of the vari-spaced ruled grating, mounted within the flat field spectrometer, facilitated accurate and speedy alignment of the grating and detector. The entire spectrometer was housed in a custom built cylindrical vacuum chamber, onto which an Andor Technology™ EEV 15-11 CCD detector was attached. A pair of gold mirrors, orientated at a grazing angle of 8° and located between the laser plasma source and the grating, served as a double reflection low pass filter. Consequently, photons possessing an energy in excess of 300eV were effectively eliminated. A two-dimensional CCD detector was used to record XUV spectra and was displaced vertically (z-direction) in order to scan across dispersed spectral light at the spectrometer focal plane. Positioning of the detector was performed by hand when the spectrometer chamber was vented to atmospheric pressure.

Figure 3.20: 5.6 metre grazing incidence spectrometer-based system for recording of time integrated picosecond XUV emission spectra of low to high-Z laser produced plasmas

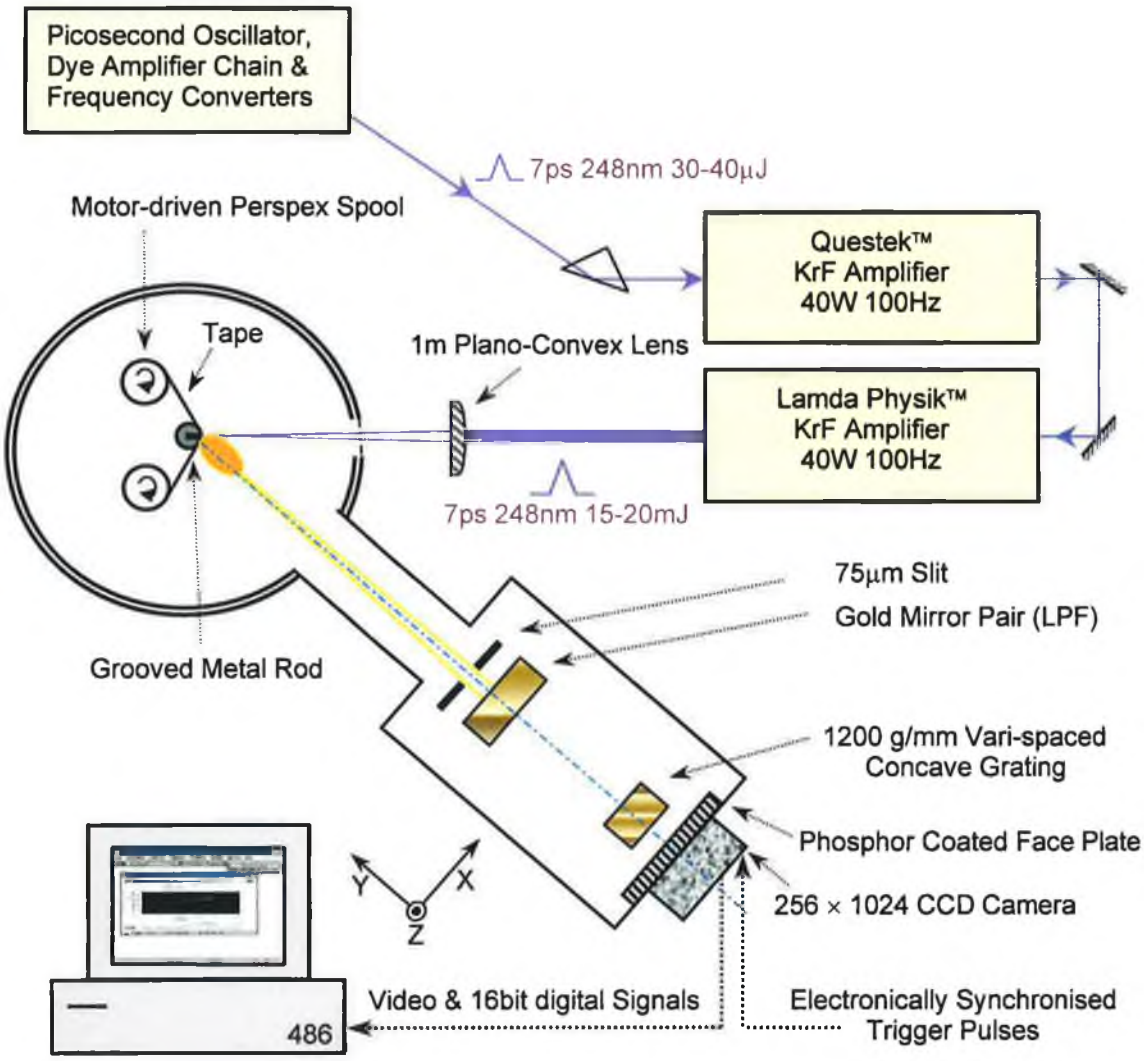

The Andor Technology™ CCD camera recorded visible photons produced when dispersed XUV photons were incident on a phosphor coated fibre optic faceplate coupled to the front surface of the CCD array. CCD integration was initiated when an electronic pulse derived from the excimer laser arrived at the camera control unit. The analog video signal integrated by the CCD array during an exposure was then digitised by a 16bit analog-to-digital converter (0 to 65,536 dynamic range) in the camera control unit before being relayed to a 486 PC via an Andor Technology™ interface card for display and manipulation within the Andor Technology™ *Instaspec* software package.

All source target materials were mounted in a cylindrical stainless steel chamber (50cm in diameter, 60cm high) that could be vacuum-isolated from the spectrometer chamber

via a gate valve. Separate turbo pumps, backed by rotary pumping lines, were attached to both target and spectrometer chambers. Typical system pressures of ~5×10^{-5} mbar were achieved when the gate valve was opened to permit pressure equalisation of both chambers.

The 7ps, 248nm, 15-20mJ laser pulses, amplified in single pass mode in a pair of KrF excimer amplifiers, were focused using a 1m *f*/10 plano-convex quartz glass lens to an irradiance of ~10^{13} W/cm^2 onto both continuously moving tape and rotating cylindrical targets. The motor-driven tape drive mechanism consisted of two circular Perspex spools (diameter=50mm) separated by ~10cm (Figure 3.20). Metallic and polymer tape targets (4mm wide, ~50μm thick and several metres long) were wound onto each spool and threaded around a grooved metal rod located between both spools. The metal rod served to prevent vertical (z-direction) slipping of the tape thus ensuring the continuously moving tape always remained at the laser focus. With most tape materials, except for that of tungsten, the laser drilled a hole through the tape. A horizontal slot machined though the top of the rod behind the laser focus prevented rod material being exposed to incident laser light and possible plasma generation at the rod surface. The entire spool and rod arrangement could be moved in all three dimensions (via a series of motors) for accurate positioning of tape materials at the laser focus (see Figure 3.20). The speed of the tape could be adjusted in accordance with the laser repetition rate and a typical speed of 1 to 2 cm/sec was chosen for a laser repetition rate of 10Hz. Experiments performed by Turcu et al. (1993) using an X-ray pinhole camera to view the laser plasma source concluded that the position of the laser focal spot only drifts by less than ± 2μm from shot-to-shot. The tape width of 4mm was sufficient to ensure that the tape material did not break and fitted the modified cassette tape drive mechanism, which formed the core of the target drive system.

Cylindrical rod target materials were connected to a motor driven rotating mount. This mount was also capable of vertical (z-direction) motion, thus permitting a helical motion of the target rod surface. A CCD camera operating in the visible region (with a microscope objective attached to its front face) and mounted at one of the viewing ports located at the side of the cylindrical target chamber was used to view the rotating target rod. The position of target rods held in the rotating mount was adjusted in order to minimise the degree of precession that was observed on a video screen connected to the CCD camera head.

The experimental system shown in Figure 3.20 was subsequently adapted (1997) in order to permit DLP-type photoabsorption studies. Details of this modification and overall system changes are outlined in the following section.

3.2.3.1.2 Picosecond XUV-DLP Photoabsorption Studies

The XUV grazing incidence spectrometer-based system used to record time integrated XUV emission spectra (Figure 3.20), was adapted in order to facilitate XUV DLP photoabsorption studies by replacing the RAL cylindrical target chamber with the DCU 1m target chamber cube (Figure 3.21 and 3.22). As previously mentioned in Section 3.1.3.3 the 1m target chamber (Figure 3.8) can accommodate the mounting of two target materials separated by a maximum distance of 47mm. DLP studies performed at RAL focused on the evolution of the relative populations of atomic and ionic species in a thorium plasma plume with sub-nanosecond time resolution. Planar thorium targets (20mm×6mm×1mm) were mounted (as in DCU) in the x-y-z target holder/manipulator and a cylindrical tungsten rod target (ϕ=10mm) was placed in one of the target holders mounted on top of the target chamber cube (see Section 3.1.3.3.1 for a description of target holders). The flange used to attach a BK7 glass window (ϕ=95mm) to the side of the target chamber cube was replaced with a custom-built flange designed to hold two circular windows (ϕ=30mm). These were a BK7 window and a UV grade silica window with good transmission of 1064nm and 248nm laser light respectively. Two plano-convex lenses manufactured from the same two materials were used for focusing the 1064nm (135mm *f*/5) and 248nm (125mm *f*/5) laser pulses (Figure 3.21).

The 7ps, 248nm, 15-20mJ UV pulses, amplified in double pass mode in a single KrF excimer amplifier, were focused to an irradiance of ~10^{13} W/cm^2 onto the cylindrical tungsten surface to produce a laser plasma emitting in the XUV on a picosecond time scale. The Q-switched Nd:YAG laser shown in Figure 3.21 was incorporated into the RAL laser system and its 10ns, 1064nm, ~300mJ pulses were focused to an irradiance of ~10^{11} W/cm^2 onto the surface of planar thorium targets to produce an absorbing plasma plume. The 248nm pulse was synchronised to the Pockels cell of the Nd:YAG laser and a Stanford™ DG535 delay generator was used to insert the delay, Δt, between

Figure 3.21 *5.6 metre grazing incidence spectrometer-based system for recording of picosecond XUV DLP photoabsorption spectra of atomic and ionic laser plasma species*

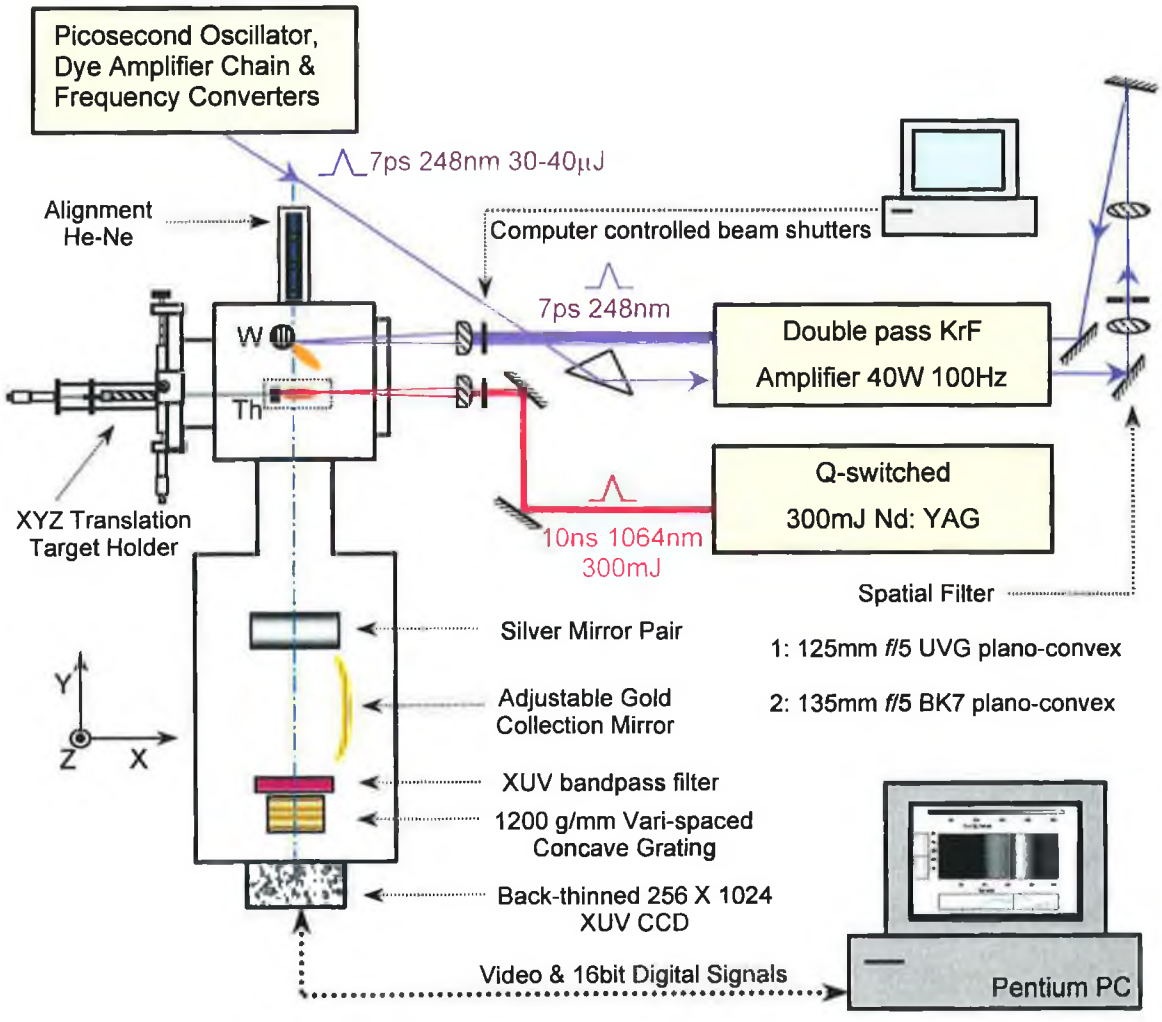

Figure 3.22 *Photograph of picosecond XUV DLP experimental set-up at RAL*

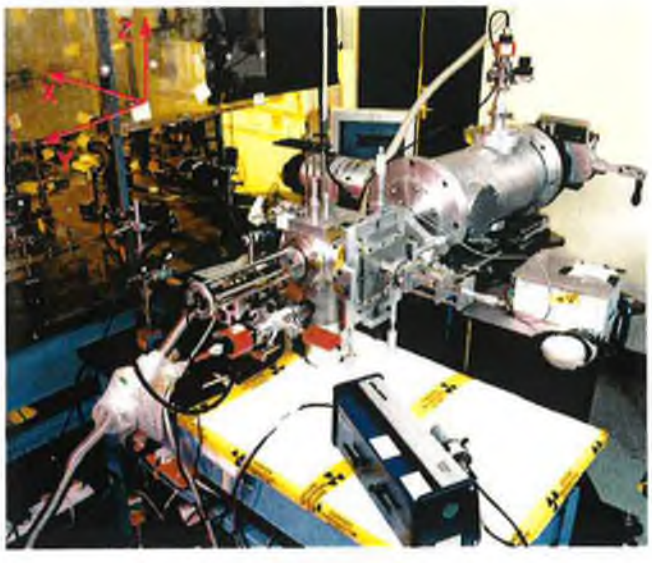

both laser pulses. Also, a Pockels cell was incorporated into the RAL laser system after the dye amplifier chain and before the frequency converting crystals (see Figure 3.19) in order to select only one of the two pulses (separated by 12ns) amplified during the 20ns pump cycle of the XeCl excimer laser pumping the dye amplifier chain. The XeCl and KrF excimer lasers were operated at a repetition rate of 12Hz during DLP experiments. Two computer controlled electro-mechanical beam shutters were opened simultaneously for a programmable period of time in order allow a pre-determined number of laser shots to reach the target materials.

As with the experimental system used to measure time integrated XUV emission spectra, a 5.6m grazing incidence flat field spectrometer was again used to disperse XUV light in the 5 to 20nm (240 to 60eV) region. However, light incident on the grating was confined to an XUV transmission window of typically 100 to 200eV. This was achieved by inserting a silver mirror pair and an XUV thin film transmission filter into the spectrometer. The combined operation of both of these components provided filtering action at visible, VUV and hard X-ray photon energies[6]. An adjustable cylindrical gold collection mirror (160mm long, 10mm wide) was added to the spectrometer system between the filtering elements (Figure 3.21) in order to increase the XUV flux incident on the vari-spaced ruled grating and ultimately dispersed along the spectrometer focal plane. A back-thinned 256 × 1024 pixel Andor Technology™ (DO420-BN) CCD was used for direct recording of XUV photons without the need for conversion to visible wavelengths and the corresponding fibre-optic coupling required. Further details on the Andor Technology™ CCD systems (front-illuminated and back-illuminated) used in this work and their influence on the spectrometer spectral resolution and overall performance are outlined in Section 3.2.3.3.1.

[6] Calculations to obtain the individual transmission characteristics of the of the silver/gold mirror pair, thin films of different materials and thickness and the XUV transmission window resulting from the combination of these two filtering elements are outlined in Chapter 4, Section 4.2.1 (FFS emission studies) and Section 4.2.6 (FFS absorption studies)

3.2.3.2 5.6m Grazing Incidence Flat Field Spectrometer

Central to the operation of the flat field spectrometer, used for both XUV emission and XUV DLP photoabsorption experiments, is a spherical concave grating with vari-spaced grooves. As with conventional spectroscopic instruments operating in the XUV region, light is incident on the grating at grazing angles of incidence thus giving rise to the associated problems of astigmatism and other aberrations at the focal plane of the grating. Since the time of Rowland, concave gratings have been ruled with straight, parallel and equi-spaced grooves resulting in a curved focal plane. As a result, cylindrical photographic films or detector carriages designed to accurately traverse along the Rowland circle of the grating have been required. However, since the 1970's, concave gratings with curved and vari-spaced rulings have been produced both holographically and mechanically. The resulting aberrations differ dramatically from those of conventionally ruled gratings (Choi et al. 1997). In particular, the meridional imaging property is such that the curved focal field associated with an equi-spaced grating is flattened and diffracted rays are therefore focused onto a plane that is flat and nearly normal to these rays (Harada & Kita 1980). Such focusing conditions are ideal for the speedy and accurate location of a flat photographic plate or a photoelectric detector array. As with a conventionally ruled concave grating, reduced focusing in the sagittal plane of the vari-spaced concave grating results in astigmatic imaging of a point source. The use of a separate toroidal coupling optic or a toroidal grating can reduce the effect of this aberration and therefore enable stigmatic or quasi-stigmatic imaging (Nakano et al. 1984, Choi et al. 1997). A toroidal mirror was not inserted into the spectrometer system used in these studies due to the associated difficulty involved in accurate alignment of the entrance slit, mirror and grating.

The spectrometer was operated in two different modes, one employing an entrance slit and the second with the entrance slit removed. Studies without the entrance slit improved throughput and yielded increased single shot sensitivity. The addition of a 75μm entrance slit located between the laser plasma source and the grating permitted higher resolution studies of XUV line and continuum emission from low and high-Z target materials respectively. Plasma light of photon energy >300eV was almost eliminated upon double reflection from the gold (1995) / silver (1997) mirror pair oriented at a grazing incidence angle of 8°/10° with respect to incident laser plasma radiation. In this configuration the mirror pair behaved as an optical low pass filter

(LPF). Due to the parallel alignment of the planar mirrors (30mm×20mm×5mm) separated by 1.5mm, emergent light was parallel to incident light but displaced vertically (z-direction) by ~1.5mm (see Figure 4.1, Section 4.2.1 Chapter 4). The position of the grating was adjusted vertically in order to coincide with the relocation of the system optic axis.

3.2.3.2.1 Hitachi™ Diffraction Grating

The Hitachi™ spherical concave diffraction grating used during the RAL experiments is the same as that used by Kita and co-workers (1983) in an XUV grazing incidence spectrograph system. The grating is 30mm long (y-direction) and 50mm wide (x-direction) in the direction of the groove ruling (Figure 3.23). Its curved, variable spacing grooves are produced mechanically on a gold-coated surface with a nominal groove ruling of 1200 grooves/mm. The groove spacing varies from 0.69 to 0.99μm over the ruled length of 30mm. The groove spacing σ (in mm) at position ω (the distance in mm from the grating centre along the y-axis of Figure 3.23) is calculated using

$$\sigma = \sigma_o \Big/ \left(1 + \frac{2b_2}{R}\omega + \frac{3b_3}{R^2}\omega^2 + \frac{4b_4}{R^3}\omega^3 \right) \tag{3.12}$$

where σ_o is the nominal groove spacing (in mm), R is the radius of curvature of the grating (in mm) and b_2, b_3 and b_4 are unit-less vari-spacing ruling parameters which ultimately influence the aberrations at the focal plane of the concave grating (Kita et al. 1983). b_2 is chosen in order to obtain a flat focal field whereas b_3 and b_4 determine the importance of higher order aberrations (e.g. coma-type aberrations).

The surface of the grating is blazed at an angle of 3.2°, resulting in a maximum conversion efficiency of incident radiant flux into first order light at 10nm. The radius of curvature (R) of the spherical concave profile of the gratings front face is 5649mm (~5.6m). The grating was held in a motor driven mount within the spectrometer, which yielded a linear motion in the z direction and an angular adjustment about the grating centre.

Figure 3.23 *Schematic overview of the positioning of the vari-spaced spherical concave diffraction grating, the entrance slit and the detector (at the focal plane) within the 5.6m flat field spectrometer (all dimensions in mm)*

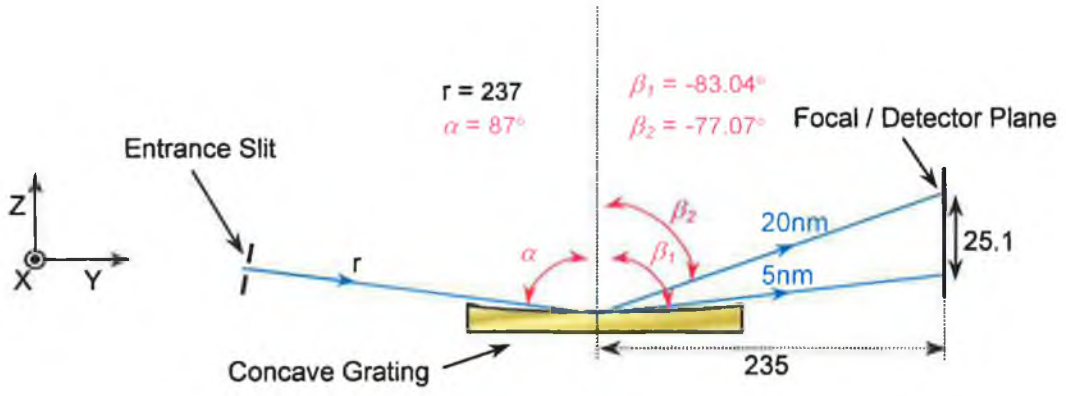

3.2.3.3 Performance of the 5.6m Grazing Incidence Flat Field Spectrometer System

The concave grating was mounted in the horizontal (x-y) plane and light was dispersed along a focal plane in the vertical z-direction. The orientation and position of the focal plane depended on the angle at which light was incident on the grating (α). A range of focal curves calculated by Kita and co-workers (1983) for the grating used in this work is shown in Figure 3.24 for different values of α. A value of α = 87° was used throughout RAL experiments and the corresponding angles of diffraction (β_1 and β_2) and the slit-grating-detector distances are shown in Figure 3.23. Between 30 and 75mm (along the z direction) in Figure 3.24, the 87° focal curve is ~linear corresponding to focusing of dispersed light in the vertical (z-x) plane.

Diffraction of XUV wavelengths (λ) by the vari-spaced spherical concave grating is described using the grating equation

$$m\lambda = \sigma_o(\sin\alpha + \sin\beta) \tag{3.13}$$

where m is the spectral order, α is the angle of incidence and β is the angle of diffraction determined using

$$L = -235\cot\beta \tag{3.14}$$

Figure 3.24: Calculated focal curves for various angles of incidence (α) subtended at the centre of the Hitachi™ vari-spaced concave grating with σ_o=1200 grooves/mm (from Kita et al. 1983)

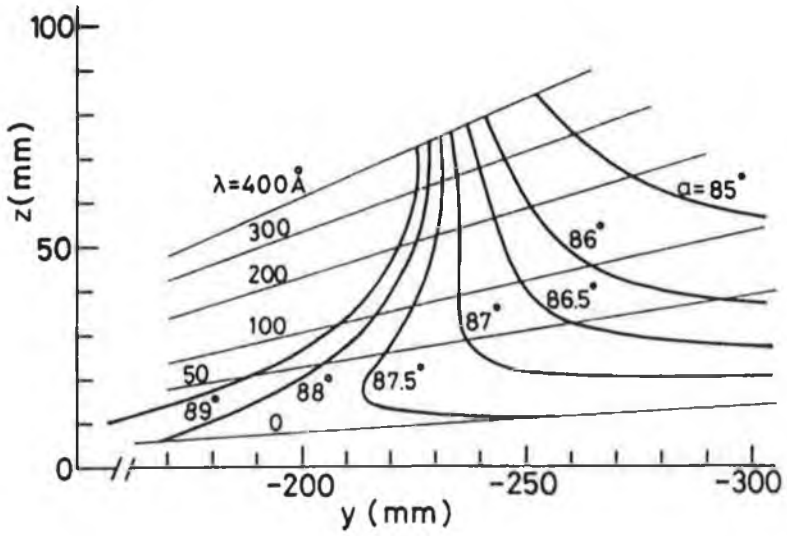

where L (in mm) is the vertical distance of the spectral image from the y-axis (Kita et al. 1983). For the Hitachi™ grating used in this work the reciprocal linear dispersion $d\lambda / dl$ was calculated (using 3.15 and 3.16) to vary from 0.43 to 0.77 nm/mm over the grating's 5 to 20nm wavelength range, which was dispersed over a distance of 25.1mm (see Figure 3.23).

3.2.3.3.1 Resolution with Front- and Back-Illuminated CCD Detector Systems

The front illuminated Andor Technology™ EEV 15-11 CCD, used for XUV emission experiments (1995), has a 1024 × 256 pixel array with a 27 × 27μm pixel size. A rare earth phosphor scintillator coating on a 150 × 70mm fibre optic faceplate with a 6μm channel diameter, was butt coupled to an integral fibre optic faceplate on the front surface of the CCD. The magnification of the system from the scintillator to the CCD front face is ×1. The 27.6mm (1024 × 27μm) length of the detector covered a spectral region from 6 to 23nm (206 to 54eV). Figure 3.25 shows a Mylar® ($C_{10}H_8O_4$) plasma emission spectrum recorded in this region using a 75μm entrance slit located 237mm from the grating centre. The Mylar® plasma was produced when a 1m focal length plano-convex lens focused ~10mJ, 7ps, 248nm pulses onto a cylindrical target. The

laser repetition rate was 10Hz and the detector integration time of 50 seconds resulted in the accumulation of plasma light from 1000 laser shots (2×7ps pulses per KrF cycle). The spectrum in Figure 3.25 was obtained by vertically binning and then summing six independent CCD images recorded at -25°C. A series of spectral lines at 7nm illustrate the system spectral resolution. The detector region from pixel 85 to 118 covers a wavelength range from 7.21 to 7.66nm within which eight emission lines from six and seven times ionised oxygen lie. The peak of one O VII line at 7.3900nm falls at pixel 99 (Line No.3). The higher wavelength peak shown in the inset of Figure 3.25, again a

Figure 3.25: 6000 shot integrated Mylar® XUV emission spectrum (~ 6 to 23nm) recorded using a front-illuminated fibre-optically coupled CCD detector system

Line	Wavelength (nm)	
1	6.2005	O VIII
2	6.7725	O VIII
	6.7789	O VIII
3	7.3900	O VII
4	7.7695	O VII
5	8.1914	O VII
6	8.6100	O VII
7	9.1078	O VII
8	9.3915	O VI
9	9.5082	O VI
10	10.5413	C VI
	10.5463	C VI
11	11.3842	C VI
	11.3899	C VI
12	13.4473	O V
13	14.2122	O V
14	14.4837	O V
15	17.5670	C V

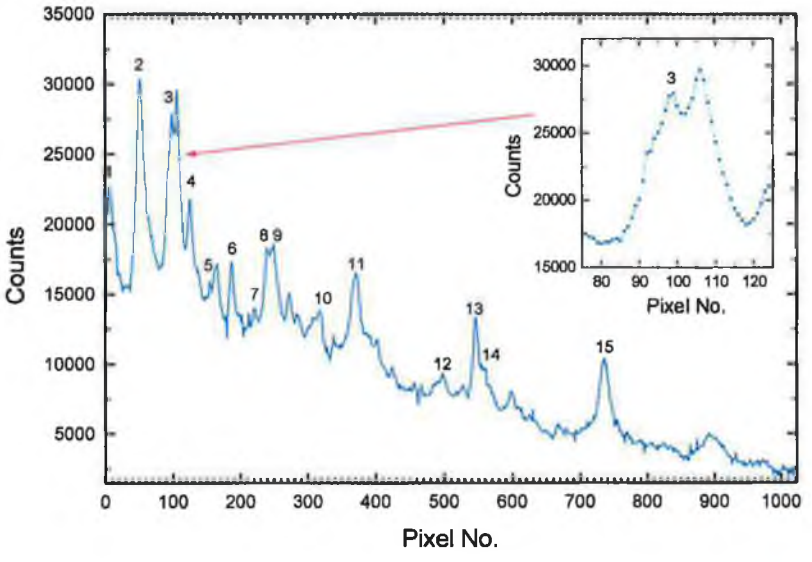

convolution of several spectral lines, does not fall at the wavelength of any particular oxygen transition. The wavelength value at this peak, which is just resolved with respect to peak no. 3 over seven pixels, is 7.4973nm. The system spectral resolution ($\lambda/\Delta\lambda$) is at best ~82 for a reciprocal linear dispersion of 0.4985nm/mm corresponding to 0.0130nm/pixel at 7.5nm (with $\alpha = 87°$). The spectral resolution, as determined by the Nyquist spatial frequency of the front-illuminated CCD detector, varies from ~64 to 185 over the 5 to 20nm wavelength range of the flat field spectrometer system.

The 1024×256 pixel back-thinned surface of the Andor Technology™ DO420-BN CCD used for DLP photoabsorption studies (1997) was placed directly at the focal plane of

the flat field spectrometer. The 26.6mm (1024 × 26μm) length of the detector covered the entire spectral region of 5 to 20nm (240 to 60eV) dispersed by the grating. Of particular experimental interest within this spectral region was the wavelength interval from 8 to 16nm (155 to 75eV) where the thorium 5d photoabsorption spectrum resides. Figure 3.26 shows an aluminium emission spectrum recorded in this region. The aluminium plasma was produced when a 125mm focal length plano-convex lens focused ~16mJ, 7ps, 248nm pulses onto a cylindrical target. The laser repetition rate was 12Hz and the electro-mechanical shutter in front of the KrF laser output was opened for 5 seconds resulting in the integration of plasma light from 60 laser shots (1×7ps pulse per KrF cycle due to the presence of the Pockels cell pulse picker used in this later experiment). The spectrum in Figure 3.26 was obtained by vertically binning (over 10 pixels) the CCD image. The spectral intensity falls off below 8nm and above 14nm due to the XUV transmission filter (see Chapter 4, Section 4.2.6 for further details).

Figure 3.26 *60 shot aluminium XUV emission spectrum (~ 8 to 16nm) recorded using a back-thinned CCD detector system*

Line	Wavelength (nm)	
1	8.5515	Al VI
2	9.0858	Al VI
3	9.2875	Al VI
4	9.5624	Al VI
5	9.9260	Al V
6	10.0616	Al VI
7	10.4047	Al VI
8	10.7620	Al VI
9	11.1589	Al IV
10	11.8497	Al V
11	12.4030	Al IV
12	12.4550	Al IV
13	12.5529	Al V
14	12.6068	Al V
15	13.0411	Al V
16	13.1438	Al V
17	13.5523	O V
18	16.0074	Al IV
19	16.1688	Al IV

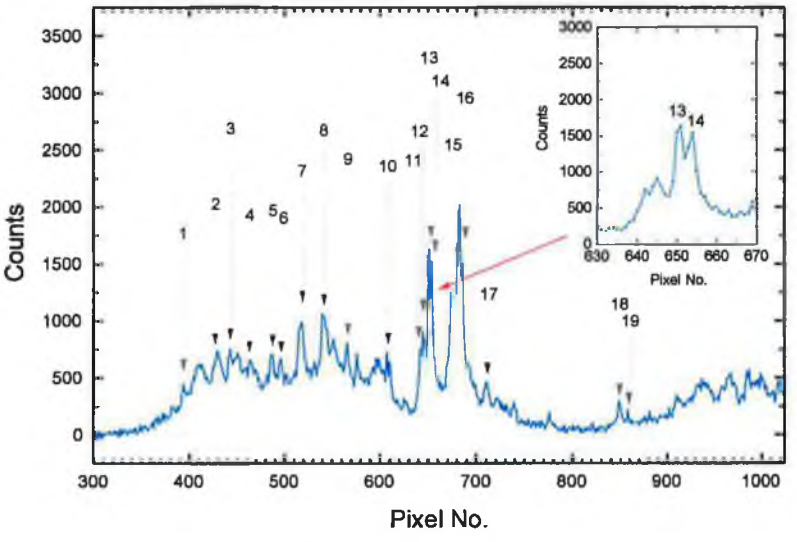

The minimum resolvable wavelength interval $\Delta\lambda$ was determined using two closely spaced Al V lines at 12.5529nm and 12.6068nm which were just resolved. The reciprocal linear dispersion of the Hitachi™ grating at 12.5nm (for α = 87°) is 0.625nm/mm, corresponding to 0.016nm/pixel. The wavelength separation between the

two Al V lines was 0.054nm, corresponding to three to four pixel spacings. From Figure 3.26 it can been seen that both Al V lines are resolved over three to four pixels and so the spectral resolution ($\lambda/\Delta\lambda$) at 12.5nm (99eV) is ~220. The spectral resolution, as determined by the back-illuminated CCD detector, varies from ~130 to 320 over the 5 to 20nm wavelength range of the flat field spectrometer system. In summary, direct recording of XUV photons at the CCD surface, thus eliminating the need for fibre-optic coupling of optical photons, serves to increase the flat field spectrometer spectral resolution by approximately a factor of two.

3.2.4 Picosecond XUV Streak Camera

3.2.4.1 System Overview

The XUV streak camera-based system shown in Figure 3.27 and Figure 3.28 was used to perform time resolved measurements of the intensity of broadband XUV continuum (~100 to 200eV) emitted from a series of high-Z picosecond plasmas. The high temporal resolution, dynamic range and sensitivity of XUV/soft X-ray streak camera devices have resulted in their increasing application to studies designed to probe high density, high temperature laser plasmas emitting XUV/soft X-rays on a picosecond time scale (Murnane et al. 1989a,b, 1990, Cobble et al. 1992, Shepherd et al. 1995). Studies utilising streak camera technology include inertial confinement fusion, x-ray laser research and radiation confinement research (Tsakiris and references therein, 1990).

A Kentech Instruments™ low magnification XUV streak camera system was vacuum coupled to the RAL cylindrical target chamber and used in this work to perform time resolved but spectrally and spatially integrated XUV emission studies. As with XUV spectroscopic studies, laser plasmas were produced by irradiation of tape and rod targets with 7ps, 248nm, ~15 to 20mJ laser pulses. A 35cm focal length plano-convex lens focused laser light to an on-target irradiance of ~10^{13} W/cm^2.

Figure 3.27: Streak camera-based experimental system for recording the duration of picosecond XUV continuum emitted from high-Z plasmas

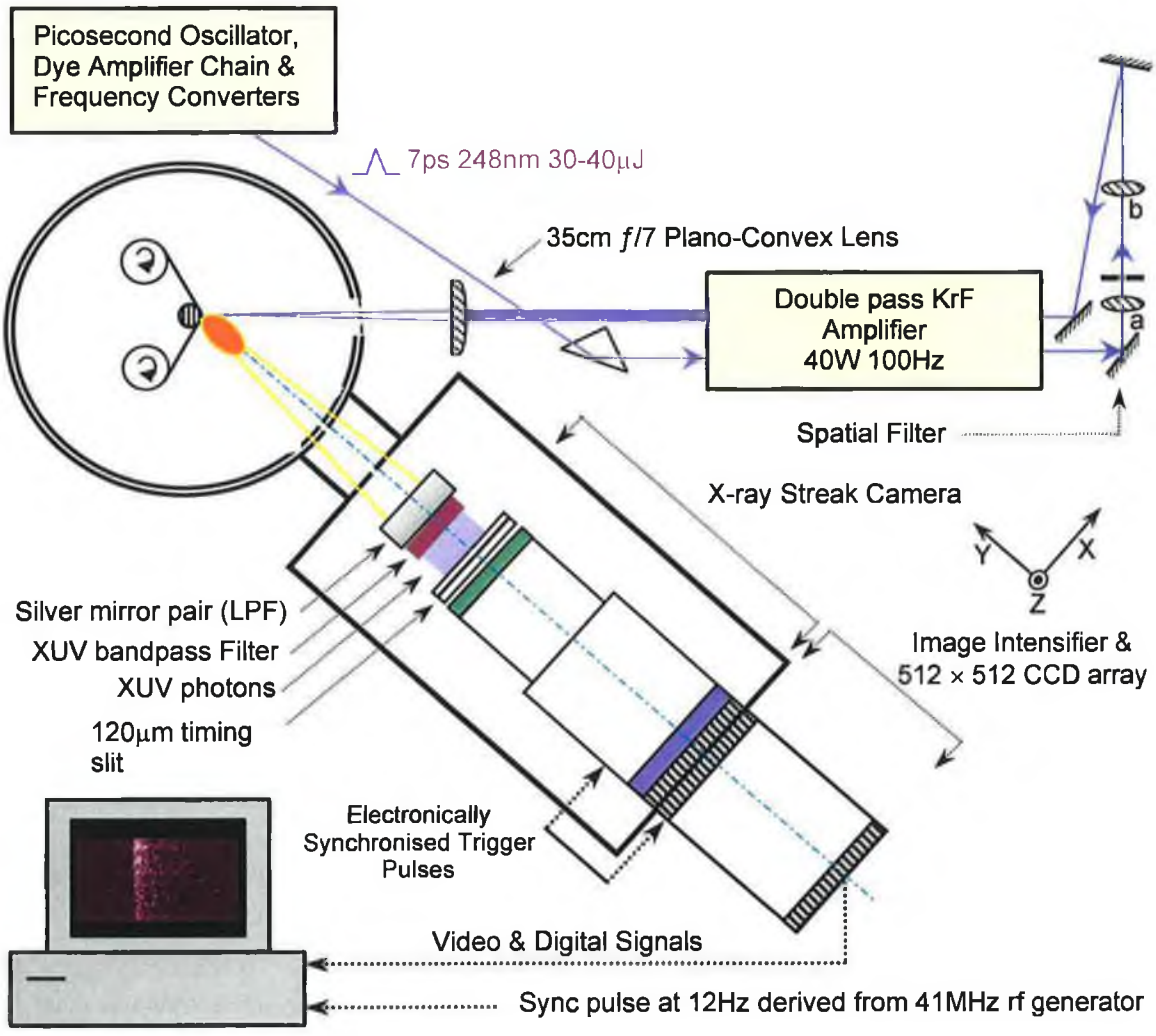

Figure 3.28: Photograph of streak camera system coupled to the RAL target chamber

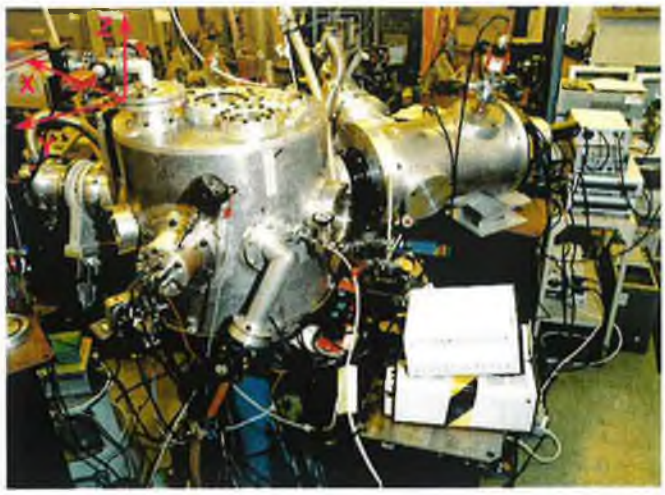

The streak camera head was mounted within a custom built vacuum chamber and the distance from the laser plasma source to the camera front-end (timing slit) was ~900mm. Vacuum pressure within both target and streak camera chambers was maintained at ~1.5×10^{-5} mbar using a liquid nitrogen cold finger and separate turbo and rotary pumping systems attached to each chamber. The presence of electron focusing optics in the streak camera head imposed a maximum pressure requirement of 1.3×10^{-4} mbar and a trip switch was used to cut power to the camera head in the event of a breach in vacuum pressure.

A silver mirror pair, operating at a grazing incidence angle of 10° and placed along the optic axis between the plasma source and the streak camera, was again used to eliminate radiation above 300eV. A thin film filter defined an XUV transmission window, as in XUV-DLP spectroscopic studies, which ranged from approximately 100 to 200eV.

Streaked images (at visible photon energies) emerging from a fibre optic faceplate at the back end of the streak camera were amplified using a Photonic Science™ 'Dark Star' optical image intensifier. Visible images amplified by the 'Dark Star' were readout as a video signal from an integral fibre optically coupled front illuminated 512 × 512 pixel CCD array. Triggering of the streak camera sweep circuitry in order to initiate recording of a streaked image was achieved electronically using a 12Hz signal derived from the 41MHz RF generator which arrived 3μs before the 20ns KrF trigger pulse.

The spatial filtering arrangement located at the back-end of the final KrF amplifier in Figure 3.27 was inserted during streak camera measurements in order to control the amount of incoherent nanosecond ASE laser radiation transmitted to the target surface (see Section 4.3.3 Chapter 4 for explanation). This permitted investigation of the influence of varying levels of ASE pulse energy and picosecond laser pulse energy on the duration of XUV continuum emitted from high-Z laser plasmas. Different spatial filtering configurations used during experimental investigations are detailed in Section 4.3.3 Chapter 4.

3.2.4.2 Kentech™ XUV Streak Camera System

3.2.4.2.1 Operating Principles and System Specifications

Following plasma production, XUV photons emerging from the silver mirror pair and thin film transmission filter combination are incident on a slit (known as the timing slit) located at the front end of the streak camera head. Ultimately, an image of this slit is swept across the final image plane of the streak camera so that temporal variations in XUV intensity at the slit are recorded as a spatial distribution along an axis (x axis in Figure 3.27) perpendicular to that of the timing slit (z axis). XUV photons are converted to electrons using a photocathode located after the timing slit. The electron bunch has a temporal intensity distribution similar to that of the incident XUV photons and is swept across a phosphor screen at the image plane under the influence of a voltage ramp.

In this work, a caesium iodide (CsI) photocathode (25mm in length) deposited on a 0.1μm Formvar® ($C_5H_7O_2$) substrate was used with a 120μm timing slit width. The photocathode was biased at –15kV with respect to a grounded anode slit, towards which the electron bunch is accelerated. Additional acceleration of the electron bunch is achieved using an extraction mesh structure biased at –10.9kV and located between the photocathode and anode. Without the increase in electron velocities provided by the mesh structure, the thermal spread in electron energies would dominate the spread in transit times from the photocathode to the phosphor screen and would consequently destroy the camera's temporal resolution. A series of electron optics also negatively biased at –11.5kV and located between the mesh and anode serves to focus the electron bunch. After emerging from the anode gap, the electron bunch passes between a pair of oppositely biased deflection plates to which a linear ramp potential is applied. The potential of the negatively and positively biased deflection plates is ramped to +1.7kV and –1.7kV respectively. The slope of these ramped potentials determines the sweep rate which, for the Kentech™ steak camera, varies from approximately 50 to 900ps/mm. After emerging from the deflection plates, the streaked (swept) electron bunch strikes a P20 phosphor coated onto a 48mm diameter fibre optic faceplate. The active area of the faceplate is 40mm in diameter and the steak camera operates as a low magnification (×1.2) device, which images electrons produced over the 25mm length of the photocathode onto 40mm of the phosphor. A few tens of photons at visible wavelengths are produced for each electron incident on the phosphor. These photons propagate down

the 5μm diameter fibre channels of the glass faceplate which is in turn butt coupled to the fibre optic faceplate of the Photonic Science™ 'Dark Star' visible image intensifier.

3.2.4.2.2 Photonic Science™ Image Intensified CCD Detector

The 'Dark Star' image intensifier amplifies low light visible signals through the combined action of a photocathode coated on an MCP structure and a phosphor coated fibre optic bundle fused to the front face of the 512 × 512 pixel CCD array. The S25 photocathode has optimum sensitivity at blue/green wavelengths with its spectral response extending from 400 to 900nm. Photoelectrons emerging from the photocathode are accelerated towards the phosphor coated fibre optic bundle, which is tapered down to the 9.7 × 9.7mm area of the CCD array (19μm pixel size). The gain of the intensifier is manually adjustable over a 100:1 range using a control voltage from –3V (minimum gain) to +3V (maximum gain). The gain varies nonlinearly with voltage. The video signal from the CCD can also be amplified within a camera control unit using a manual gain that is variable over a 10:1 range. During experiments, video signals from the camera control unit were digitised (8 bit) and captured for display and manipulation using a frame grabber hardware/software package (from Oxford Framestore Applications™) and a 486 PC.

3.2.4.2.3 Performance and Temporal Resolution of Combined Streak Camera and Image Intensifier Detector System

The temporal resolution with which measurements of picosecond XUV emission durations were made was determined by the combined operation of both the Kentech™ streak camera and the Photonic Science™ image intensifier. The temporal resolution of the combined detector system results from the convolution of a number of factors within each individual detector. Factors contributing to temporal broadening of the instrument response function of the streak camera system are as follows. Firstly the non-swept (static) image of the streak camera timing slit has a finite width (Δx) when imaged at the

streak camera phosphor. The contribution of the static image (t_{static}) to the instrument time resolution can be approximated using ($t_{static} = \Delta x/v$), where v is the camera sweep speed (Murnane et al. 1990). It therefore follows that high sweep speeds serve to reduce the magnitude of t_{static}. A second contribution to the streak camera time resolution is due to the energy distribution of photoelectrons emitted by the photocathode. This results in different electron traversal times through the electron accelerating/focusing optics and so a temporal elongation of the electron bunch (t_{pc}). Space charge effects such as inter-electron Colombic repulsion also lead to additional elongation of the electron bunch. Other instrumental factors contributing to broadening of the streak camera temporal response function include aberrations in the electron optics, the finite size of the sweep plates and stray magnetic fields. The collective contribution of these factors is termed t_{other}. The total streak camera instrument temporal response function (t_{inst}) is therefore given by (Murnane et al. 1989)

$$t_{inst} = \sqrt{(t_{static})^2 + (t_{pc})^2 + (t_{other})^2} \tag{3.15}$$

The response of the streak camera to a given transient x-ray emission event (t_{meas}) is a combination of the streak camera response function (t_{inst}) and the actual emission duration ($t_{x\text{-}ray}$), assuming Gaussian pulse profiles,

$$t_{meas} = \sqrt{(t_{inst})^2 + (t_{x-ray})^2} \tag{3.16}$$

The image intensifier contains a photocathode element similar to that of the streak camera. The effect of this element in contributing to the temporal instrument response function of the image intensifier is similar to that outlined above for the streak camera. The MCP structure is directly coupled to the phosphor coated tapered fibre optic bundle and so broadening of electron bunches upon acceleration across a gap region (as in a CEMA) is eliminated. Factors such as shear distortion of the tapered fibre optic conduit coupled to the CCD front surface can also contribute to broadening of the instrument response function.

During experiments, the static (non-swept) image of the timing slit as imaged by the streak camera-image intensifier system was measured (t_{static}) as an approximation to the total temporal response function of the combined system. Ideally the total temporal response function (t_{inst}) could be measured using a short pulse (typically a few hundred femtoseconds), whose duration is shorter than any of the various mechanisms responsible for temporal broadening within each of the detectors. The measured static response function on the combined detector system is shown in Figure 3.29. The XUV

flux emitted from a gold laser produced plasma and incident on the timing slit of the streak camera remained approximately constant[7]. Gold plasmas were produced when 15 to 20mJ, 7ps, 248nm laser pulses were focused to an irradiance of ~10^{13} W/cm^2 on a gold tape target using a 35cm focal length *f*/7 plano-convex lens. The ultimate signal integrated by the CCD detector increases non-linearly with increased intensifier gain, which is adjustable over a scale of 1 to 10. In the inset of Figure 3.29 all static response functions are normalised, thus showing a corresponding non-linear increase in width with intensifier gain. When recording streaked data, the lowest possible value of intensifier gain (in the range 3 to 7) was chosen, depending on the available picosecond XUV photon fluxes from different target materials. Below a value of 3, the signal-to-noise ratio was less than 4:1 and above 7, saturation of the peak generally began to occur, thus broadening the static response function further. The static response functions shown in Figure 3.29 were vertically binned and then averaged over 280 pixels. An estimate of the picosecond XUV emission duration t_{xuv} can be obtained by deconvolving the measured streak image with the appropriate static instrument function recorded under similar experimental conditions (see Chapter 4, Section 4.3.2.1).

Figure 3:29 *Variation in the static response of the combined streak camera-image intensifier system with increasing intensifier gain. All static response curves are normalised in figure inset*

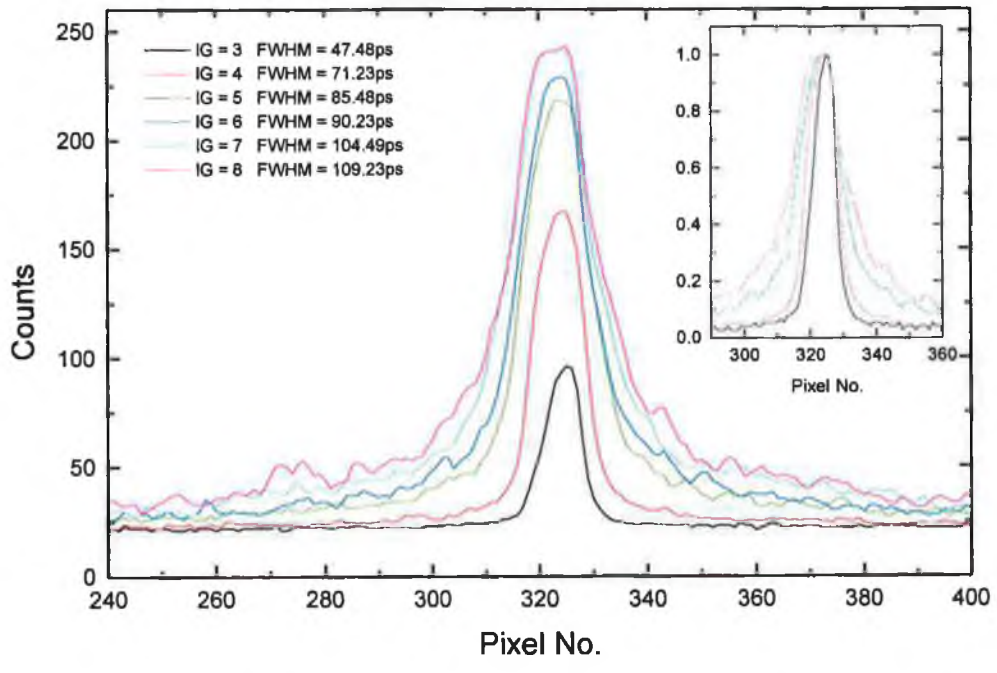

[7] The picosecond XUV laser plasma flux may vary from laser shot to laser shot due to fluctuations in the laser energy.

The duration of the static instrument functions shown in Figure 3.29 was calculated on the basis of an average sweep speed of 4.8ps/pixel that was used during the recording of all streaked emission data. The lower the value of intensifier gain chosen, the narrower the static response function and the corresponding streaked image obtained, thus enabling a more accurate prediction of t_{xuv}. The FWHM of the static instrument function at a given intensifier and video gain differed when measured using light from different laser plasmas due to differences in available XUV photon flux. Therefore, the intensifier/video gain settings at which saturation of the static instrument function occurred differed. Consequently, the static instrument function was recorded for each of the different plasma types studied and for each of the intensifier/video gain settings used. During experimental work, the video gain remained fixed at its maximum value. Operating at high video gain and low intensifier gain serves to prolong the lifetime of the intensifier.

Chapter Four

Development and Characterisation of a Picosecond XUV Continuum Laser Plasma Light Source

The design and development of a picosecond XUV continuum laser plasma light source emitting in the 100 to 200eV energy region are discussed in this chapter. Spectral characterisation of the source was performed using a 5.6m flat field XUV spectrometer system. Source properties such as the spectral profile, single-shot sensitivity, spectral reproducibility and flux reproducibility were investigated in order to assess the suitability of the source for application to DLP pump-probe type experiments. The temporal evolution of XUV continuum emission pulse widths from the picosecond laser plasma source were recorded using an XUV streak camera and the influence of amplified spontaneous emission (ASE) and picosecond laser energy on XUV emission durations was studied.

4.1 Introduction and Key Experimental Objectives

Rapid advances in laser technology over the last decade have resulted in the development of ultra-fast picosecond and femtosecond large-scale and table-top laser systems capable of attaining ultra-high peak powers in the petawatt (10^{15} W) and terawatt (10^{12} W) regimes respectively (Backus et al. 1998). Short lived, high-density laser plasmas produced during the interaction of ultra-short, ultra-intense laser pulses with solid target materials serve as bright and efficient sources of picosecond and sub-picosecond X-rays over a broad photon energy range from 10's of eV to MeV (Murnane et al. 1994, Nickles et al. 1996, Workman et al. 1996). Generation of short pulse laser plasma x-ray radiation is easily achievable using a table-top laboratory based laser system, whereas other short pulse X-ray sources such as synchrotrons and X-ray lasers are restricted to large-scale scientific facilities. The duration of synchrotron radiation is restricted by the spatial extent of electron bunches (which is limited by space charge effects) and so minimum X-ray pulse durations reside in the picosecond regime e.g. 40ps X-ray pulse durations within the 2 to 5nm (620 to 250eV) region at the ALS (Murnane et al. 1994). Both picosecond and subpicosecond incoherent (line and continuum) X-ray emission durations in the 0.0012 to 10nm (1MeV to 120eV) region have been produced using ultra-fast laser pulses with durations of ~0.5 to several 10's of picoseconds and on-target irradiances in the range 10^{15} to 10^{18} W/cm^2 (Murnane et al. 1989a, Kmetec et al. 1992, Kieffer & Chaker 1994, Schappert et al. 1994, Umstadter et al. 1995, Pelletier et al. 1996). Recent developments in both laser plasma and synchrotron X-ray sources have resulted in the emission of coherent femtosecond X-rays from both source types. 300fs X-ray pulses at 0.04nm (30keV) have been generated following 90° Thompson scattering between infrared terawatt laser pulses and highly relativistic synchrotron electrons (Schoenlein et al. 1996). Chang and co-workers (1998) have produced coherent X-ray pulses, a few femtoseconds in duration, within the 2.3 to 4.4nm 'water window' spectral region. This was achieved using the process of high-harmonic generation from the interaction of a 25fs Ti:sapphire laser pulse with noble gas atoms.

High time-resolved studies of a diverse range of transient physical, chemical and biological processes are permitted using picosecond/femtosecond soft x-ray/hard x-ray sources. Fundamental processes such as the breaking and formation of molecular bonds and molecular vibration and rotation occur on a time scale of picoseconds to

femtoseconds. Short pulse laser-plasma based time-resolved x-ray diffraction studies permit probing of the evolution and dynamics of atomic-scale motion of molecules, surfaces and solids (Rose-Petruck et al. 1999).

In a pump-probe type experiment, Balmer and co-workers (1989) first utilised a picosecond X-ray source to probe an expanding aluminium plasma in a point-projection type geometry. 100ps and 600ps 2ω Nd:YAG laser pulses focused to ~10^{15}W/cm^2 produced X-ray continuum emission from high-Z materials (ytterbium and tungsten) in the 0.45 to 0.75nm wavelength region where the broadband X-ray pulse duration was the same as that of the incident laser pulse. The duration of X-ray emission ultimately defined the temporal resolution with which the atomic/ionic dynamics of the absorbing aluminium plasma were probed. Davidson and co-workers (1990) working with the Vulcan Nd:Glass laser at the EPSRC Central Laser Facility (RAL) extended the point-projection technique to lower, soft X-ray/XUV wavelengths, by replacing the familiar Bragg grating with a flat field grating. In the 3 to 30nm region they measured broadband soft X-ray/XUV continuum durations of ~100ps emitted from a thulium (Z=69) plasma produced when 60J, 100ps, 532nm (ASE free) Nd:Glass pulses were focused to an intensity of ~10^{15}W/cm^2. This result, along with the observation by Carroll and co-workers (1978, 1980) of extensive 'line-free' XUV (4 to 200nm) continuum emission in high-Z metals, served as precursors to the development and characterisation of a picosecond XUV continuum source during the course of this work (Meighan et al. 1997). The source was produced at the Central Laser Facility (RAL) using a KrF-based laser system delivering 15-20mJ, 7ps, 248nm laser pulses that were focused to a moderate on-target irradiance of ~10^{13}W/cm^2 on the surface of high-Z metals. Our primary application for such a source is to picosecond time-resolved DLP pump-probe photoabsorption studies, and more specifically to probing the evolution of thorium actinide ions in the first 50ns after initiation of the sample thorium plasma (Meighan et al. 2000).

Conventionally, nanosecond lasers (~10 to 100ns), generating pulses of moderate energy (10's to 100's of mJ) and focused to on-target irradiances up to ~10^{12}W/cm^2, have been used to produce both VUV and XUV continuum sources for use as backlighting probes in DLP-type experiments. As mentioned earlier in Chapter 2 (Section 2.1.5.2), XUV emission durations are comparable with the laser pulse width (Mosnier et al. 1996) and increase to typically hundreds of nanoseconds with decreasing

photon energy into the VUV (Breton & Papoular 1973, Carroll et al. 1980). The temporal resolution achievable using long pulse nanosecond lasers is therefore restricted to at best several tens of nanoseconds. The production of a picosecond XUV continuum source (using picosecond laser pulses) permits the probing of an absorbing plasma plume with increased temporal resolution. This is particularly important at times soon after the creation of the absorbing plasma (0→50ns) when the usual ~20ns XUV continuum pulse integrates over the early history of the plasma. Higher ionic charge states, produced early in the evolution of the absorbing sample plasma, can therefore be investigated in greater detail using a picosecond XUV continuum pulse.

When developing the picosecond XUV continuum source during this work a number of key experimental goals and source criteria were established. Laser plasma sources suited to DLP-type studies should ideally produce short pulse emission in the wavelength region of interest and also should be of small dimensions (several hundred microns), thus providing adequate temporal and spatial resolution with which to probe the absorbing plasma plume. Also, backlighting sources should emit extensive regions of 'line-free' continuum radiation. XUV spectroscopy was used to establish both the laser conditions and the target materials suited to the production of picosecond continuum radiation in the 5 to 20nm region. Factors important to DLP studies such as the spectral reproducibility, spectral purity, time-integrated XUV flux and single-shot sensitivity of the backlighting continuum source were measured. Also, the XUV flux reproducibility with repeated laser shots at one focal position on the surface of the backlighting target material was investigated. A streak camera system was used to perform time-resolved, spectral and spatially integrated measurements of the XUV continuum emission from a series of high-Z target materials. The influence of both nanosecond amplified spontaneous emission (ASE) pulse energy and picosecond laser pulse energy on emission durations was investigated for picosecond plasmas produced from tungsten tape targets.

The experimental configurations used for flat field XUV spectroscopic measurements and XUV streak camera measurements are detailed in Chapter 3, Section 3.2.3.1.1 and Section 3.2.4.1 and the results obtained using both of these experimental systems are detailed in Section 4.2 and Section 4.3 respectively.

4.2 Time Integrated, XUV Spectroscopy of a Picosecond Laser Plasma Light Source

4.2.1 XUV Transmission Bandwidth of Flat Field Spectrometer System – Emission Studies

The wavelength range covered by the flat field spectrometer system was determined by the reflectivity of the gold mirror pair reflection filter and the spectral efficiency of the gold-coated vari-spaced grating. These components are represented schematically in Figure 4.1 and also in Figure 3.20, Chapter 3. The reflection efficiency of plasma light

Figure 4.1: Schematic representation of the various components within the XUV flat field spectrometer system

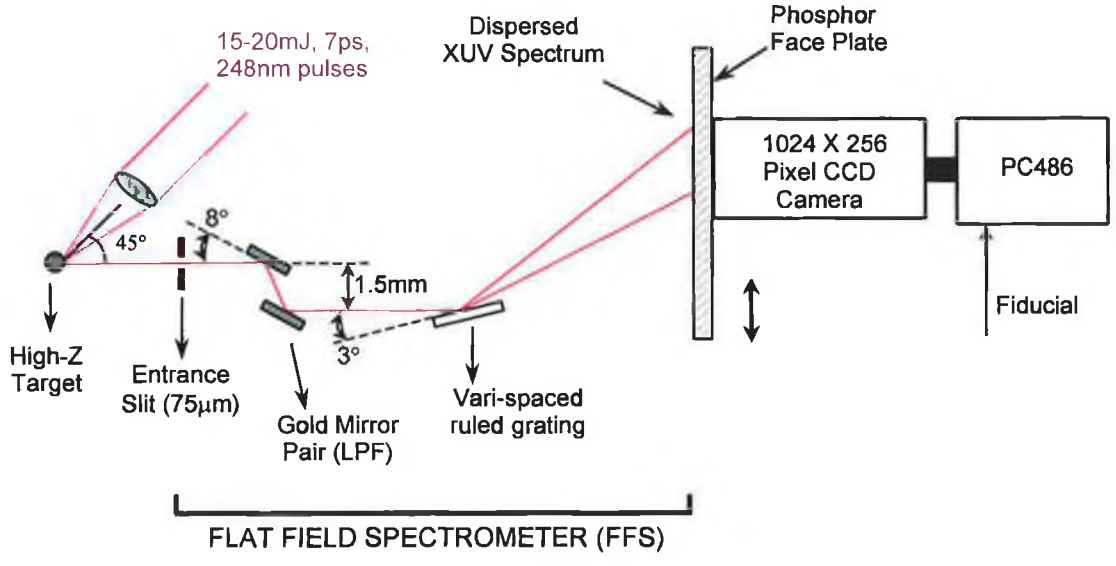

incident on a single planar gold mirror at an 8° grazing angle of incidence was calculated using a code, known as the SF code (see reference list), and is shown as the blue curve in Figure 4.2. The SF code permits calculation of the reflectivity and the transmission/absorption of a range of different types of atomic and molecular thin films using a database of pre-determined XUV and soft X-ray optical constants. The exact thickness of the gold mirror surface was unknown, however it lay in the region of 0.1 to 1μm. The SF code yielded the same spectral reflectivity profile for an 8° angle of incidence within this thickness range and so an exact value was not required for accurate calculation. The combined response of the gold mirror pair was obtained (inset in Figure 4.2) by squaring the reflection efficiency for a single gold mirror. Within the

Figure 4.2: Reflectivity of a single planar gold mirror (—) and the combined reflectivity of a gold mirror pair (—) for an 8° grazing angle of incidence in the XUV to soft X-ray spectral region from 60 to 360eV

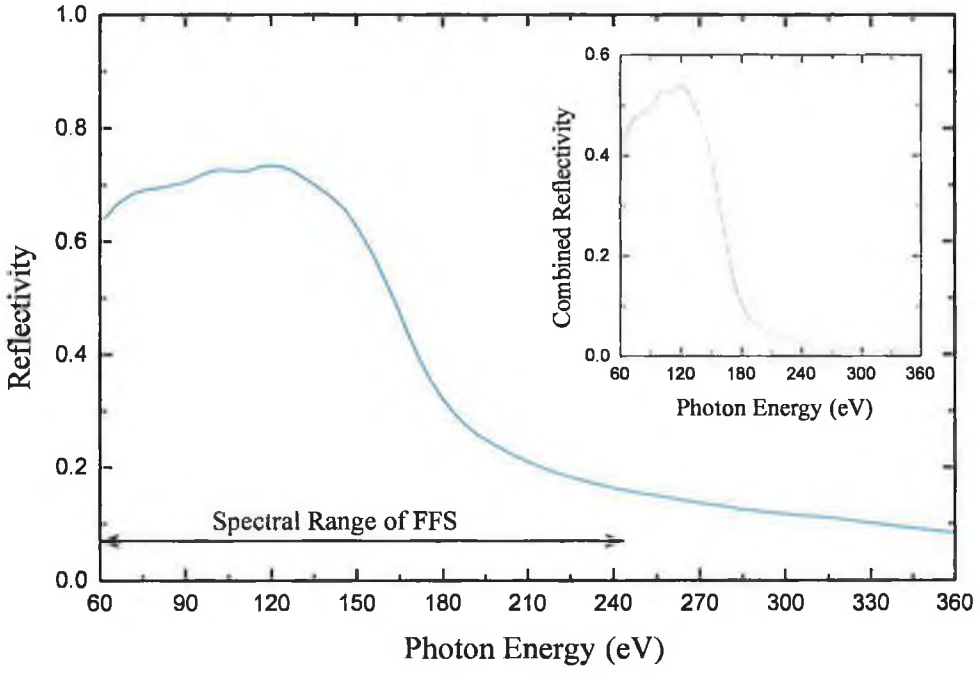

XUV region, from 60 to 150eV, the combined reflectivity of the gold mirror pair remains above 40%, whereas for energies above 200eV the reflectivity has dropped to below 5% and thus the gold mirror pair acts as a low pass filter. For photon energies above 300eV the reflectivity is less than 1% and as a result plasma light at soft x-ray photon energies is virtually eliminated. The combined reflectivity of the gold mirror pair begins to increase below 200eV and so higher order contributions due to light in the 100 to 200eV region begin to appear below 100eV. As a result of the filtering action of the gold mirror pair, the XUV/soft X-ray region from 100eV to 200eV is virtually free from order sorting problems.

The spectral reflection efficiency of the Hitachi™ vari-spaced grating is unknown and so its effect could not be removed from the emission spectra presented here. All emission studies were performed in the 60 to 250eV energy region defined by the vari-spaced grating and subsequent results presented are confined to the XUV free spectral range between 100 and 200eV.

4.2.2 Transition from Line to Continuum Emission in the XUV spectral region

In order to investigate the conditions under which extensive regions of 'line-free' XUV continuum emission could be observed, a series of target materials ranging from low- to high-Z were used for plasma production. A 1m *f*/10 UV grade plano-convex lens was used to focus 15-20mJ, 7ps, 248nm laser pulses to an irradiance of ~10^{13}W/cm^2 onto continuously moving tape and rotating cylindrical targets *in vacuo*. The XUV emission spectra from Mylar™ ($C_{10}H_8O_4$) and copper tape targets, and also samarium, lead and gold rods were recorded using the phosphor-coated and fibre-optically coupled front-illuminated Andor Technology™ EEV 15-11 CCD detector coupled to the XUV flat field spectrometer system (see Figure 3.20, Chapter 3). Time integrated, predominantly first order spectra of Mylar™, copper and samarium, recorded with the FFS operating in high resolution mode ($\lambda/\Delta\lambda \approx 64$ at 5nm and ≈185 at 20nm with a 75μm entrance slit), are shown in the 100 to 200eV energy range in Figure 4.3. The spectra shown are uncorrected for the combined reflectivity of the gold mirror pair and the vari-spaced grating. Calibration data available on the spectral response of the rare earth phosphor coating on the integral fibre-optic face plate of the EEV 15-11 CCD detector was used

Figure 4.3: Comparison of low, medium and high-Z plasma spectra showing the transition from predominantly line to continuum XUV emission

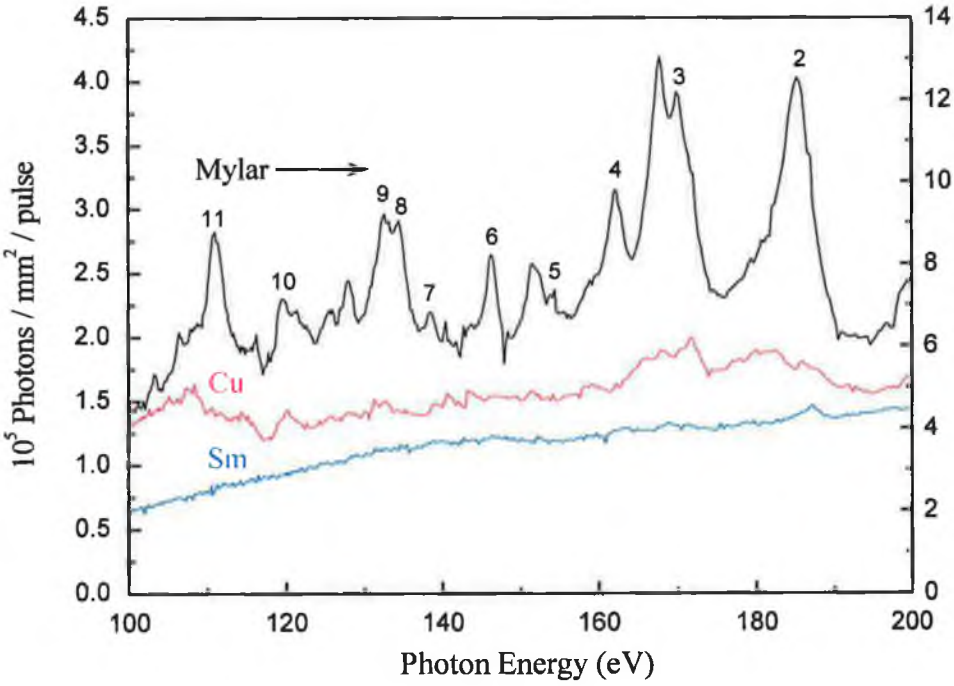

to convert counts/pixel to photons/mm^2 at the focal plane of the spectrometer (MacPhee & Lewis 1994). The rare earth phosphor output is known to increase ~linearly with increasing photon energy, E, in the XUV region of study. The intensity of the true XUV signal incident on the phosphor coating $I_{true}(E)$ in photons/mm^2 can be determined using

$$I_{true}(E) = C_{meas}(E) \times S(E) \tag{4.1}$$

where $C_{meas}(E)$ is the XUV signal as measured by the CCD (in counts/mm^2) and $S(E)$, measured in photons/count, is the detector sensitivity as determined by the phosphor conversion efficiency and the silicon quantum efficiency at the phosphor fluorescence wavelength. For the EEV 15-11 CCD, however, visible photons emitted by the rare earth phosphor are matched to the sensitivity peak of the silicon based CCD. Therefore, the overall system sensitivity, $S(E)$, varies ~linearly with increasing incident photon energy. MacPhee and Lewis used pre-calibrated photographic plates and hydrogen-like carbon emission lines at 3.374 and 18.217nm in order to calibrate the EEV 15-11 CCD detector system. The detector sensitivity was found to vary from 22.546 photons/count at 18.217nm (68.06eV) to 3.660 photons/count at 3.374nm (367.47eV). Therefore $S(E)$, using a linear approximation, takes the form

$$S(E) = -0.063(E) + 26.839 \tag{4.2}$$

$I_{true}(E)$ was determined for the Mylar™, copper and samarium spectra shown in Figure 4.3 using equations (4.2) and (4.1) where the CCD pixel size is 7.29×10^{-4} mm^2 (27μm×27μm). The CCD integration time was set at 50s, thus accumulating light from 500 KrF laser shots for a repetition rate of 10Hz. Each spectrum in Figure 4.3 represents an average of the accumulation of 500 KrF laser pulses on target. Each 20ns long KrF pulse amplifies two picosecond pulses, separated by 12ns, and each having a mean energy of 15mJ per pulse. Hence the number of photons/mm^2/ps-pulse incident on the phosphor is half that shown in Figure 4.3. The left-hand side y-axis in Figure 4.3 refers to copper and samarium emission spectra, whereas the corresponding axis on the right hand side refers to that of the Mylar™ spectrum. The intensity of Mylar™ exceeds that of copper and samarium due to the fact that Mylar™ plasma emission is concentrated into a relatively small number of spectral lines in the VUV and XUV energy regions. Continuum emission, on the other hand, is spread right throughout the VUV and XUV energy range where oscillator strengths are distributed over many transitions rather than just a few as in the case of Mylar™.

The transition from predominantly line emission to 'line-free' continuum emission as the target atomic number is increased is evident. At high resolution, samarium produces a smooth, virtually featureless continuum, which is consistent with results observed by Carroll and co-workers (1978, 1980) and Bridges and co-workers (1986) in a similar XUV energy range using samarium plasmas produced by nanosecond laser pulses. Also, subsequent to the work presented here, O'Sullivan and co-workers (1999) observed bands of continuum emission in the 4 to 16nm XUV region from samarium plasmas produced using 500mJ, 150ps, 1064nm Nd:YAG laser pulses.

XUV emission observed from copper (Figure 4.3) is more intense than that from samarium but with increased line structure, thus reducing its attractiveness as a backlighting continuum source for photoabsorption applications. Nicolosi and co-workers (1981) observed relatively smooth continuum emission in the 3 to 8nm (410 to 155eV) soft X-ray region from copper ions in a plasma produced using a ~10J, 14ns ruby laser pulse. According to the collisional-radiative model of Colombant and Tonon (1973), an electron temperature of 390eV and an average charge state of 15 were achieved in the copper plasmas produced by Nicolosi and co-workers compared with values of 120eV and 10 times ionised in the copper plasmas discussed here. The intensity of Bremsstrahlung and recombination continuum emission scales as ξ_{av}^{2} and ξ_{av}^{4} respectively (where ξ_{av} is the average ionic charge state in the plasma plume). In the copper plasmas produced by Nicolosi and co-workers (1981) increased levels of Bremsstrahlung and recombination continuum emission appear to dominate any discrete line structure which may be present.

Mylar™ emission lines numbered 2 to 11 in Figure 4.3 have been identified previously (see Figure 3.25, Chapter 3) as those resulting from transitions occurring in the highly charged ions O^{5+} to O^{7+} and C^{5+} present in the Mylar™ plasma plume. The Mylar™ spectrum possesses high levels of underlying continuum arising from both radiative recombination and bremsstrahlung emission processes. Under the same laser irradiance conditions (~10^{13}W/cm^2) samarium plasmas are sufficiently heated in order to produce an average ionic charge state of ~Sm^{14+}, as estimated using equation 2.19 (Chapter 2, Section 2.1.4.4) from Colombant and Tonon (1973). In high-Z ($Z \geq 62$) nanosecond plasmas produced by Carroll and co-workers (1978, 1980) species up to and including sixteen times ionised were calculated, again using the collisional-radiative model of Colombant and Tonon, to reside in the plasma plume. In such an ionised regime for a

rare earth plasma, the 4f wavefunction has collapsed, which results in ionic ground states containing 4f electrons[1]. As mentioned in Chapter 2 Section 2.1.5, the close proximity of the 4f, 5s and 5p electron binding energies following/during 4f wavefunction collapse results in many excited configurations lying close to a given ionic ground state. This gives rise to a near continuous band of low lying ionic states (O'Sullivan 1983). Transitions from the many terms among such closely lying states can result in hundreds of thousands of closely spaced lines that are weakened due to the distribution of oscillator strength over a huge number of transitions. This gives rise to the formation of broad, and to a large extent, featureless bands of quasi-continuum each the result of an Unresolved Transition Array (UTA). Recently O'Sullivan and co-workers (1999) have observed, using the Cowan atomic structure code (1981), that the inclusion of configuration interaction (CI) effects among initial and final bound states within UTA's switches on LS forbidden transitions. This serves to further increase line density and smooth out the observed quasi-continuum, resulting in a more realistic simulation of experimentally observed spectra.

The most dominant UTA feature observed in rare-earth XUV emission spectra is that arising from 4d→4f transitions (Carroll & O'Sullivan 1982, O'Sullivan 1983). For samarium, this UTA is located in the 7 to 9nm (177 to 138eV) region of the emission spectra of Sm VI to Sm XVI ions. In the case of such ions, the 4f wavefunction has collapsed and significant overlap between the 4d and 4f wavefunctions results in the 4d→4f UTA being the strongest observable transition array. This UTA contributes to the samarium emission profile recorded in Figure 4.3. O'Sullivan and co-workers (1999), using 500mJ, 150ps, 1064nm laser pulses focused to an on-target irradiance of close to 10^{13} W/cm^{-2}, observed a strong modulation of the underlying continuum emission in the 7 to 8.5nm region arising from intense 4d→4f emission lines. Such a strong modulation of the continuum profile is not evident in our recorded samarium spectra and it appears that both the processes of bremsstrahlung and recombination radiation dominate over, or at least equal, that of the 4d→4f UTA. The resulting suppression of the 4d→4f UTA could be due to plasma opacity effects, whereby the higher *f*-value transitions within the UTA are more favourably absorbed than lower *f*-value continuum transitions (see equation (2.22), Section 2.1.5, Chapter 2). According to the collisional-radiative model of Colombant and Tonon (1973), Nd:YAG-produced

[1] Collapse of the 4f wavefunction in rare earth elements, in general, occurs at $\xi \geq 6$, where ξ is the ionic charge state (O'Sullivan 1983).

samarium plasmas (at ~10^{13} W/cm^{-2}) produced by O'Sullivan and co-workers (1999) achieve an electron temperature, T_e, of ~800eV and an average charge state, ξ_{av}, of 24 compared with corresponding values of ~140eV and 14 for KrF-produced samarium plasmas (also at ~10^{13} W/cm^{-2}). The profile of 4d→4f emission will vary for different ion stages emitting within the plasma plume and contributions from various ion stages tend to overlap as $\Delta n=0$. Consequently, the modulation of underlying continuum in the 7 to 9nm region of emission spectra from samarium plasmas produced under different laser conditions will vary.

Both the processes of bremsstrahlung and recombination radiation are the main sources of continuum emission in the observed copper spectrum (Figure 4.3). Also, there is a higher degree of line emission contributing to the total copper spectral profile, whose resulting intensity exceeds that of samarium. Mylar™, whose spectral profile is dominated by strong line emission sitting on a high continuum background, produces the brightest emission in the region of interest (100 to 200eV).

4.2.3 XUV Continuum Emission from High-Z Metal Plasmas

The relative intensities of XUV continua produced from the high-Z plasmas of lead, gold and samarium are shown in Figure 4.4. All plasmas were produced under similar conditions to those discussed in Section 4.2.2, whereby a 1m focal length *f*/10 UV grade plano-convex lens was used to focus 15-20mJ, 7ps, 248nm laser pulses to an irradiance of ~10^{13}W/cm^2 onto rotating cylindrical rods of lead, gold and samarium *in vacuo* (see Figure 3.20, Chapter 3 and Figure 4.1 for experimental set-up). The flat field spectrometer was operated in imaging mode (75μm entrance slit removed) during recording of these spectra, thus permitting increased XUV flux to fall on the detector plane. The CCD integration time was set at 5s, thus accumulating light from 50 KrF laser shots for a repetition rate of 10Hz. Each spectrum in Figure 4.4 represents an average of the accumulation of 50 KrF laser pulses on target. As before, each KrF pulse amplifies two picosecond pulses and so the number of photons/mm^2/ps-pulse incident on the phosphor is half that shown in Figure 4.4. The spectra are again shown uncorrected for the combined grating/gold mirror pair reflectivity. Removal of the

Figure 4.4: Comparison of XUV continuum emission spectra obtained from a number of high-Z plasmas with the flat field spectrometer operated in slit-less, imaging mode

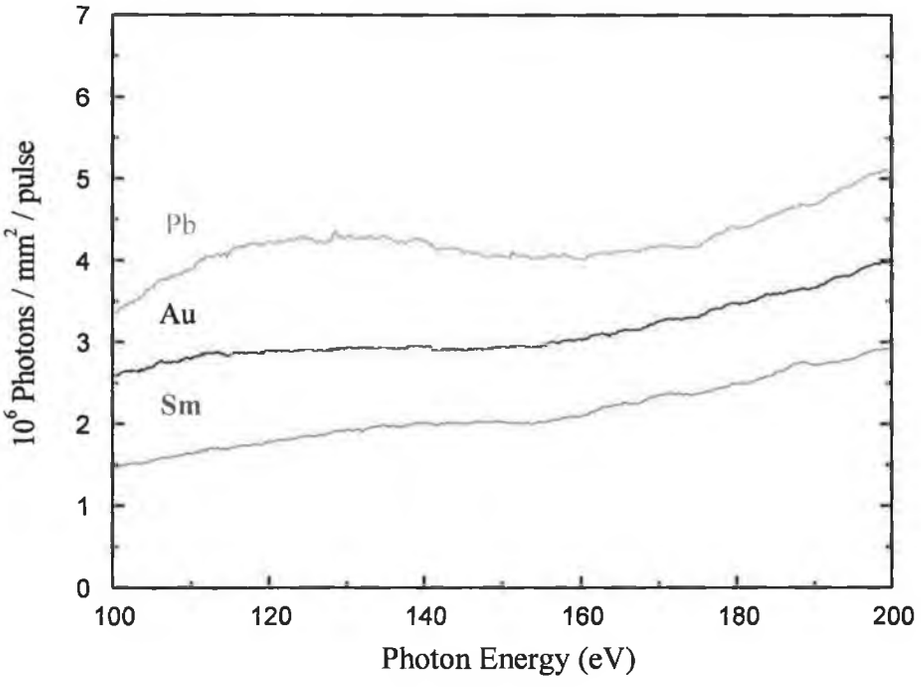

spectrometer entrance slit results in an intensity gain of ~200 in the XUV signal measured at the detector plane. The high degree of similarity between the spectral emission profiles from the three high-Z plasmas studied suggests that the observed intensity modulation is in effect due to the combined grating/gold mirror pair reflectivity rather than true emission features.

All three elements emit smooth 'line-free' continuum in the 100 to 200eV XUV region studied. Lead, the heaviest of the three elements, produces the brightest continuum. However, due to its softness and hence the high degree of surface damage caused at the focal spot of the laser, a harder high-Z metal is more suited to picosecond XUV continuum production. As mentioned previously (Chapter 2 Section 2.1.5), the intensity of recombination and bremsstrahlung radiation increase with increasing atomic number due to an increase in ξ_{av}, the average ionic charge state in the plasma plume. In Figure 4.4, the intensity of XUV continuum emission follows this trend, increasing from samarium (Z=62), through gold (Z=79), to a maximum at lead (Z=82).

4.2.4 Single-Shot Sensitivity of Picosecond XUV Continuum Light Source

The single shot sensitivity of the source-spectrometer system was investigated with the FFS operating in imaging mode as before. A single shot emission spectrum from a lead plasma, accumulated over a 75ms CCD integration time, is compared with the average of five similarly accumulated single shot spectra in Figure 4.5. The average flux for the single shot spectrum is 2.8×10^6 photons/mm^2/KrF-pulse (1.4×10^6 photons/mm^2/ps-pulse) at 200eV. This result serves to demonstrate the suitability of the XUV continuum source to the study of dynamic absorbing species such as atoms and ions within a second laser plasma plume (DLP). However, it is important to note that the system gain could be significantly increased through the use of a grazing incidence toroidal coupling optic. This would permit studies with an increased signal-to-noise ratio and dynamic range, thus preventing complete absorption of the continuum signal in energy regions where the absorption cross section of the plasma plume under study is high. Such an addition to the spectrometer system could also result in a reduction of the inherent astigmatism associated with a vari-spaced grating operating in the grazing incidence regime.

Figure 4.5: Comparison of single shot and five-shot averaged lead continuum emission spectra recorded with the flat field spectrometer operated in slit-less, imaging mode

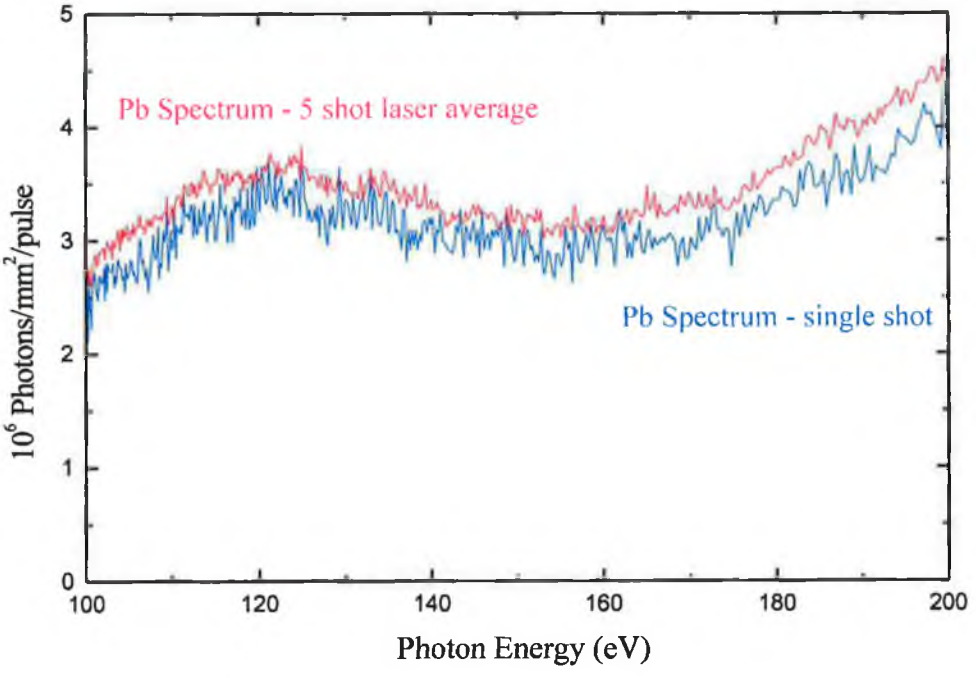

4.2.5 Spectral Reproducibility and Flux Reproducibility of Picosecond XUV Continuum Light Source

In order to investigate the spectral reproducibility of the picosecond XUV continuum source, two consecutive lead spectra were accumulated over 5s (100 × 7ps laser shots) each (I_1 and I_2). The ratio of I_1/I_2 was calculated and this procedure was repeated for a series of similarly recorded pairs of spectra. Results obtained are shown in Figure 4.6. The ratios obtained lie within ±5% of an expected value of unity and are displaced by unity from each other in Figure 4.6 for clarity. This result serves to demonstrate the high degree of reproducibility of the spectral content of the XUV continuum source. Also the fact that each ratio (I_1/I_2) equals a value of one indicates the good shot-to-shot reproducibility of flux levels and also a very low stray light contribution to the recorded continuum signals.

Figure 4.6: Ratios of a series of consecutive 100-shot lead spectra recorded under identical experimental conditions yield values within ±5% of unity

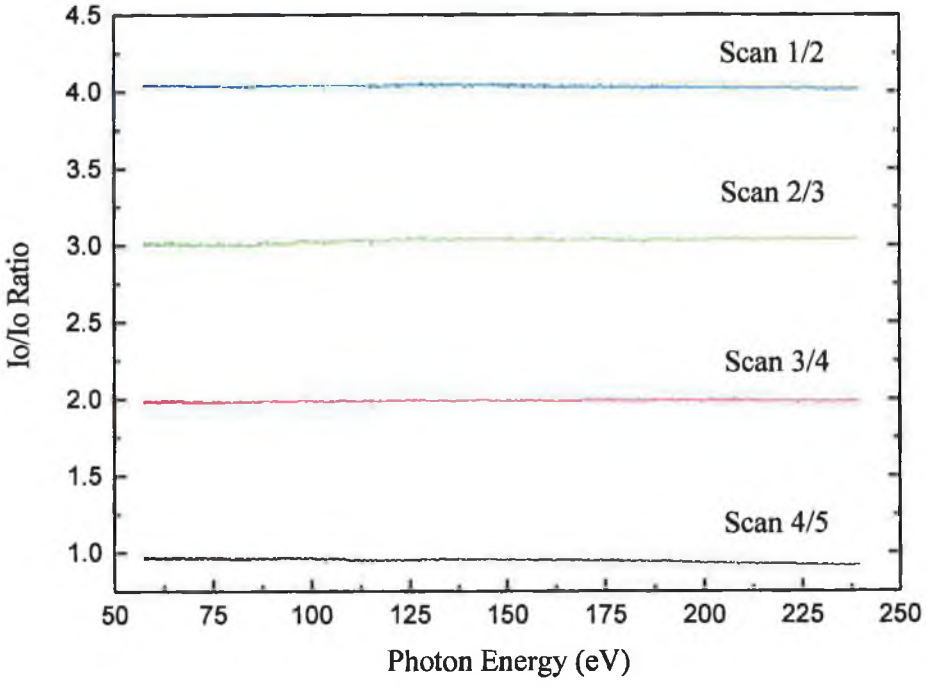

The flux reproducibility of picosecond XUV continuum emission was investigated further during DLP studies (1997) using the FFS and an Andor Technology™ back-illuminated CCD detector (see Figure 3.21, Chapter 3). A high-Z tungsten backlighting plasma was produced under similar conditions to those used in emission-only studies

(1995), whereby a 125mm *f*/5 UV grade plano-convex lens was used to focus 15-20mJ, 7ps, 248nm laser pulses to an irradiance of ~10^{13}W/cm^2 onto a cylindrical tungsten rod *in vacuo*. Two 60 KrF-shot tungsten continuum spectra, each accumulated over 5s at 12Hz are shown in Figure 4.7. A Pockels cell was used to switch out a single picosecond pulse at each trigger of the KrF amplifier. Therefore both spectra shown represent the accumulation of light from 60 laser pulses and not 120 as would have been the case in previous studies (1995). Also, the position of the UV laser focal spot on the tungsten target surface remained unchanged over the 180 laser shots fired. Between the acquisition of both backlighting (I_o) emission spectra shown, a thorium absorption spectrum (I) was recorded and a further 60 laser shots were fired at the tungsten surface. As a result, the emission spectra shown in Figure 4.7 were accumulated for laser shots 1 to 60 and 121 to 180. The average detector counts in the 80 to 150eV energy region fall from 4,419 (shots 1 to 60) to 3,893 (shots 121 to 180), which constitutes a drop of only 12% in continuum intensity. Therefore, over 180 laser shots on-target, the XUV continuum intensity level is sufficiently bright (good signal-to-noise ratio) and stable enough to perform DLP photoabsorption studies.

Figure 4.7: *Variation in tungsten XUV continuum intensity over 180 KrF laser shots with no re-optimisation of the UV laser focal position on the tungsten target surface*

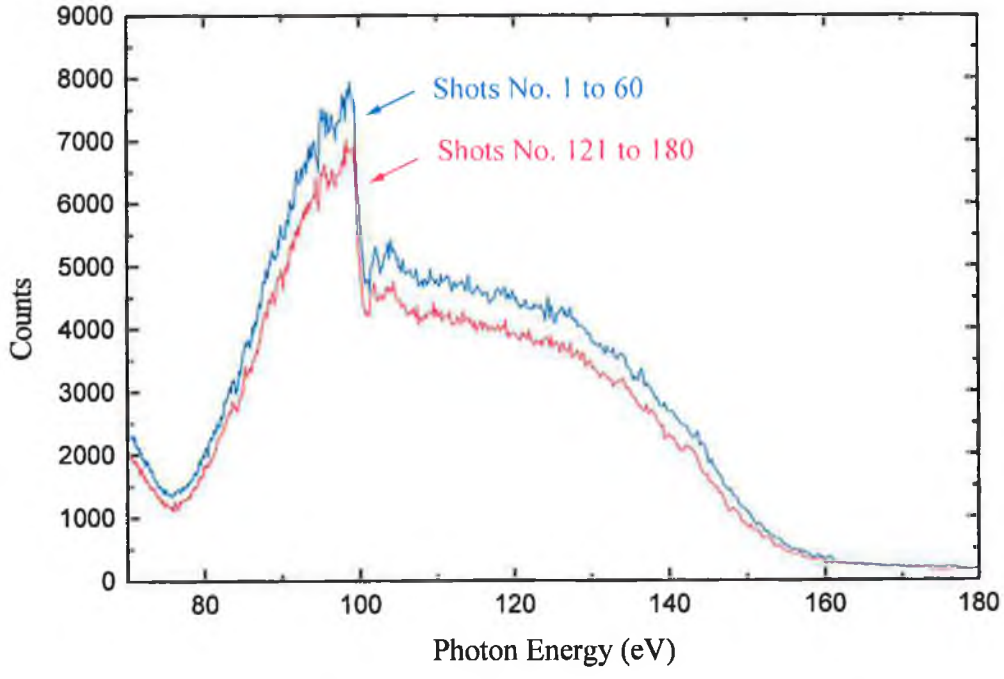

4.2.6 XUV Transmission Bandwidth of Flat Field Spectrometer System – DLP Photoabsorption Studies

The tungsten XUV continuum emission profile shown in Figure 4.7 is modulated by a number of different factors. Firstly, the sharp fall in intensity at ~100eV indicates the onset of silicon L-shell XUV photoabsorption above the silicon L-edges $2p_{1/2}$ at 99.8eV and $2p_{3/2}$ at 99.2eV. This is due to the fact that XUV photons are absorbed directly by the silicon structure of the back-thinned, back-illuminated CCD detector used. Secondly, the gold coated vari-spaced grating, a silver mirror pair low pass filter, a gold coated collection mirror and a thin film XUV transmission filter modulate the transmission of the FFS system so as to define an XUV bandpass window ranging from 80 to 150eV. The reflectivity (at a 10° grazing angle of incidence) of a single planar mirror coated with a 1μm film of silver (—) and a pair of such mirrors (—) was calculated using the SF code and is shown in Figure 4.8. The reflectivity profile in the 60 to 360eV energy region for the silver mirror pair is very similar to that calculated for the gold mirror pair operating at an 8° angle of incidence (see Figure 4.2). The transmission bandwidth in the 60 to 180eV region is slightly narrower for the silver

Figure 4.8: Reflectivity of a single planar silver mirror (—) and the combined reflectivity of a silver mirror pair (—) for a 10° grazing angle of incidence in the XUV to soft X-ray spectral region from 60 to 360eV

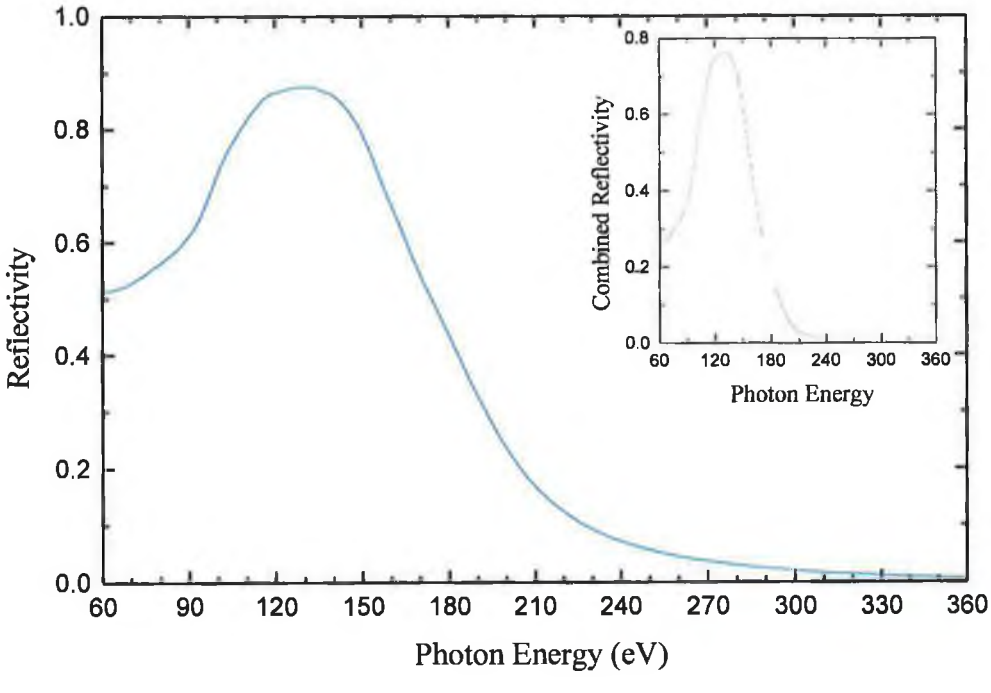

mirror pair, but the combined reflectivity in this region reaches a maximum of 76% compared to a lower value of 54% for the gold mirror pair. The reflectivity of the silver mirror pair also falls below 5% above 200eV, thus defining a similar free spectral range of 100 to 200eV.

The XUV bandpass filter inserted into the FFS consisted of a 0.1μm film of molybdenum deposited on a 0.4μm CH polymer support substrate. The individual transmission of the molybdenum (—) and CH (—) films were calculated using the SF code and are shown in Figure 4.9 along with their combined transmission (—). The thin film filter was mounted in the FFS between the adjustable gold collection mirror and the

Figure 4.9 *Transmission of 0.1μm molybdenum thin film (—), 0.4μm CH polymer substrate (—) and the total transmission of the composite XUV bandpass filter (—)*

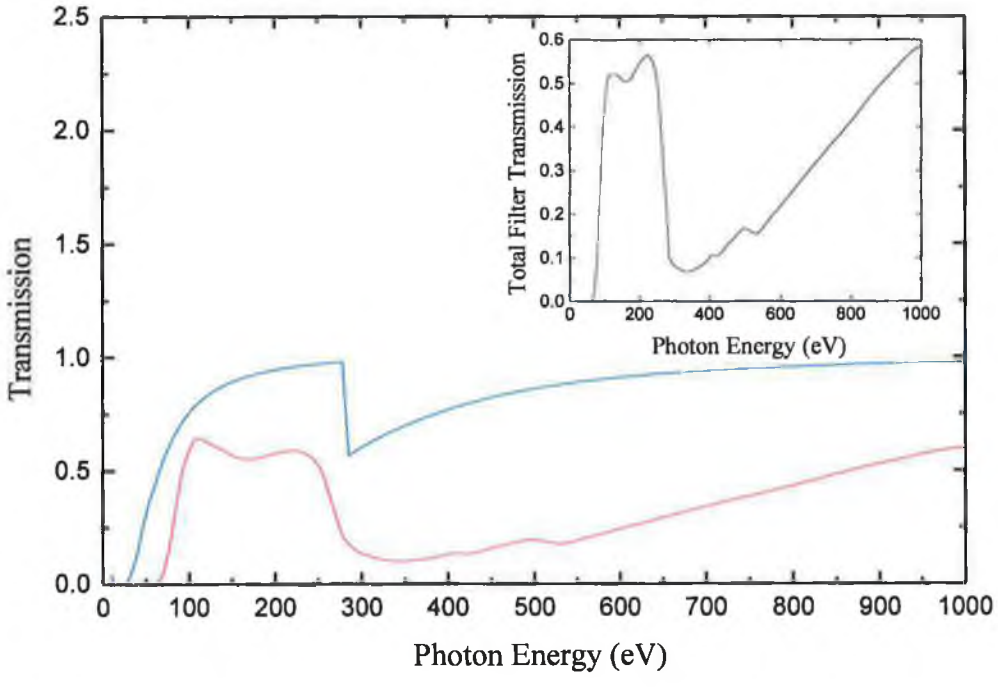

vari-spaced grating (see Figure 3.21, Chapter3). Like the silver mirror pair, the spectral transmission of the thin film filter is optimum at XUV photon energies, with the total filter transmission remaining above 45% in the 100 to 200eV region. A sharp drop in CH transmission at ~280eV corresponds to carbon K-edge at 284.2eV and a similar but more prolonged drop in molybdenum transmission in the 250 to 500eV region corresponds to M shell absorption, where the M-edges straddle the energy region from 227.9eV (M_V) to 506.3eV (M_I). The increasing thin film transmission in the soft X-ray

and X-ray spectral regions is negated by the silver mirror pair, whereas VUV, UV and visible photon energies transmitted by the silver mirror pair are efficiently blocked by the thin film filter. Consequently, the level of stray light falling on the detector is reduced, thus resulting in more accurate measurements of relative photoabsorption cross sections in DLP experiments. The combined spectral transmission of the silver mirror pair and thin film filter has a FWHM of ~65eV centred at 130eV and is shown in Figure 4.10.

Figure 4.10 Combined XUV transmission bandpass as defined by a 0.1μm molybdenum /0.4μm CH thin film and a silver mirror pair

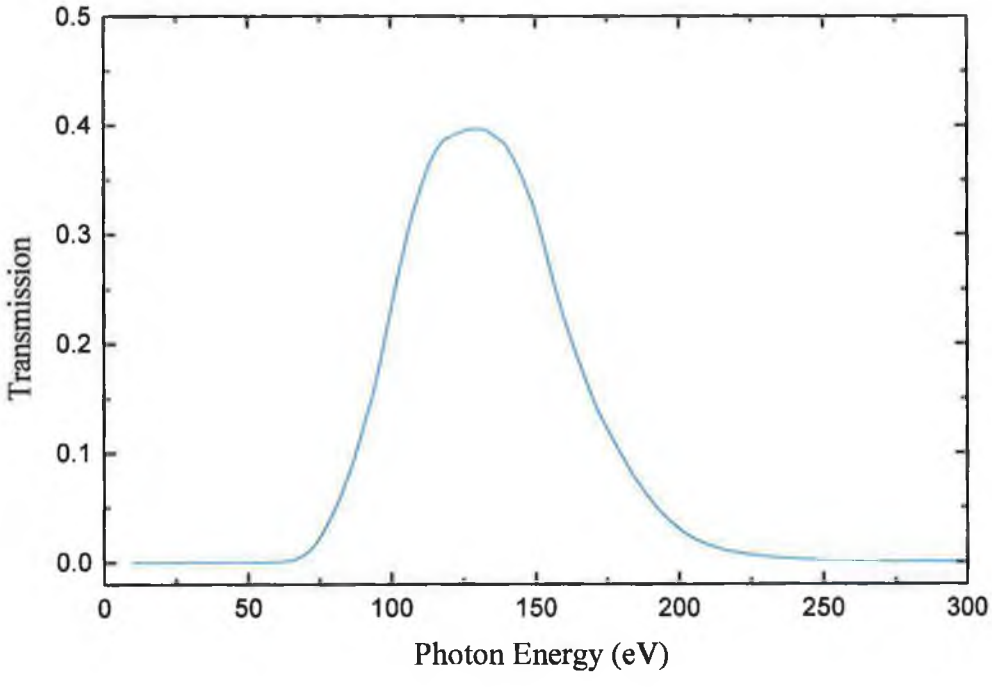

Tungsten backlighting plasmas discussed in Section 4.2.5 and the spectrometer filtering components discussed in this section were used in thorium DLP photoabsorption experiments discussed in Chapter 5, Section 5.4.2.1.

4.3 Time Resolved, Broadband XUV Emission Measurements of Picosecond Laser Plasma Light Source

4.3.1 XUV Transmission Bandwidth of Streak Camera System

The various optical components inserted between the picosecond laser plasma source and the Kentech™ streak camera are represented schematically in Figure 4.11 (also Figure 3.27, Chapter 3) and were chosen in order to define a similar XUV transmission bandpass to that used in FFS-DLP studies (see Figure 4.10). This permitted measurement of laser plasma emission durations integrated over the 75 to 225eV XUV

Figure 4.11: Schematic representation of the various components within the XUV streak camera system

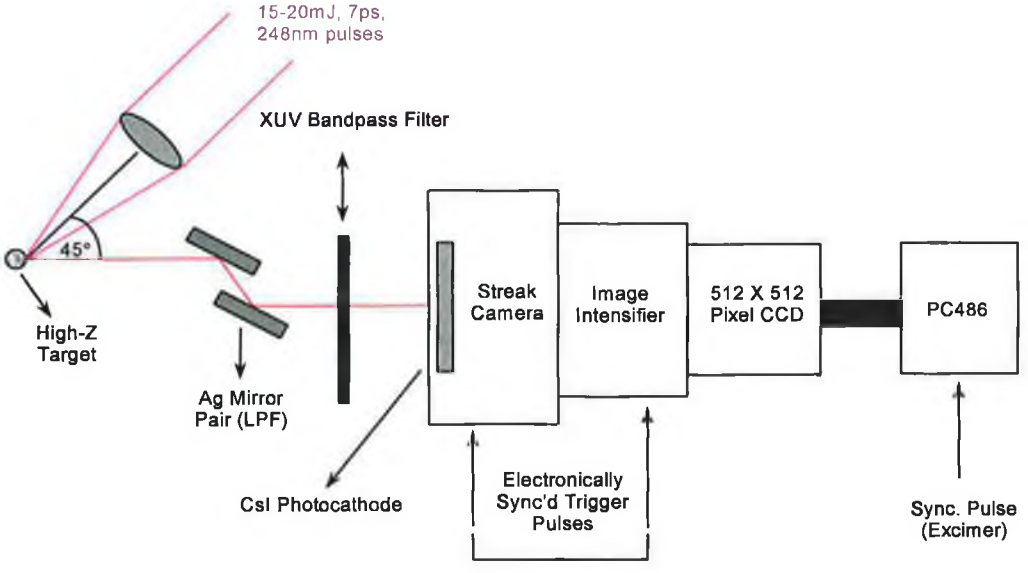

energy region. A silver mirror pair low pass filter, again operated at a 10° grazing angle of incidence, provided the same spectral response as that shown in Figure 4.8. A thin film XUV bandpass filter (0.185μm of molybdenum on 0.159μm of CH), having a similar composition but different thickness to that used in FFS DLP studies was inserted between the silver mirror pair and the streak camera timing slit. The combined filtering action of the these two components, including that of the 0.1μm Formvar® ($C_5H_7O_2$) support substrate for the CsI photocathode, is shown in Figure 4.12. The transmission of the 0.1μm Formvar® substrate alone is shown in the inset of Figure 4.12 and is similar to that of CH with an additional absorption edge at 543.1eV, the oxygen K-edge. The total system transmission, as before, has a FWHM of ~65eV centred at 130eV. The peak transmission at 130eV however, is reduced from 40% to 20%.

Figure 4.12 *Combined XUV transmission bandpass as defined by a 0.185μm molybdenum /0.159μm CH thin film, a silver mirror pair and a 0.1μm Formvar® photocathode substrate (—). The transmission of the 0.1μm Formvar® substrate alone is shown in the inset (—)*

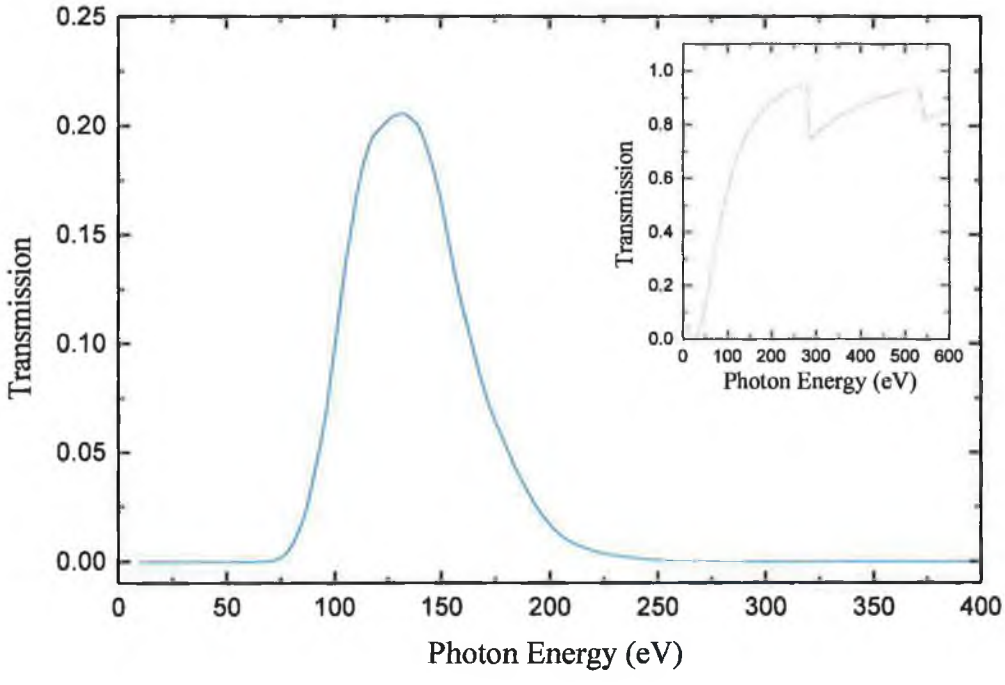

4.3.2 Picosecond XUV Emission from High-Z Metal Plasmas

The duration of broadband XUV continuum emission was investigated and measured for a series of high-Z picosecond laser plasmas in order to assess the potential of this source type for use as a high temporal resolution continuum probe in DLP-type photoabsorption experiments. Plasmas were produced when 15-20mJ, 7ps, 248nm laser pulses were focused using a 35cm *f*/7 UV grade plano-convex lens to an irradiance of 10^{13} W/cm^2 onto continuously moving tungsten, gold and lead tape targets and a rotating samarium cylindrical rod. The experimental set-up used to perform these measurements is shown in Figure 4.11 and Figure 3.27, Chapter 3, with the system spectral transmission as defined in the previous section. A CCD image of a typical streak emission profile from a picosecond tungsten plasma is shown in the upper half of Figure 4.13 and is shown vertically binned and averaged in the lower half of the figure. The process of vertical binning sums the total charge accumulated in each of the 512 vertical pixel columns of the CCD array, resulting in a two rather than three-dimensional readout. The sweep speed of the streak camera was set to an average value

Figure 4.13: CCD image and vertically binned streaked emission profile from a picosecond tungsten laser plasma

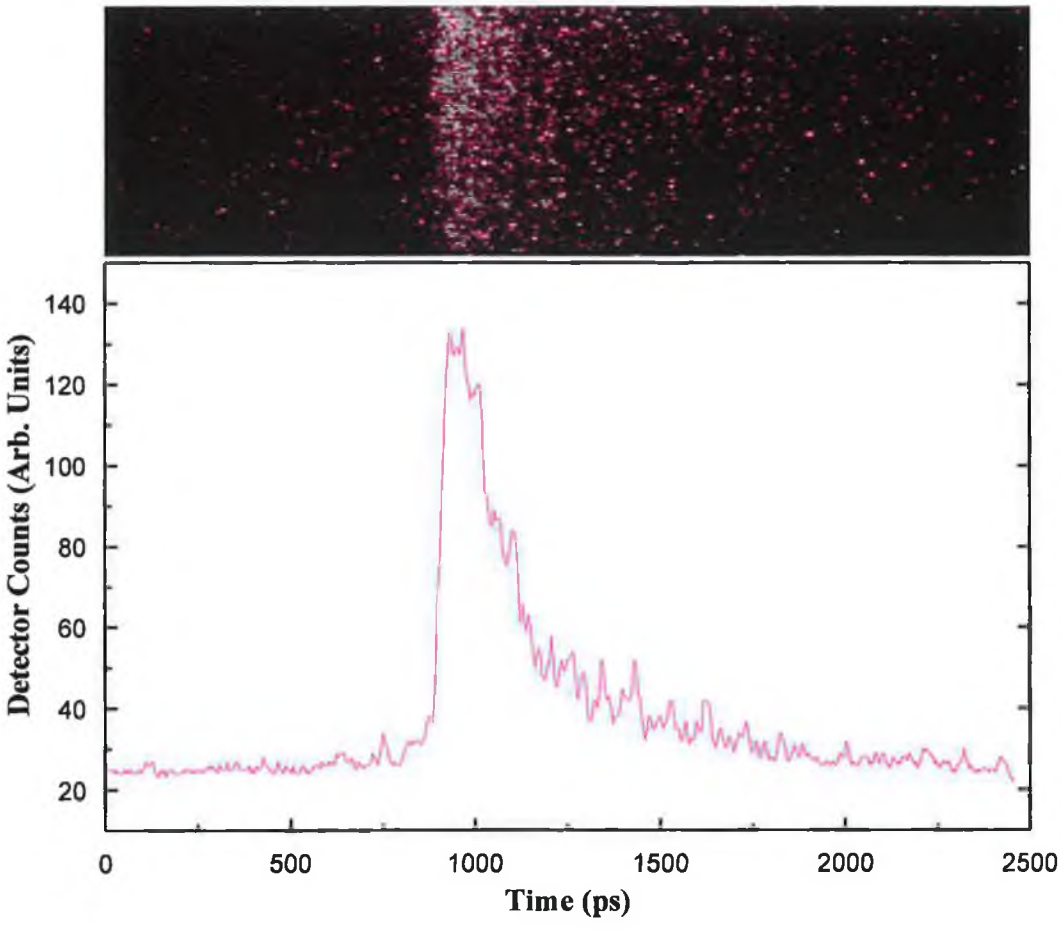

of 4.8ps/pixel and varied linearly from 5ps/pixel at pixel 1 of the Photonic Science™ CCD to 4.6ps/pixel at pixel 512. The FWHM of the tungsten emission profile shown is 210ps, a factor of 30 greater than the 7ps incident UV laser pulse. The 'Dark Star' intensifier gain was set to a value of 7 (see Chapter 3, Section 3.2.4.2.3) and the CCD video gain was set to its maximum value. For the streaked image shown in Figure 4.13 the static instrument response function has a FWHM of approximately 62ps. This represents a lower estimate (t_{static}) of the effect of instrument temporal broadening and therefore the emission duration obtained upon deconvolution of the measured streak profile (t_{meas}) with this approximate instrument function is an upper estimate of the true duration of XUV emission (t_{xuv}).

The XUV emission durations recorded for the high-Z materials tungsten, gold, lead and samarium are presented in Table 4.1. Each FWHM value represents the average of 7 different streak images, all of which were vertically binned and averaged over 130 pixels. For a given target material, all streak images were recorded using the same

Table 4.1: Summary of XUV continuum emission durations for a series of high-Z plasmas produced using 15-20mJ, 7ps, 248nm laser pulses at 10^{13}W/cm^2

Continuum Target	Average FWHM (ps)	Std. Deviation (ps)
Lead	133	± 42
Tungsten	194	± 43
Samarium	237	± 38
Gold	243	± 34

streak camera/image intensifier settings. The intensifier gain used for different target materials varied from 4 to 7, whereas the CCD video gain was set to maximum and the streak camera average sweep speed was set to 4.8ps/pixel for all targets studied. Determination of relative XUV flux yields from each high-Z laser plasma was not possible because different intensifier gain settings were used during recording of streak emission profiles from the different laser plasma types. Due to the fact that the intensifier gain varies from 4 to 7 (see Figure 3.29, Chapter 3), the width of the static instrument function used to record the streak profiles varies from metal to metal. A direct inter-comparison of the XUV emission durations from each metal plasma is not possible before deconvolution of the measured streak profiles with the relevant static instrument function. The process of deconvolution removes the effects of instrumental broadening, resulting in an approximation to the upper limit of the true XUV emission duration t_{xuv}.

The significant standard deviation associated with each FWHM measurement shown in Table 4.1 is due to a number of factors such as fluctuations of up to ±50% in picosecond laser pulse energy. Additional factors contributing to the observed fluctuation in XUV picosecond durations are explored further in Section 4.3.4. Also, XUV pulse durations were observed to vary with picosecond laser pulse energy rather than with nanosecond ASE pulse energy. This result is discussed further in Section 4.3.3 and Section 4.3.4.

Due to the level of noise on each of the streak profiles used to compile Table 4.1 and the associated difficulty in calculating the FWHM of such profiles, a locally weighted least squares curve fitting method was used to smooth raw data before calculation of the tabulated FWHM values. In this method, described by Chambers et al. (1983), a

weighted least squares linear fit is initially performed over a range of points (x_k, y_k) about each data point (x_i, y_i). The number of data points (x_k, y_k) within this range is $2q$, where q is a percentage of the total number of data points and the value of q is chosen by the user before iteration. The higher the percentage value selected the greater the degree of smoothing attained. When computing a smoothed value $(x_i, \bar{y}_i)$ for the data point (x_i, y_i), the weighting given to a point (x_k, y_k) within a distance d_i of (x_i, y_i) is

$$t_i(x_k) = T\left[\frac{x_i - x_k}{d_i}\right] \tag{4.3}$$

where d_i is the distance from x_i to its q^{th} nearest neighbour along the x-axis, and T, the weighting function is defined as

$$T[u] = \begin{cases} (1-|u|^3)^3 & \text{for } |u|<1 \\ 0 & \text{otherwise} \end{cases} \tag{4.4}$$

A fitted point $(x_i, \bar{y}_i)$ for a given raw data point (x_i, y_i) is determined using a weighted linear least squares method whereby values of the coefficients a and b are found which minimise the expression

$$\sum_{k=i-q}^{i+q} t_i(x_k)(y_k - a - bx_k)^2 \tag{4.5}$$

If $\bar{a}$ and $\bar{b}$ are the optimum values that achieve a minimum, then the fitted value $\bar{y}_i$ for a y_i raw data value at x_i is

$$\bar{y}_i = \bar{a} + \bar{b}x_i \tag{4.6}$$

This approximation method is particularly insensitive to anomalous data points due to the incorporation of a second weighting function based on calculated residuals r_i

$$r_i = y_i - \bar{y}_i \tag{4.7}$$

where this second weighting function, known as the robustness[2] weighting function is defined as

$$w(x_k) = B\left[\frac{r_i}{6m}\right] \tag{4.8}$$

where m is the median of the absolute values of the residuals r_i

$$m = \text{median}\,|r_i| \tag{4.9}$$

and B, is defined as

[2] This weighting function reduces the influence of anomalous data points on the ultimate curve fit, thus increasing the robustness of this curve fitting method.

$$B[u]=\begin{cases}(1-u^2)^2 & \text{for } |u|<1\\ 0 & \text{otherwise}\end{cases} \tag{4.10}$$

High values of r_i, corresponding to anomalous data points (e.g. noise fluctuations), are assigned a low weighting factor and their influence on the ultimate fitted curve is reduced following a second weighted least squares linear fit that now uses the product of both the original and the robustness weighting functions.

Following implementation of this method, the smoothed streak emission profiles show a slowly varying exponential decay with reduced noise content even when a low percentage of sample data points is chosen (q=1%). A simpler n-point (n = 3, 5, 9...) Savitsky-Golay smoothing function follows noise fluctuations in the streak profile more closely, resulting in increased modulation of the smoothed streak emission profile[3].

The overall shape of the streak profiles observed for all of the high-Z metal plasmas studied follow a similar trend. Initially, there is a sharp rise in XUV photon flux due to rapid heating of a dense plasma region followed by a more gradual, exponential fall off due to slower cooling during expansion of the plasma plume (see Figure 4.13). The XUV photon signal is also modulated by intrinsic, random fluctuations, which for a steady photon source emitting over a given time interval, are described by a Poisson probability distribution of the form (Barford 1985)

$$P(r,\mu)=e^{-\mu}\frac{\mu^r}{r!} \tag{4.11}$$

where $P(r, \mu)$, the probability of detecting r photons over a given time interval is dependent on μ, the expected (average) number of photons. In the case of a continuously varying (non-steady) photon signal emitted from a transient source such as a picosecond laser plasma, the degree of fluctuation (noise) on the measured streak profiles cannot be calculated as the square root of the mean number of photons detected, as would be the case for a steady photon source. Instead, the worst case signal to noise ratio (SNR) was estimated using equation (4.12), which is a good approximation for transient signals with noise fluctuating according to a Poisson statistical distribution

$$SNR=\frac{S_{max}}{\sqrt{S_{max}}}=\sqrt{S_{max}} \tag{4.12}$$

[3] Upon deconvolution, the single peak of streak emission profiles smoothed using the Savitsky-Golay method are resolved into a number of 'false' peaks due to the high degree of noise modulation on the smoothed pulse profile.

where S_{max} is the maximum (peak) value of the streak signal. The Poisson noise fluctuation on S_{max} is proportional to $\sqrt{S_{max}}$ and therefore the signal to noise ratio is just $\sqrt{S_{max}}$. Due to differing levels of XUV flux emitted by the various target materials, the signal to noise ratio in the observed streak profiles varied. This fact was accounted for during smoothing of the raw streak profiles using the locally weighted least squares curve fitting method by choosing different percentage values (q) and hence different degrees of smoothing for the streak profiles from different target materials. In Figure 4.14 a typical samarium streak emission profile is compared with a lead streak profile (—). Also shown is the locally weighted least squares curve fitted to each streak profile (—). The signal to noise ratio in the raw data streak profiles, calculated using equation (4.12), is 7.5 in the case of samarium and 10.3 in the case of lead. There is also additional noise on the streak signals due to the streak camera – image intensifier – CCD detection system. For a fixed intensifier gain, video gain and exposure time this

Figure 4.14: Comparison of lead and samarium XUV streak profiles (—) with the corresponding 1% (Pb) and 3% (Sm) locally weighted least squares curve fits (—)

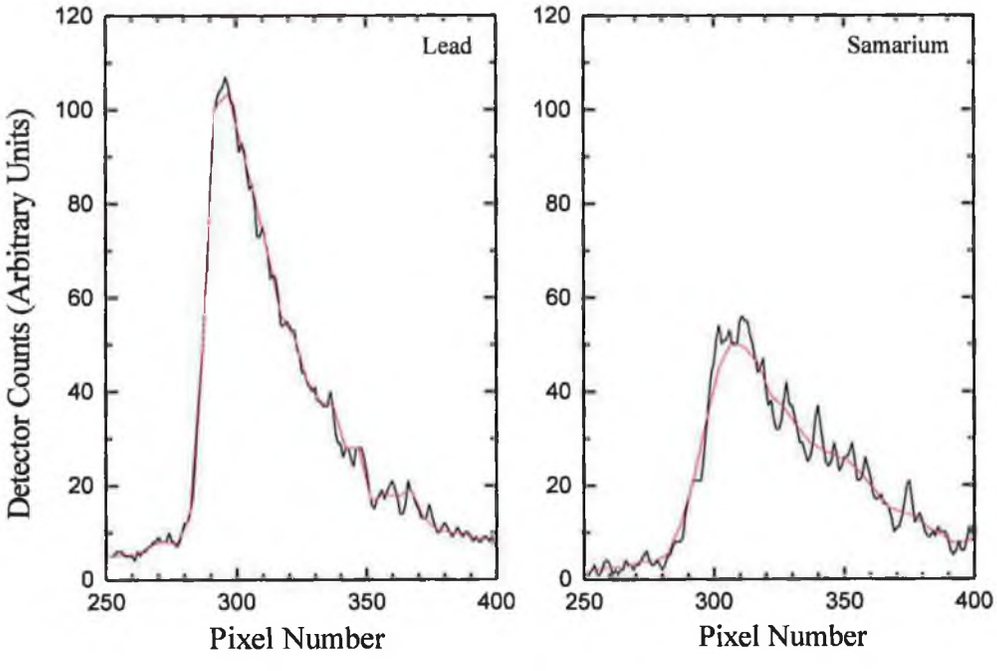

noise level is assumed to be fairly constant. For a set of streak results emitted from a single plasma type and recorded under the same conditions, the signal to noise ratio calculated using equation (4.12) served as a relative value which was then used to best determine the percentage of total raw data points selected for smoothing of streak

profiles. Because the signal to noise ratio was similar for similarly recorded streak profiles, only one percentage value (q) was required to smooth the set of seven streak profiles used to calculate an average picosecond XUV duration from each plasma type. For samarium streak profiles a value of q = 3% was chosen, compared with a value of q = 1% for the reduced degree of smoothing required for lead streak profiles (Figure 4.14).

Percentage values of q = 2% and q = 3% were chosen for tungsten and gold respectively depending on average signal to noise ratios calculated from the XUV emission profiles of each plasma type. The percentage value (q) selected was kept as low as possible in order to ensure that the curve was an accurate representation of the original streak profile in terms of peak height and FWHM. Excessive smoothing, which results when the percentage value selected is too high, leads to significant lowering of the peak value, and a corresponding increase in the FWHM of the streak profile.

From Table 4.1 it can be seen that the average FWHM is less than 243ps. This result, even before deconvolution, indicates a significant improvement in the temporal resolution attainable with a high-Z continuum backlighting source for use in DLP pump-probe type experiments. Previously, XUV continuum emission durations from nanosecond laser produced plasmas were comparable to that of the exciting laser pulse, typically a few to 10's of nanoseconds in duration (Mosnier et al. 1996). An upper estimate[4] of the true XUV emission duration, t_{xuv}, can be obtained by deconvolving the streak profiles used to calculate the above results with the appropriate static instrument functions. Results from such deconvolution calculations are discussed in Section 4.3.2.1.

4.3.2.1 Deconvolution of Measured Streak Emission Profiles with Static System Instrument Function

In order to determine an upper estimate of the true XUV emission durations from the various high-Z picosecond plasmas studied, a deconvolution algorithm was applied to

[4] The measured static instrument function gives a lower estimate of the combined streak camera and image intensifier instrumental broadening and therefore deconvolving it with a streak emission profile gives an upper estimate of t_{xuv}, the true XUV emission duration.

the measured streak data. A maximum likelihood deconvolution approach was chosen on the basis of its statistical reliability, which derives from its explicit inclusion of Poisson or Gaussian noise types. This eliminates the need for pre-filtering of raw data, which is a subjective process depending on the filter type chosen and its associated frequency bandpass, thus giving scope for a relatively high degree of subjectivity in the final deconvolved outcome. The 'SSRes' maximum likelihood code within the Spectra Calc™ (see reference list) software package accounts for a Poisson noise limited detector and was used to calculate all deconvolution results presented here.

The maximum likelihood algorithm requires the following information for successful implementation,

(i) $I(\mathrm{x}) = \{i_1, i_2, \ldots, i_n\}$, the measured streak profile that has been distorted by the measuring instrument (streak camera/image intensifier).

(ii) $M(\mathrm{x}) = \{m_1, m_2, \ldots, m_n\}$, the system impulse response (instrument) function, which is an un-streaked static image of the streak camera timing slit recorded using same video and intensifier gain settings used for recording of streak data.

(iii) An uncertainty estimate, which is the noise fluctuation expressed as a percentage of the data maximum.

$I(x)$, the measured data set represents the convolution ($\otimes$) of the instrument function $M(x)$ with $O(\mathrm{x}) = \{o_1, o_2, \ldots, o_n\}$, the true, undistorted streak profile, plus Poisson noise fluctuations, $N(\mathrm{x}) = \{n_1, n_2, \ldots, n_n\}$

$$I(x) = O(x) \otimes M(x) + N(x) \tag{4.13}$$

The maximum likelihood method calculates the most probable data set $O(\mathrm{x})$, which, based on the available knowledge of the measuring instrument performance and the degree of uncertainty in the measurement due to noise, would result in the measured streak profile $I(x)$. Each measured data point i_j is related to o_j by the equation

$$i_j = (o \otimes m)_j + n_j \tag{4.14}$$

where the probability of obtaining a particular value of i_j for a given value of o_j when the random noise n_j fluctuates according to a Poisson statistical distribution is

$$p(i_j|o) = \frac{(o \otimes m)_j^{\,i_j}\, \mathrm{e}^{-(o \otimes m)_j}}{i_j!} \tag{4.15}$$

The noise is un-correlated, in that, noise values n_j and n_i are independent of each other for all values of j and $i \leq n$ and ≥ 1. Therefore the likelihood of observing the data set $I(\mathrm{x}) = \{i_1, i_2, \ldots, i_n\}$ is the product of the probabilities for each i_j value

$$p(i_1, i_2, \ldots, i_n | o_1, o_2, \ldots, o_n) = \prod_{j=1}^{n} \frac{(o \otimes m)_j^{i_j} \, \mathrm{e}^{-(o \otimes m)_j}}{i_j!} \tag{4.16}$$

The ultimate aim of the maximum likelihood method is to maximise p, thus obtaining the most probable data set $O(\mathrm{x}) = \{o_1, o_2, \ldots, o_n\}$. Application of the maximum likelihood deconvolution algorithm to the streak profiles measured during this work provides an increased insight into the true temporal history of XUV light pulses emitted from the picosecond high-Z plasmas studied.

In order to calculate the degree of uncertainty in the streak data for input to the maximum likelihood algorithm, an exponential decay curve was fitted to the fall-off in the streak profiles, which were smoothed using the locally weighted least squares approximation method. The percentage values used to smooth the streak profiles obtained from the various metal plasmas were the same as those used in the previous section. The best-fit curve in all cases was found to be the sum of two exponentially decaying profiles with different decay times t_1 and t_2

$$y = y_0 + A_1 \, exp\left(-\frac{(x - x_o)}{t_1}\right) + A_2 \, exp\left(-\frac{(x - x_o)}{t_2}\right) \tag{4.17}$$

where A_1 and A_2 are constants and x_0 and y_0 define the x- and y-axis offsets. An example of such a curve fit is shown in Figure 4.15 for the 1% smoothed lead streak profile of Figure 4.14. Equation (4.12) can no longer be used to estimate the signal to noise ratio because noise fluctuations have been reduced due to smoothing of the streak profile. Instead, the fall-off in the smoothed streak profile and the exponential curve fit were subtracted (inset Figure 4.15) and the rms noise fluctuation, which is given as

$$\frac{n_{max} + |n_{min}|}{\sqrt{2}} \tag{4.18}$$

was calculated for each smoothed streak profile before deconvolution. n_{max} and n_{min} are the maximum and minimum values about y=0 (see inset in Figure 4.15).

Before deconvolution of a smoothed streak profile, the appropriate static instrument function was also smoothed with the same percentage value. The deconvolved result is an approximation to the true XUV emission profile and will be the same regardless of

Figure 4.15: Double exponential decay curve (- - -) fitted to the decay of a 1% locally weighted least squares approximation to a lead XUV streak profile (—) and the resultant subtraction of both curves (—)

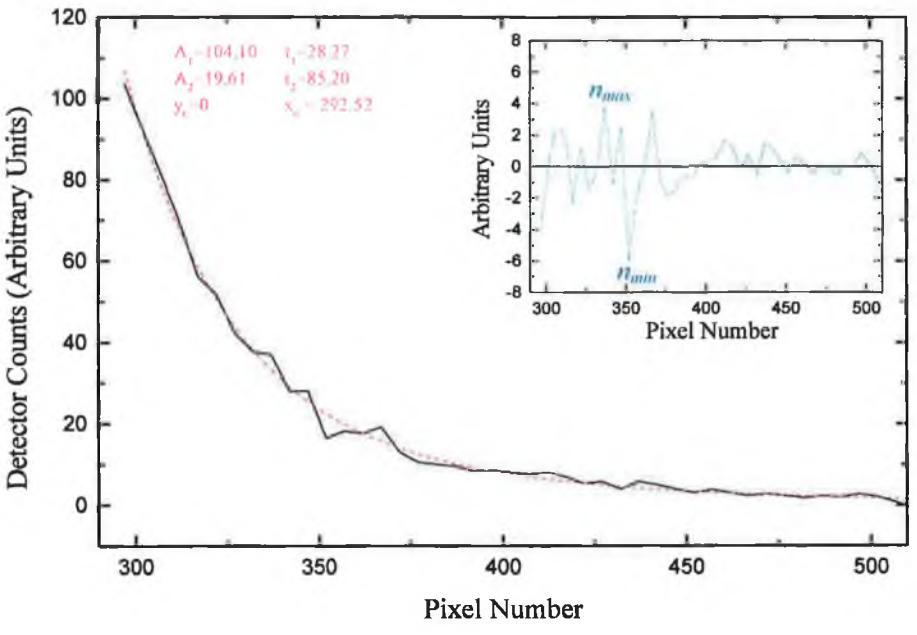

Figure 4.16: Static streak camera/image intensifier instrument function (—, — 1% smooth), lead streak emission profile (—, — 1% smooth) and deconvolved streak profile (—)

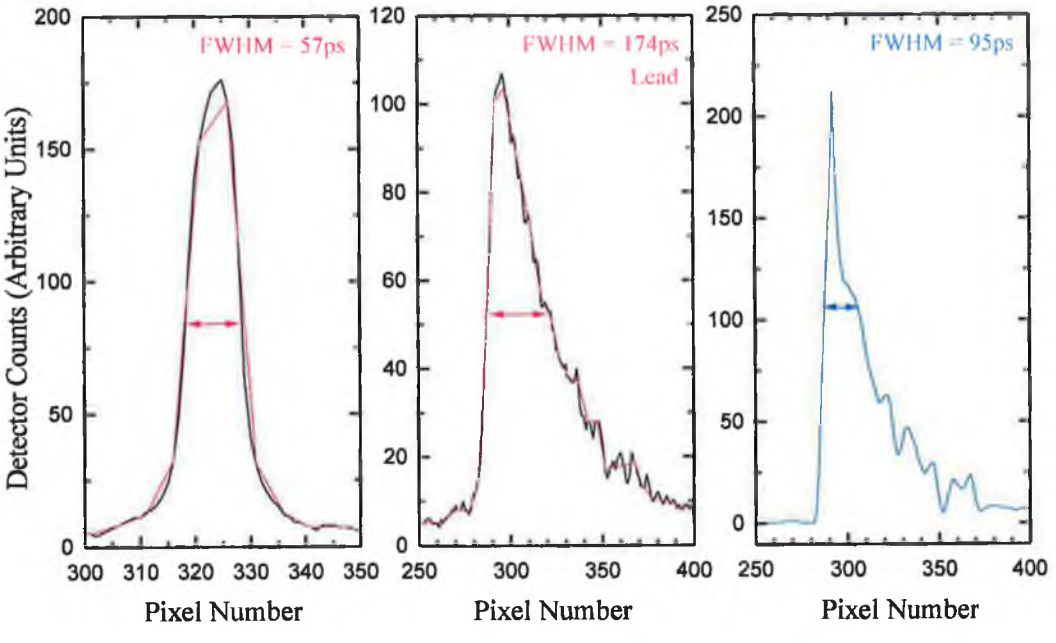

the degree (or absence) of smoothing applied to both the streak profile and the instrument function. The static instrument function and the 1% locally weighted least squares approximation to it used in the deconvolution of the 1% smoothed lead streak profile of Figure 4.14 are shown in Figure 4.16. Also shown is the deconvolved result following application of the maximum likelihood algorithm with an uncertainty estimate of 6.7%. Upon deconvolution with an instrument function whose FWHM = 57ps, the FWHM of the 1% smoothed streak profile is reduced by 45%, from 174ps to 95ps.

The results obtained for each high-Z metal following deconvolution and averaging of each of the same seven streak profiles used to obtain the mean FWHM values of Table 4.1 are presented in Table 4.2. These results indicate a similar degree of reduction in FWHM durations for each metal studied. Percentage reductions of 31 to 40% constitute a significant reduction in comparison with the un-deconvolved picosecond XUV emission durations of Table 4.1 and, as stated earlier, these durations represent an upper estimate of t_{xuv}. For all four metals, the standard deviation about the deconvolved average result is lower than the standard deviation before deconvolution (Table 4.1). This is due to the fact that the deconvolved curve, *O(x)*, is a calculation of the most probable streak profile when the degree of uncertainty due to Poisson noise is accounted for. Therefore measurements of the FWHM of deconvolved streak profiles *O(x)* do not

Table 4.2: *Summary of deconvolved picosecond XUV continuum emission durations for a series of high-Z plasmas, calculated using a maximum likelihood deconvolution algorithm*

Continuum Target	Average FWHM (ps)	Standard Deviation (ps)	%Decrease in FWHM
Lead	80	± 35	40
Tungsten	120	± 27	38
Samarium	163	± 20	31
Gold	146	± 15	40

vary as much due to local noise fluctuations as they do for un-deconvolved streak profiles *I(x)*. The standard deviation observed in the deconvolved results is attributable, as in the case of un-deconvolved results, to fluctuations of up to ±50% in the picosecond

laser pulse energy. The origins of this fluctuation are explored in Section 4.3.4.

The approximation (equation (3.16)) used by Murnane and co-workers (1989b) to determine t_{xuv} when t_{inst} (or t_{static}) and t_{meas} are known, yields significantly longer durations for t_{xuv} than the values obtained upon deconvolution of the streak profiles measured in this work. For example, in the case of the 1% smoothed lead streak profile of Figure 4.16 where t_{meas}=174ps (FWHM) and t_{static}=57ps (FWHM), t_{xuv} is calculated to be 164ps (FWHM), corresponding to a 6% reduction in FWHM. Equation (3.16) is based on the assumption that both the instrument function and measured streak pulses have a Gaussian profile. This approximation does not hold for the asymmetric streak profiles observed here, where a more detailed deconvolution procedure is required to remove instrumental effects and extract information on the true nature of picosecond XUV continuum emission.

4.3.3 Influence of Amplified Spontaneous Emission (ASE) on XUV Continuum Pulse Length

It has been widely observed that when Amplified Spontaneous Emission (ASE) generated in laser amplifiers is of sufficient intensity for plasma generation, and is incident on a target surface before the arrival of a short laser pulse (fs, ps), radiation emission durations in the XUV to X-ray (several keV) region are longer than in the case of a direct short pulse – target interaction (Murnane et al. 1989a,b, Kapteyn et al. 1990, Kieffer & Chaker 1994, Maksimchuk et al. 1996). This behaviour is a consequence of the increased density scale length (L) within the ASE generated pre-plasma. Consequently, thermal conduction and hydrodynamic expansion rates are reduced, resulting in slower cooling rates and therefore longer emission durations.

During the final amplification of picosecond pulses within the KrF excimer amplifier in the RAL laser system used during XUV emission studies, a 20ns (FWHM) ASE pulse of similar duration to that of the KrF pump cycle and at a repetition rate of 12Hz was produced. XUV emission durations were investigated for varying levels of ASE pulse energy ultimately delivered to the target surface. Control of ASE energy levels was achieved using a spatial filtering arrangement assembled at the rear of the KrF excimer

amplifier as shown in Figure 3.27 Chapter 3. Insertion of different pinholes/irises with varying diameters between the two lenses of the spatial filtering arrangement permitted control of the relative levels of nanosecond ASE and picosecond pulse energies in the final laser pulse delivered to the target. The first lens (marked 'a' in Figure 3.27) was a 5cm focal length plano-convex lens, which focused UV laser light onto a pinhole placed at its focus. ASE light, due to its spatial and temporal incoherence forms a larger focal spot than that of coherent picosecond light, and therefore the ASE content in the 20ns KrF laser pulse is attenuated upon traversal through the pinhole. A second, 35cm focal length plano-convex lens (marked 'b' in Figure 3.27), serves to expand and re-collimate the KrF pulse to ensure efficient depletion of the excimer amplifier energy volume during the second pass through it.

The duration of streaked XUV emission profiles was measured for plasmas produced when 7ps UV laser pulses were focused to an irradiance of ~10^{13}W/cm^2 onto tungsten tape targets by means of the same 35cm focal length *f*/7 plano-convex lens as that used for previous streak measurements (Figure 3.27). Also, the same experimental configuration, e.g. silver mirror pair, XUV bandpass filter, streak camera/image intensifier was used. The use of a variable iris and several pinholes covering a 100 to 500μm diameter range permitted variation of the ASE power/picosecond power ratio from 0.5 to 1.6. The results obtained are shown in Figure 4.17 and serve to demonstrate the insensitivity of XUV pulse durations to ASE over the range of ASE power/ picosecond power ratios attainable. Each data point in Figure 4.17 represents the average FWHM of five tungsten XUV streak profiles and is plotted with its associated standard deviation. The ASE pulse energy varied from ~8 to 45mJ depending on the pinhole/iris diameter used in the spatial filtering arrangement. The diameter of damage craters at the focus of the 20ns ASE/ps KrF laser pulse on the surface of the various tape and rod targets was measured to be ~100μm using an optical microscope. Additional surface damage extending over a region of ~450μm × ~200μm was due to the larger focal area of the ASE laser light. However most of the ASE pulse energy, like that of the picosecond pulse, is deposited over the ~100μm spot size. The resulting on-target irradiance due to ASE pulse energy alone ranged from ~5×10^9 to ~3×10^{10} W/cm^2 and was sufficient for plasma generation. As a result, ASE radiation arriving at the target surface before that of picosecond laser radiation produced a dilute nanosecond pre-plasma.

Figure 4.17: Plot of the mean tungsten XUV continuum emission pulse width vs. ASE power/picosecond power per 20ns KrF laser pulse (the picosecond energy per pulse is shown beside each data point)

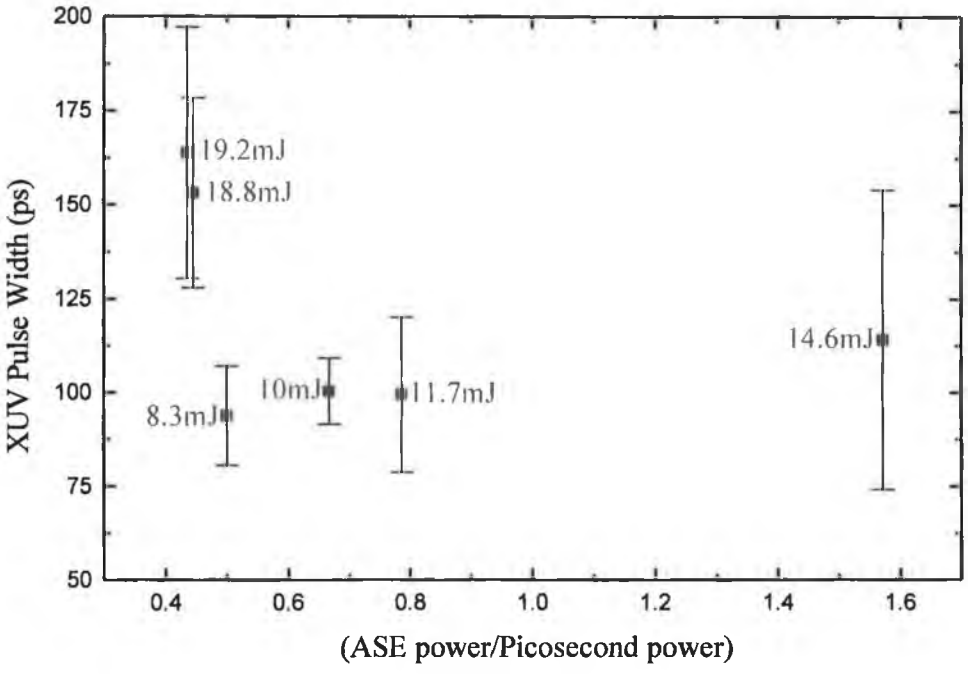

For all of the streak emission results discussed in Section 4.3.2 and Section 4.3.2.1 a 200μm diameter pinhole was inserted into the spatial filtering arrangement. This resulted in an average ASE pulse energy of 17mJ and an average picosecond pulse energy of 19mJ. If a single 7ps pulse was incident directly on the target surface with an on-target irradiance of 3.5×10^{13} W/cm^2 a plasma with a steep electron density profile and therefore a short density scale length (L) would be produced. The plasma scale length depends on the wavelength of the laser used and more importantly on the laser pulse duration (Wülker et al. 1994). Irradiating, for example, a tungsten target with a 7ps, 248nm laser pulse results in a density scale length L of ~0.4μm, which is determined using equation (4.19) from Kruer (1988),

$$L = c_s \tau \tag{4.19}$$

where τ is the duration of the laser pulse and c_s (ms^{-1}), the ion acoustic velocity, is

$$c_s = \sqrt{\frac{ZT_e}{m_i}} \tag{4.20}$$

where Z is the ionic charge state, T_e (in Joules) is the electron temperature and m_i is the ionic mass. Z and T_e were calculated to be ~20 and ~310eV for a tungsten plasma using the collisional-radiative equations (2.19) and (2.20) of Colombant and Tonon (1973) detailed in Chapter 2. The ion acoustic velocity, c_s, was therefore calculated to be ~0.6 ×

10^7 cm s^{-1} resulting in a plasma scale length of ~0.4μm after 7ps. For laser pulses ≥10ps in duration most of the picosecond pulse energy is absorbed at critical density ($n_c = 2 \times 10^{22}$ cm^{-3} at 248nm) rather than at near solid densities as is the case for shorter pulse durations (Umstadter et al. 1995). Time scales for x-ray emission in plasmas typically scale as L/c_s, whereby the plasma has expanded to twice its scale length (Bernstein & Comisar 1970). Therefore, for a direct picosecond pulse-target interaction, x-ray/XUV emission durations would be expected to be on the same order as that of the laser pulse. Such a result was observed by Davidson et al. (1990) where XUV (3 to 30nm) emission durations having a FWHM of 100ps were observed when a 100ps 532nm ASE-free laser pulse was incident on a high-Z thulium target.

XUV emission durations observed in this work were an order of magnitude greater than the laser pulse, e.g. ~100ps for tungsten (see Table 4.2). This is due to the arrival of ASE radiation at the target surface approximately 12ns prior to the arrival of a 7ps pulse. The electron density profile in the resulting nanosecond pre-plasma formed at ~1×10^{10} W/cm^2 is not as steep as in the case of a direct picosecond pulse – target interaction. As a result, when the 7ps pulse is incident on the pre-plasma ~12ns after its formation, the density scale length L is longer and is now ~27μm. The ion velocity of ~0.2×10^6 cm s^{-1} is lower due to lower values of Z (=4) and T_e (=2.5eV) in the ASE generated plasma. The 7ps pulse is absorbed at lower electron densities before reflection at its critical density in the longer scale length nanosecond pre-plasma (Wülker et al. 1994). Ion velocities will increase within the picosecond energy deposition region and assuming a value of $c_s \approx 10^7$ cm s^{-1}, the effective scale length for absorption of the 7ps pulse within the nanosecond pre-plasma will become ~10μm. The approximation L/c_s yields the experimentally observed X-ray/XUV emission durations which are on the order of ~100ps (see Table 4.2). X-ray/XUV emission durations are expected to increase in the longer scale length pre-plasma due to reduced recombination rates (which are directly proportional to n_e and inversely proportional to T_e) which pertain in a slower cooling nanosecond plasma plume. Wülker and co-workers (1994) observed a linear increase in X-ray emission durations with increasing pre-plasma scale length, a result which is implicit in the approximation that X-ray emission durations scale as L/c_s.

Throughout the experimental work, ASE levels could not be reduced below a minimum of 8mJ per 20ns KrF pulse and therefore the temporal and spectral properties of XUV

continuum emission could not be studied in a direct laser - target rather than laser - plasma regime. It is expected that elimination or at least reduction of ASE levels below that required for plasma generation would result in even shorter XUV emission durations than those observed.

Determination of more detailed information on the plasma conditions contributing to the observed spectral and temporal XUV emission requires a time-dependent numerical simulation such as that of Djaoui and Rose (1992). Changes in the electron density and temperature gradients during the hydrodynamic expansion of the plasma result in changes to the relative importance of various atomic processes such as collisional ionisation, excitation and de-excitation, photoabsorption, radiative de-excitation and spontaneous emission, radiative recombination and three body recombination, all of which determine the ionisation balance within the plasma plume.

4.3.4 Influence of Picosecond Laser Pulse Energy on XUV Continuum Pulse Length

Also shown in Figure 4.17 is the average picosecond energy per 7ps UV laser pulse. This value varied from ~8 to 19mJ due to varying degrees of attenuation, resulting from the use of different pinhole/iris diameters. For an ASE power/picosecond power ratio between 0.4 to 0.5 the XUV FWHM clearly increases with increasing picosecond pulse energy. This relationship is demonstrated further in Figure 4.18 where the mean XUV tungsten continuum emission pulse width is now plotted against the mean picosecond energy per 7ps laser pulse. A similar result has been observed by Workman et al. (1995, 1996) who observed an increase in soft X-ray (177 to 276eV) pulse widths from an aluminium plasma with increasing on-target irradiance (2×10^{15} to 2×10^{17} W/cm^2) using 0.4ps ASE-free 532nm laser pulses. Pelletier and co-workers (1996) also observed increased soft X-ray (200 to 300eV) emission pulse widths when increasing the on-target irradiance (1×10^{17} to 5×10^{17} W/cm^2) of 0.4ps ASE-free 527nm laser light incident on copper and tantalum target materials. Workman and co-workers (1995, 1996) attributed the increase in soft X-ray emission durations to increased electron temperatures (T_e) at higher laser irradiances. They noted that this dependence of soft X-ray emission duration on laser irradiance serves to indicate that emission at such

Figure 4.18: Dependence of the mean XUV continuum emission pulse duration from a tungsten plasma on the mean picosecond energy per 7ps UV laser pulse

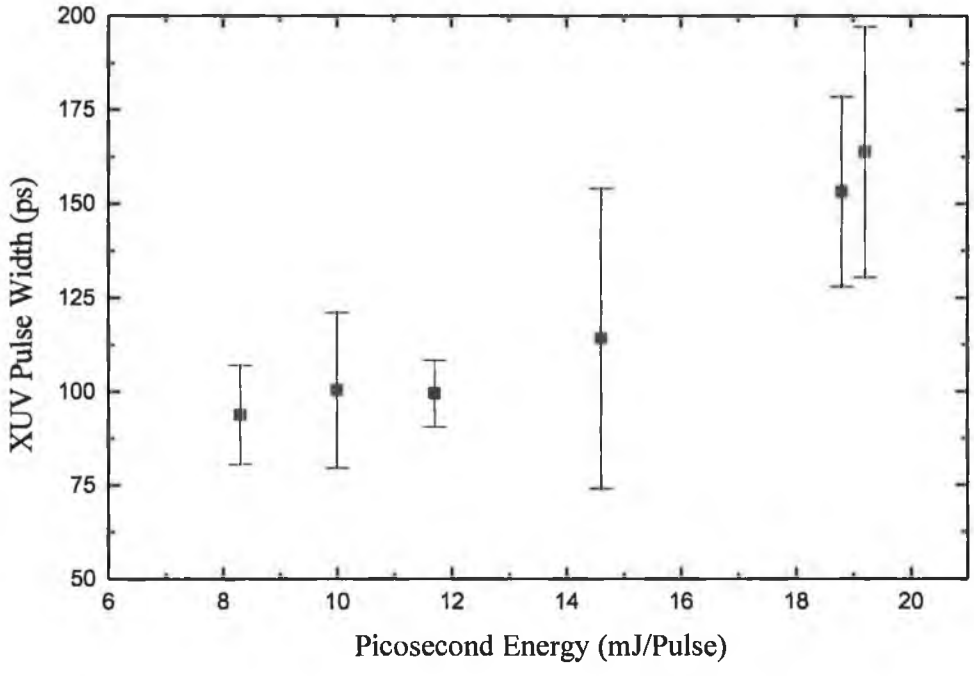

wavelengths is generated in highly collisional regions within the plasma plume. In such plasma regions, emission at a particular wavelength for an excited atom or ion changes linearly with the ratio of the population density of the upper exited level to that of the lower excited level (n_u/n_l) involved in the particular transition. The ratio of the collisional de-excitation rate to the collisional excitation rate and also the ratio of the recombination rate to the collisional ionisation rate both scale as

$$\exp(-h\nu_{ul}/kT_e) \tag{4.21}$$

where h is Planck's constant, ν_{ul} is the frequency difference between upper and lower states and k is Boltzmann's constant. When the peak electron temperature is high, equation (4.21) approaches one, resulting in a small difference between rates and therefore, for a given change in T_e there will be a small change in the ratio of n_u/n_l and also a small change in emission levels. As the plasma expands and cools, emission levels will fall off slowly resulting in longer emission durations than in the case where the peak electron temperature is initially lower and hence (from equation (4.21)) n_u/n_l varies more dramatically with changes in T_e. This effect, although observed at higher laser irradiances (2×10^{15} to 2×10^{17}W/cm^2) than used to produce the plasmas studied here (10^9 to 10^{13}W/cm^2), suggests that the XUV emission observed here also originates in dense, highly collisional plasma regions. If, on the other hand, collisional de-

excitation rates were lower than those of spontaneous emission rates (as would be the case in lower density plasma regions), spontaneous emission would constitute the main source of XUV photons. Consequently there would be very little dependence of XUV pulse durations on electron temperature and hence laser irradiance.

XUV continuum pulse durations increase slowly from 95 to 115ps for picosecond pulse energies between 8 and 15mJ. Above 15mJ pulse widths appear to rise more steeply. As mentioned previously, a 200μm diameter pinhole was inserted into the spatial filtering arrangement for all of the streak emission results discussed in Section 4.3.2 and Section 4.3.2.1. This resulted in an average energy of 19mJ per 7ps pulse incident on the various target materials. This high average picosecond pulse energy resulted in relatively long XUV continuum emission durations but also resulted in increased XUV photon flux. This result is important when applying the XUV continuum source to a pump-probe type application (e.g. a DLP experiment), where a balance between XUV photon flux levels and XUV pulse duration must be attained. Also, the atomic number of the source target material influences XUV/soft X-ray emission durations. Workman and co-workers (1995) observed that for a given on-target laser irradiance, the duration of X-ray (236eV) emission from a gold (high-Z) plasma was shorter than that from a copper (low-Z) plasma when ASE-free 0.4ps, 532nm laser pulses were used for plasma production. They attributed this effect to the increased electron density in the high-Z plasma plume and hence increased electronic conductivity and cooling rates.

The relatively large standard deviation associated with each set of measurements recorded for a particular ASE power/picosecond power ratio is due to fluctuations in the energy per 7ps UV laser pulse (see Figures 4.17 & 4.18, Table 4.1 & 4.2). The KrF based picosecond UV laser system fires two 7ps pulses separated by 12ns at 12Hz. The relative intensity of both picosecond pulses varies with respect to their temporal position relative to the gain profile of the KrF pump cycle. This time delay changes with respect to the 41MHz picosecond pulse train due to a jitter in the firing of the KrF amplifier. Therefore, Epulse1/Epulse2 varies widely (where 'Epulse' is the energy per picosecond pulse), whereas the average picosecond pulse energy, (Epulse1+Epulse2)/2, is more stable. The XUV streak camera, which is electronically synchronised to the repetition rate of the KrF amplifier, records over a 2.5ns timing window at 12Hz. Due to the jitter associated with firing the KrF amplifier, XUV plasma light resulting from a single 7ps pulse or either of two 7ps pulses amplified during the 20ns KrF pump cycle is detected

by the streak camera. As a result there is a fluctuation in both integrated XUV photon flux and XUV continuum emission durations due to differences in the energy per picosecond pulse. ASE laser energy alone was not sufficient to register an XUV signal on the streak camera when the picosecond pulse train was prevented from entering the KrF amplifier during firing. Therefore, streaked XUV signals resulted from a picosecond pulse – nanosecond plasma interaction at different times during the temporal evolution of the nanosecond pre-plasma. If the first picosecond pulse, incident on the pre-plasma during the early stages of the pre-plasma evolution, was the one detected, then the density scale length (L) would be shorter than in the case of the second picosecond pulse arriving 12ns later. Shorter density scale lengths result in shorter X-ray pulse durations (Murnane et al. 1989a, Wülker et al. 1994). Hence one would expect variations in the XUV continuum pulse duration (even when firing under fixed laser conditions) depending on which of the pair of picosecond pulses produced the XUV continuum emission pulse that was detected by the streak camera.

4.4 Conclusions and Future Development/Application of the Picosecond XUV Continuum Laser Plasma Light Source

The high-Z laser plasma light source developed and characterised both spectrally and temporally at the Rutherford Appleton Laboratory emits smooth line-free continuum over the 100 to 200eV XUV region on a ~100ps time scale. The ability to produce this source using a 'table-top' picosecond laser system permits versatility in its incorporation into different experimental regimes. The primary motivation for development of such a source during the course of this work was to further enhance the DLP photoabsorption technique. Emission durations on a picosecond time scale at XUV photon energies permit probing of the atomic/ionic dynamics of a sample plasma plume with increased atomic/ionic state selectivity due to increased temporal resolution. The XUV inner shell photoabsorption spectra of more highly charged ions produced early in the evolution of the sample plasma plume can now be probed. Previously, when nanosecond laser pulses were used for source plasma production, nanosecond XUV emission durations resulted in the integration of ionic photoabsorption over several nanoseconds, thus preventing detailed studies of the early (first 10ns) sample plasma evolution, during which short-lived higher ions are produced.

Future development of the picosecond XUV continuum source involving alteration of source properties such as XUV emission duration, XUV photon flux and radiation type (line or continuum) would permit increased application of the source to different pump-probe type applications having differing source requirements. XUV pulse durations can be decreased by elimination, or at least reduction, of ASE laser energy below the plasma production threshold. Reduction of ASE levels resulting in an increase in the short laser pulse contrast ratio is achieved using saturable absorbers at long laser wavelengths, e.g. 790nm (Maksimchuk et al. 1996), self-induced plasma shuttering (Murnane et al. 1991a), preferential amplification of higher intensity ps/fs pulses rather than lower intensity ASE radiation using harmonic conversion of the laser frequency (2ω, 3ω,..) (DeMaria et al. 1971), and spatial filtering coupled with dispersing prisms in a dye laser system (Bakker et al. 1999). Changing the excitation laser from the picosecond KrF system used in this work to a femtosecond system such as a Ti:sapphire laser (Backus et al. 1998) would result in deposition of laser energy at near solid densities over shorter density scale lengths, thus giving rise to shorter XUV/X-ray emission durations due to rapid plasma expansion and thermal conduction (Nickles et al. 1996). Higher XUV/X-ray yields have been observed when the increased volume of a pre-plasma is heated by a short laser pulse (Kyrala et al. 1994, Ahn et al. 1996, Steingruber et al. 1996). As mentioned previously such increased XUV/X-ray photon flux is achieved at the expense of emission durations, which are observed to increase. Grooved and low-density (porous) target surfaces such as those used by Murnane and co-workers (1994) to increase the conversion efficiency of laser energy to X-rays could be utilised in order to increase XUV/X-ray photon flux yields.

The incorporation of a toroidal optic between the picosecond XUV continuum source and the flat field grating in the experimental set-up of Figure 3.20 Chapter 3 would result in increased XUV flux falling on the streak camera timing slit, thus enabling dispersed rather than broadband XUV emission to be streaked. This permits a more detailed study of XUV emission particularly when studying line emission, which predominates later during plasma evolution. Low- to medium-Z targets with strong line emission in the XUV spectral region could be used for monochromatic imaging of a sample plasma of the same target material in order to map the dynamics of a particular atomic/ionic charge state with picosecond temporal resolution. Recently, such VUV monochromatic imaging of a calcium plasma with nanosecond temporal resolution from a nanosecond continuum source plasma has been performed (Hirsch et al. 2000).

Chapter Five

6p and 5d Inner Shell Photoabsorption and Emission Studies of ThI to ThVII

In this chapter the 6p → 6d and the 5d → $\overline{5,\varepsilon f}$ giant dipole resonances in the inner shell photoabsorption spectra of atomic thorium are compared to theoretical spectra computed using both the Relativistic Hartree-Fock (HFR) and the Relativistic Time Dependent Local Density Approximation (RTDLDA) methods. The atomic processes contributing to the formation and decay of the observed giant dipole resonance features are detailed. The collapse of the broad asymmetric 5d → $\overline{5,\varepsilon f}$ giant dipole resonance feature in atomic thorium to discrete Rydberg-like structure in ions up to Th^{6+} along the thorium isonuclear sequence has been measured in temporally resolved DLP studies using both the picosecond XUV continuum laser plasma light source developed in this work and nanosecond laser plasma light sources. The measured relative 5d photoabsorption cross sections of Th to Th^{6+} are compared to RTDLDA calculations.

5.1 Introduction and Key Experimental Objectives

The XUV inner shell photoexcitation and photoionisation spectra of lanthanide solids, molecules, atoms and ions in the vicinity of the 4d-subshell ionisation limits have been the subject of much experimental and theoretical research effort since the mid-1960's (Connerade et al. 1987). Giant dipole resonance features, appearing close to the 4d ionisation limits in the atomic photoionisation spectrum of the earlier lanthanides and preceding elements, collapse to Rydberg-like structure in the discrete 4d photoexcitation spectrum as one moves up isoperiodic (Richter et al. 1989a,b), isoelectronic (Köble et al. 1995), isoionic (Koizumi et al. 1996) and isonuclear sequences (Lucatorto et al. 1981). Similar studies in the vicinity of 5d subshell excitation in the actinide elements are limited to only a dozen or so examples (see Section 1.1.6, Chapter 1) and prior this work no studies on actinide ions have been published.

In order to address this issue, the 5d $\rightarrow$ $\overline{5,\varepsilon}$f giant dipole resonance in neutral atomic thorium and its collapse to Rydberg-like structure with progression along the thorium isonuclear sequence has been studied (Meighan et al. 2000). Thorium atoms and ions are produced in a plasma plume and the time-resolved DLP photoabsorption technique is used to probe the thorium atom/ion evolution within the plume at XUV photon energies of 70 to 150eV. The XUV energy region straddles the 5d-subshell ionisation limits, thus permitting the study of both 5d photoexcitation and photoionisation. Wendin (1984) and Wendin and Kerr Del Grande (1985) have computed the absolute 5d photoabsorption cross sections of thorium and uranium respectively. The relative photoabsorption cross section of atomic thorium measured here is compared with that calculated by Wendin (1984).

Wendin (1984) also predicted the existence of two strong resonance structures at lower photon energies, which he ascribed to a 6p $\rightarrow$ 6d giant dipole resonance feature in the discrete 6p photoexcitation spectrum of atomic thorium. In order to test this prediction, similar time-resolved DLP photoabsorption studies of a laser produced thorium plasma were performed in the VUV energy region of 17 to 32eV, within which photon energy range the 6p-subshell ionisation limits are located. This permitted observation and study of the 6p $\rightarrow$ 6d giant dipole resonance in atomic thorium for the first time (Meighan et al. 1999) and also the collapse of this resonance structure with increasing ionisation along the thorium isonuclear sequence.

Both of the measured 5d → $\overline{5,\varepsilon f}$ and the 6p → 6d giant dipole resonance profiles in atomic thorium have been compared, where possible, with existing solid state 5d and 6p photoelectron (Fuggle et al. 1974) and FEELS (Cukier et al. 1980) data, and also with molecular photoionisation results (Connerade et al. 1980b). Such comparisons provide a greater insight into the behaviour of the atomic giant dipole resonance feature (and therefore the spatial extent of the 5f and 6d wavefunctions) in the transition from the atomic, via the molecular, to the solid state thorium environment.

A number of computational tools have been used in the analysis of the atomic and ionic thorium relative photoabsorption cross sections. In particular, attention focused on the computation of photoabsorption features in neutral thorium (5d and 6p regions) and the higher ions ThV, ThVI and ThVII (5d region) due to the reduced complexity of their ground state configurations in comparison with those of ThII, ThIII and ThIV. Within the thorium plasma plume, complete spatial and temporal isolation of a given ground state atom/ion is impossible and therefore measured photoabsorption cross sections represent the integration of contributions from several atomic and ionic species in different stages of excitation. A Relativistic Time Dependent Local Density Approximation (RTDLDA) code (Liberman & Zangwill 1984) was used to compute absolute total photoionisation cross sections in the 5d region for ThI to ThVII. Also, the Cowan (1981) suite of atomic structure codes was used to perform term dependent Hartree-Fock calculations of the 6d and 5f effective potentials $V_{eff}(r)$ in ThI and ThV respectively, and also to compute the absolute cross section of ThI (Martins 2000) in the 6p and 5d energy regions.

All DLP experimental investigations performed at the CLPR in DCU utilised a nanosecond high-Z plasma as a source of both VUV and XUV continuum emission in order to probe the 6p and 5d regions of atomic and ionic thorium respectively. XUV pulse durations were on the order of 20ns, increasing to ~100ns at VUV photon energies. At the LSF in RAL, the picosecond XUV continuum source developed during this work (Meighan et al. 1997, 2000) was used to probe the atomic/ionic dynamics of a nanosecond absorbing thorium plasma in the 5d region, with increased temporal resolution (<200ps).

5.2 VUV Absorption Spectrum of Atomic Thorium

5.2.1 DLP Experimental Set-up and Procedure for VUV Photoabsorption Measurements in Atomic Thorium

The experimental system used for VUV normal incidence DLP photoabsorption studies has already been shown in Figure 3.2 Chapter 3. Atomic thorium absorption spectra were recorded using the Acton Research Corp.™ 1m normal incidence spectrometer. VUV light dispersed by this instrument was recorded by a Photometrics™ 1024×1024 back-thinned CCD (used in place of the PDA/MCP/OMA configuration shown in Figure 3.2). The CCD permitted recording of relative photoabsorption cross sections with increased spectral resolution and dynamic range. The CCD controller produced a single 5V TTL pulse as it opened a mechanical shutter in the CCD camera head for exposure to VUV radiation. This TTL pulse was used to trigger a Mitsubishi™ F1-20P Programmable Logic Controller (PLC), which in turn generated a $0 \rightarrow 24$V square wave pulse train with a variable number of pulses. This pulse train triggered the flashlamp and Q-switch circuitry of the SL404 and SL803 Nd:YAG lasers via the Stanford™ delay generator. VUV spectra were integrated over 100 laser shots for a 20s CCD exposure time and a 5Hz pulse train from the PLC. During spectral acquisition the CCD camera head was cooled to -35°C using a Peltier cooler.

The combination of a 50μm spectrometer entrance slit and a 24μm wide CCD pixel size resulted in a spectral resolution that varies from ~500 to ~1150 over the 35 to 80nm (35 to 15eV) energy region (see Section 3.1.3.5.1 Chapter 3). A secondary 500μm space resolving slit, placed between the thorium plasma and the entrance slit of the spectrometer (marked 'S' in Figure 3.2), was used to select a region of the absorbing plasma plume which had a vertical extent of ~300μm and a horizontal extent of ~ 500μm.

A 110mm focal length *f*/3.7 plano convex silica lens focused 280mJ of 1064nm laser light in 15ns (SL404) onto a cylindrical tungsten target resulting in an on-target irradiance of $\sim 6\times10^{10}$ W/cm^2. 830mJ, 15ns Nd:YAG laser pulses (SL803) were focused to a lower irradiance of $\sim 1.5\times10^{9}$ W/cm^2 on a planar thorium target using a 115mm focal length *f*/3.8 plano convex lens which was defocused by 10mm. The resultant spot size of ~ 3mm on the thorium surface, coupled with the reduced on-target irradiance,

resulted in the production of a large volume plasma with an estimated electron temperature, according to the collisional-radiative theory of Colombant and Tonon (1973), of approximately 4eV (equation (2.20) Chapter 2). The average ion stage was then calculated, using equation (2.19) Chapter 2, to be Th^{5+}. Such plasma conditions resulted in the production of a low temperature plasma plume favouring the study of atomic thorium rather than higher ion stages, particularly at long inter-laser time delays Δt. The first ionisation potential of ThI is 6.075 ±0.124eV (Sugar 1974) and due to the low initial electron temperature, which is reduced further at Δt = 600ns, the thorium ion density is expected to be low.

Absorption spectra were obtained using

$$\sigma(E)\overline{nl} = log\left(\frac{I_0(E)}{I(E) - I_f(E)}\right) \tag{5.1}$$

where $\sigma(E)$ is the absorption cross section at photon energy E and $\overline{nl}$ is the thorium column density integrated along the line of sight. $I_0(E)$ represents the tungsten continuum emission from the backlighting plasma, $I(E)$ is the total intensity on the detector in the presence of the absorbing plasma and $I_f(E)$, the emission from the thorium plasma. In order to reduce the amount of front plasma emission $I_f(E)$ falling on the detector, the thorium planar target was tilted by ~13° with respect to the optic axis of the spectrometer (see Figure 5.1). This was achieved by rotating the front face of the

Figure 5.1 *Schematic representation of the method adopted in both VUV and XUV DLP experimental regimes for the occlusion of front (sample) plasma emission $I_f(E)$*

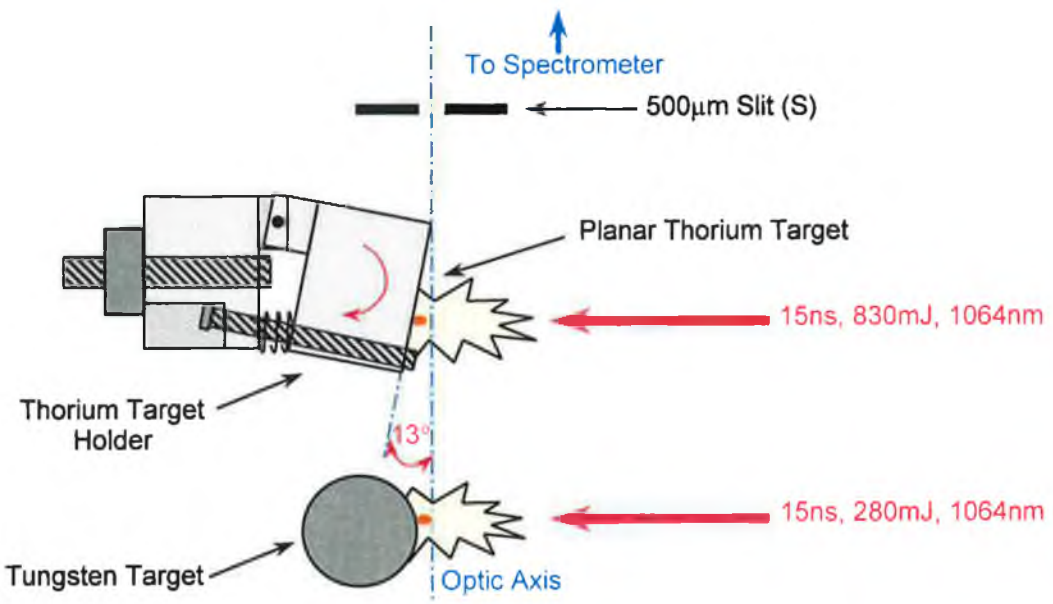

specially designed holder within which the thorium target was placed (see Figure 3.10 Chapter 3). As a result, the target holder edge nearest the 500μm space resolving slit 'S', occluded the brightest VUV emitting region of the thorium plasma plume.

5.2.2 6p→6d Giant Dipole Resonance in the VUV Photoabsorption Spectrum of Atomic Thorium

The optimum DLP time and space conditions for observation of the atomic thorium 6p photoabsorption cross section were determined to be Δt = 600ns and Δx = 0.5mm respectively. An inter-laser time delay of 600ns was determined to be sufficient in order to permit probing of predominantly neutral thorium species at a sufficient density for absorption studies. Previous time and space resolved DLP studies of laser-produced plasmas have shown that at time delays in excess of ~500ns the plasma plumes are composed almost exclusively of neutral species, particularly in the region close to the target surface (Carroll & Costello 1986, 1987, Kiernan et al. 1994). As can be seen from Figure 5.2, similar behaviour was observed in this experiment. The level of absorption

Figure 5.2 *6p relative photoabsorption cross sections in the 17eV (pixel 200) to 30eV (pixel 1800) energy region measured using the DLP technique for Δt = 500ns (—), 600ns (—) and 700ns (—). All photoabsorption cross sections are normalised in figure inset*

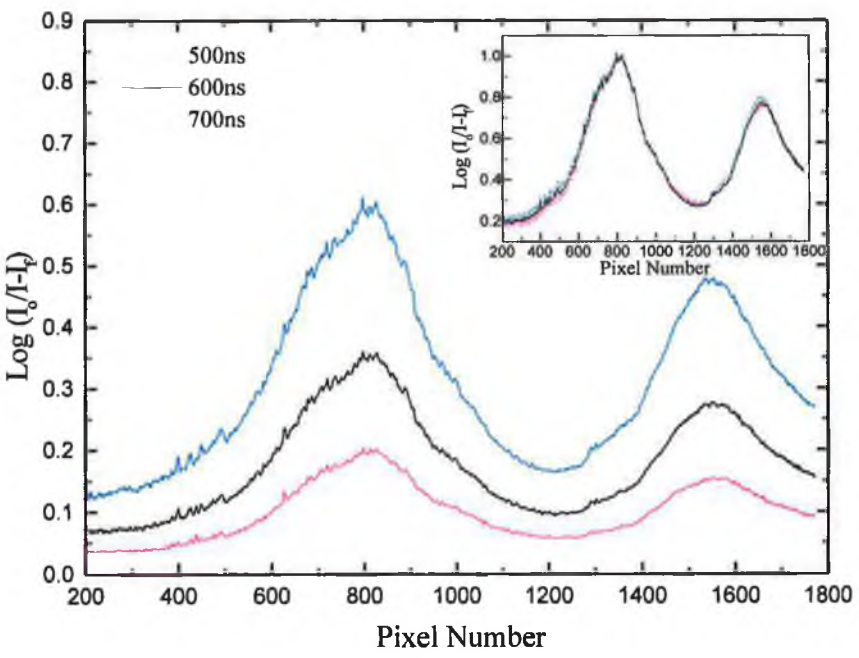

decreased as Δt increased due to a reduced column density, but the profile of the absorption spectrum did not change character for 500ns $\leq \Delta t \leq$ 700ns (see the inset of Figure 5.2 where each spectrum in normalised between 0 and 1). This indicated that VUV light was absorbed by atomic species in a similar state of excitation within the range 500ns $\leq \Delta t \leq$ 700ns. For $\Delta t \geq$ 800ns the plume density became too low to yield a sufficient absorption signal.

The value of Δx = 0.5mm that was chosen defines the distance between the edge of the thorium target holder nearest the 500μm space resolving slit 'S' and the optic axis. The actual displacement of the thorium target surface from the optic axis ($\Delta x'$) was variable from 2.1 to 3.4mm depending on the location of the laser focal spot over the 6mm width of the tilted thorium surface. The optimum value of $\Delta x'$ lay within this range and was chosen in order to obtain maximum reduction in the levels of VUV emission from the thorium plasma. During recording of the 600ns spectrum, the position of the laser focal spot on the thorium target surface remained unchanged. The front plasma emission signal $I_f(E)$ varied from a minimum of 0.6% to a maximum of 5.4% of $I_0(E)$. Before acquisition of $I_0(E)$, $I(E)$ and $I_f(E)$ a 20s background signal was accumulated with the CCD camera shutter closed. This background of typically 2000 counts per pixel was then subtracted from each of $I_0(E)$, $I(E)$ and $I_f(E)$.

The photoabsorption spectrum recorded at Δt = 600ns is compared with the calculated 6p photoabsorption cross section of Wendin (1984) in Figure 5.3. Oxygen I to V emission lines from a beryllium oxide plasma were used to calibrate the 15-33eV energy range shown to within an uncertainty of ±0.03eV. Wendin (1984) calculated the 6p photoabsorption cross section using a Local Density Random Phase Approximation (LDRPA) method. This method incorporates spin-orbit splitting of core levels (determined experimentally) into a non-relativistic framework for determination of atomic photoabsorption cross sections. The overall profile of the experimental spectrum is in good general agreement with the calculation apart from an energy shift of ~3 to 4eV. The twin peak structure in the spectrum is attributable to spin-orbit splitting of the 6p hole, with the higher energy peak broader and lower in both the theoretical and experimental spectra. The ratio of the maximum value of the lower energy peak to that of the higher energy peak is 1.31 in the experimental spectrum, which compares favourably to a value of 1.35 in the theoretical one. However, the computed peak

Figure 5.3 Comparison of relative (measured) and total (calculated, Wendin (1984)) 6p photoabsorption cross sections of atomic thorium

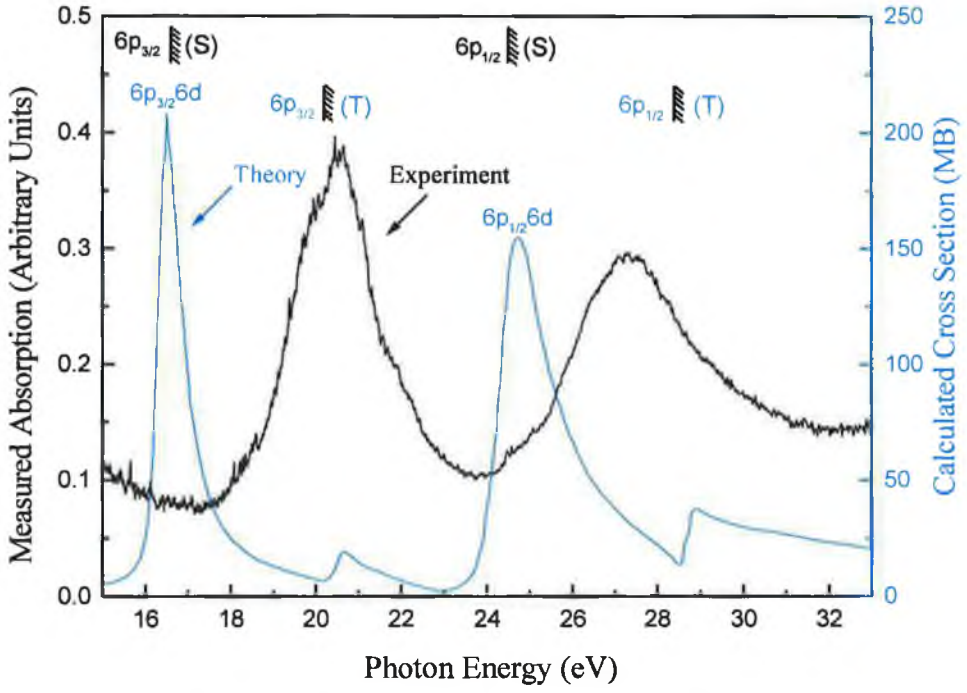

widths are narrower than those observed experimentally and relative peak positions do not coincide. Reasons for these discrepancies are firstly due to the fact that the LDRPA theory used by Wendin did not account for multiplet splitting, which if included would result in broader and lower calculated peaks. Secondly, thorium atoms in low-lying metastable states close to the atomic ground state could be populated at the electron temperatures attained during plasma production. Hence the measured spectrum may contain contributions from both ground and low-lying metastable states which are superimposed on each other. This issue is explored further at a later stage in Section 5.2.4 and Section 5.2.5.

Weak discrete structure between 15 and 20eV in the experimentally measured 6p photoabsorption spectrum (Figure 5.3) appears to arise from absorption by oxygen atoms within the thorium plasma plume. An oxide layer forms on the surface of thorium metal when it is exposed to air. Before acquisition of spectral data, this oxide layer was removed from the focal spot region of the target surface by pre-firing of the laser. However some residual oxygen appears to remain, even after firing several hundred laser shots. The weak spectral features in Figure 5.3 can be attributed to neutral oxygen 2s and 2p transitions, which are detailed in Table 5.1. A similar observation was made

by van Kampen and co-workers during 6p → 6d investigations in atomic uranium (van Kampen, 1998).

Table 5.1 *2s and 2p transitions in atomic oxygen (OI) modulating the 6p photoabsorption cross section of atomic thorium (ThI)*

	Atomic Transition	Energy Region (eV)
OI	$1s^2 2s^2 2p^4 \rightarrow 1s^2 2s^2 2p^3 3d$	15.34 - 15.44
OI	$1s^2 2s^2 2p^4 \rightarrow 1s^2 2s 2p^5$	15.64 - 15.66
OI	$1s^2 2s^2 2p^4 \rightarrow 1s^2 2s^2 2p^3 4d$	16.11 - 16.15
OI	$1s^2 2s^2 2p^4 \rightarrow 1s^2 2s^2 2p^3 ns$, n′d, n=4 to 11 & n′=3 to 16	16.34 - 17.11
OI	$1s^2 2s^2 2p^4 \rightarrow 1s^2 2s^2 2p^3 ns$, n′d, n=7 to 14 & n′=5 to 18	18.09 - 18.59

The $6p_{3/2,1/2}$ solid state ionisation limits obtained by photoelectron spectroscopy of a thorium film (Fuggle et al. 1974), shown in Figure 5.3, are labelled 'S' and lie at 16.6eV and 24.5eV respectively. The corresponding atomic limits calculated by Wendin (1984) lie, as expected, at higher energies and are labelled 'T' in Figure 5.3. If the computed cross section of Wendin (1984) is shifted to higher photon energies (~ +3 to +4eV) then it comes into reasonable coincidence with the measured spectrum and the corresponding peaks and limits are assigned as follows. The $6p_{3/2}6d$ peak lies at 20.6eV and the $6p_{1/2}6d$ lies at 27.2eV. The feature at ~21eV in the computed spectrum of Wendin which he attributes to the $6p_{3/2}$ limit may explain the small shoulder in the experimental spectrum at 24.4eV. In order to observe the feature predicted by Wendin to lie at ~29eV, the atomic photoabsorption spectrum of thorium was recorded using the 2.2 metre XUV grazing incidence spectrometer (Figure 3.14 Chapter 3) with improved spectral resolution and signal to noise ratio. As in 1m DLP 6p photoabsorption studies, a 110mm focal length *f*/3.7 plano convex lens focused ~300mJ, 15ns, 1064nm Nd:YAG (SL404G) laser light onto a cylindrical tungsten target. Also, a 100mm *f*/3.8 plano convex lens focused ~800mJ, 15ns, Nd:YAG (SL803) laser pulses onto a planar thorium target. The 6p photoabsorption spectrum recorded at Δt = 700ns, Δx = 0mm and averaged over 60 laser shots is shown in the inset of Figure 5.4. The 2.2m spectrometer entrance slit width was set at 20μm and aluminium VI to IX emission lines were used to calibrate the 25 to 40eV energy range to within an uncertainty of ±0.03eV. The spectral

Figure 5.4 *Comparison of relative atomic thorium 6p photoabsorption cross sections recorded using a 1m normal incidence spectrometer (—) and a higher-resolution 2.2m grazing incidence spectrometer (—)*

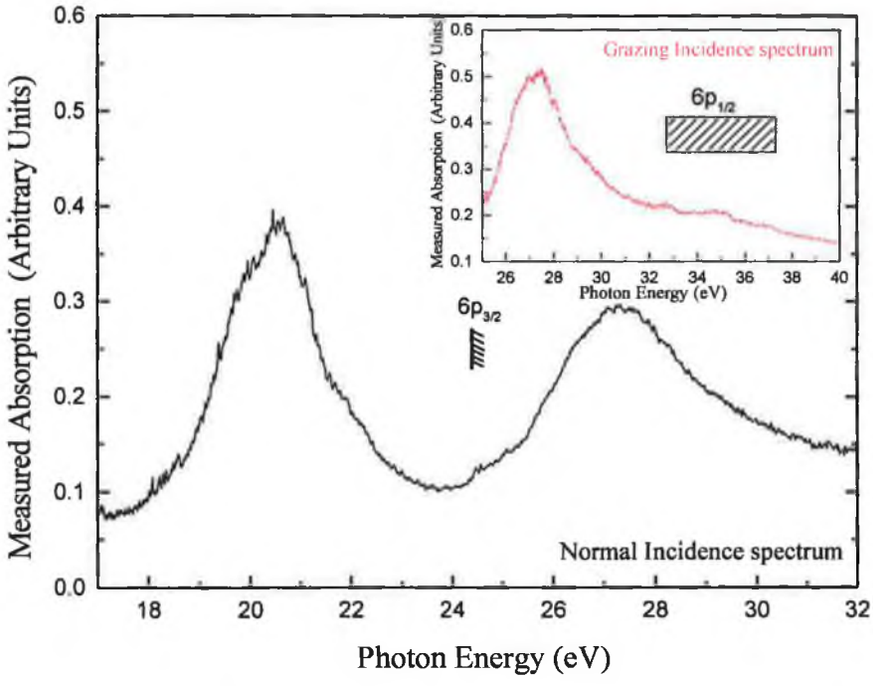

resolution varied from ~1860 at 25eV to ~1425 at 40eV. As in 1m studies, the brightest VUV emitting region of the thorium plasma was again occluded by tilting the thorium target holder (see Figure 5.1).

The lower energy limit of the 2.2m XUV spectrometer overlaps the high energy limit of the 1m VUV spectrometer and permits observation of the higher energy $6p_{1/2}6d$ peak at 27.2eV Three weak shoulders are observed at approximately 32.1eV, 34.0eV and 36.6eV in the 2.2m 6p photoabsorption profile. Adding 3 to 4eV to Wendin's value for the $6p_{1/2}$ limit brings it into close proximity with these features and hence they are assigned as $6p_{1/2}$ limits. The limits appear as a series of weak features in the measured spectrum while they appear as a single edge in the theoretical spectrum of Wendin, as the latter did not take into account fine structure.

5.2.3 Atomic Processes Contributing to the Observed 6p→6d Giant Dipole Resonance Profile in Atomic Thorium

The $6p_{3/2}6d$ and $6p_{1/2}6d$ peaks lie in the discrete 6p photoabsorption spectrum, below their respective $6p_{3/2}$ and $6p_{1/2}$ limits, and decay predominantly via autoionisation processes into adjacent continua. Both peaks can autoionise into both 7s and 6d valence continua and for the $[Rn]6d^27s^2$ ground state configuration of ThI, the available autoionisation channels following 6p photoexcitation are as follows

$$\begin{aligned}(\mathrm{ThI})\ 6p^6 6d^2 7s^2 + h\upsilon \xrightarrow[\text{photoexcitation}]{} (\mathrm{ThI}^*)\ 6p^5 6d^3 7s^2 &\longrightarrow (\mathrm{ThII})\ 6p^6 6d^3\, \varepsilon l \quad (7s^{-2}) \\ &\longrightarrow (\mathrm{ThII})\ 6p^6 6d^2 7s\, \varepsilon l \quad (6d^{-1}7s^{-1}) \\ &\xrightarrow[\text{autoionisation}]{} (\mathrm{ThII})\ 6p^6 6d 7s^2\, \varepsilon l \quad (6d^{-2})\end{aligned} \tag{5.2}$$

In experimentally measured spectra (see for example Figure 5.3), the $6p_{3/2}6d$ peak is higher, narrower and more symmetric, whereas the higher energy $6p_{1/2}6d$ peak is lower and broader with a more pronounced asymmetric profile. The increased relative width of the $6p_{1/2}6d$ peak is attributed to the fact that it is located above the $6p_{3/2}$ ionisation limit and can therefore decay via an additional $6p_{3/2}$ inner shell continuum channel. Decay via this additional channel requires a spin-flip to occur whereby the spin orientation of the 6p hole 'flips' from $6p_{1/2}$ to $6p_{3/2}$ during $6p^{-1}$ decay (following 6p photoexcitation) resulting in ionisation into the $6p_{3/2}$ continuum.

$$\mathrm{ThI}[Rn]6p^6 6d^2 7s^2 + h\upsilon \rightarrow 6p_{1/2}^{-1} 6d^3 7s^2 \rightarrow 6p_{3/2}^{-1} 6d^2 7s^2 + \varepsilon s, \varepsilon d \tag{5.3}$$

The inclusion of spin-flip decay channels of $6p_{1/2}6d$ excited states in relativistic Hartree-Fock (HFR) calculations performed by van Kampen and co-workers (2000) for 6p→6d excitations in atomic uranium was seen to contribute to the reduced peak height and increased relative width of the $6p_{1/2}6d$ peak. Similarly, in the case of atomic thorium, the inclusion of the spin-flip process in HFR calculations of the 6p→6d photoabsorption cross section produces a more accurate representation of the experimentally observed relative 6p peak heights and widths (see Section 5.2.5), thus confirming the importance of this process for atoms in this region of the periodic table.

The position of the $6p_{3/2}6d$ and $6p_{1/2}6d$ peaks in the discrete 6p photoexcitation spectrum below their respective $6p_{3/2}$ and $6p_{1/2}$ ionisation limits indicates that the 6d

wavefunction is collapsed in atomic thorium. Term dependent Hartree-Fock Cowan code (Cowan 1981) calculations of the 6d potential for all terms (^{1}S, ^{1}D, ^{1}G, ^{3}P, ^{3}F) of the [Rn]6d^{2}7s^2 ground state of atomic thorium indicate the existence of a single-well 6d potential which has a similar profile for all LS terms (Figure 5.5). There is no

Figure 5.5 *6d effective potentials calculated using the HFR method (Cowan 1981) for all terms (^{1}S, ^{1}D, ^{1}G, ^{3}P, ^{3}F) of the [Rn] 6d^{2}7s^2 ground state of atomic thorium (all curves overlap exactly)*

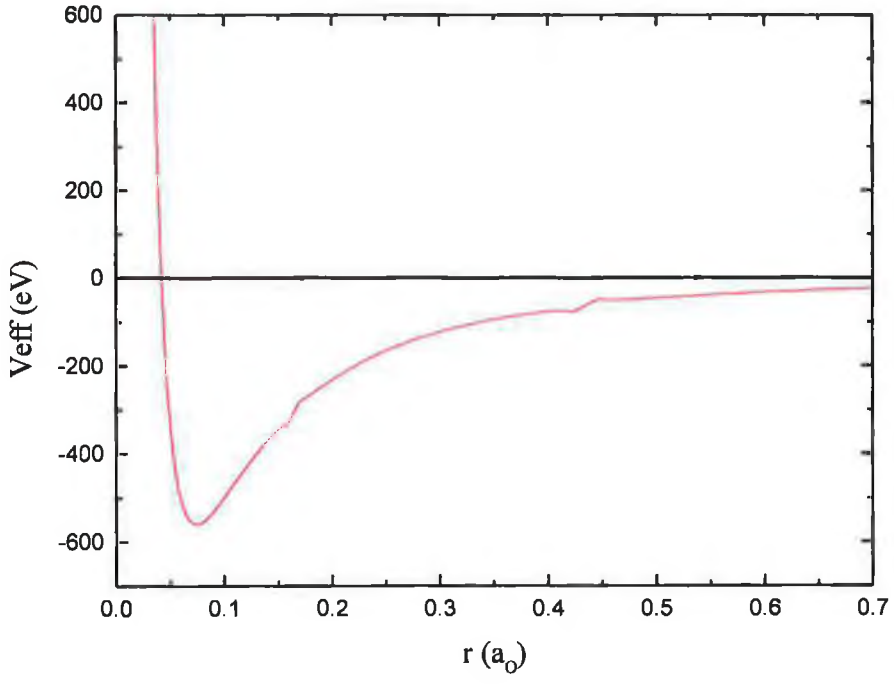

evidence of a double well potential that could support delocalised d eigenstates. Instead, the 6d wavefunction appears to be collapsed in atomic thorium and it appears that it is largely photoexcitation followed by autoionisation rather than direct photoionisation processes that contribute to the observed cross section. However, as mentioned in Chapter 1 Section 1.18, Kucas and Karazija (1998) have stressed the importance of computing individual wavefunctions for each electron (m) of an (nl)^m orbital in order to elucidate the true nature of wavefunction collapse. It is insufficient to use the same radial orbital for all electrons occupying a given nl subshell (for a given term). In specific, spin-polarised calculations can automatically permit the calculation of a one-electron radial orbital for each electron within a given nl subshell, resulting in a more accurate interpretation of the processes underlying the formation of giant dipole resonance features. Using this method for $4d^{10}4f^N \rightarrow 4d^9 4f^{N+1}$ transitions in lanthanide

atoms, Kucas and Karazija (1998) observed that the complete collapse of 4f orbitals does not occur for $4d^9 4f$ configurations until the middle of the lanthanide series at the transition from europium (Z=63) to gadolinium (Z=64).

In the Section 5.2.5, a relativistic Hartree-Fock method is used to calculate the 6p photoabsorption cross section of atomic thorium. Comparison between the calculated and measured (relative) 6p cross sections permits the investigation of the different atomic states of ThI that are thermally populated within the thorium plasma plume and consequently contribute to the measured 6p cross section. The electron/ion temperature, which changes during the temporal and spatial evolution of the plasma, will determine the ionisation balance and consequently the different absorbing thorium species at a given space and time within the plume. In Section 5.2.4 the temporal evolution of electron temperature within the thorium plasma plume has been calculated, and for an inter-laser time delay (Δt) of 600ns, it is used to predict the atomic states above the ThI $[Rn]6d^2 7s^2$ ($^3F_2$) ground state that are potentially populated when the thorium plasma is probed at this instant.

5.2.4 Calculation of the Temporal Evolution of Electron Temperature in the Expanding Thorium Plasma Plume

The temporal evolution of the electron temperature (T_e) within the thorium plasma plume, following termination of the exciting laser pulse (15ns, 1064nm, 800mJ), was calculated using a theoretical plasma model formulated by Singh and Narayan (1990) and is shown in Figure 5.6. After the initial heating/ablation phase that occurs during the nanosecond laser pulse, rapid expansion of the plasma plume is modelled as an adiabatic expansion in the vacuum environment.

$$X(t)\left[\frac{d^2X}{dt^2}\right] = \frac{kT_o}{M}\left[\frac{X_o Y_o Z_o}{X(t)Y(t)Z(t)}\right]^{\gamma-1} \qquad t > \tau \qquad (5.4)$$

Where $X(t)$, $Y(t)$ and $Z(t)$ are the dimensions of the expanding plasma plume in three orthogonal directions. X_o, Y_o and Z_o are the initial edges of the plasma after termination of the laser pulse of duration τ. k is the Boltzmann constant and T_o is the isothermal temperature after the initial heating of the laser pulse. γ is the ratio of the specific heat capacities at constant pressure and constant volume and M is the atomic mass of the

Figure 5.6 *Calculation of the temporal evolution of the electron temperature in a thorium plasma plume during adiabatic expansion in the vacuum environment following termination of the nanosecond laser pulse*

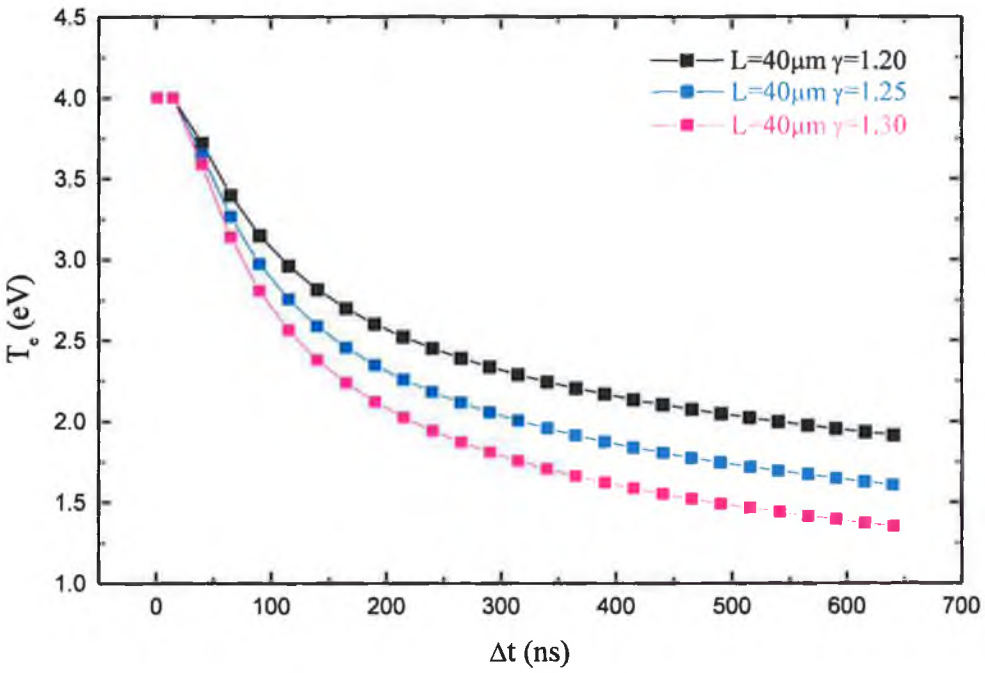

target species. The three curves shown in Figure 5.6 correspond to calculations with different values of γ. Singh and Narayan (1990) recommend using a value of γ between 1.2 and 1.3 for a plasma. X_o is the spatial extent of the plasma plume along the direction of the incident laser beam after termination of the laser pulse and it is perpendicular to the target surface for normal laser incidence. X_o is therefore equivalent to L, the plasma scale length, and was calculated to be ~40μm (equation 4.19 Chapter 4) for a thorium ion velocity, $c_s \cong 2.9 \times 10^5$ cm s^{-1} (equation 4.20 Chapter 4) when an average ionic charge state of Th^{5+} and a collisional-radiative equilibrium electron temperature of ~4eV are attained during the laser pulse. From Figure 5.6 it can be seen that the electron temperature has fallen to between ~1.4 and 1.9eV 600ns after plasma initiation within the range of $\gamma = 1.2$ to 1.3 and that the rate of decrease in T_e increases with increasing γ.

The closest lying ThI metastable terms to the ThI $[Rn]6d^27s^2$ ($^3F_2$) ground state and also low-lying metastable ThI* states are shown in Table 5.2. For an average calculated electron temperature of ~1.65eV (600ns after plasma initiation), the triplet terms of the ThI $[Rn]6d^27s^2$ configuration, lying within 0.62eV of the $^3F_2$ ground state term, are expected to have a significant population. Also, a few of the lower energy ThI* states, in

particular the ThI* [Rn]6d^{3}7s, may also be populated. States metastable with respect to the atomic ground state can be populated within the plasma plume by either electron impact or radiative recombination, or a combination of these processes. Depopulation of metastable states occurs via collisional processes since photon emission is dipole forbidden. In order to make an accurate estimate of the population of such states a knowledge of collisional excitation rates for production of various metastable states, radiative recombination rates (into metastable states), and electron-ion/atom collisional de-excitation rates is required. In addition, these rates must be included in a self consistent way with a hydro-code in order to fully model the evolution of metastable state populations in both space and time (see e.g. Djaoui & Rose 1992). Despite the unavailability of this information at present, HFR calculations of the 6p photoabsorption cross sections for the first five terms ($^3F_2$, $^3P_0$, $^3F_3$, $^3P_1$, $^3F_4$) of the ThI [Rn]6d^{2}7s^2 configuration have been used to generate a synthetic spectrum, which reproduces the major features such as overall profile, relative heights and relative widths of the $6p_{3/2}6d$ and $6p_{1/2}6d$ peaks in the experimentally measured 6p cross section (see Section 5.2.5).

Table 5.2 *Even ground state and excited state metastable configurations of ThI (from Blaise and Wyart 1992)*

Even ThI Configurations			Wavenumber (cm^{-1})	Energy (eV)
ThI	6d^{2}7s^2	($^3F_2$)	0	0
		($^3P_0$)	2 558	0.3172
		($^3F_3$)	2 869	0.3557
		($^3F_2$)	3 688	0.4568
		($^3P_1$)	3 865	0.4793
		($^3F_4$)	4 962	0.6152
ThI*	6d^{3}7s	($^5F_1$)	5 563	0.6897
ThI*	5f7s^{2}7p	($^3G_3$)	18 432	2.2853
ThI*	6d7s7p^2	†	20 000 ± 10 000	2.4797 ± 1.2399
ThI*	6d^4	($^5D_0$)	21 176	2.6255
ThI*	5f6d7s7p	($^5I_4$)	22 098	2.7398
ThI*	5f^{2}7s^2	($^3H_4$)	27 496	3.4091
ThI*	5f6d^{2}7p	($^5K_5$)	35 301	4.3768

† No specific term designation given

5.2.5 Term Dependent Hartree-Fock Calculations of the 6p Photoabsorption Cross Section of Atomic Thorium

A scaled configuration-interaction relativistic Hartree-Fock calculation of the 6p cross section of ThI was performed by Martins (2000) using the Cowan suite of atomic structure codes (1981). This calculation is compared with the experimental 6p relative photoabsorption cross section measured in this work. The initial interacting ThI [Rn]$6d^2 7s^2$, ThI* [Rn]$6d^3 7s$ and ThI* [Rn]$6d^4$ configurations chosen are shown in Table 5.3 (a,b,c). Inner shell 6p→6d photoexcitation produces the excited state configurations labelled (a′,b′,c′) which decay predominantly via autoionisation and interact with underlying continuum states produced by direct 6p photoionisation (a″,b″,c″). This interaction produces the asymmetric 'Fano' profiles (Fano 1961) of the observed 6p

Table 5.3 *Initial (a,b,c), excited (a′,b′,c′) and continuum (a″,b″,c″,a‴,b‴,c‴) configurations of ThI used in HFR atomic structure (Cowan code (1981)) calculations of the ThI 6p cross section*

Type of Configuration	Transition(s)	Configuration(s)
Initial states		(a) $6p^6 6d^2 7s^2$ (b) $6p^6 6d^3 7s$ (c) $6p^6 6d^4$
Discrete excited states	6p → 6d	(a′) $6p^5 6d^3 7s^2$ (b′) $6p^5 6d^4 7s$ (c′) $6p^5 6d^5$
Direct 6p ionisation	6p → εs, d	(a″) $6p^5 6d^2 7s^2$ + εs, d (b″) $6p^5 6d^3 7s$ + εs, d (c″) $6p^5 6d^4$ + εs, d
Autoionisation	$7s^{-2}$	(a‴) $6p^6 6d^3$ + εp, f
	$7s^{-1}\ 6d^{-1}$	(a‴) $6p^6 6d^2 7s$ + εp, f (b‴) $6p^6 6d^3$ + εp, f
	$6d^{-2}$	(a‴) $6p^6 6d 7s^2$ + εp, f (b‴) $6p^6 6d^2 7s$ + εp, f (c‴) $6p^6 6d^3$ + εp, f

resonance peaks. The calculated 6p cross sections for each of the $^3F_2$, $^3P_0$, $^3F_3$, $^3P_1$, $^3F_4$ terms of the ThI [Rn]$6d^27s^2$ ground state configuration are shown in Figure 5.7, where 200, 400, 600 and 800 MB are added to the $^3P_0$, $^3F_3$, $^3P_1$ and $^3F_4$ terms respectively to displace them sequentially for clarity. The overall double-peak structure due to spin orbit splitting of the 6p core hole is evident in all computed cross sections, with the higher energy $6p_{1/2}6d$ peak broader and lower in all cases. This is due to the inclusion of spin flip decay processes (such as (5.3)) in the HFR calculation, which results in broader autoionising resonances due to the shorter lifetime of excited states which now have additional continuum channels available for decay. Due to the increased width (ΔE_{ij}) of these autoionising levels, the resonances merge together resulting in apparently less discrete structures in the $6p_{1/2}6d$ peak than that of the $6p_{3/2}6d$ peak.

Figure 5.7 *HFR calculations of the 6p cross sections for the lowest $^3F_2$ LS term of the ThI [Rn]$6d^27s^2$ ground state configuration and four terms ($^3P_0$, $^3F_3$, $^3P_1$, $^3F_4$) of this configuration lying within 0.62eV of the $^3F_2$ term*

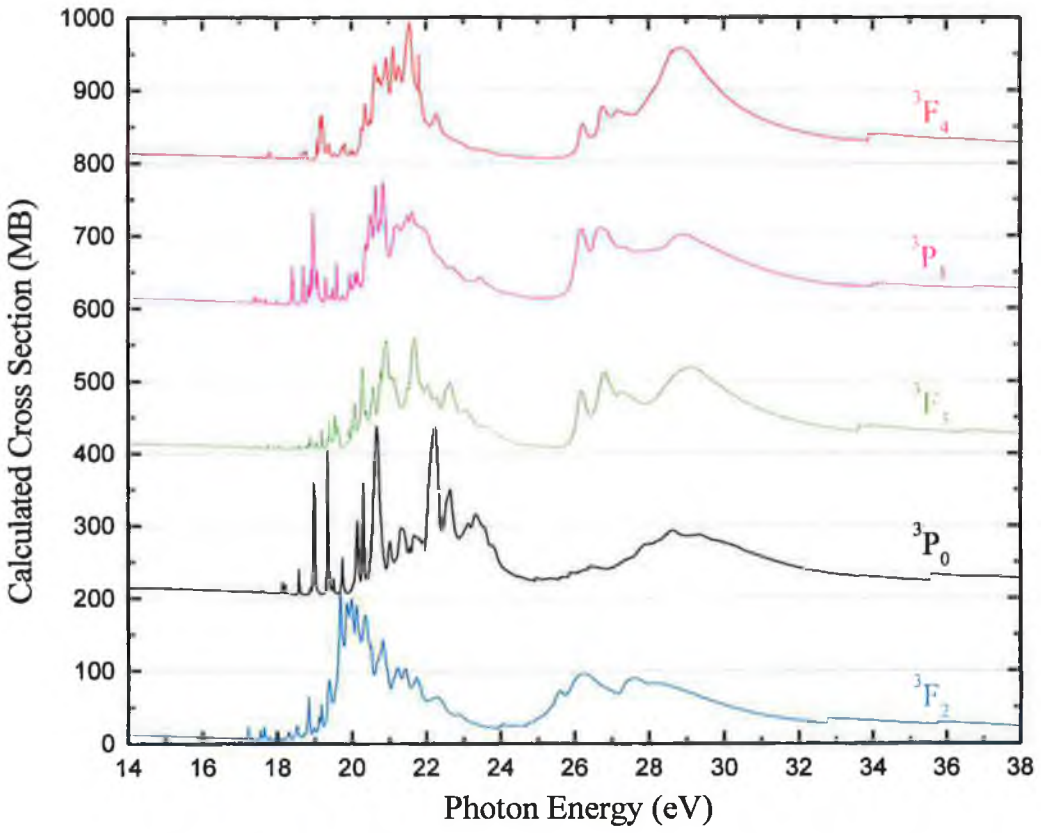

The computed 6p cross section of the lowest ($^3F_2$) term of the ThI [Rn]$6d^27s^2$ ground state configuration is compared to the measured 6p photoabsorption cross section in Figure 5.8. It is evident that consideration of this term alone is insufficient to describe

Figure 5.8 *Comparison of the measured 6p relative photoabsorption cross section of atomic thorium with a configuration interaction relativistic Hartree-Fock calculation for the lowest ($^3F_2$) LS term of the ThI [Rn]6d^{2}7s^2 ground state (HFR calculation is shifted by –1.2eV)*

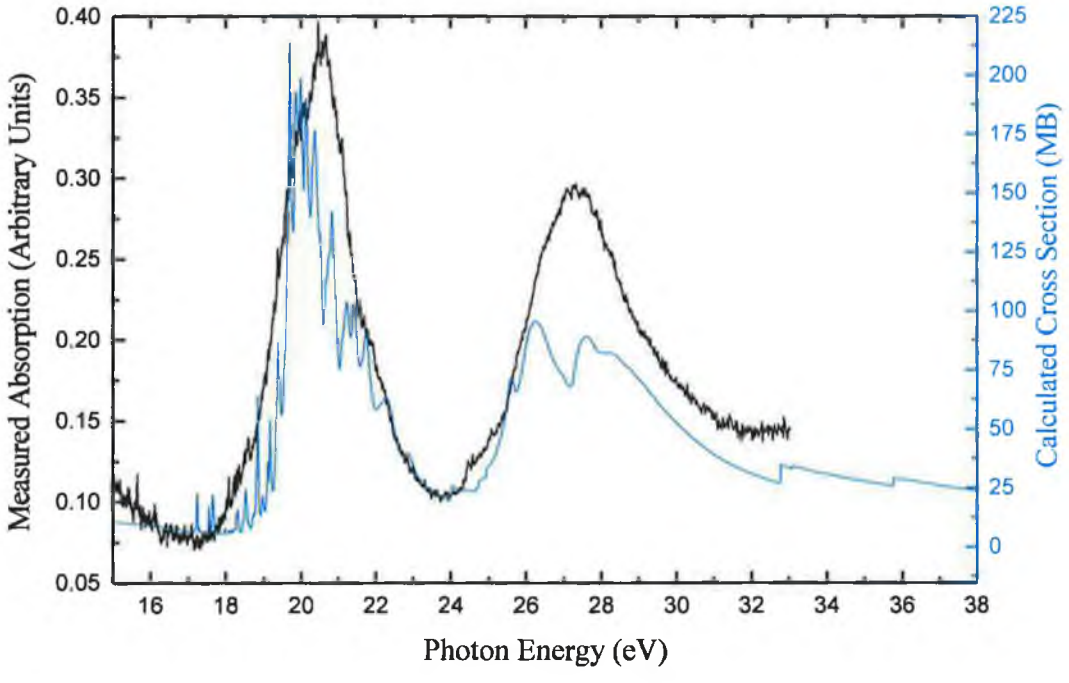

the experimental cross section due to the high degree of structure and also the fairly large discrepancy in relative peak heights. Following convolution of the calculated $^3F_2$ cross section with a 0.03eV FWHM Lorentzian profile, simulating the instrument function of the VM-521 1m normal incidence spectrometer at 25eV, the high degree of structure remained unchanged.

As mentioned in Section 5.2.4, at an electron temperature of ~1.65eV 600ns after plasma initiation, it is possible that a number of even parity states are contributing to the absorption signal. A synthetic spectrum was computed by performing a weighted sum over the first five terms of the ThI [Rn]6d^{2}7s^2 ground state configuration. The total synthetic spectrum is

$$\sigma_t = \frac{\sum_i \omega_i \sigma_i}{\sum_i \omega_i} \tag{5.5}$$

where σ_i is the cross section of the ith term and ω_i, the statistical weighting of each term, is given by

$$\omega_i = g_i \exp\left(-\frac{E_i}{kT}\right) \tag{5.6}$$

where thermodynamic equilibrium is assumed. g_i is the statistical weight of each lower level, i.e. $g_i = (2J+1)$, where J is the total angular momentum quantum number of the term under consideration. E_i is the energy of the ith term above the ground state $^3F_2$ term (see Table 5.2). kT is the plasma temperature, which is equal to the electron temperature when the plasma plume has thermalised after the initial heating of the laser pulse has terminated and electrons, atoms and ions are assumed to be at the same temperature. The result of this calculation is shown in Figure 5.9, where the computed synthetic

Figure 5.9 *Comparison between measured 6p photoabsorption cross section of atomic thorium (—) and a synthetic 6p → 6d cross section (—) computed by summing statistically weighted HFR cross sections for the $^3F_2$, $^3P_0$, $^3F_3$, $^3P_1$, $^3F_4$ terms of the ThI [Rn]6d^{2}7s^2 ground state configuration (HFR calculation is shifted by –1.2eV)*

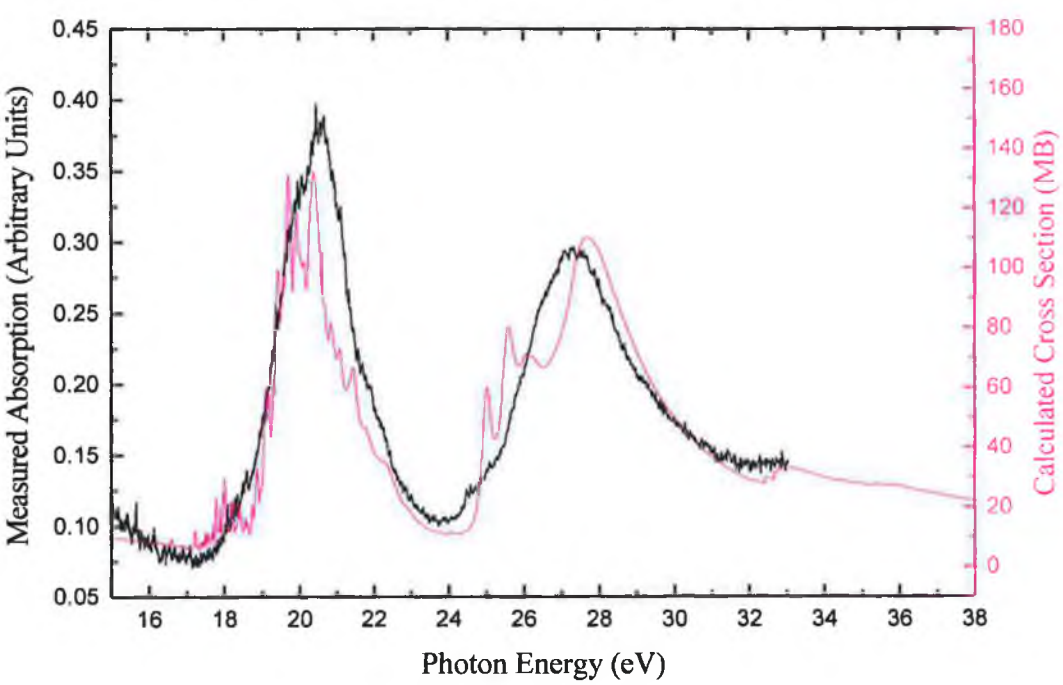

spectrum is compared to the measured 6p relative photoabsorption cross section. This results in a more accurate reproduction of the experimentally observed cross section than in the case when only the $^3F_2$ term is considered. There is improved agreement between relative peak heights and peak widths, with a reduced level of structure in the $6p_{3/2}6d$ peak.

In the HFR calculation, the metastable states ThI* [Rn]5f7s^{2}7p and ThI* [Rn]6d7s7p^2 lying between the ThI* [Rn]6d^{3}7s and ThI* [Rn]6d^4 states (see Table 5.2) were

neglected due to the complexity of their term structure and hence the increased computational difficulty. Excitation from terms of the ThI $[Rn]6d^27s^2$ configuration to excited configurations containing 5f and 7p electrons would result in computation of an increased number of autoionising resonances that will merge together to result in the appearance of reduced structure within each of the 6p peaks thereby improving overall comparison with experiment.

5.2.6 Evolution in the Profile of the 6p Photoabsorption Cross Section along the Thorium Isonuclear Sequence

The profile of the 6p→6d giant dipole resonance in atomic thorium changes dramatically along the thorium isonuclear sequence. Observation of this effect is achieved experimentally by reducing the inter-laser time delay (Δt) in order to probe higher stages of ionisation produced during earlier stages in the evolution of the thorium plasma plume. The evolution from two broad, mainly featureless autoionising resonances in the 6p photoabsorption cross section of ThI, to highly structured spectra of ionic thorium, with decreasing Δt, is shown in Figures 5.10 to 5.12. This collapse of the neutral resonance profile is indicative of the transfer of oscillator strength from inner shell excitations 6p→6d in ThI, to valence excitations 6p→nl in thorium ions such as $Th4^+$ ($6p^6$) and more highly charged thorium ions.

The 6p relative photoabsorption cross sections shown in Figures 5.10 to 5.13 were recorded using the DLP experimental technique on the VM-521 1 metre normal incidence spectrometer at the CLPR (see Figure 3.2 Chapter 3). The Photometrics™ 1024×1024 back-thinned CCD (detailed in Section 3.1.3.4.1 Chapter 3) was used to record spectra in place of the PDA/MCP/OMA configuration shown in Figure 3.2.

The photoabsorption spectra shown in Figures 5.10 to 5.13 were recorded under similar experimental conditions to those used in recording the 6p neutral profiles shown in Figure 5.2 Chapter 5. A 110mm focal length $f/3.7$ plano convex silica lens focused ~280mJ of 1064nm laser light in 15ns (SL404) onto a cylindrical tungsten target resulting in an on-target irradiance of $\sim 6\times10^{10}$ W/cm^2. 830mJ, 15ns Nd:YAG laser pulses (SL803) were focused to a lower irradiance of $\sim 1.5\times10^{9}$ W/cm^2 on a planar

Figure 5.10 *Evolution in the profile of the 6p relative photoabsorption cross section of thorium from predominantly neutral species for an inter-laser time delay $\Delta t \geq 500ns$, to ionised species for $\Delta t \leq 500ns$ ($\Delta x=0.5mm$, $\Delta x'=2.1$ to $3.4mm$). Each spectrum is vertically displaced for clarity*

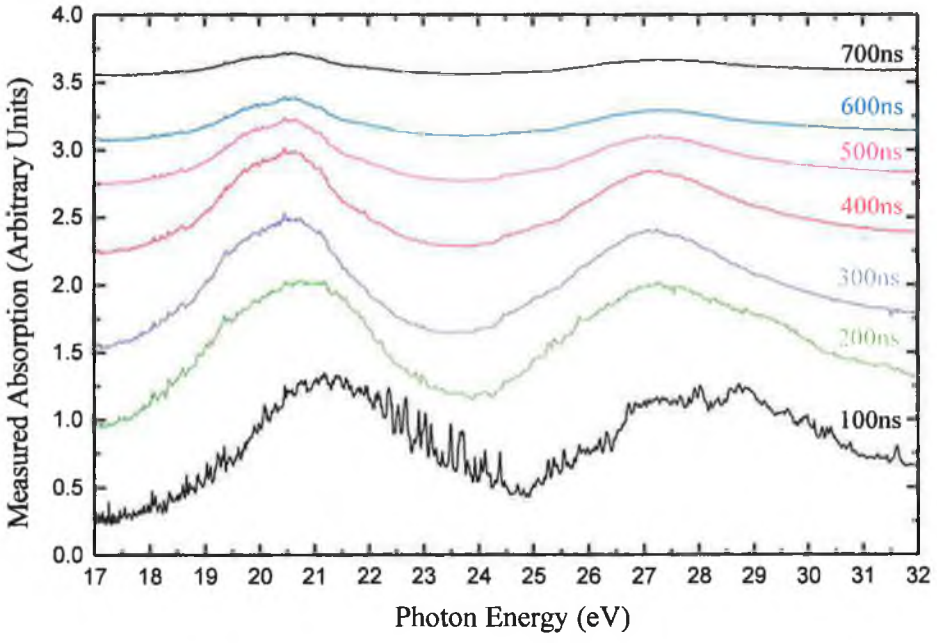

Figure 5.11 *Evolution in the profile of the 6p relative photoabsorption cross section of ionic thorium for inter-laser time delays, $30ns \leq \Delta t \leq 50ns$ ($\Delta x=0.1mm$, $\Delta x'=1.6$ to $2.9mm$). Each spectrum is vertically displaced for clarity*

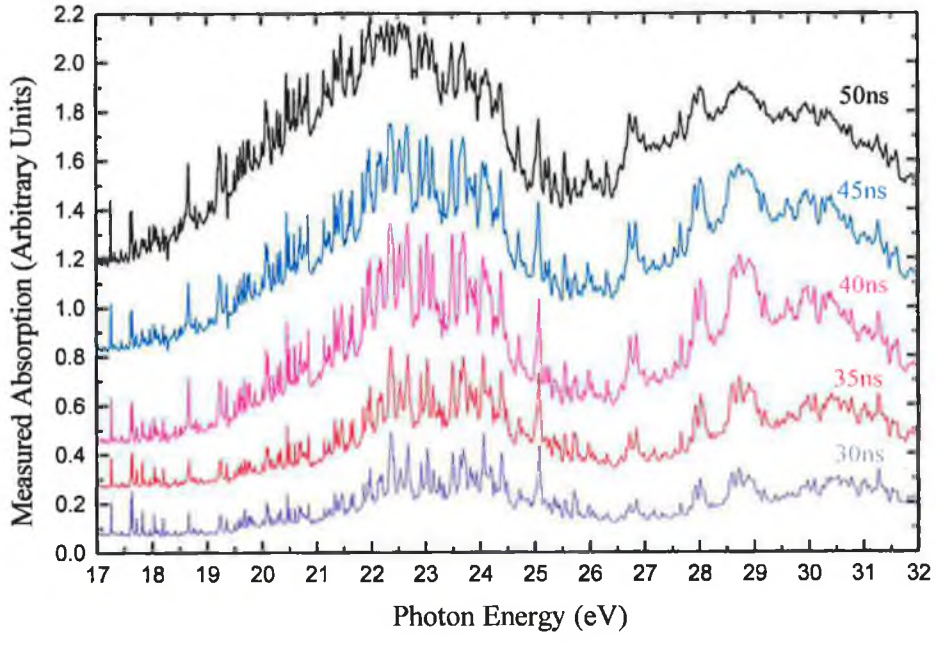

Figure 5.12 *Evolution in the profile of the 6p relative photoabsorption cross section of ionic thorium for inter-laser time delays, 5ns ≤ Δt ≤ 25ns (Δx=0.1mm, Δx'=1.6 to 2.9mm). Each spectrum is vertically displaced for clarity*

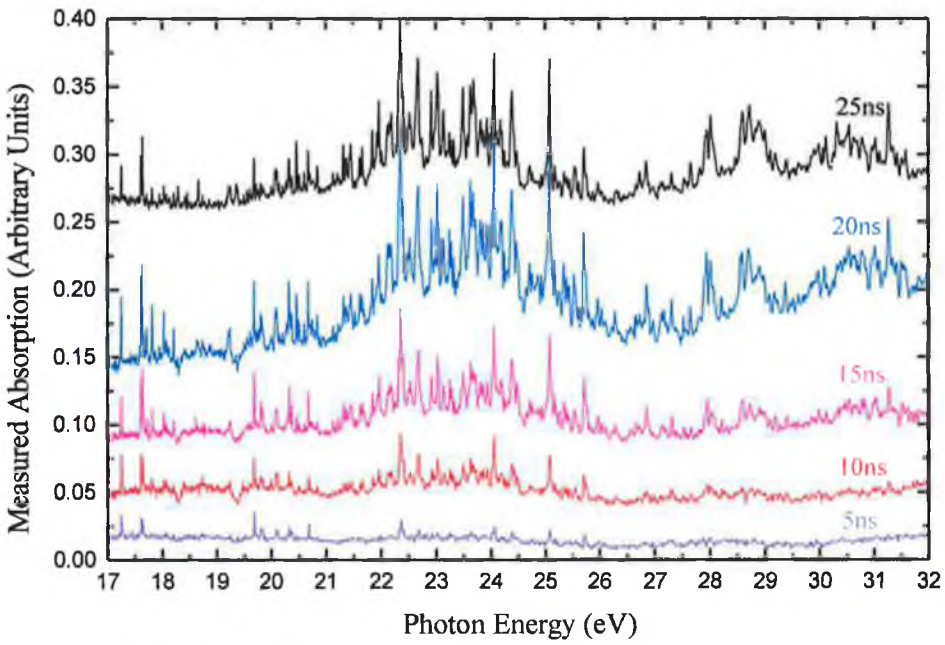

Figure 5.13 *Comparison of the 6p relative photoabsorption cross section of ionic thorium recorded at an inter-laser time delay of Δt=25ns (Δx=0.1mm, Δx'=1.6 to 2.9mm) with the VUV emission signal from a thorium plasma (Δx=1.0mm)*

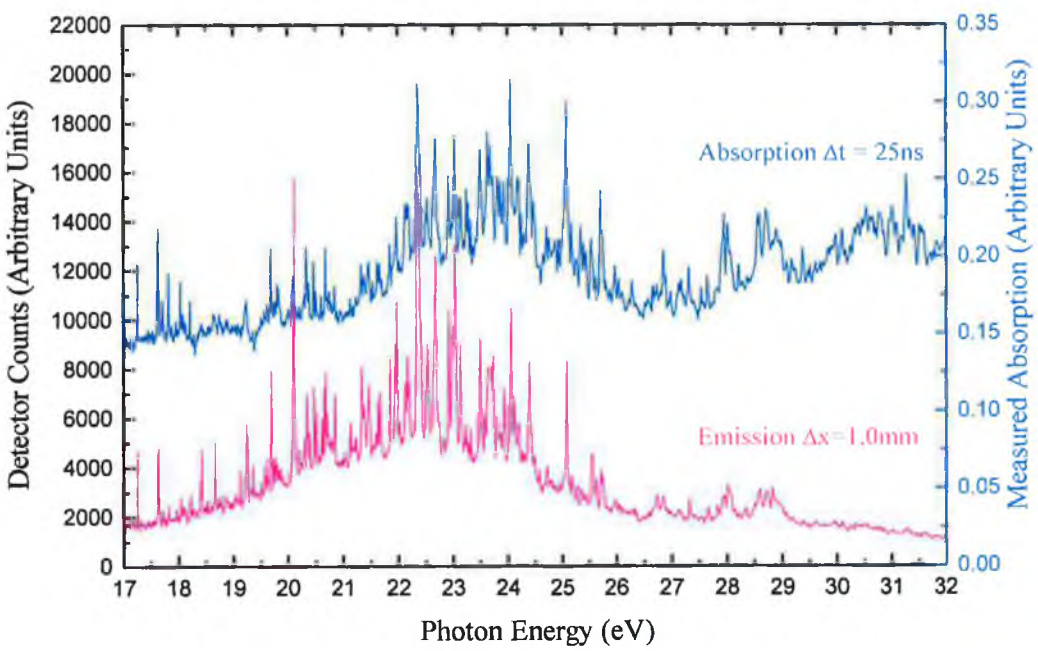

thorium target using a 115mm focal length *f*/3.8 plano convex lens which was defocused by 10mm. The resultant spot size was ~3mm on the thorium surface, which was tilted by ~13° with respect to the optic axis of the spectrometer in order to reduce VUV emission from the thorium plasma (see Figure 5.1 Chapter 5). Δx was set at 0.5mm (Figure 5.10) and due to occulsion, the actual displacement of the thorium target surface from the optic axis (Δx′) was variable from 2.1 to 3.4mm and is determined by the choice of location of the laser focal spot over the 6mm width of the tilted thorium surface. The nominal target displacement (Δx) is 0.1mm and the actual plasma displacement (Δx′) lies within the range of 1.6 to 2.9mm in Figures 5.11 and 5.12. Spatial resolution in the horizontal plane at the absorbing thorium plasma plume was ~500μm and was defined by the combination of a 500μm vertical space resolving slit parallel to the 50μm spectrometer entrance slit. The spatial resolution in the vertical plane was ~300μm and was determined by the 6mm length of the spectrometer entrance slit. 100 laser-shot $I_0(E)$, $I(E)$ and $I_f(E)$ spectra were integrated over a 20 second CCD exposure time (at –35°C) and relative photoabsorption cross sections were determined using equation 5.1 Chapter 5.

The profile of the 6p→6d giant dipole resonance in atomic thorium changes dramatically as one moves up along the thorium isonuclear sequence to ionic thorium. The broad autoionising resonances in the neutral 6p photoabsorption cross section collapse to a series of 6p valence transitions in ionic thorium. Observation of this effect is achieved experimentally by reducing the inter-laser time delay (Δt) in order to probe higher ions produced earlier during the evolution of the thorium plasma plume. In Figures 5.10 to 5.12, Δt is varied from 700ns to 5ns.

In Figure 5.13, the 25ns 6p photoabsorption spectrum from Figure 5.12 is compared with a thorium emission signal recorded at Δx = 1.0mm. This thorium emission spectrum was recorded under the same experimental conditions as those shown in Figure 5.14, where a tightly focused 115mm focal length *f*/3.8 plano convex lens focused ~830mJ, 15ns, Nd:YAG (SL804) laser pulses to an irradiance of $\sim 7\times10^{11}$ W/cm^2 on the surface of a planar thorium target. The thorium target was again tilted by ~13° with respect to the optic axis of the spectrometer. Δx was varied from 0.5mm to 2.0mm (Figure 5.14) and as the thorium target was withdrawn from the optic axis (increasing Δx), VUV emission intensity levels decreased from predominantly

Figure 5.14 *Evolution of thorium VUV emission in the 6p region from predominantly continuum emission (Δx=0.5mm) to line dominated emission (Δx=2.0mm) in less dense plasma regions. Δx=2.0mm spectrum is displaced by –500 counts for clarity*

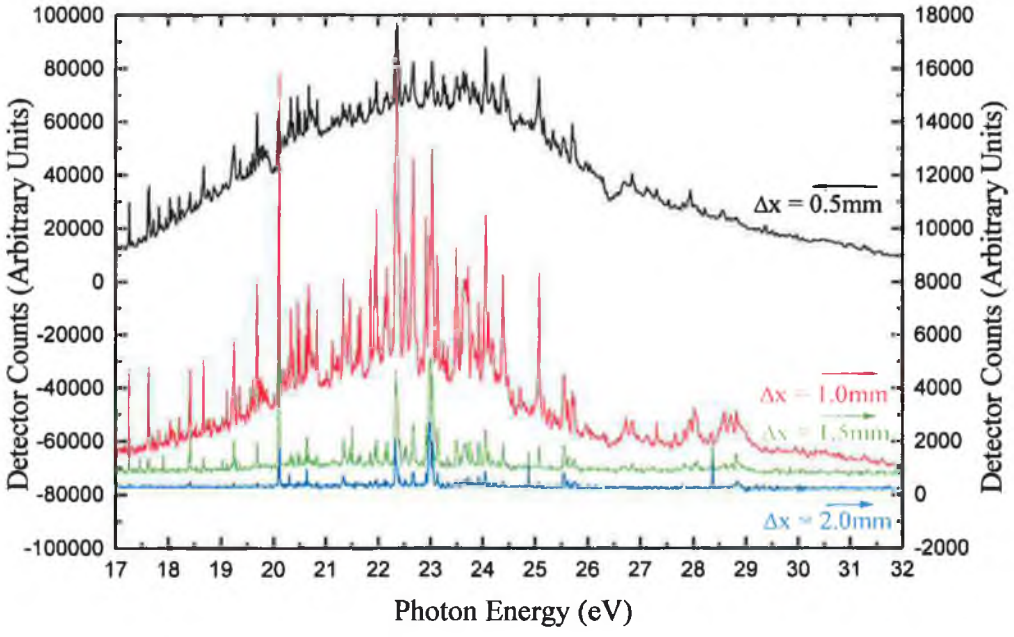

continuum emission from hot, dense plasma regions, to line emission from higher ions streaming out during the early stages of plasma evolution. Emission spectra were integrated over 100 laser shots during a 20 second CCD exposure time (at –35°C). As the thorium target was withdrawn from the spectrometer optic axis over 0.5mm intervals, the 115mm focal length lens was advanced by 0.5mm intervals toward the thorium surface in order to maintain the same focusing conditions.

5.2.7 Comparison of the 6p→6d Giant Dipole Resonance Profile in the Atomic and Solid State Environments of Thorium

The 6p atomic photoabsorption spectrum (Δt = 600ns, Δx = 0.5mm) measured with the 1m VUV spectrometer is compared to Fast Electron Energy Loss Spectroscopy (FEELS) data recorded by Cukier et al. (1980) for a thorium thin film in Figure 5.15. Also shown are Fuggle's (1974) $6p_{1/2}$ and $6p_{3/2}$ solid state limits. By performing a self-consistent quantitative analysis of fast electron energy loss spectra, Cukier et al. (1980) determined the complex dielectric constant of thorium over the energy range of study

Figure 5.15 *Comparison of relative atomic (—) and derived solid (—) 6p photoabsorption cross sections obtained experimentally for a thorium thin film (Cukier et al. 1980)*

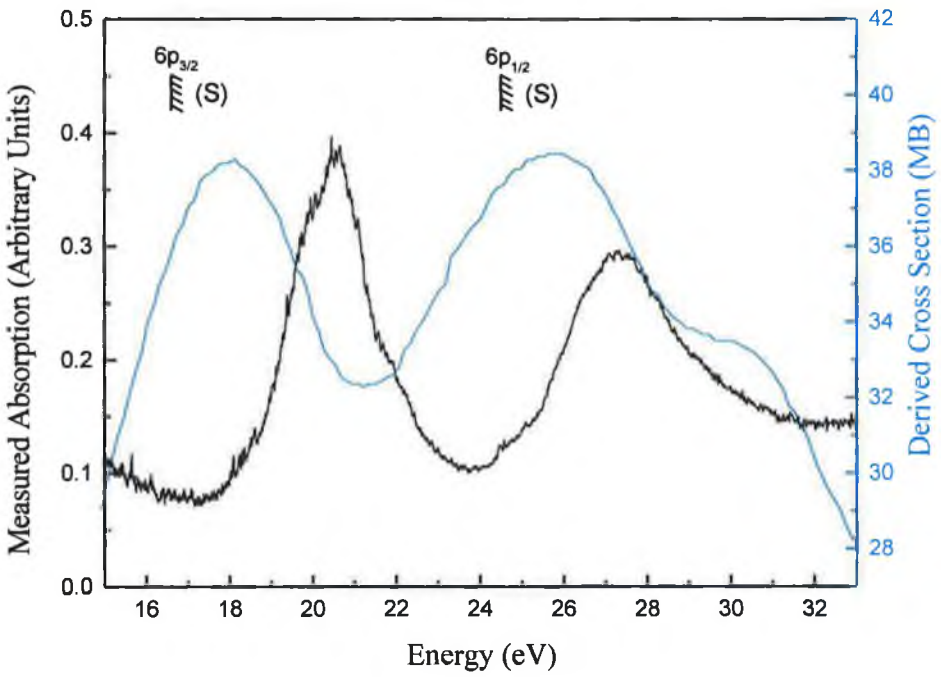

and then derived the photoabsorption cross section (σ) from optical constants calculated using a Kramers-Kronig analysis (Wehenkel 1975). The FEELS spectrum, like the atomic spectrum, has a double peak structure resulting from the $6p_{1/2} - 6p_{3/2}$ spin-orbit splitting. The solid peaks, as expected, lie at lower energies and are shifted by 2 to 3eV from the atomic peaks. Both the relative intensities and widths of the peaks differ between the solid and atom. Plasmon oscillations, arising from the collective oscillation of conduction electrons, and also inter-band electronic transitions are believed to modulate the low energy region of the FEELS spectrum (Cukier et al. 1980). It appears that these effects contribute to both the increased widths of the solid 6p peaks and also, in particular, to the additional relative intensity of the higher energy peak when compared with the photoabsorption data.

5.2.8 Comparison of the 6p→6d Giant Dipole Resonance Profile in Atomic Thorium and Uranium

The 6p photoabsorption spectrum of atomic thorium is compared in Figure 5.16 to that of atomic uranium, the only other actinide element for which similar atomic photoabsorption investigations have been performed. Van Kampen and co-workers (2000) measured the relative 6p photoabsorption cross section of atomic uranium using the DLP experimental set-up and similar conditions to those used in the thorium studies reported here. Also, the 1m normal incidence VUV spectrometer (at the CLPR) was used with back-thinned CCD photoelectric detection in the study of both actinide elements. Both spectra display a double peak 6p → 6d giant dipole resonance profile arising from spin-orbit splitting of the 6p core hole.

The lower and higher energy uranium peaks at 21.5eV and 30eV result from $6p_{3/2} \rightarrow 6d$ and $6p_{1/2} \rightarrow 6d$ excitations, and both peaks reside, as in the case of their counterparts in thorium, in the 6p photoexcitation spectrum of atomic uranium below their respective

Figure 5.16 *Comparison of atomic thorium (—) and uranium (—) 6p → 6d photoabsorption cross sections recorded photoelectrically, using the DLP technique, on the VM-521 1m normal incidence VUV spectrometer*

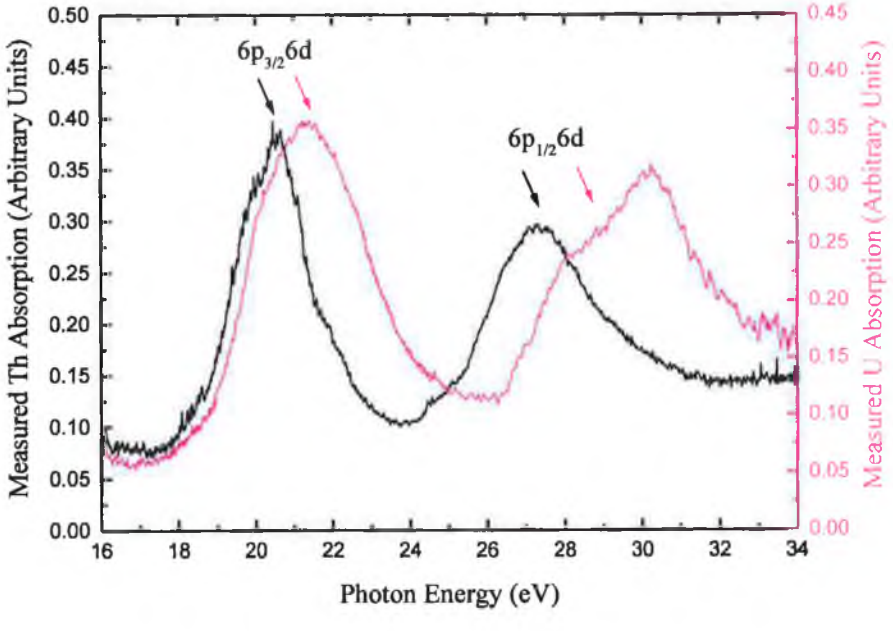

$6p_{3/2}$ and $6p_{1/2}$ limits. These limits have been calculated to lie at 24.6eV ($6p_{3/2}$) and 33.7eV ($6p_{1/2}$) by van Kampen and co-workers (2000) who used the Cowan code (1981) to perform relativistic Hartree-Fock atomic structure calculations. The 6d wavefunction in atomic uranium, as in the case of thorium, appears to be collapsed and it is largely photoexcitation followed by autoionisation rather than direct photoionisation processes that contribute to the observed 6p cross section.

As in the case of thorium, the low energy peak is higher, narrower and more symmetric whereas the high energy peak is lower and broader with a more pronounced asymmetric profile. The inclusion of spin-flip decay channels of $6p_{1/2}6d$ excited states in the relativistic Hartree-Fock calculations performed by van Kampen and co-workers was seen to contribute to the broadening and lowering of the $6p_{1/2}6d$ peak due to additional decay channels to the $6p_{3/2}$ continuum

$$U[Rn]6p^6 5f^3 6d7s^2 + h\upsilon \rightarrow 6p_{1/2}^{-1} 5f^3 6d^2 7s^2 \rightarrow 6p_{3/2}^{-1} 5f^3 6d7s^2 + \varepsilon s, \varepsilon d \qquad (5.7)$$

Consequently, the atomic uranium 6p cross section calculated by van Kampen and co-workers accurately represented the relative peak heights and widths of the experimentally observed $6p_{3/2}6d$ and $6p_{1/2}6d$ peaks.

The $6p_{3/2}6d$ and $6p_{1/2}6d$ peaks are separated by ~8.5eV in uranium and ~6.6eV in thorium due to the increased strength of the spin-orbit interaction in the higher Z atom. The atomic uranium 6p photoabsorption spectrum is shifted to higher energies by ~1eV with respect to the thorium 6p photoabsorption spectrum. This relatively small energy shift is attributable to efficient screening by 5f electrons of the additional nuclear charge that occurs on progression from Z=90 to Z=92. 5f electrons are now present in the ground state of uranium due to increasing localisation of the 5f wavefunction as it collapses with progression along the actinide series.

5.3 XUV Absorption Spectrum of Atomic Thorium

5.3.1 DLP Experimental Set-up and Procedure for XUV Grazing Incidence Photoabsorption Measurements in Atomic Thorium

The 5d relative photoabsorption cross section of atomic thorium in the 80 to 150eV XUV energy region was recorded using the 2.2m grazing incidence spectrometer-based DLP system shown in Figure 3.14 Chapter 3 and detailed in Section 3.1.4, Chapter 3. Optimum DLP temporal (Δt) and spatial (Δx) conditions for probing predominantly neutral species in the thorium plasma plume were similar to those used to record the 6p relative photoabsorption cross section of atomic thorium (Section 5.2.2). In Figure 5.17, the higher energy peak of the 5d $\rightarrow$ $\overline{5,\varepsilon}$f giant dipole resonance is shown for inter-laser time delays of 600ns $\leq \Delta t \leq$ 900ns and for Δx = 0.1mm. The level of absorption decreases as Δt increases due to the reduced column density ($\overline{nl}$) of the absorbing species. The overall profile of the resonance peak however remains unchanged (see inset Figure 5.17), thus indicating absorption from the same thorium species, which, for

Figure 5.17 *5d relative photoabsorption cross sections in the 97eV (pixel 0) to 125eV (pixel 1000) energy region measured using the DLP technique for Δt = 600 ns (—), 700ns (—), 800ns (—) and 900ns (- -). All photoabsorption cross sections are normalised in figure inset*

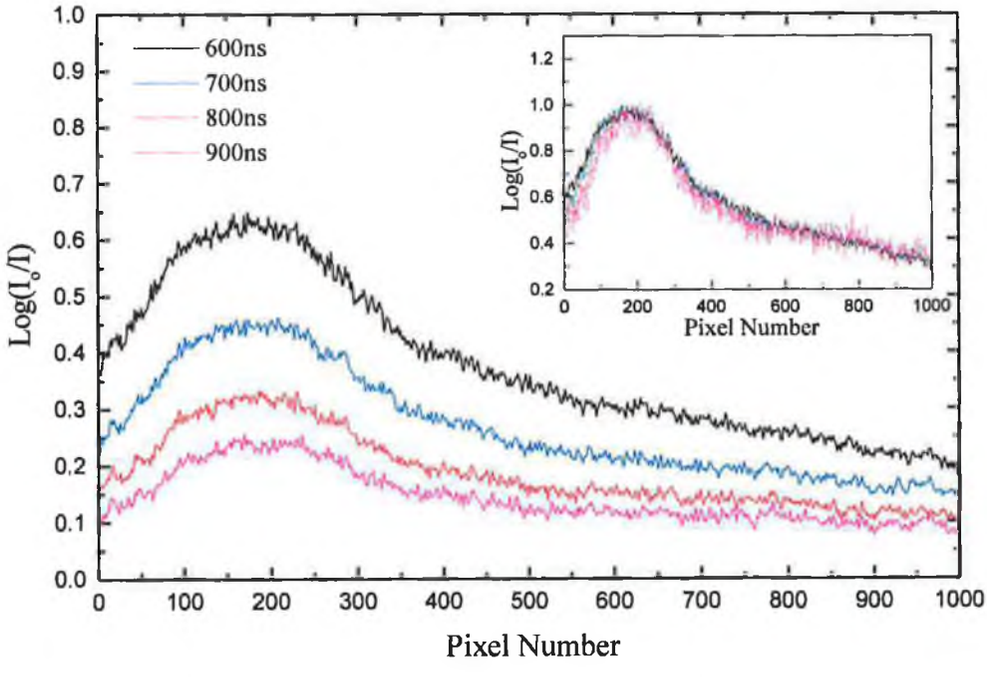

time delays in excess of 500ns, are predominantly neutral. A 110mm *f*/3.7 plano convex silica lens focused 15ns, ~300mJ, 1064nm laser pulses onto a cylindrical tungsten target in order to produce the XUV continuum source plasma. The absorbing thorium plasma was produced when a 100mm focal length *f*/4.5 plano convex silica lens focused 15ns, ~800mJ, 1064nm laser pulses onto a planar thorium target. 10 laser-shot $I_0(E)$ and $I(E)$ spectra were used to calculate the absorption spectra shown in Figure 5.17. $I_f(E)$ was not distinguishable over the background detector counts in the 80 to 150eV XUV energy region when the thorium target was tilted slightly. Aluminium lines IV to VII, emitted from an aluminium laser produced plasma, were used to calibrate the 80 to 106eV XUV energy range to within ±0.02eV and the 106 to 150eV energy range to a lower accuracy of ±0.07eV due to blends of many closely spaced aluminium lines in this region. The 2.2m spectrometer entrance slit width was set at 20μm during recording of the 5d photoabsorption spectrum of atomic thorium. A 20μm slit width was chosen over a 10μm slit width in order to increase the XUV photon flux incident on the CEMA/MCP/PDA detector when using the lower power laser (SL404) to produce the tungsten backlighting XUV continuum source plasma.

The intensity of thorium front plasma emission $I_f(E)$ observed in the XUV energy region was significantly lower than that in the VUV energy region for similar plasma conditions. This is attributed to the fact that at VUV photon energies, 6p photoexcitation in thorium ions, Th^{4+} ($6p^6$) and higher, populated within the nanosecond thorium plasma plume, results in valence transitions which decay exclusively via photon emission. On the other hand, XUV photoexcitation of the more tightly bound 5d subshell electrons in similar ionic thorium species is still an inner shell excitation whose favoured method of decay is via autoionisation and hence plasma emission is not a problem. The reduced levels of XUV front plasma emission could be completely eliminated during experimental studies in the 5d region using the method of occlusion outlined in Section 5.2.1 and demonstrated in Figure 5.1. XUV absorption spectra were then calculated by omitting the $I_f(E)$ term in equation (5.1). Also, due the reduced levels of XUV front plasma emission, the absorbing thorium plasma could be probed closer to the target surface (Δx = 0.1mm in Figure 5.17) where higher densities of neutral species, which do not experience additional acceleration due to repulsive Coulombic forces, are found to reside at long (100's ns) delays.

At 100eV, the spatial resolution of the 2.2m grazing incidence spectrometer at the absorbing plasma plume, 20mm in front of the tungsten continuum source plasma, was calculated (using Shadow™) to be ~500μm (vertical) × ~800μm (horizontal) for an entrance slit width of 10μm (Moloney 1998). That is to say that the 'footprint' of the XUV beam, subtended by the spectrometer and its associated optics at the absorbing plasma position, was approximately rectangular with dimensions of ~500μm × 800μm. Using an entrance slit width of 20μm, the spatial resolution at the absorbing plasma plume would be expected to decrease slightly.

5.3.2 5d → $\overline{5,\varepsilon}$f Giant Dipole Resonance in the XUV Photoabsorption Spectrum of Atomic Thorium

The 5d relative photoabsorption cross section measured during this thesis work is only the second such measurement performed on the free thorium atom. The first experimental observation was made by Carroll and Costello (1986), who applied the DLP technique to record the 5d → $\overline{5,\varepsilon}$f giant dipole resonance in atomic thorium using photographic plates. The CEMA/MCP/PDA photoelectric detector system attached to the 2.2m spectrometer system used in this work has the added advantage of a linear response to incident photon flux and consequently, relative photoabsorption cross sections can be accurately determined without the need for correction. Both measurements of the relative 5d photoabsorption cross section are shown in Figure 5.18. The photoabsorption spectrum shown in Figure 5.18 was recorded under the same source (tungsten) and absorbing (thorium) plasma conditions as detailed in Section 5.3.1, where Δx = 0.1mm and Δt = 650ns. 60-shot $I(E)$ and $I_0(E)$ spectra were used to determine the absorption profile. Carroll and Costello probed a similar thorium plasma plume, produced using defocused 1J, 25ns ruby laser pulses at time delays 500ns ≤ Δt ≤ 800ns with XUV continuum light from a tungsten source plasma formed with an Nd:Glass (4J, 15ns) laser.

Both measurements compare favourably in terms of overall spectral profile and relative peak splitting. Additional structure on the higher energy peak of the photographic measurement (120 to 125eV) is attributed to residual ionic absorption. In the

Figure 5.18 *Comparison of the 5d → $\overline{5,\varepsilon f}$ giant dipole resonance profile in atomic thorium recorded using the CEMA/MCP/PDA photoelectric detector system on the 2.2m grazing incidence spectrometer (—) with an earlier photographic measurement (—) by Carroll and Costello (1986)*

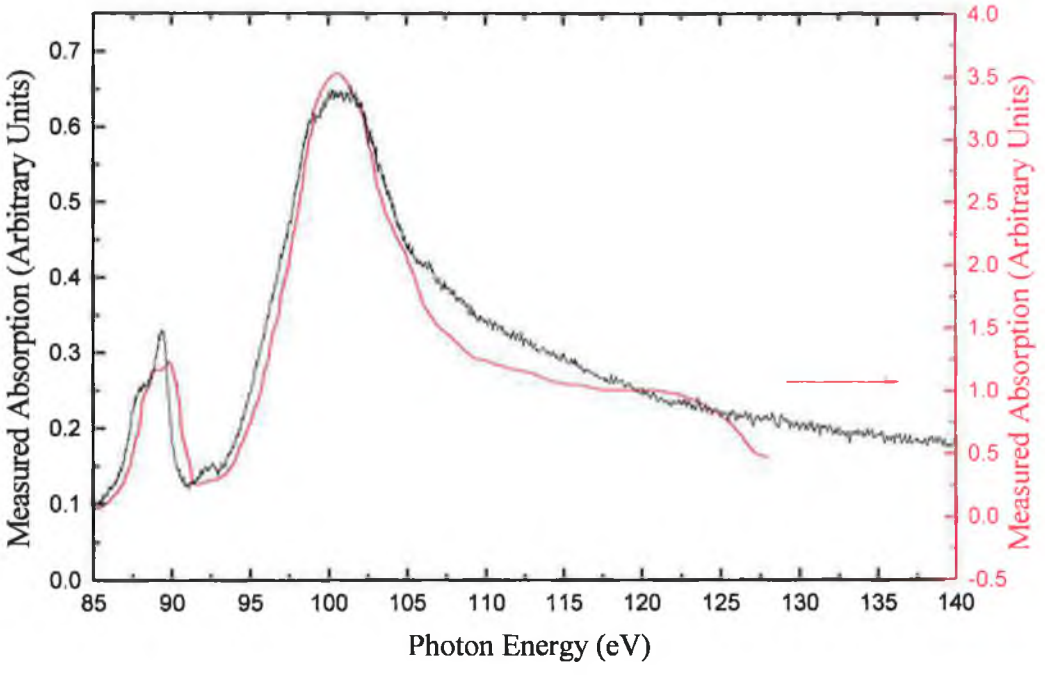

photographic measurement, the ratio of the maximum of the higher energy peak to that of the lower energy peak is ~2 compared to a value of ~3 for the photographic measurement. The FWHM of the lower energy peak is approximately 3eV in both measurements, whereas the FWHM of the higher energy peak is ~9eV in the photographic measurement and ~15.5eV in the photoelectric measurement. The reduced width of the higher energy peak in the photographic measurement could result from the non-linearity in response of the photographic plates used. It could also be partly due to the presence of different absorbing atomic/ionic species within two thorium plasma plumes produced using different laser wavelengths and different laser focusing conditions, despite the fact that both plasmas are probed at similar time delays $\Delta t \geq$ 500ns. The ionic structure in the 120 to 125eV region on the higher energy peak of the photographic measurement supports this argument.

The 5d relative photoabsorption cross section recorded in this work is compared in Figure 5.19 with a LDRPA calculation of the 5d photoionisation cross section of atomic thorium performed by Wendin (1984). In the 5d region, the exchange interaction is now comparable if not greater than that of the spin-orbit interaction due to the large

Figure 5.19 Comparison of relative (measured) and total (calculated, Wendin (1984)) 5d photoabsorption cross sections of atomic thorium

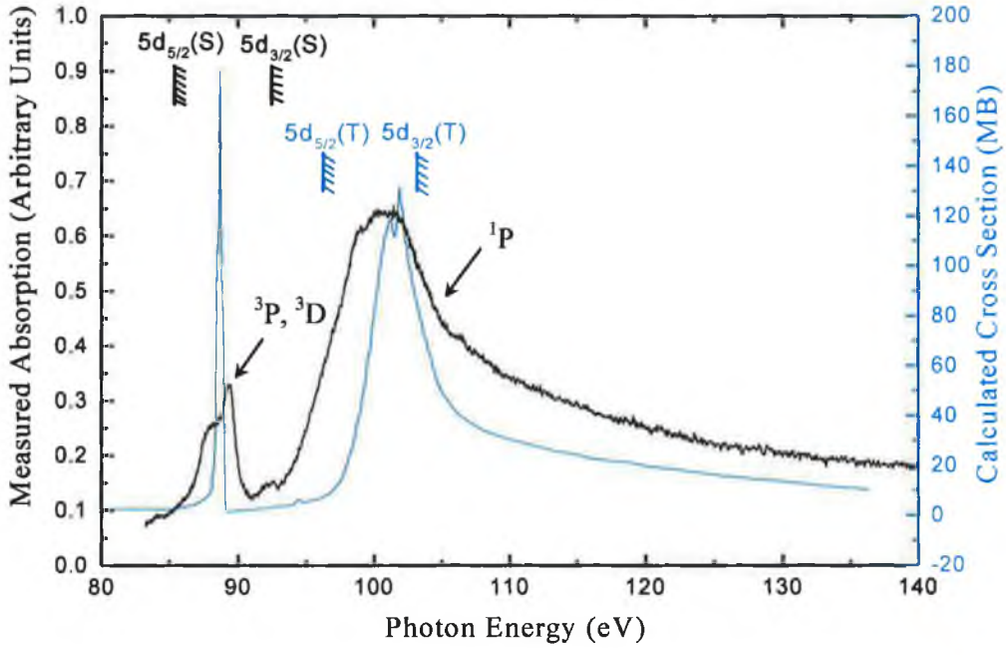

5d-5f overlap. As a result, singlet excited state terms are pushed to higher energies than those of triplet terms, resulting in the twin peak structure observed in both calculated and measured cross sections. The location of the calculated peaks, and also their relative splitting, are in good agreement with those observed experimentally. Again, as in the case of the LDRPA calculation of the 6p cross section in atomic thorium (Wendin 1984), the calculated peaks are too narrow due to the fact that multiplet splitting is not accounted for. Also, Wendin notes that 5d Auger processes (e.g. shake up and shake down), not included in the calculation, would lead to further broadening of the lower energy peak. The atomic $5d_{5/2}$ and $5d_{3/2}$ ionisation limits shown in Figure 5.19, are calculated in the LDRPA calculation using the solid state limits of Fuggle et al. (1974) that are also shown in Figure 5.19. The lower energy singlet peak lies below the lower $5d_{5/2}$ atomic ionisation limit (denoted 'T' in Figure 5.19), whereas the higher energy triplet peak straddles the $5d_{3/2}$ atomic ionisation limit. Due to the position of the calculated peaks relative to the two 5d ionisation limits, it is expected that the triplet peak, lying in the 5d photoexcitation spectrum, will decay predominantly via autoionisation processes, whereas both autoionisation and direct photoionisation processes would be expected to contribute to the higher energy singlet peak.

Experimental observations by van Kampen and co-workers (2000) based on uranium photoion data suggest that in the uranium atom, the 5f wavefunction is more or less collapsed, and that discrete 5d→5f autoionising transitions are mainly responsible for the observed 5d → f giant dipole resonance profile in the 80 to 150eV XUV region. Thorium is a lighter actinide element and the degree of localisation of the 5f wavefunction is expected to be less than in the case of uranium. Therefore a reduction in the importance of discrete 5d→5f autoionising transitions relative to direct 5d photoionisation to a 5f 'continuum like' state is expected. Term dependent relativistic Hartree-Fock calculations of the 5d cross section in atomic thorium have been performed (Martins 2000) in order to investigate the processes contributing to the experimentally observed 5d → $\overline{5,\varepsilon f}$ giant dipole resonance. Also, re-calculation of the $5d_{5/2}$ and $5d_{3/2}$ ionisation limits of atomic thorium using the HFR method predicts that the $5d_{3/2}$ ionisation limit is located close to the maximum of the higher energy triplet peak. As a result, it is expected that the process of direct 5d photoionisation to a 'continuum–like' 5f state ($\overline{5,\varepsilon f}$) is largely responsible for the observed resonance feature in atomic thorium.

5.3.3 Term Dependent Hartree-Fock Calculations and RTDLDA Calculations of the 5d Photoabsorption Cross Section of Atomic Thorium

Term dependent relativistic Hartree-Fock calculations of the 5d cross section of ThI were performed by Martins (2000) using the Cowan suite of atomic structure codes (1981). The initial (a), excited (a′) and continuum (a″ and a‴) configurations used to calculate the 5d cross section are detailed in Table 5.4. The process of direct 5d photoionisation of the ThI $[Rn]6d^27s^2$ ground state configuration and also the process of 5d → 5f photoexcitation (ThI $[Rn]6d^27s^2$ → ThI$^*5d^96d^27s^25f$) followed by autoionisation were included in calculations. The 5d cross section $\sigma(E)$ for a given term of the ThI ground state configuration was calculated according to the procedure outlined for 6p → 6d calculations in Section 5.2.5. As in 6p→6d calculations, the cross section for each of the $^3F_2$, $^3P_0$, $^3F_3$, $^3P_1$ and $^3F_4$ terms of the ThI ground state (see Table 5.2) was calculated.

Table 5.4 *Initial (a), excited (a') and continuum (a'', a''') configurations of ThI used in HFR atomic structure (Cowan code (1981)) calculations of the ThI 5d cross section*

Type of Configuration	**Transition(s)**	**Configuration(s)**
Initial state		(a) $5d^{10}6s^26p^66d^27s^2$
Discrete excited state	$5d \rightarrow 5f$	(a') $5d^96s^26p^66d^27s^25f$
Direct 5d ionisation	$5d \rightarrow \varepsilon p, f$	(a'') $5d^96s^26p^66d^27s^2 + \varepsilon p, f$
Autoionisation	$5f^{-1}\,7s^{-1}$	(a''') $5d^{10}6s^26p^66d^27s + \varepsilon p, f$
	$5f^{-1}\,6d^{-1}$	(a''') $5d^{10}6s^26p^66d7s^2 + \varepsilon p, f$
	$5f^{-1}\,6p^{-1}$	(a''') $5d^{10}6s^26p^56d^27s^2 + \varepsilon s, d$
	$5f^{-1}\,6s^{-1}$	(a''') $5d^{10}6s6p^66d^27s^2 + \varepsilon p, f$

Predominantly neutral thorium species are expected to reside in the thorium plasma plume for inter-plasma time delays (Δt) in excess of 500ns. For the measured 5d photoabsorption spectrum recorded at Δt = 650ns (see Figure 5.18), the electron temperature within the plasma plume is expected to be similar to that calculated using the plasma model of Singh and Narayan (1990) in Section 5.2.4. As a result, the population of metastable even parity states within plasmas used in 5d studies is similar to that in plasmas used in 6p studies, and therefore the cross section of the same five low-lying terms ($^3F_2$, $^3P_0$, $^3F_3$, $^3P_1$, $^3F_4$) of the ThI $[Rn]6d^27s^2$ ground state was determined in both 6p and 5d HFR calculations.

The scaling of the direct (F^k) and exchange (G^k) Slater integrals (see Appendix I) in HFR calculations of the 5d cross section was found to have a dramatic influence on the width of the main resonance singlet peak and also on its position relative to the lower

energy triplet peak. The effect of varying the scaling of the Slater integrals while keeping the spin-orbit scaling at 99% is shown for the $^3P_0$ term of the ThI [Rn]$6d^27s^2$ ground state in Figure 5.20. An initial scaling of 80% resulted in a broad higher energy singlet peak, with a FWHM of ~20eV and an inter-peak splitting of ~17eV, compared

Figure 5.20 *Calculated HFR 5d cross sections for the $^3P_0$ term of the ThI [Rn]$6d^27s^2$ ground state configuration for different scaling of the Coulomb integrals, 80% (—), 75% (– –), 70% (—), 66% (– –), and a fixed spin-orbit scaling of 99%*

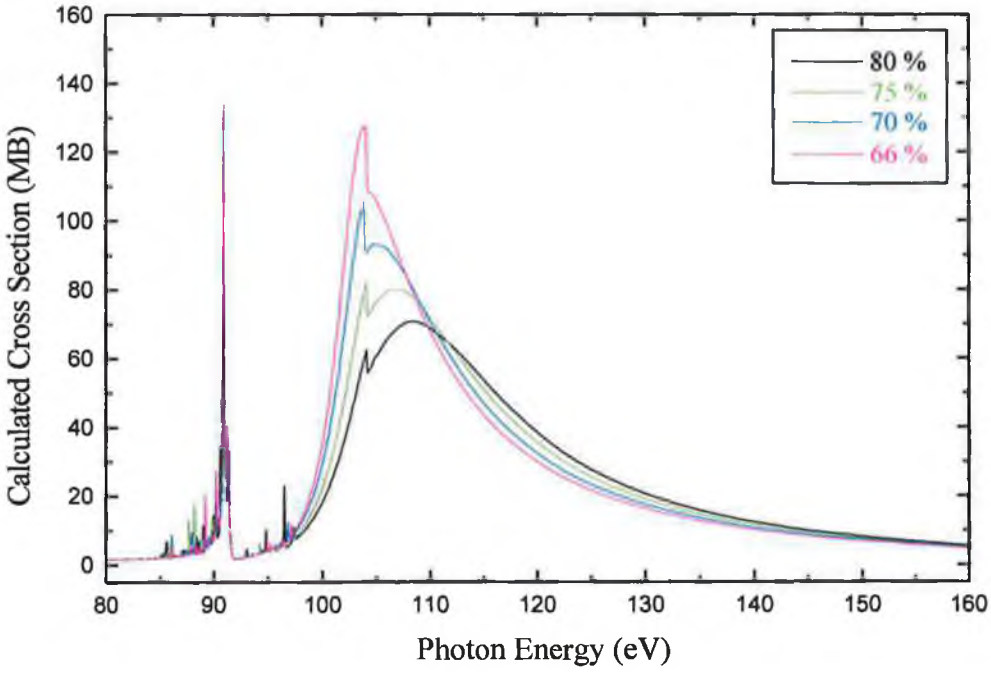

with an experimental FWHM of ~15.5eV and splitting of ~11eV (Figure 5.18). As the scaling of the Slater integrals was reduced from 80% to 66% the width of the higher energy peak decreased and the position of its maximum moved to lower energies and closer to a stationary lower energy triplet peak. Sugar (1972) suggested using 66% scaling of Slater integrals for HF calculations of d→f transitions in giant dipole resonance energy regions. For HFR calculations of the 5d→5f cross section of ThI, 66% scaling results in a ~10eV FWHM of the higher energy peak and an inter-peak splitting of ~13eV. These results compare more favourably with experimental measurements and 66% scaling of the Slater integrals was used to compute the five low-lying even terms of the ThI [Rn]$6d^27s^2$ ground state shown in Figure 5.21. The $5d_{5/2}$ and $5d_{3/2}$ ionisation limits of ThI were calculated to lie at 96.3eV and 104.1eV respectively. The $5d_{3/2}$ ionisation limit appears as a sharp edge on the higher energy peak of all the calculations

shown in Figure 5.20. Therefore as the scaling of the Slater integrals is reduced, the peak of the resonance sweeps downward in energy towards the $5d_{3/2}$ ionisation limit.

Figure 5.21 *HFR calculations (66% Coulomb scaling, 99% spin-orbit scaling) of the 5d cross sections for the lowest $^3F_2$ LS term of the ThI [Rn]$6d^27s^2$ ground state configuration and four terms ($^3P_0$, $^3F_3$, $^3P_1$, $^3F_4$) of this configuration lying within 0.62eV of the $^3F_2$ term*

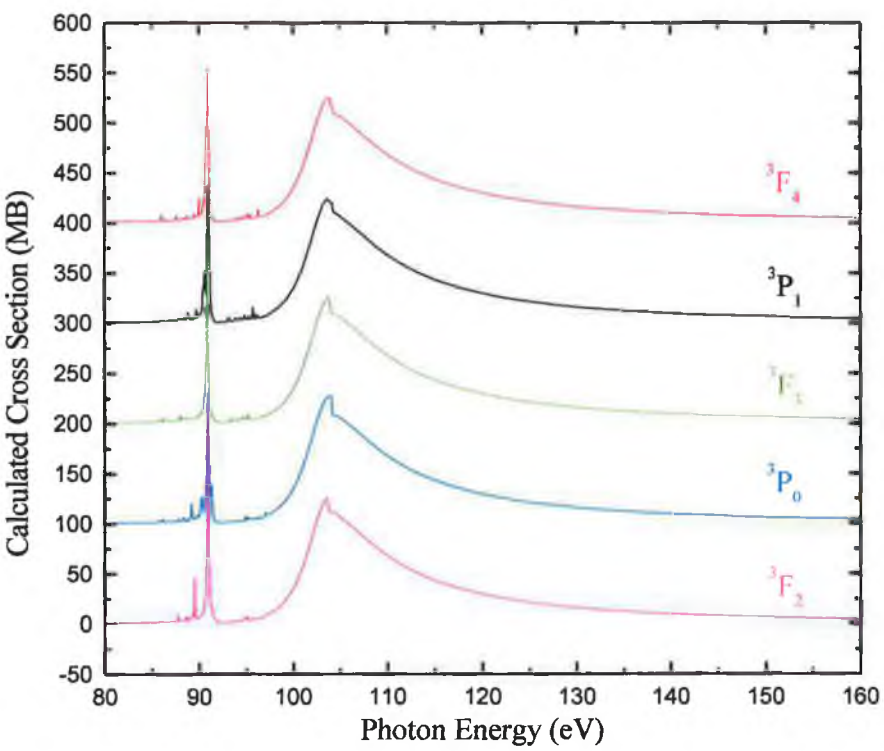

In Figure 5.21, offsets of 100, 200, 300 and 400 MB have been added to the calculated cross sections of the $^3P_0$, $^3F_3$, $^3P_1$ and $^3F_4$ terms respectively in order to displace them sequentially for clarity. The profile of the calculated 5d cross section is very similar for all five terms. As in the case of HFR calculations of the 6p cross section, a synthetic spectrum was computed by performing a weighted sum over all of the five low-lying terms of the ThI [Rn]$6d^27s^2$ ground state configuration using equation (5.5), where the statistical weighting ω_i of each term was determined using equation (5.6). As mentioned previously, the electron temperature was assumed to be similar to that calculated in Section 5.2.4 and a value of 1.65eV was used to compute the 5d synthetic spectrum. The synthetic 5d spectrum is shown in Figure 5.22, where it has been shifted by –3.2eV in order to coincide with the measured relative 5d photoabsorption cross section. Also shown are the calculated $5d_{5/2}$ and $5d_{3/2}$ ionisation limits of atomic thorium, which after

Figure 5.22 *Comparison between the measured 5d photoabsorption cross section of atomic thorium (—) and a synthetic 5d cross section (—) computed by summing statistically weighted HFR cross sections for the $^3F_2$, $^3P_0$, $^3F_3$, $^3P_1$, $^3F_4$ terms of the ThI [Rn]$6d^27s^2$ ground state configuration (HFR calculation is shifted by –3.2eV)*

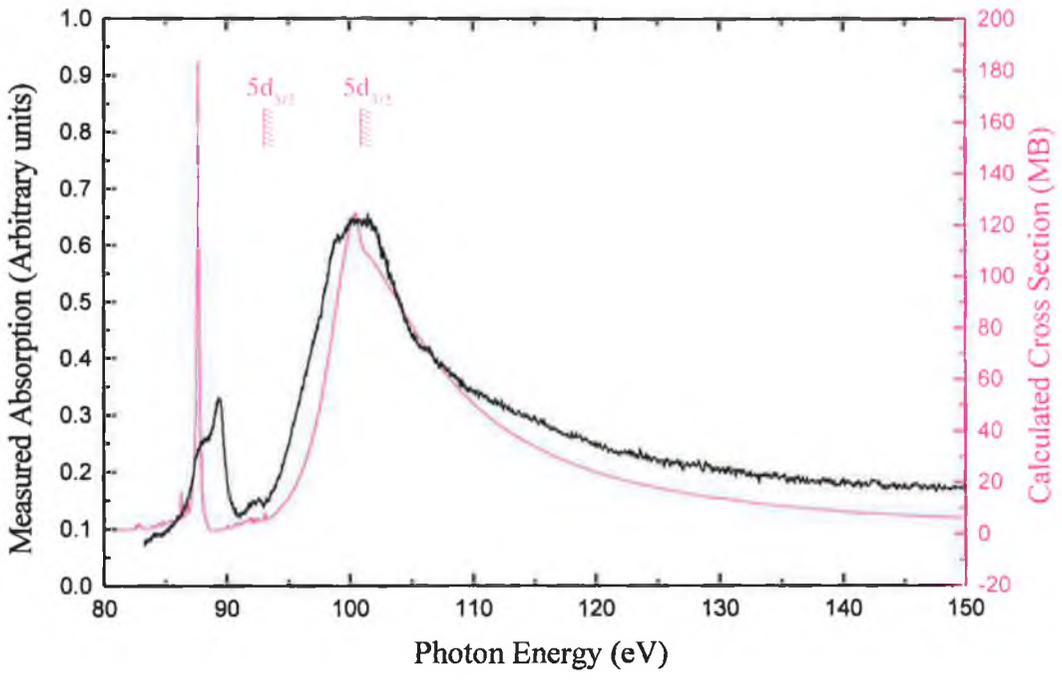

a similar displacement of –3.2eV, lie at 93.1eV and 100.9eV respectively.

The lower energy triplet peak of the HFR calculation and the measured feature lie (at 87.7 and 89.5eV respectively) in the discrete 5d photoexcitation spectrum below the $5d_{5/2}$ ionisation limit. As mentioned previously this peak is formed by inner shell 5d→5f photoexcitation to collapsed $5d^95f$ triplet terms (Th $5d^{10}$ ($^1S_0$) $6d^27s^2$ + hυ→ Th* $5d^95f$ (^3P, ^3D) $6d^27s^2$) followed by autoionisation into the adjacent 7s and 6d valence continua and also the 6p and 6s inner shell continua. The higher energy singlet peak straddles the $5d_{3/2}$ ionisation limit with a large portion of its profile lying in the $5d_{3/2}$ photoionisation spectrum. Consequently, the main giant dipole resonance feature in ThI is formed by photoexcitation followed by autoionisation,

$$\text{Th } 5d^{10}(^1S_0)\ 6d^27s^2 + h\upsilon \rightarrow \text{Th}^*\ 5d^9(^1P)\ 6d^27s^25f \rightarrow \text{Th}^+\ 5d^{10}\ (6s^26p^66d^27s^2)^{-1} + \varepsilon l$$

and also by direct photoionisation to a short-lived 'continuum-like' $\overline{5,\varepsilon f}$ state which tunnels through a confining centrifugal potential barrier in the 5f potential, resulting in a free εf electron.

$$Th\ 5d^{10}(^1S_0)\ 6d^27s^2 + h\upsilon \rightarrow Th^*\ 5d^9(^1P)\ 6d^27s^2\ \overline{5,\varepsilon f} \rightarrow Th^+\ 5d^96d^27s^2 + \varepsilon f$$

As mentioned previously (Section 1.2.4.2, Chapter 1), the latter process can be described as a resonant Auger decay. In the former process of inner shell photoexcitation, autoionisation can occur by decay into the same valence and inner shell continua as those available to the lower energy triplet peak and to an additional $5d_{5/2}$ continuum channel via the 'spin-flip' decay process (which is included in HFR calculations)

$$Th\ 5d^{10}6s^26p^66d^27s^2 + h\upsilon \rightarrow Th^*\ 5d_{3/2}^{-1}6s^26p^66d^27s^25f \rightarrow Th^+\ 5d_{5/2}^{-1}6s^26p^66d^27s^2 + \varepsilon p, \varepsilon f$$

Due to the position of the $5d_{3/2}$ limit at the centre of the main resonance peak it would appear that in atomic thorium, terms in addition to ^3D and ^3P of the $5d^95f$ excited configuration (i.e. terms built on $ThI^*\ 5d^95f\ (^1P)\ (6d^27s^2)\ ^{2S+1}L_J$) have started to collapse.

As in the LDRPA calculation of the 5d cross section of atomic thorium by Wendin (1984), the lower energy triplet peak is too narrow and its cross section is too high relative to the higher energy peak. In the case of the HFR calculation performed here, this may be due to the omission of other decay channels involving shake up of the Th^+ ion core. The inclusion of 5d→np transitions and 5d→mf (^3P, ^3D) (for m>5) may also serve to broaden the triplet peak. In Figure 5.23, the synthetic 5d spectrum is convolved with a 0.12eV FWHM Lorentzian profile simulating the instrument function of the 2.2m grazing incidence spectrometer at 100eV (see Section 3.1.4.4, Chapter 3 for a discussion of the 2.2m spectrometer resolution). Although convolution serves to broaden the triplet peak and lower its maximum relative to the singlet peak, the inclusion of the processes mentioned above in a more detailed HFR calculation is expected to produce a broader triplet peak width.

The LDRPA theoretical model applied by Wendin (1984) to calculate the 5d and 6p photoabsorption cross sections of atomic thorium differs from independent particle Hartree-Fock calculations, in that it is a many-body approach which considers the collective response of the atom to the driving photon field. Such collective effects are the sharing of excitation energy among electrons and also electron correlation effects. A similar many body approach is the non-relativistic Time Dependent Local Density Approximation (TDLDA) of Zangwill and Liberman (1984) and the relativistic version, RTDLDA (Liberman & Zangwill, 1984), which is outlined in Appendix I. In Figure

Figure 5.23 *Synthetic 5d spectrum generated by convolving the total HFR cross section of ThI [Rn]6d^{2}7s^2 (from Figure 5.22) with a Lorentzian profile (0.12eV FWHM) that simulates the instrument function of the 2.2m grazing incidence spectrometer at 100eV*

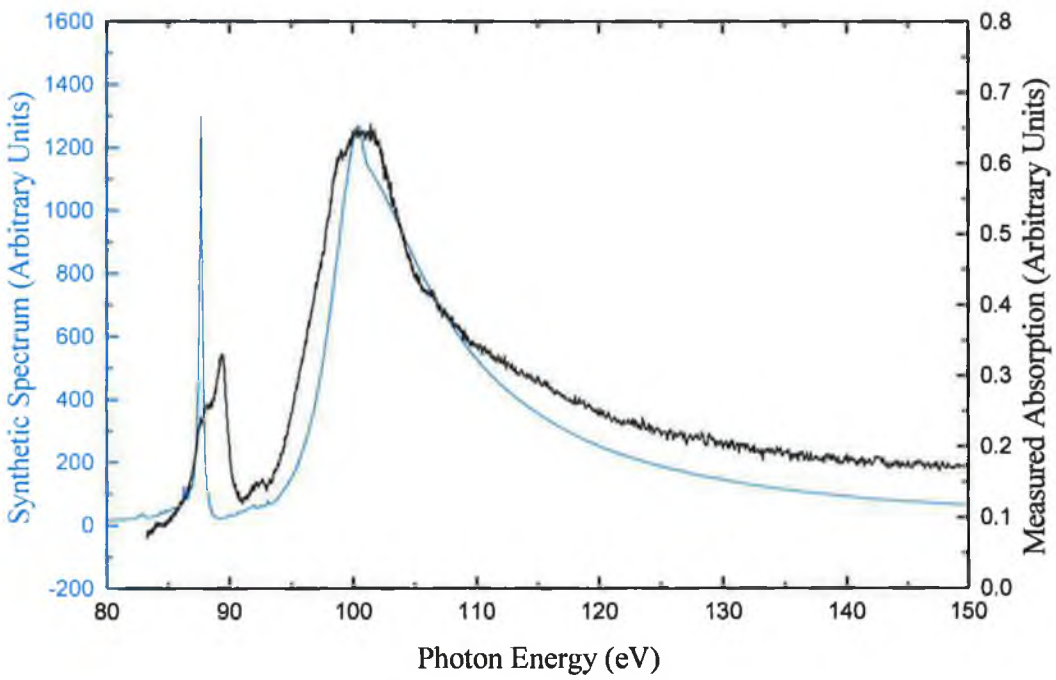

5.24, RTDLDA calculations of the 5d photoionisation cross section of ThI [Rn]6d^{2}7s^2 for all three possible spin orientations of the open 6d^2 subshell (↓↓, ↑↑, ↑↓) are compared to the experimentally measured relative 5d photoabsorption cross section. For RTDLDA calculations, 85% scaling of the Slater exchange integrals was found to give best agreement with the experimentally measured 5d cross section in terms of peak splitting, peak widths and the energy location of the overall giant resonance profile (which has not been displaced in energy). Non-relativistic TDLDA calculations of the 5d photoionisation cross section yield one large giant resonance peak. In this case, exchange splitting of the singlet and triplet 5d^{9}5f terms of ThI* is not sufficient to split the resonance into the two peaks observed experimentally. In RTDLDA calculations however, the additional splitting of the singlet and triplet 5d^{9}5f terms caused by the spin-orbit interaction between the 5d hole and the 5f electron results in an accurate reproduction of the experimentally observed peak splitting[1]. In Figure 5.24 the calculated lower energy triplet peak has not fully converged and it is expected to have a higher maximum value.

[1] Wendin (1984) calculated the spin-orbit to exchange splitting ratio to be ~0.5 in the 5d excitation region of atomic thorium.

Figure 5.24 *Comparison of the measured relative 5d photoabsorption cross section of ThI with RTDLDA calculations of the absolute 5d cross section of ThI [Rn]$6d^2 7s^2$ for all possible spin orientations of the open $6d^2$ subshell ($\downarrow\downarrow$, $\uparrow\uparrow$, $\uparrow\downarrow$)*

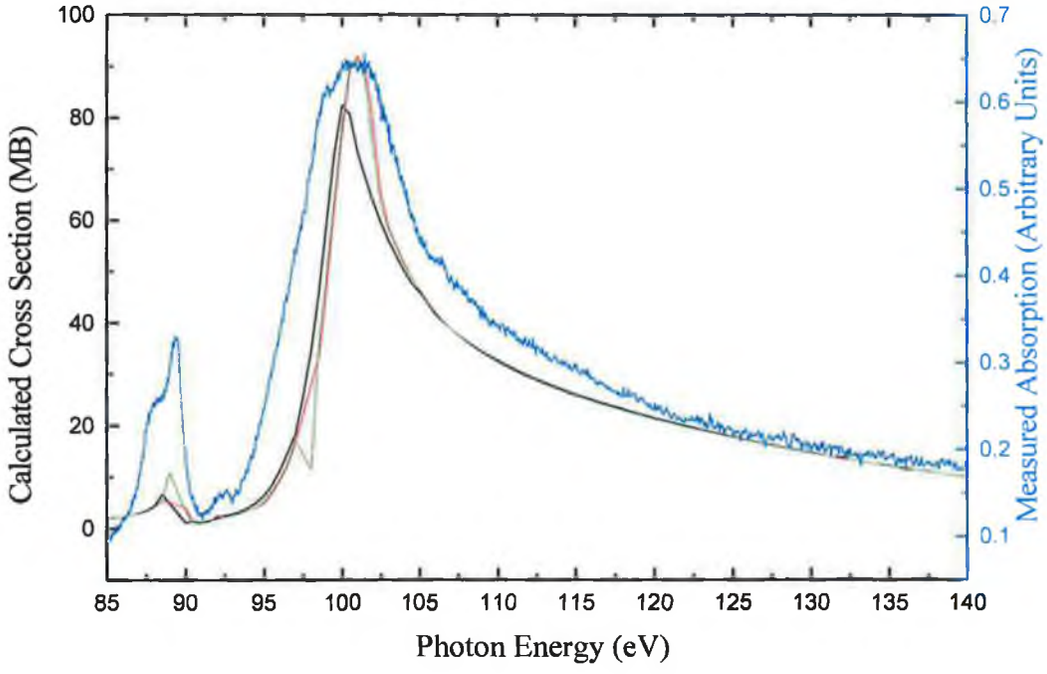

All three theoretical methods (LDRPA, HFR and RTDLDA), despite different approaches, reproduce the overall features of the 5d cross section and calculate the maximum cross section of the higher energy peak of the giant dipole resonance to lie between 80 and 130 MB.

5.3.4 Comparison of the 5d → $\overline{5,\varepsilon}$f Giant Dipole Resonance Profile in Atomic, Molecular and Solid State Thorium

In Figure 5.25 the measured 5d relative photoabsorption cross section of atomic thorium is compared with experimental measurements in the molecular (ThF_4, Connerade et al. 1980b), compound (ThF_4, Cukier et al. 1980) and pure solid (Th, Cukier et al. 1978, 1980) environments. Connerade and co-workers (1980b) measured the relative 5d photoabsorption cross section of ThF_4 vapour produced in an inductively heated furnace at the Bonn 500 MeV synchrotron. Cukier and co-workers (1978) measured the

Figure 5.25 *Comparison of the thorium 5d → $\overline{5,\varepsilon}$f giant dipole resonance profile in the atomic (— this work), molecular (— ThF_4, Connerade et al. 1980b), compound (— ThF_4, Cukier et al. 1980) and pure solid (— Cukier et al. 1978, — Cukier et al. 1980) environments*

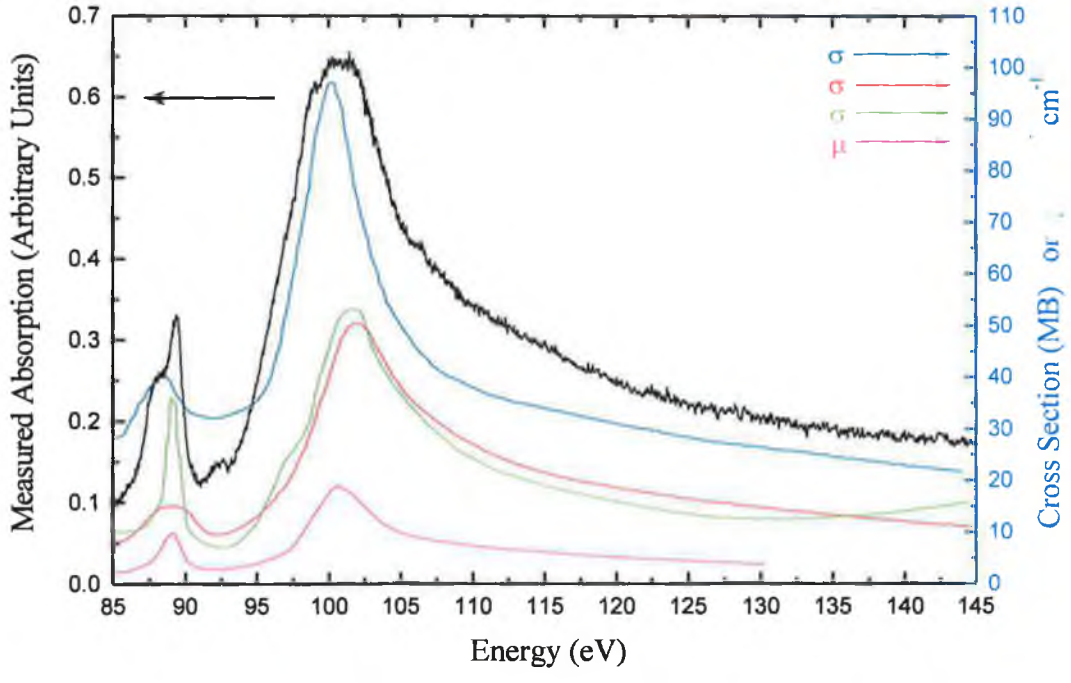

absorption coefficients (μ) of thorium in the 5d energy region by passing XUV light from the ACO storage ring through thorium thin films. In 1980, Cukier and co-workers used the technique of Fast Electron Energy Loss Spectroscopy (FEELS) to measure the complex dielectric constants of thorium and thorium tetraflouride in the 5d XUV region. From these measurements, they derived the photoabsorption cross section (σ) from optical constants calculated using a Kramers-Kronig analysis (Wehenkel 1975).

The high degree of similarity between all of these measurements has been noted previously (Connerade et al. 1980b, Carroll & Costello 1986), and it is evident that the 5d → $\overline{5,\varepsilon}$f giant dipole resonance present in the atomic 5d photoabsorption spectrum retains its overall profile in different molecular, compound and pure solid environments. Consequently, it appears that the 5f potential is, to a large extent, unaffected upon phase transition from the atomic to the solid state environment and therefore retains its atomic nature.

5.3.5 Comparison of the 5d → $\overline{5,\varepsilon f}$ Giant Dipole Resonance Profiles in Atomic Thorium and Uranium

The 5d → $\overline{5,\varepsilon f}$ giant dipole resonance features in the inner shell XUV photoabsorption spectra of atomic thorium and atomic uranium are compared in Figure 5.26. The 5d relative photoabsorption cross section of uranium was measured by van Kampen and co-workers (2000) at the CLPR using the 2.2m grazing incidence spectrometer. Similar DLP (spatial and temporal) parameters and plasma conditions were used in the

Figure 5.26 *Comparison of the 5d → $\overline{5,\varepsilon f}$ giant dipole resonance profiles in the inner shell photoabsorption spectra of atomic thorium (—) and uranium (—) recorded using the 2.2m grazing incidence spectrometer-based DLP system at the CLPR*

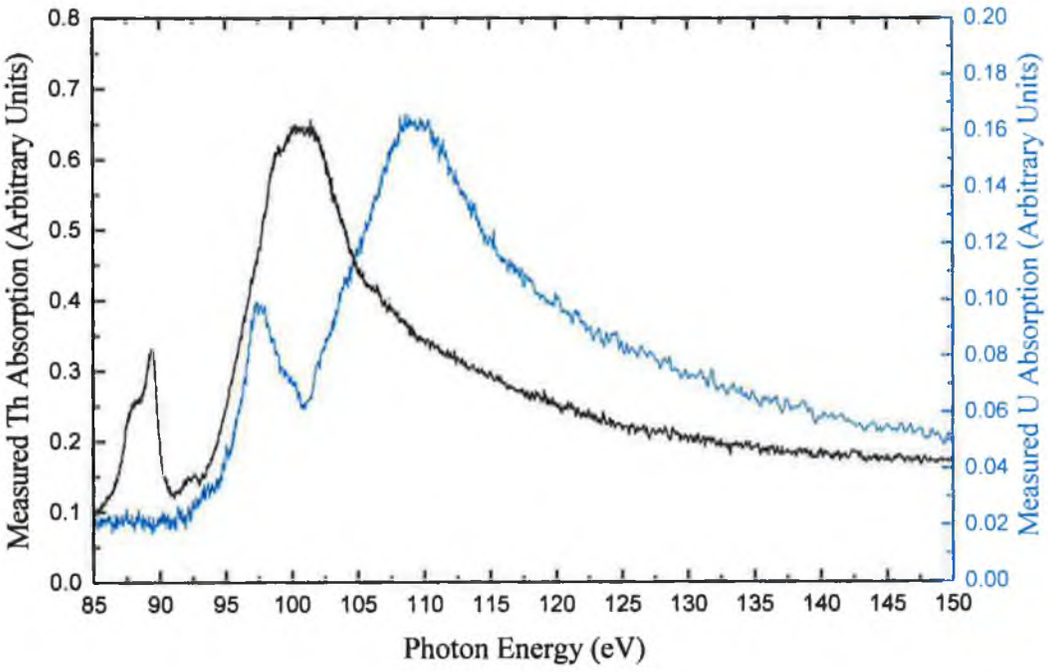

recording of both 5d spectra. The giant dipole resonance lies, as expected, at higher excitation energies in the heavier uranium atom. The exchange and spin-orbit interactions, which are of comparable importance in atomic uranium (Wendin 1984), split the giant dipole resonance feature into two distinguishable peaks as in thorium. The distribution of oscillator strength between both peaks is similar for both atoms, where the ratio of the maximum of the higher energy peak to that of the lower energy peak is 1.6 (U) and 1.9 (Th). Also, the inter-peak splitting of both resonances is very similar,

having a value of ~11eV in both spectra. Van Kampen and co-workers (2000) calculated (using similar HFR calculations to those used in this work) a value of 101eV for the lowest 5d limit, thus placing the lower energy peak in the discrete 5d photoexcitation spectrum as in the case of the lower energy thorium peak. The FWHM of the main resonance peak in uranium is ~25eV compared with ~15.5eV in thorium. The increased complexity of the uranium ground state $[Rn]5f^{3}6d7s^{2}$ relative to that of thorium results in a greater number of initial and excited state terms. Van Kampen and co-workers (2000) ascertained that the main resonance peak is formed by mainly discrete autoionising transitions, as the 5f wavefunction is believed to be more or less collapsed in atomic uranium. The greater number of autoionising channels available for decay from the increased number of excited state terms in uranium give rise to its increased width relative to the thorium main resonance peak.

5.4 XUV Absorption Spectra of Ionic Thorium (ThI to ThVII)

5.4.1 DLP Experimental Set-up and Procedure for XUV Photoabsorption Measurements in Ionic Thorium

DLP photoabsorption studies of ionic thorium in the 80 to 150eV XUV energy region were performed using both the 2.2m grazing incidence spectrometer system at the CLPR (see Figure 3.14 Chapter 3) and the flat field spectrometer system developed at RAL (see Figure 3.21 and Figure 3.22, Chapter 3). Time resolved studies of the evolution of the profile of the 5d $\rightarrow$ $\overline{5,\varepsilon}$f giant dipole resonance with increasing ionisation along the thorium isonuclear system were performed in both experimental regimes by reducing Δt (the inter-laser time delay) from ~500ns to 0ns. Also, in order to produce sufficient densities of thorium ions for photoabsorption studies, the laser power density on the surface of the thorium target was kept as high as possible using tightly focused plano convex lenses. Due to a small focal spot and the resulting high energy density on the thorium target, the formation of pits (100's of microns deep) after 10's of laser shots resulted in a rapid retreat in the position of the hot core of the thorium plasma plume from the spectrometer optic axis into such pits. When studying ions, it is necessary to probe this hot plasma region and therefore in order to maintain similar plasma conditions during the accumulation of a single absorption spectrum, the number

of laser shots used was deliberately lower than in the case of atomic studies. Again, as in atomic XUV photoabsorption studies, a slight degree of occlusion was required to eliminate/reduce thorium front plasma emission.

5.4.2 Collapse of the 5d → $\overline{5,\varepsilon f}$ Giant Dipole Resonance along the Thorium Isonuclear Sequence

The evolution in the profile of the relative 5d photoabsorption cross section with increasing ionisation along the thorium isonuclear sequence is shown in Figures 5.27 to 5.29. The spectra shown were recorded using the 2.2m grazing incidence spectrometer-based DLP system and the absorption at each inter-laser (inter-plasma) time delay was calculated using 20 laser-shot $I_0(E)$ and $I(E)$ spectra. $I_f(E)$ was not distinguishable over the background detector counts in the 80 to 150eV XUV energy region when the thorium target was tilted slightly and withdrawn from the spectrometer optic axis by

Figure 5.27 *Evolution in the profile of the 5d relative photoabsorption cross section of thorium from predominantly neutral species at Δt =500ns, to ionised species for inter-laser delays 200ns $\leq \Delta t \leq$ 500ns and Δx=0.1mm*

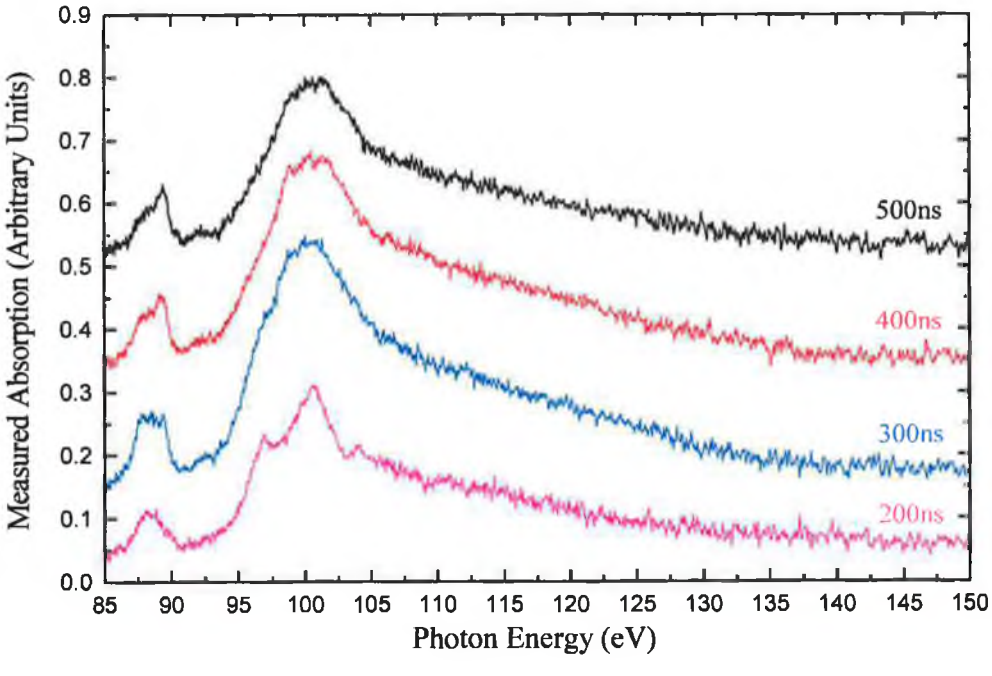

Figure 5.28 *Evolution in the profile of the 5d relative photoabsorption cross section of ionic thorium for inter-laser delays 60ns ≤ Δt ≤ 100ns and Δx=0.1mm*

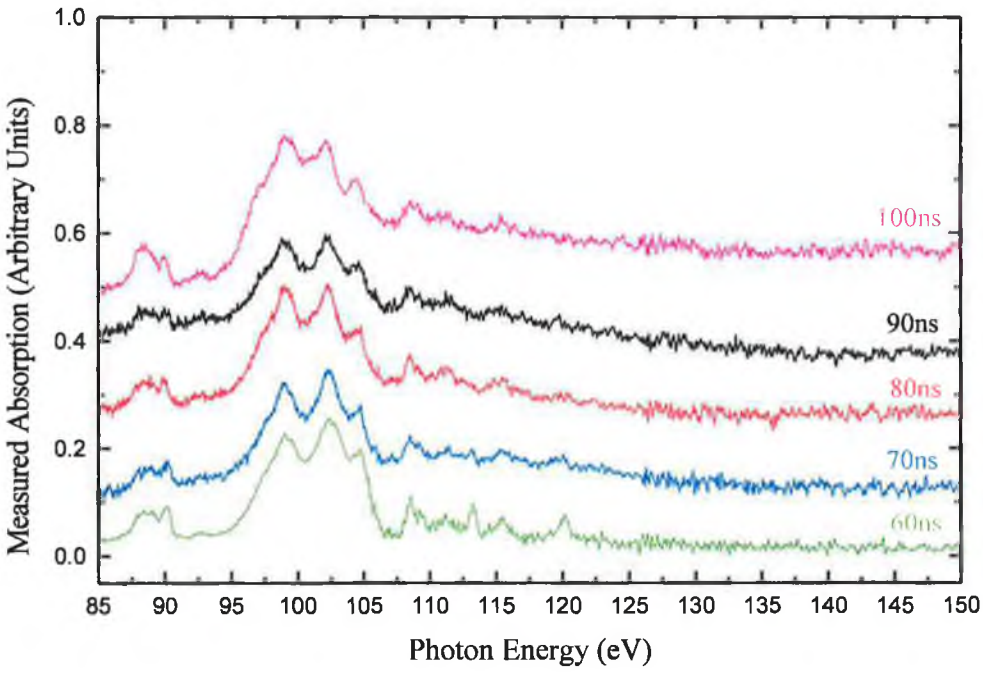

Figure 5.29 *Evolution in the profile of the 5d relative photoabsorption cross section of ionic thorium for inter-laser delays 50ns ≤ Δt ≤ 10ns and Δx=0.1mm*

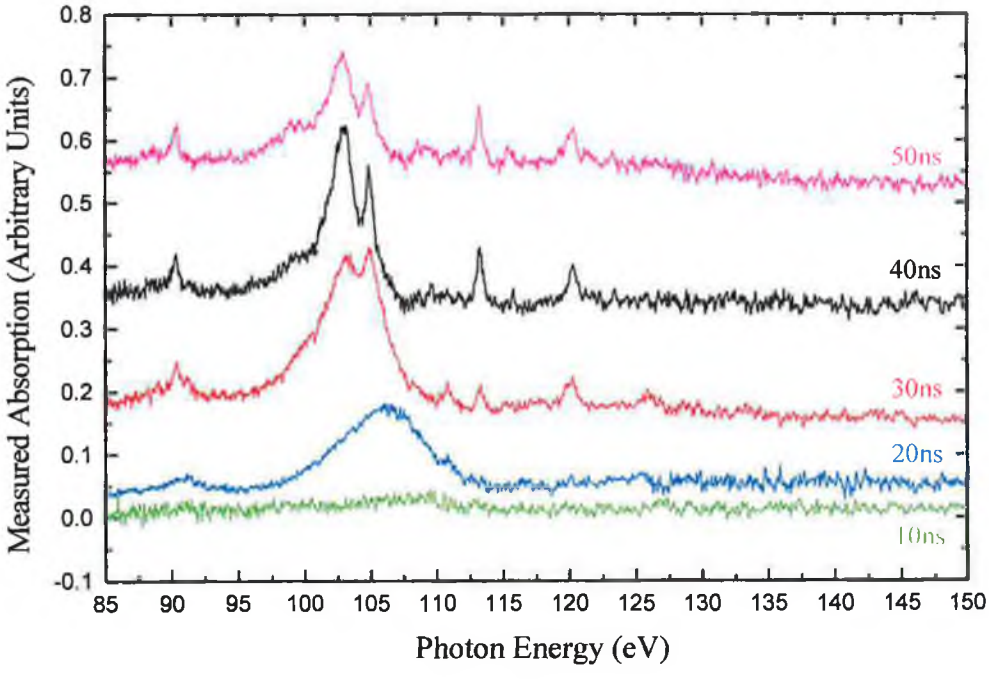

0.1mm (Δx). The absorbing thorium plasma was produced when ~930mJ, 15ns, 1064nm (SL803) laser pulses were focused using a 110mm focal length *f*/3.7 plano convex lens to an irradiance of ~8×10^{11}W/cm^2 on the surface of a planar thorium target. A 100mm focal length *f*/4.5 plano convex lens focused ~330mJ, 15ns, 1064nm (SL404) laser pulses to an irradiance of ~ 3×10^{11}W/cm^2 on a cylindrical tungsten surface in order to produce the continuum backlighting plasma. A spectrometer entrance slit width of 10μm was used during these photoabsorption studies.

The 5d → $\overline{5,\varepsilon}$f giant dipole resonance profile appears very similar for inter-laser (inter-plasma) time delays from 1000ns to 400ns, with no major changes to its overall profile. Below 400ns however, the giant resonance changes dramatically and there is a radical re-distribution of oscillator strength as the main resonance peak collapses into a series of narrower discrete features. This collapse occurs as Δt is reduced and the absorbing thorium plasma is probed earlier during its evolution, thus permitting observation of higher ion stages travelling at higher velocities from the hot thorium plasma core. At 300ns additional structure begins to appear at ~97eV on the rising edge of the main resonance peak. By 200ns this structure begins to develop into a peak. An additional peak at ~104eV on the high energy side of the main resonance peak also appears at Δt = 200ns and the main resonance peak now starts to split. By 100ns the main 5d → 5f singlet peak has split into a series of four peaks at approximately 99, 102, 104 and 109eV. Also, the lower energy triplet peak begins to develop a double-peak structure. As Δt is decreased further from 100 to 60ns the overall structure of the 5d cross section does not change that dramatically but there is increasing definition of each peak and additional discrete structure begins to appear at higher energies (at approximately 113, 115 and 120eV) at 60ns. This discrete structure is 'Rydberg-like' and its appearance signifies the occurrence of wavefunction collapse. The 5f wavefunction which appears to a large extent to be un-collapsed in neutral thorium collapses into the inner potential well of the 5f potential with increasing ionisation, thus becoming a bound state in the discrete 5d photoexcitation spectrum. The broad peaks, retaining most of the oscillator strength in the 95 to 105eV energy region, arise from 5d→5f photoexcitation followed by autoionisation. Following 5f wavefunction collapse, higher nf wavefunctions also contract towards the inner core of the atom and the probability of excitation to nf Rydberg states increases as the centrifugal barrier is reduced. The high degree of 5d-5f overlap however results in the dominance of these 5d→5f transitions over higher

5d→nf transitions. At 50ns the 99eV peak appears to belong to a lower ion stage than that of its nearest neighbours at 103eV and 105eV (now shifted slightly from 102eV and 104eV respectively) due to the reduction in its relative intensity. Both peaks at 103 and 105eV remain until 30ns. The lower energy triplet peak (located at 90eV) has narrowed significantly by 50ns and its intensity decreases from 50 to 10ns but its structure remains largely unchanged. At 20ns, only a single broad peak at 106eV is observed in the region of 5d→5f excitation. Rydberg structure, which may be present at higher energies, may be too weak to observe at the low ion densities in the very early stages of plasma evolution. Also, with increasing contraction of the 5f wavefunction in higher ion stages, the degree of 5d-5f overlap increases further, thus increasing the concentration of oscillator strength into this channel. The increased width of this peak results from reduced autoionising lifetimes of $5d^9 5f$ excited states in higher thorium ions due to reduced screening of the nuclear potential. This broad 5d→5f peak originates from ion stages believed to be Th^{6+} or higher. This assumption is based on the results of HFR calculations of the 5d cross sections of Th^{4+}, Th^{5+} and Th^{6+} reported in Section 5.4.3.

A study of both the individual charge states and also the excitation balance within each ion-stage of thorium contributing to the evolving 5d photoabsorption cross section along the thorium isonuclear sequence is complicated by a number of factors. Firstly, the number of open subshells in the ground states of the ions Th^+ to Th^{3+} (see Table 5.5) and also in the $(5d^9 5f)$ excited configurations of these ions, results in complex ground and excited term structures and increased computational difficulty. Secondly,

Table 5.5 *Ground state electronic configurations of Th to Th^{7+}*

Atom / Ion	**Ground State Configuration**
Th	$[Rn]6d^2 7s^2$
Th^+	$[Rn]6d^2 7s$
Th^{2+}	[Rn]6d5f
Th^{3+}	[Rn]5f
Th^{4+}	$6p^6$
Th^{5+}	$6p^5$
Th^{6+}	$6p^4$
Th^{7+}	$6p^3$

integration over a number of different ion stages in the thorium plume is an additional complication in the interpretation of experimentally observed results.

Configuration interaction Hartree-Fock calculations of the 5d cross sections of the ions Th^{4+} $6p^6$, Th^{5+} $6p^5$ and Th^{6+} $6p^4$ having simpler ground state electronic configurations have been performed and results obtained are detailed in Section 5.4.3. These ions appear early during the evolution of the thorium plasma plume for an inter-laser time delay of 30 to 50ns (see Figure 5.24). RTDLDA calculations of the 5d cross sections of Th to Th^{6+} reproduce the experimentally observed re-distribution of oscillator strength from the 5d $\rightarrow$ $\overline{5,\varepsilon f}$ giant dipole resonance in atomic thorium to discrete Rydberg-like structure with progression to higher charge states along the thorium isonuclear sequence (see Section 5.4.4). In Section 5.4.2.1 results from the picosecond XUV continuum laser plasma light source (developed at RAL) used to probe a nanosecond thorium plasma plume similar to those produced at the CLPR are discussed.

5.4.2.1 Application of Picosecond XUV Continuum Laser Plasma Light Source to the Study of 5f Wavefunction Collapse

A schematic representation of the flat field spectrometer-based DLP system used at RAL to perform time resolved measurements of the XUV 5d relative photoabsorption cross section in atomic and ionic thorium is shown in Figure 5.30. The XUV transmission bandwidth of the spectrometer system (100 to 200eV), as defined by the various mirror/filter components shown, has been detailed previously in Section 4.2.6 Chapter 4. The thorium absorbing plasma was generated by focusing 300mJ, 15ns, 1064nm output pulses from a Q-switched Nd:YAG laser to a spot size ~100μm in diameter (and an irradiance of ~3×10^{11} W/cm^2) onto a planar thorium surface using a 135mm focal length *f*/5 plano convex lens. The short pulse XUV continuum laser plasma was produced when 15-20mJ, 7ps, 248nm laser pulses, amplified in double pass mode in a single KrF excimer amplifier, were focused to an irradiance of ~10^{13} W/cm^2 onto the surface of a cylindrical tungsten rod using a 125mm *f*/5 plano convex lens. The 7ps UV laser pulse was synchronised to the Pockels cell of the Nd:YAG laser and the inter-laser pulse delay could be varied in the range of 5 to 500ns with a jitter of ±0.5ns.

Figure 5.30 *Schematic representation of the XUV flat field experimental system used for time resolved DLP photoabsorption studies along the thorium isonuclear sequence*

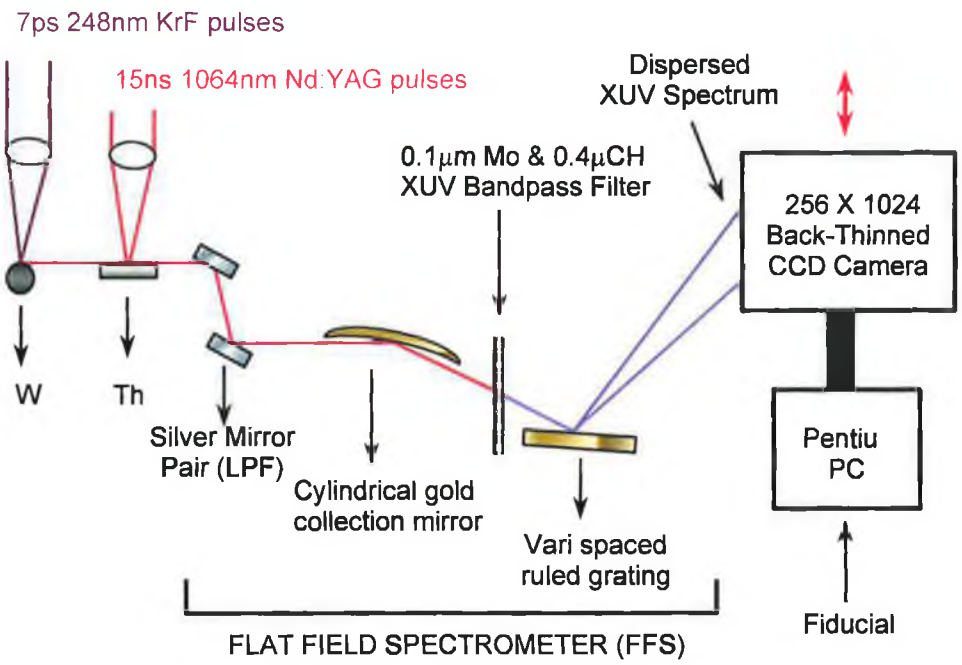

The effective footprint at the thorium target position of the XUV beam emerging from the source plasma was determined by the geometric acceptance of the spectrometer and its associated optics and was estimated to be <100μm and ~100μm in the vertical and horizontal directions respectively.

The results of a time resolved study of the evolution of the 5d photoabsorption spectrum of atomic/ionic thorium with decreasing inter-laser (inter-plasma) time delay are shown in Figure 5.31. Each spectrum is integrated over 60 laser shots (12Hz laser repetition rate, 5s CCD integration time) and has an offset added in order to sequentially displace each spectrum for clarity. Also shown in Figure 5.31 are selected 5d photoabsorption spectra (from Figures 5.27, 5.28 and 5.29) that were recorded at similar inter-laser time delays at DCU and display similar structure.

The collapse of the 5d $\rightarrow$ $\overline{5,\varepsilon f}$ giant dipole resonance in atomic thorium to discrete Rydberg-like structure in higher thorium ions is clearly demonstrated in both sets of experimental results. Rydberg-like structure above 110eV in the 30 to 50ns RAL spectra is more intense relative to the main 5d→5f structure than in the DCU spectra. This is due to the fact that high ion densities in the RAL thorium plasma have resulted in

saturation of the main 5d→5f resonance peak for 30ns ≤ Δt ≤ 50ns. Also, the broad 5d→5f feature located at ~106eV in the DCU 20ns spectrum (~Th^{7+}) is not evident in RAL spectra at short inter-laser delays Δt. This is due to the lower on-target laser irradiance conditions in the RAL experiment (~3×10^{11} W/cm^2) compared with the DCU experiment (~8×10^{11}W/cm^2). Very tight focusing of high energy laser pulses on the thorium target surface is critical for production of sufficient densities of higher charge states suitable for photoabsorption studies.

Figure 5.31 *Inter comparison of RAL and DCU time resolved XUV 5d photoabsorption spectra of a thorium laser-produced plasma showing the collapse of the atomic 5d → $\overline{5,\varepsilon f}$ giant dipole resonance profile to Rydberg-like structure with increasing ionicity as Δt is decreased*

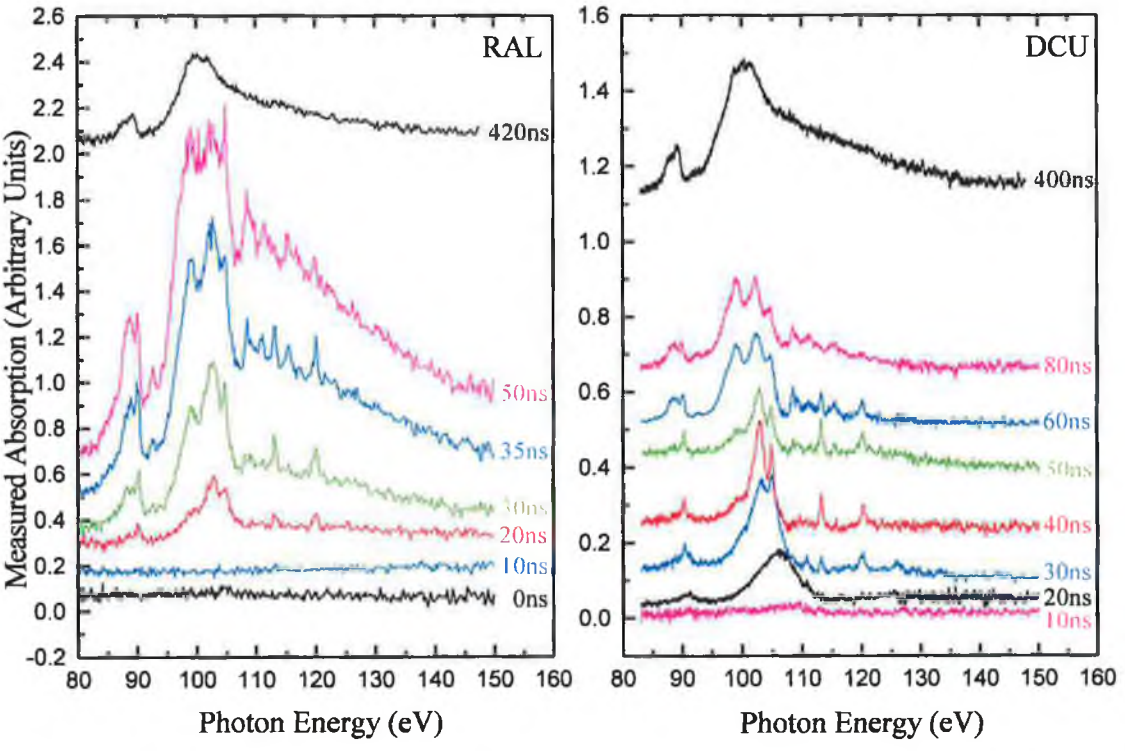

The results presented in Figure 5.31 demonstrate the suitability of the picosecond XUV continuum source to DLP photoabsorption studies. A reduction in the inter-laser jitter (±0.5ns) would permit probing of the absorbing plasma plume at smaller Δt intervals, thus permitting increased ion stage selectivity. This is particularly important for time delays in the region of 50 to 200ns where the observed photoabsorption spectra are very complex, consisting of absorption contributions from many ion stages.

5.4.3 Configuration Interaction Hartree-Fock Calculations of ThV to ThVII: 5d Photoabsorption Cross Sections

Configuration interaction Hartree-Fock calculations of the 5d cross sections of Th^{4+}, Th^{5+} and Th^{6+} have been performed (McGuinness 1999) using the Cowan suite of atomic structure codes (1981). In these calculations both $5d^9nf$ and $5d^9mp$ discrete excited states have been considered. The initial (a), excited (a′) and continuum states (a″) of Th^{4+}, Th^{5+} and Th^{6+} are detailed in Tables 5.6, 5.7 and 5.8 respectively, where the ionic ground states listed in Table 5.5 have been used as initial states (a). For each ion, low-lying metastable excited configurations have been used to perform a configuration interaction type calculation. In the case of the Th^{4+} ($5d^{10}6s^26p^6$), Th^{5+} ($5d^{10}6s^26p^5$) and Th^{6+} ($5d^{10}6s^26p^4$) ground state configurations, the addition of metastable states b, c and d result in –1.3eV, –0.9eV and –0.5eV energy shifts in the average energy (E_{av}) of their respective ground state configurations. The interaction between autoionising discrete excited states and the underlying continua is not accounted for directly here as in the case of HFR calculations of the 5d cross section of

Table 5.6 *Initial (a), excited (a′) and continuum (a″) configurations of ThV used in HFR atomic structure (Cowan code (1981)) calculations of the ThV 5d cross section*

Type of Configuration	Transition(s)	Configuration(s)
Initial states		(a) $5d^{10}6s^26p^6$ (b) $5d^{10}6s^26p^46d^2$ (c) $5d^{10}6s^26p^26d^4$ (d) $5d^{10}6s^26p^47s^2$
Discrete excited states	$5d \rightarrow nf, mp$	(a′) $5d^96s^26p^6nf$ (n=5 to 12) (a′) $5d^96s^26p^6mp$ (m=7 to 14)
Autoionisation	nf^{-1} or mp^{-1}, $6p^{-1}$	(a″) $5d^{10}6s^26p^5 + \varepsilon s, d, g$
	nf^{-1} or mp^{-1}, $6s^{-1}$	(a″) $5d^{10}6s6p^6 + \varepsilon p, f, h$
	$6p^{-2}$	(a″) $5d^{10}6s^26p^4nf + \varepsilon s, d, g$ (n=5 to 12) (a″) $5d^{10}6s^26p^4mp + \varepsilon s, d, g$ (m=7 to 14)

Table 5.7 *Initial (a), excited (a′) and continuum (a″) configurations of ThVI used in HFR atomic structure (Cowan code (1981)) calculations of the ThVI 5d cross section*

Type of Configuration	**Transition(s)**	**Configuration(s)**
Initial states		(a) $5d^{10}6s^26p^5$ (b) $5d^{10}6s^26p^36d^2$ (c) $5d^{10}6s^26p^37p^2$ (d) $5d^{10}6s^26p^37s^2$
Discrete excited states	5d → 6p, nf, mp	(a′) $5d^96s^26p^6$ (a′) $5d^96s^26p^5$nf (n=5 to 12) (a′) $5d^96s^26p^5$mp (m=7 to 14)
Autoionisation	nf^{-1} or mp^{-1}, $6p^{-1}$	(a″) $5d^{10}6s^26p^4$ + εs, d, g
	nf^{-1} or mp^{-1}, $6s^{-1}$	(a″) $5d^{10}6s6p^5$ + εp, f, h
	$6s^{-2}$	(a″) $5d^{10}6p^6$ + εs, d, g

Table 5.8 *Initial (a), excited (a′) and continuum (a″) configurations of ThVII used in HFR atomic structure (Cowan code (1981)) calculations of the ThVII 5d cross section*

Type of Configuration	**Transition(s)**	**Configuration(s)**
Initial states		(a) $5d^{10}6s^26p^4$ (b) $5d^{10}6s^26p^26d^2$ (c) $5d^{10}6s^26p^37p$
Discrete excited states	5d → 6p, nf, mp	(a′) $5d^96s^26p^5$ (a′) $5d^96s^26p^4$nf (n=5 to 12) (a′) $5d^96s^26p^4$mp (m=7 to 14)
Autoionisation	nf^{-1} or mp^{-1}, $6p^{-1}$	(a″) $5d^{10}6s^26p^3$ + εs, d, g
	nf^{-1} or mp^{-1}, $6s^{-1}$	(a″) $5d^{10}6s6p^4$ + εp, f, h
	$6s^{-2}$	(a″) $5d^{10}6p^5$ + εs, d, g

atomic thorium. In the HFR calculation for each ion, spin-orbit energy integrals were un-scaled with 90% and 66% scaling for the F^k and G^k Slater integrals respectively. For all ions, both autoionising decay channels in which the excited nf or mp electron is a participator or spectator in the decay of $5d^9nf$ and $5d^9mp$ excited states are considered. The HFR calculation determines the transition energies E_{ij} between the initial (i) and final (j) excited states and also the weighted oscillator strengths ($g_i f_{ij}$), where g_i is the statistical weight or degeneracy (2J+1) of a given energy level with total angular momentum J. A HFR autoionisation calculation is then performed using the same excited and final state (ion plus continuum electron) configurations in order to determine ΔE_{ij}, the widths of autoionising levels within the $5d^9nf$ and $5d^9np$ configurations. An approximation to each 'partial' cross section $\sigma(E)$ is then calculated separately for each term of the ionic ground state configuration. This is performed by assigning to each resonance at E_{ij}, an oscillator strength f_{ij} and a normalised Lorentzian profile $\Phi(E)$, of width ΔE_{ij}, the width of the autoionising resonance. $\sigma(E)$ is then calculated using

$$\sigma(E) = 109.71 f_{ij} \Phi(E) \tag{5.8}$$

where σ is in MB and E is in eV. The calculated 5d cross sections for all terms of the Th^{4+} ($^1S_0$), Th^{5+} ($^2P_{1/2,3/2}$) and Th^{6+} ($^1S_0$, $^1D_2$, $^3P_{0,1,2}$) ground state configurations are shown in Figure 5.32, where 1000 MB and 2000 MB have been added to the Th^{5+} and Th^{4+} cross sections respectively in order to displace them sequentially for clarity. For each ion, each term of the ground state configuration has been directly summed without any weighting to produce the cross sections shown. The 5d cross section of all of the ions is dominated by a broad feature between 100 and 110eV. This feature is mainly due to 5d→5f (singlet) autoionising transitions, with 5d→5f (triplet) transitions lying, as in ThI, at approximately 15eV below the main triplet peak. Above 110eV, narrower $5d^9nf$ and $5d^9np$ Rydberg structure appears. The increasing number of terms in each ground state from Th^{4+} to Th^{6+} results in an increase in the number of available transitions contributing to the cross section. This is evident in Figure 5.32, where the complexity of each cross section increases from Th^{4+} to Th^{6+}. Also, the overall cross section, in particular that of 5d→5f transitions, increases with additional term structure and the location of the main 5d→5f peak shifts to higher energies with increasing ionisation. The intensity of the main 5d→5f peak increases relative to that of higher energy Rydberg structure with increasing ionisation due to the increased 5d-5f overlap and the corresponding increase in 5d-5f transition probabilities.

Figure 5.32 *Calculated HFR 5d cross sections of Th^{4+} (—), Th^{5+} (—) and Th^{6+} (—) produced by directly summing all terms of each ionic ground state configuration*

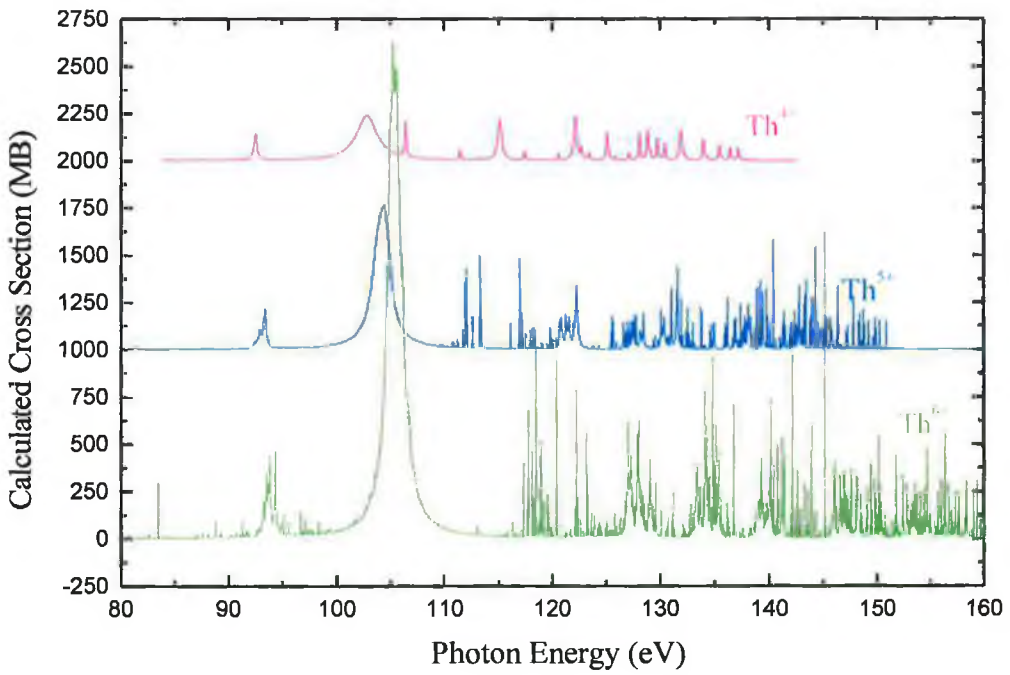

A synthetic spectrum for each charge state (Th^{4+}, Th^{5+} and Th^{6+}) was computed by performing a weighted sum over all terms in each ionic ground state configuration using equation (5.5), where the statistical weighting ω_i of each term was determined using equation (5.6). The electron temperature within both DCU and RAL thorium plasma plumes was estimated to be ~10eV using the Collisional - Radiative model of Colombant and Tonon (1973). For a 10eV uranium plasma, they calculated the dominant ion stage to be U^{5+}. The electron temperature in the thorium plasma, 20 to 50ns after its initiation, is expected to have a similar value of ~10eV due to the observation of Th^{4+} to Th^{6+} charge states at these inter-laser delays.

The synthetic spectrum for each ion was then convolved with a 0.4eV FWHM (R=250 at 100eV) Gaussian profile used to simulate the instrument function of the flat field spectrometer (RAL) and a 0.1eV FWHM (R=1000 at 100eV) Gaussian profile simulating the instrument function of the 2.2m grazing incidence spectrometer (DCU). The convolved spectra are compared to experimental spectra in Figures 5.33 (RAL) and 5.34 (DCU). In both figures, the computed cross sections have been shifted by -2.2eV (Th^{4+}), -1.3eV (Th^{5+}) and -0.5eV (Th^{6+}) in order to bring them into coincidence with the experimental photoabsorption cross section which contains absorption contributions

Figure 5.33 *Comparison of thorium ionic photoabsorption spectrum (RAL) recorded at Δt=20ns, Δx=0.1mm with synthetic 5d spectra of Th^{4+} (—), Th^{5+} (—) and Th^{6+} (—) computed by summing statistically weighted HFR cross sections for each term of each ionic ground state configuration*

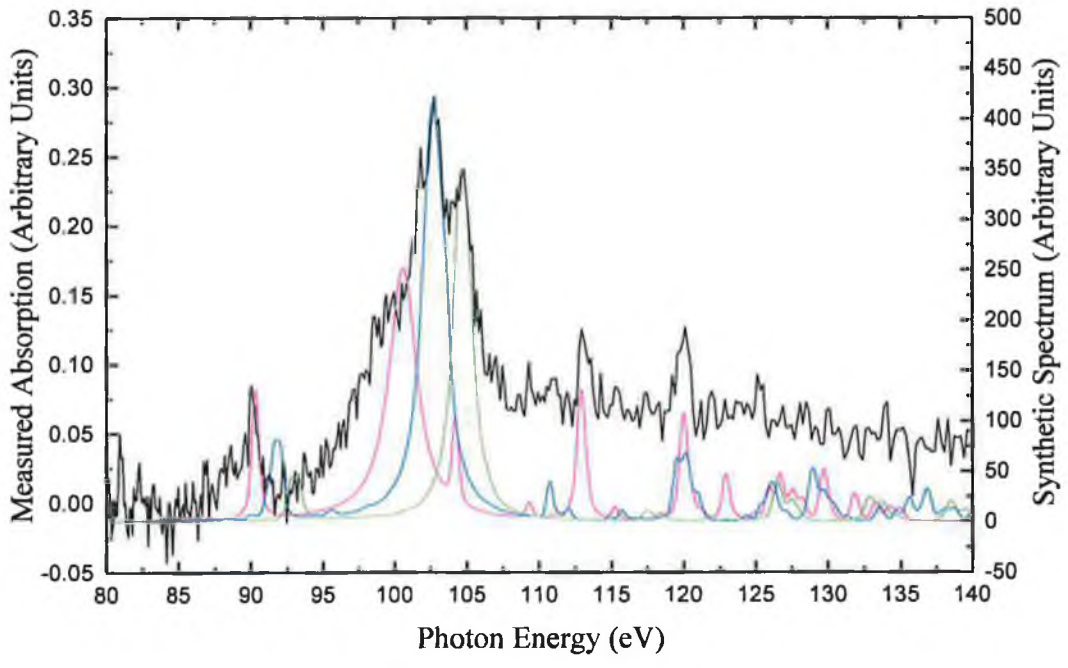

Figure 5.34 *Comparison of thorium ionic photoabsorption spectrum (DCU) recorded at Δt=50ns, Δx=0.1mm with synthetic 5d spectra of Th^{4+} (—), Th^{5+} (—) and Th^{6+} (—) computed by summing statistically weighted HFR cross sections for each term of each ionic ground state configuration*

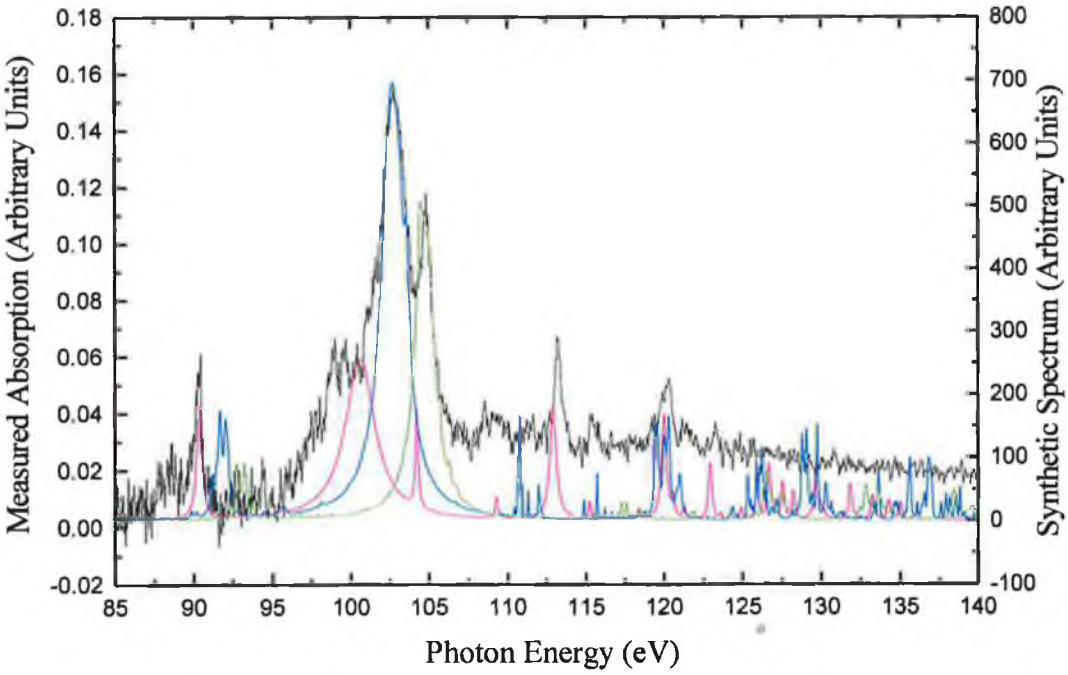

from all three ion stages. In Figure 5.33, the calculated cross sections have been multiplied by 1.00 (Th^{4+}), 1.10 (Th^{5+}) and 0.70 (Th^{6+}) in order to account for the variation in the ion density of each charge state. In Figure 5.34, the calculated cross sections were multiplied by 1.00, (Th^{4+}), 1.78 (Th^{5+}) and 0.95 (Th^{6+}).

In both Figures 5.33 and 5.34, the synthetic spectra are in good agreement with the experimentally recorded photoabsorption cross sections. The main 5d→5f (singlet) peak in each spectrum is split into three secondary peaks arising from the integration of absorption contributions from Th^{4+}, Th^{5+} and Th^{6+} where the main 5d→5f peak is seen to move to higher energies with increasing ionic charge (see Figure 5.32). When the inter-laser time delay Δt drops below 50ns (see Figure 5.29) Rydberg structure above 110eV decreases and by 20ns the 5d→5f (singlet) structure dominates the photoabsorption cross section. This is due to a combination of the reduced intensity of Rydberg transitions with increasing ion stage (as the relative oscillator strength of 5d→5f transitions increases) and also the lower density of higher ionic charge states very early in the evolution of the plasma plume.

In the calculated and experimental spectra of Th^{4+}, Th^{5+} and Th^{6+} the 5f wavefunction appears to be collapsed, giving rise to a typical Rydberg series in the discrete 5d photoexcitation spectrum. In order to investigate this further, term dependent Hartree-Fock with exchange (HXR) calculations of the effective 5f potential (V_{eff}) and the 5f radial wavefunction ($P_{5f}(r)$) for the terms (^1P, ^3P, ^3D) in the Th^{4+*} $5d^96s^26p^65f$ excited state configuration (accessible from the Th^{4+} $6p^6$ ($^1S_0$) ground state) were performed using the Cowan code (1981). Th^{4+} was chosen as a suitable candidate for calculation because of its simple closed shell configuration ($5d^{10}6s^26p^6$), which after 5d→5f excitation remains a relatively simple configuration (Th^{4+*} $5d^96s^26p^65f$) of 10 terms for which the F^k and G^k coefficients are tabulated (Condon & Odabasi 1980). The results of the term-dependent HXR calculation are shown in Figure 5.35, where the 5f radial wavefunction for each term $P_{5f}(r)$ has been squared in order to obtain the radial probability distribution function (see Section 1.1.7 Chapter 1).

V_{eff} and $P_{5f}^2(r)$ for all the terms (^1P, ^3P, ^3D) of the Th^{4+*} $5d^96s^26p^65f$ configuration overlap exactly and V_{eff} appears as a single-well potential with no evidence of a centrifugal barrier or an outer well to support delocalised nf eigenstates. On the basis of HXR calculations all terms of the 5f wavefunction appear to be collapsed in Th^{4+*} and

Figure 5.35 *5f effective potentials calculated using the HXR method (Cowan 1981) for the terms (^1P, ^3P, ^3D) of the Th^{4+*} $5d^9 6s^2 6p^6 5f$ excited state (all curves overlap exactly)*

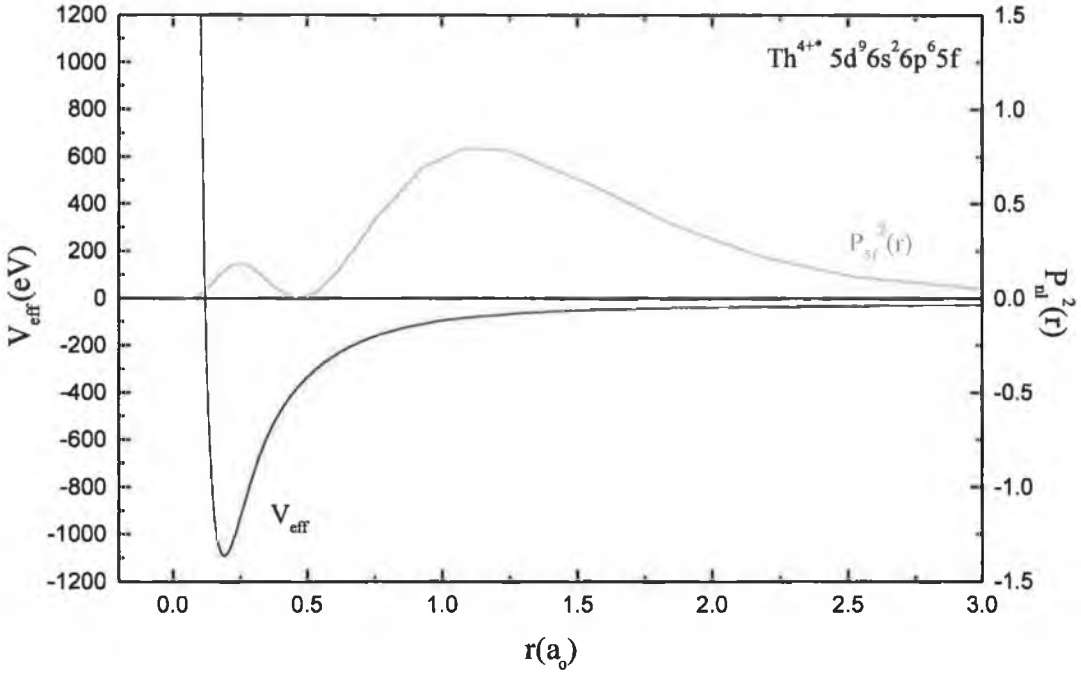

therefore 5d→5f transitions reside in the discrete 5d spectrum of Th^{4+}. This is also the case for 5d→5f transitions in the higher ions Th^{5+} and Th^{6+} where the 5f wavefunction will have contracted further towards the ionic core due to reduced screening of the nuclear charge. In the progression from Th to Th^{4+} the 5f wavefunction undergoes a term dependent collapse and 5d→5f transitions move from the photoionisation spectrum of Th to the photoexcitation spectrum of Th^{4+} where all the $5d^9 5f$ terms become bound states of the inner 5f potential well. The photoabsorption cross sections of Th to Th^{6+}, calculated in Section 5.4.4 using the RTDLDA method, demonstrate the transfer of oscillator strength from the 5d photoionisation spectrum to the 5d photoexcitation spectrum along the thorium isonuclear sequence. In particular, the distribution of oscillator strength in the 5d cross sections of the ion stages Th^+ to Th^{3+}, which were not computed using the HFR method, can be studied.

5.4.4 RTDLDA Calculations of ThI to ThVII: 5d Photoabsorption Cross Sections

RTDLDA calculations of the 5d photoabsorption cross sections of ThI to ThVII were performed using the ground state atomic/ionic configurations listed in Table 5.5. The Slater exchange integrals were scaled at 85% in all calculations and the results obtained are shown in Figure 5.36. Offsets of 55, 150, 250, 450, 600 and 750 MB were added to the Th^{5+}, Th^{4+}, Th^{3+}, Th^{2+}, Th^{+} and Th cross sections respectively to aid clarity of observation. Also shown are the $5d_{5/2}$ and $5d_{3/2}$ ionisation limits for Th^{+} to Th^{5+} calculated using the HFR method (Martins 2000) and detailed in Table 5.6. These limits have been extracted from calculations of the direct 5d photoabsorption cross section of each thorium atom/ion, neglecting all fine structure of the 5d thresholds and therefore

Table 5.9 *$5d_{5/2}$ and $5d_{3/2}$ ionisation limits of Th^{+} to Th^{5+} calculated using the HFR method (Cowan code)*

Ion	$5d_{5/2}$ limit (eV)	$5d_{3/2}$ limit (eV)
Th^{+}	105.5	112.3
Th^{2+}	115.3	122.1
Th^{3+}	123.6	130.2
Th^{4+}	132.4	139.3
Th^{5+}	146.0	153.5

they represent the lowest estimate of each 5d limit. The RTDLDA calculations reproduce the overall spectral features observed during the evolution of the 5d photoabsorption cross section along the thorium isonuclear sequence. The bulk of the oscillator strength is transferred from the 5d $\rightarrow$ $\overline{5,\varepsilon f}$ giant dipole resonance lying predominantly in the photoionisation spectrum of atomic thorium above the upper ($5d_{3/2}$) ionisation limit. By Th^{+}, the main giant resonance peak begins to split into two main features. At Th^{2+} the bulk of the oscillator strength, once concentrated in the main 5d$\rightarrow$5f resonance, has now been re-distributed into a series of discrete autoionising Rydberg-like features lying in the discrete 5d photoexcitation region. In Th^{3+}, Th^{4+} and Th^{5+} Rydberg transitions appear at higher and higher energies as the 5d limits move to higher and higher energies. Despite the appearance of increasing numbers of higher energy Rydberg-like transitions, a major portion of the oscillator strength in the calculated cross sections remains concentrated in the 95 to 110eV region of 5d$\rightarrow$5f

Figure 5.36 *Comparison of a DLP time resolved study of the evolution of the 5d photoabsorption cross section along the thorium isonuclear sequence with 5d cross sections of ThI to ThVII calculated using the RTDLDA method*

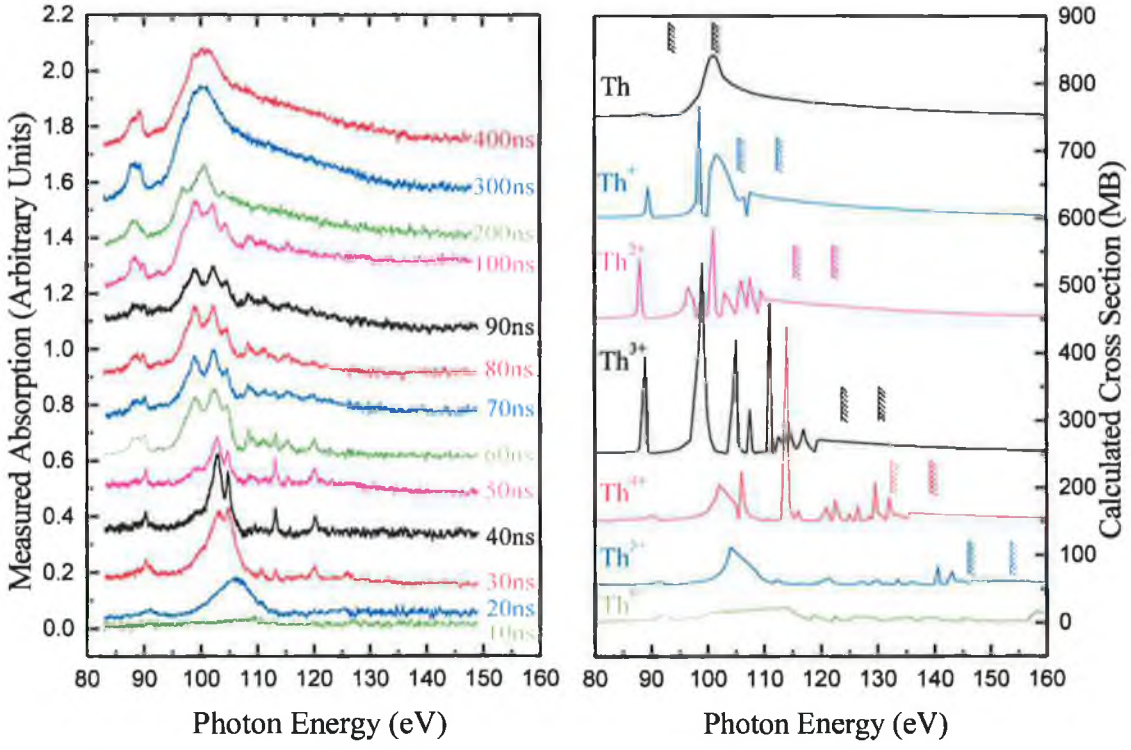

excitation. A similar effect is observed in the experimentally recorded 5d photoabsorption spectra from 60 to 30ns. Photoabsorption peaks in the 95 to 110eV region in the calculated Th^{3+} to Th^{6+} spectra have not converged and their cross section is higher than that shown in Figure 5.36. Similar to HFR calculations of the Th^{6+} photoabsorption cross section discussed in Section 5.4.3, RTDLDA calculations also indicate that by Th^{6+} the importance of the single large autoionising 5d→5f feature located between 95 and 115eV increases relative to any higher energy Rydberg structure. Again this feature has not fully converged in the Th^{6+} RTDLDA calculation and the cross section has been multiplied by a factor of ten in order to permit observation of single broad 5d→5f feature. Despite being un-converged, the Th^{6+} cross section in Figure 5.36 still serves to illustrate the concentration of oscillator strength in a single broad feature that is present in the 20ns experimental photoabsorption spectrum.

5.5 Conclusions and Future Work on Thorium and other Actinide Atoms and Ions

6p VUV Region

In this chapter the relative 6p photoabsorption cross section of atomic thorium was investigated in the 17 to 32eV VUV photon energy range using the DLP technique. The results obtained represent the first measurement of the 6p cross section of an actinide atom. The profile of the 6p→6d giant dipole resonance and the position of both peaks relative to the $6p_{1/2,3/2}$ limits are found to be similar to existing theoretical many body calculations (Wendin 1984). Relativistic Hartree-Fock calculations, based on an independent particle approach that considers the interaction of discrete excited states with underlying continua, also predict the experimentally observed 6p→6d giant dipole resonance profile. Term dependent relativistic Hartree-Fock calculations of the 6d potential in ThI indicate that the 6d wavefunction is collapsed for all terms in the atomic ground state configuration. A comparison of the 6p→6d atomic giant dipole resonance with a solid state FEELS measurement of a thorium thin film (Cukier et al. 1980) demonstrated the survival of the resonance in the solid state environment due to its origins deep within the atom, close to the atomic nucleus.

Time resolved measurements of the relative 6p photoabsorption cross section along the thorium isonuclear sequence were performed in the VUV normal incidence regime using the DLP technique (see Section 5.2.6). As the inter-laser (inter-plasma) delay is decreased, the profile of the 6p→6d giant dipole resonance in atomic thorium changes dramatically while moving up along the thorium isonuclear sequence. The broad autoionising resonances in the neutral 6p photoabsorption cross section collapse to a series of 6p valence transitions in ionic thorium. The 6p photoabsorption spectra of thorium (or any actinide) ions have not yet been studied and much future work remains in the investigation of the atomic processes contributing to the evolution of the 6p cross section along the thorium isonuclear sequence. In the VUV region 6p spatially resolved emission studies of the thorium plasma plume will assist in the analysis of ionic photoabsorption spectra due to the appearance of valence excitations in emission (see Figure AIII.4). The addition of a 'gated' detection system to the 1m normal incidence spectrometer would permit time-resolved emission studies of the thorium plasma plume resulting in greater ion stage selectivity.

6p and 5d investigations performed as part of this thesis work serve as a stimulus for similar photoabsorption studies in actinide atoms and ions and such studies are already underway (van Kampen et al. 2000). The radioactivity, and possible toxicity and short half-lives of actinide elements require experimental ingenuity to overcome these obstacles which have previously hindered actinide photoabsorption studies.

5d XUV Region

In this chapter, XUV inner shell 5d photoabsorption spectra along the thorium isonuclear sequence (Th to Th^{6+}) have been measured for the first time in an actinide element. Measurements demonstrate the transfer of oscillator strength from the 5d photoionisation spectrum to the discrete 5d photoexcitation spectrum as the $5d \rightarrow \overline{5,\varepsilon f}$ giant dipole resonance in atomic thorium collapses to discrete Rydberg-like structure in ionic thorium. Such radical changes in the 5d photoabsorption cross section arise from the increased localisation of the 5f wavefunction and ultimately its complete collapse into the ionic core at higher ion stages. Term dependent Hartree-Fock with exchange calculations indicate that by Th^{4+}, the 5f wavefunction is collapsed in all terms of the $5d^9 6p^6 5f$ excited configuration. RTDLDA calculations of Th to Th^{6+} 5d photoabsorption cross sections reproduce the evolution of the collapse and the re-distribution of oscillator strength along the thorium isonuclear sequence. HFR calculations of Th^{4+}, Th^{5+} and Th^{6+}, considering only discrete autoionising $5d \rightarrow nf$, mp transitions[2] reproduced the experimentally observed spectra in both DCU and RAL time-resolved DLP ion studies. The interaction between both discrete and underlying continuum states was accounted for in HFR calculations of atomic thorium where the spectrum is dominated by a large $5d \rightarrow \overline{5,\varepsilon f}$ giant dipole resonance feature.

Much future work remains in 5d ionic photoabsorption studies in thorium. Increased insight into the collapse of the 5f wavefunction would be achieved using term dependent atomic structure calculations of the intermediate ion stages Th^+ to Th^{3+}. Such calculations would be complemented experimentally by using a source such as the picosecond XUV continuum laser plasma light source. A reduction in the inter-laser jitter would result in better ion stage selectivity when integrating absorption spectra over a number of laser shots. Greater isolation of ionic charge states would permit the observation of a more 'controlled' wavefunction collapse along the thorium isonuclear

[2] Where $(5 \leq n \leq 12)$ and $(6 \leq m \leq 14)$.

sequence. Increased XUV flux from the picosecond laser plasma source (obtainable using higher laser pulse powers) may permit single-shot studies with a higher signal to noise ratio. In such studies the inter-laser time delay between both laser shots can be measured directly, thus the time at which the absorbing plasma plume is probed can be determined using a fast photo-detector and the temporal resolution is not limited by the inter-laser jitter.

Resonant pumping of the thorium plasma plume using a third laser, such as a dye laser, may permit the production of higher densities of a single ionic charge species. At times in excess of 500ns after initiation of the thorium plasma, visible light from a dye laser could be tuned to a strong resonant or inter-combination transition of the neutral thorium species that predominates in the plasma plume at this time. At a sufficient power density, (~10 MW/cm^2) it is well known that an almost 100% singly charged ion column can be produced via Resonant Laser Driven Ionisation (RLDI, McIlrath & Lucatorto 1977). VUV and XUV DLP photoabsorption studies of such a thorium plasma plume would permit measurements with increased isolation of the Th^+ ion.

Modelling of the evolution of metastable state populations in both space and time within the plasma plume using a hydro-dynamic code with an atomic physics processor such as that of Djaoui and Rose (1992) would permit better understanding of the detailed ionisation/excitation balance and therefore the different absorbing species probed in DLP space and time resolved photoabsorption studies.

The DLP technique and other techniques such as photoelectron and photoion spectroscopy have all been used successfully along the lanthanide series to investigate the excitation and decay processes contributing to the formation of 4d→4f giant dipole resonance features. Similar actinide studies have been limited and it is only through continued research efforts, particularly to overcome the experimental difficulties associated with studying these elements, that a deeper understanding of actinide atomic physics will be achieved.

References

Ahn H, Nakano H, Nishikawa T and Uesugi N, 1996
Simultaneous measurement of absorption and X-ray emission from preformed plasma generated by ultrashort prepulse, Japanese Journal of Applied Physics, Vol.35, Part 2, No. 2A, p.L154-7

Backus S, Durfee III G, Murnane M M and Kapteyn H C, 1998
High power ultrafast lasers, Review of Scientific Instruments, Vol.69, No.3, p.1207-23

Baer Y, 1984
Chapter 4: Handbook on the Physics and Chemistry of the Actinides, Elsevier Science, Amsterdam. Edited by A J Freeman and G H Lander

Baier S, Köble U, Luhmann T, Martins M, Richter M and Zimmermann P, 1993
Photoion spectroscopy of atomic Ho, Er and Tm in the region of the 4d giant resonances, Journal of Physics B, Vol.26, p.4091-7

Bakker L P, Freriks J M and Kroesen G M W, 1999
A new ASE filter: the 20-fold prism monochromator, Measurement Science and Technology, Vol. 10, No.3, p.L25-L28

Baldwin G C and Klaiber G S, 1947
Photo-fission in heavy elements, Physical Review, Vol.71, No.1, p.3-10

Baldwin G C and Klaiber G S, 1948
X-ray yield curves for γ–n reactions, Physical Review, Vol.73. No.10, p.1156-63

Ballofet G, Romand J and Vodar B, 1961
Source d'émission de spectre continu s'étendant du visible à l'ultraviolet extrême, C. R. Acad. Sci. Vol.252, p.4139-41

Balmer J, Lewis C L S, Corbett R E, Robertson E, Saadat S, O'Neill D, Kilkenny J D, Back C A and Lee R W, 1989
X-ray absorption spectroscopy of laser-produced plasmas: A study of experiment and data analysis, Physical Review A, Vol.40, No.1, p.330-40

Bard E, Bruno H, Fairbanks R G and Zindler A, 1990
Calibration of the ^{14}C timescale over the past 30,000 years using mass spectrometric U-Th ages from Barbados corals, Nature, Vol.345, p.405-10

Barford N C, 1985
Experimental Measurements: Precision, Error and Truth, Published by John Wiley & Sons, p.108

Bauche J, Bauche-Arnoult C and Klapisch M, 1988
Transition arrays in the spectra of ionised atoms, Advances in Atomic and Molecular Physics, Vol.23, p.131-195

Bekefi G (Editor), 1976
Principles of laser plasmas, Published by John Wiley & Sons Inc.

Benedict U, Dabos-Seignon S, Dufour C, Luo H and Heathman S, 1989
Transuranium elements under extreme pressures, Journal of Nuclear Materials, Vol.166, p.48-55

Berkovits D, Boaretto E and Paul M, 1992
Studies of negative ion formation and interaction with a laser beam, Review of Scientific Instruments, Vol.63, No.4, p.2825-7

Bernstein M J and Comisar G G, 1970
X-ray production in laser-heated plasmas, Journal of Applied Physics, Vol.41, No.2, p.729-33

Bijkerk F and Shevelko A P, 1991
Laser-plasma XUV sources, a role for excimer lasers? Proceedings of SPIE, Vol.1503, Excimer Lasers and Applications III

Bijkerk F, Shmaenok L A, Shevelko A P, Bastiaensen R K F J, Bruineman C and van Honk A G J R, 1995
A high-power, low-contamination laser plasma source for Extreme UV lithography, Microelectronic Engineering, Vol.27, p.299-301

Billen Th, Kirsten T, Mangini A and Eisenhauer A, 1993
Resonance ionisation spectroscopy of thorium, Applied Physics B, Vol.57, p.109-12

Billen Th, Schneider K, Mangini A, Eisenhauer A and Kirsten T, 1995
Resonant laser ionisation of thorium using continuous thermal heating and pulsed laser evaporation, AIP Conference Proceedings, No.329, p.461-4

Bizau J M, Cubaynes D, Gerard P, Wuilleumier F J, Picqué J L, Ederer D L, Carré B and Wendin G, 1986
Experimental and theoretical determinations of the 5d photoionization cross section in laser-excited barium atoms between 15 and 150eV photon energy, Physical Review Letters, Vol.57, No.3, p.306-9

Blaise J and Wyart J-F, 1992
Selected constants, energy levels and atomic spectra of actinides, Laboratoire Aimé Cotton, CNRS, Orsay, France. Tables Internationales de Constantes, Paris

Boland B C, Irons F E and McWhirter R W P, 1968
A spectroscopic study of the plasma generated by a laser from polyethylene, Journal of Physics B (Proceedings of the Physical Society) Series 2, Vol.1, p.1180-91

Bransden B H and Joachain C J, 1983
Physics of atoms and molecules, Longman Scientific & Technical, Wiley Publishing

Bréchignac C and Connerade J P, 1994
Giant resonances in free atoms and in clusters, Journal of Physics B, Vol.27, p.3795-3828

Breton C and Papoular R, 1973
Vacuum-UV radiation of laser-produced plasmas, Journal of the Optical Society of America, Vol.63, No.10, p.1225-32

Briand J P, Chevallier P, Indelicato P, Ziock K P and Dietrich D D, 1990
Observation and measurement of n=2 → n=1 transitions of hydrogenlike and heliumlike uranium, Physical Review Letters, Vol.65, No.22, p.2761-4

Bridges J M, Cromer C L and McIlrath T J, 1986
Investigation of a laser-produced plasma VUV light source, Applied Optics, Vol.25, No.13, p.2208-14

Brooks M S S, Eriksson O and Johansson B, 1995
From the transition metals to the rare earths – via the actinides, Journal of Alloys and Compounds, Vol.223, p.204-10

Bykovskii Yu A, Degtyarenko N N, Elesin V F, Kozyrev Yu P and Sil'nov S M, 1971
Mass spectrometer study of laser plasma, Soviet Physics JETP, Vol.33, No.4, p.706-12

Cable M D, Hatchett S P, Caird J A, Kilkenny J D, Kornblum H N, Lane S M, Laumann C, Lerche R A, Murphy T J, Murray J, Nelson M B, Phillion D W, Powell H and Ress D B, 1994
Indirectly driven, high convergence inertial confinement fusion implosions, Physical Review Letters, Vol.73, No.17, p.2316-9

Campbell E M, 1992
The physics of megajoule, large-scale, and ultrafast short-scale laser plasmas, Physics of Fluids B, Vol.4, No.11, p.3781-99

Carillon A, Jaégle P and Dhez P, 1970
Extreme-ultraviolet continuum absorption by a laser-generated aluminium plasma, Physical Review Letters, Vol.25, No.3, p.140-3

Carroll P K and Kennedy E T, 1977
Doubly excited autoionisation resonances in the absorption spectrum of Li^+ formed in a laser-produced plasma, Physical Review Letters, Vol.38, No.19, p.1068-71

Carroll P K, Kennedy E T and O'Sullivan G, 1978
New continua for absorption spectroscopy from 40-2000Å, Optics Letters, Vol.2, No.3, p.72-4

Carroll P K, Kennedy E T and O'Sullivan G, 1980
Laser-produced continua for absorption spectroscopy in the VUV and XUV, Applied Optics, Vol.19, No.9, p.1454-62

Carroll P K and Kennedy E T, 1981
Laser Produced Plasmas, Contemporary Physics, Vol.22, p.61-96

Carroll P K and O'Sullivan G, 1981
The observation of 5d-5f resonant emission in thorium in high ion stages (≈VIII to XVI), Physics Letters, Vol.84A, No.2, p.59-61

Carroll P K and O'Sullivan, 1982
Ground-state configurations of ionic species I through XVI for Z=57-74 and the interpretation of 4d-4f emission resonances in laser-produced plasmas, Physical Review A, Vol.25, No.1, p.275-86

Carroll P K, Kennedy E T and O'Sullivan, 1983
Table-top EUV continuum light source, IEEE Journal of Quantum Electronics, Vol.QE-19, No.12, p.1807-11

Carroll P K, Costello J T, Kennedy E T and O'Sullivan G, 1984
XUV emission from uranium plasmas; the identification of U XIII and U XV, Journal of Physics B, Vol.17, p.2169-76

Carroll P K, Costello J T, Kennedy E T and O'Sullivan G, 1986
XUV emission from thorium plasmas; the identification of Th XI and Th XIII, Journal of Physics B, Vol.19, p.L651-6

Carroll P K and Costello J T, 1986
Giant-Dipole-Resonance absorption in atomic thorium by a novel two-laser technique, Physical Review Letters, Vol.57, No.13, p.1581-3

Carroll P K and Costello J T, 1987
The XUV photoabsorption spectrum of uranium vapour, Journal of Physics B, Vol.20, p.L201-5

Carroll P K and O'Sullivan G, 1991
Laser produced continua for studies in the XUV, SPIE, Vol.1503, Excimer Lasers and Applications III, p.416-27

Chaker M, La Fontaine B, Côté C Y, Kieffer J C, Pépin H, Talon M H, Enright G D and Villeneuve D M, 1992
Laser plasma sources for proximity printing or projection x-ray lithography, Journal of Vacuum Science and Technology B, Vol.10, No.6, p.3239-42

Chaker M, Pelletier J F and Kieffer J C, 1993
Materials for laser-plasma X-ray source targets applicable to lithography, Materials Aspects of X-ray Lithography Symposium, 12th-14th of April, San Francisco, Material Research Society Symposium Proceedings, Vol.306, p.151-67

Chambers J M, Cleveland W S, Kleiner B and Tukey P A, 1983
Graphical Methods for Data Analysis, The Wadsworth Statistics/Probability Series, Published by Duxbury Press, p.94

Chang Z, Rundquist A, Wang H, Christov I, Murnane M M and Kapteyn H C, 1998
Generation of coherent, femtosecond, X-ray pulses in the "water window", IEEE Journal of Selected Topics in Quantum Electronics, Vol.4, No.2, p.266-70

Cheng K T and Froese Fischer C, 1983
Collapse of the 4f orbital for Xe-like ions, Physical Review A, Vol.28, No.5, p.2811-9

Chidambaram R, Kakodkar A and Rodriguez P, 1994
Nuclear technology: power to the people, IEEE Spectrum, Vol.31, Iss.3, p.36-9

Choi I W, Lee J U, Nam C H, 1997
Space-resolving flat-field extreme ultraviolet spectrograph system and its aberration analysis with wave-front aberration, Applied Optics, Vol. 36, No.7, p.1457-66

Cobble J A, Fulton R D, Jones L A, Kryala G A, Schappert G T, Taylor A J and Wahlin E K, 1992
X-ray streak camera diagnostics of picosecond laser-plasma interactions, Review of Scientific Instruments, Vol.63, No.10, p.5116-8

Colombant D and Tonon G F, 1973
X-ray emission in laser-produced plasmas, Journal of Applied Physics, Vol.44, No.8, p.3524-37

Condon E U and Odabasi H, 1980
Atomic Structure, Cambridge University Press, p.609-10

Connerade J P, 1978a
The Non-Rydberg Spectroscopy of Atoms, Contemporary Physics, Vol.19, No.5, p.415-48

Connerade J P, 1978b
Controlling the collapse of atomic wavefunctions, Journal of Physics B, Vol.11, No.13, p.L381-4

Connerade J P and Mansfield M W D, 1975
Centrifugal barrier perturbation of the $nf\,^2F$ series in BaII, Proceedings of the Royal Society of London A, Vol.346, p.565-70

Connerade J P, Mansfield M W D, Cukier M and Pantelouris M, 1980a
Experimental evidence for the existence of a $\overline{5,\varepsilon f}$ resonantly localised continuum state in uranium, Journal of Physics B, Vol.13, p.L235-8

Connerade J P, Pantelouris M, Baig M A, Martin M A P and Cukier M, 1980b
On the resonantly localised $\overline{5,\varepsilon f}$ continuum state in thorium, Journal of Physics B, Vol.13, p.L357-61

Connerade J P, Esteva J M and Karnatak R C, 1987
Giant Resonances in Atoms, Molecules, and Solids, NATO ASI Series, Series B, Vol.151, Plenum Publishing Corporation

Connerade J P, 1992
Co-operative Effects in Atomic Physics, Advances in Atomic, Molecular, and Optical Physics, Vol.29, p.325-67

Connerade J P, 1998
Highly Excited Atoms (Chapter 5 - Centrifugal barrier effects), Cambridge University Press

Cooper J W, 1964
Interaction of maxima in the absorption of soft X-rays, Physical Review Letters, Vol. 13, No.25, p.762-4

Costello J T, Mosnier J-P, Kennedy E T, Carroll P K and O'Sullivan G, 1991
X-UV absorption spectroscopy with laser-produced plasmas; A review, Physica Scripta, Vol.T34, p.77-92

Cowan R D, 1973
The theory of rare earth energy levels and spectra, Nuclear Instruments and Methods, Vol.110, p.173-82

Cowan R D, 1981
Theory of Atomic Structure and Spectra (Berkeley, CA: University of California Press)

Crasemann B, 1985
Atomic Inner-Shell Physics, Plenum Press, New York

CRC Handbook of Chemistry and Physics, 1998-1999, 79th Edition, Editor-in-chief: David R. Lide, CRC Press Inc., Boca Raton, Florida.

Cromer C L, Bridges J M, Roberts J R, and Lucatorto T B, 1985
High-resolution VUV spectrometer with multichannel detector for absorption studies of transient species, Applied Optics, Vol.24, p.2996-3000

Cukier M, Dhez P, Gauthé B, Jaeglé P, Wehenkel Cl and Combet Farnoux F, 1978
Photoabsorption of Th and U by direct measurement and by fast electron energy loss spectra near the 5d thresholds, Journal de Physique Lettres, Vol.39, p.L315-7

Cukier M, Gauthé B and Wehenkel C, 1980
Interband, collective and atomic (p,d) excitations from 2 to 160eV in Sc, Y, lanthanides and actinides and in some of their compounds by FEELS, Journal de Physique, Vol.41, p.603-13

Cummings A, McGuinness C, O'Sullivan G, Costello J T, Mosnier J-P, Kennedy E T, 2000
Wavefunction collapse with increasing ionisation: 4d photoabsorption of Cs through Cs^{4+}, for submission to Physical Review A

Daido H, Turcu I C E, Ross I N, Watson J G, Steyer M, Kaur R, Schulz M S and Amit M, 1992
Spatial coherence of a repetitive laser-plasma point x-ray source in the water window spectral region, Applied Physics Letters, Vol.60, No.10, p.1155-7

D'Arcy R, Costello J T, Kennedy E T, McGuinness C, Mosnier J-P and O'Sullivan G, 2000
The evolution of 4d photoabsorption in Sb with increasing ionization, Journal of Physics B, Vol.33, p.1383-1401

Dardis L, 1998
VUV Emission and Absorption Spectroscopy with a Multichannel Near Normal Incidence Spectrometer, MSc. Thesis, Dublin City University (unpublished)

Davidson S J, Neely D, Lewis C L S and O'Neill D, 1990
Recent advances in the technique of point projection spectroscopy, Rutherford Appleton Laboratory Internal Report, RAL-90-026, p.13-16

DeHeer W A, Selby K, Kresin V, Masui J, Collmer M, Châtelain A and Knight W D, 1987

Collective dipole oscillations in small sodium clusters, Physical Review Letters, Vol.59, No.16, p.1805-8

DeMaria A J, Glenn W H and Mack M E, 1971
Ultrafast laser pulses, Physics Today, July, p.19-26

Denlinger J D, Rotenberg E, Warwick T, Visser G, Nordgren J, Guo J H, Skytt P, Kevan S D, McCutcheon K S, Shuh D, Bucher J, Edelstein N, Tobin J G and Tonner B P, 1995
First results from the spectromicroscopy beamline at the Advanced Light Source, Review of Scientific Instruments, Vol.66, No.2, p.1342-5

Desclaux J P, 1973
Relativistic dirac-fock expectation values for atoms with Z=1 to Z=120, Atomic Data and Nuclear Data Tables, Vol.12, p.311-406

Desclaux J P and Freeman A J, 1984
Atomic properties of the actinides in *Handbook on the Physics and Chemistry of the Actinides,* Edited by A J Freeman and G H Lander, Elsevier Science Publishers B.V.

DeShalit A and Feshbach H, 1974
Theoretical Nuclear Physics, Vol. I: Nuclear Structure, Wiley Publishing

Djaoui A and Rose S J, 1992
Calculation of the time-dependent excitation and ionization in a laser-produced plasma, Journal of Physics B, Vol.25, p.2745-62

Doyle B, 1995
A 1m Normal Incidence Multi-Channel Spectrometer for Laser Plasma Spectroscopy, MSc. Thesis, Dublin City University (unpublished)

Dunne P, O'Sullivan G and O'Reilly D, 2000
Pre-pulse enhanced narrow bandwidth soft x-ray emission from a low debris, subnanosecond, laser plasma source, Applied Physics Letters, Vol.76, No.1, p.34-6

Edelstein N M, 1995
Comparison of the electronic structure of the lanthanides and actinides, Journal of Alloys and Compounds, Vol.223, p.197-203

Ederer D L, Lucatorto T B, Saloman E B, Madden R P and Sugar J, 1975
Photoabsorption of the 4d electrons in barium, Journal of Physics B, Vol.8, No.3, p.L21-5

Ehler A W and Weissler G L, 1966
Vacuum ultraviolet radiation from plasmas formed by a laser on metal surfaces, Applied Physics Letters, Vol.8, No.4, p.89-91

Eichler B, Hübner S, Erdmann N, Eberhardt K, Funk H, Herrmann G, Köhler S, Trautmann N, Passler G and Urban F-J, 1997
An atomic beam source for actinide elements: concept and realisation, Radiochimica Acta, Vol.79, p.221-33

Elton R C, 1990
X-ray lasers, Published by Academic Press Inc.

Eriksson O, Söderlind P, Wills J M and Boring A M, 1993
First principles studies of crystal structures of f elements, Physica B, Vol.190, p.5-11

Failor B H, Gabl E F, Busch G E, Bosch R A and Gerber G L, 1990
Recent x-ray backlight source developed at KMS, Review of Scientific Instruments, Vol.61, No.10, p.2762-4

Fano U, 1961
Effects of configuration-interaction on intensities and phase shifts, Physical Review, Vol.124, No.6, p.1866-78

Fawcett B C, Gabriel A H, Irons F E, Peacock N J and Saunders P A H, 1966
Extreme ultra-violet spectra from laser-produced plasmas, Proceedings of the Physical Society, Vol.88, p.1051-3

Fischer J, Kühne M and Wende B, 1984
Spectral radiant power measurements of VUV and soft x-ray sources using the electron storage ring BESSY as a radiometric standard source, Applied Optics, Vol.23, No.23, p.4252-9

Fock V, 1930
Näherungsmethode zur Lösung des quantenmechanischen Mehrkörperproblems, Zeitschrift für Physik, Vol.61, p.126-52

Fomichev V A, Zimkina T M, Gribovskii S A and Zhukova I I, 1967
Discrete absorption by 4d electrons in the lanthanum group rare-earth metals, Soviet Physics – Solid State, Vol.9, No.5, p.1163-5

Fournier J M and Manes L, 1985
Actinides – Chemistry and Physical Properties (Chapter A: Actinide Solids-5f Dependence of Physical Properties), Edited by L Manes, Springer-Verlag

Fuggle J C, Burr A F, Watson L M, Fabian D J and Lang W, 1974
X-ray photoelectron studies of thorium and uranium, Journal of Physics F, Vol.4, p.335-42

Gamaly E G, 1994
Ultrashort powerful laser matter interaction: Physical problems, models and computations, Laser and Particle Beams, Vol.12, No.2, p.185-208

Gangrskii Yu P, Zemlyanoi S G, Markov B N, Myshinskii G V, Nesterenko V O, Vorykhalov I V, Izosimov I N, Rimskii-Korsakov A A and Smirnov V V, 1997
Production of heavy atomic clusters upon interaction of laser radiation with matter, Soviet Physics JETP, Vol.85, No.1, p.42-7

Goeppert-Mayer M, 1941
Rare-earth and transuranic elements, Physical Review, Vol.60, p.184-7

Grant I P, McKenzie B J, Norrington P H, Mayers D F and Pyper N C, 1980

An atomic multiconfigurational dirac-fock package, Computer Physics Communications, Vol.21, p.207-31

Grätz M, Tillman C, Mercer I and Swanberg S, 1996
X-ray generation for medical applications from a laser-produced plasma, Applied Surface Science, Vol.96-8, p.443-7

Griffin D C, Andrew K L and Cowan R D, 1969
Theoretical calculations of the d-, f-, and g-electron transition series, Physical Review, Vol.177, No.1, p.62-71

Gschneidner Jr. K A, 1995
Systematics in lanthanide and actinide solids, Journal of Compounds and Alloys, Vol.223, p.165-9

Haase Dietmar, 1989
Diplomarbeit, Univ. Hamburg (unpublished)

Haensel R, Rabe P and Sonntag B, 1970
Optical absorption of cerium, cerium oxide, praseodymium, praseodymium oxide, neodymium, neodymium oxide and samarium in the extreme ultraviolet, Solid State Communications, Vol.8, p.1845-8

Hahn O and Strassmann F, 1939
Über den nachweis und das verhalten der bei der bestrahlung des urans mittels neutronen entstehenden erdalkalimetalle, Naturwissenschaften Vol.27, p.11-3
English Translation: *On the identification and the behaviour of rare earth metals produced in the neutron irradiation of uranium,* American Journal of Physics, Vol.32, p.10-5 (1964)

Haire R G, 1995
Comparison of the chemical and physical properties of f-element metals and oxides: their dependence on electronic properties, Journal of Alloys and Compounds, Vol.223, p.185-96

Hamster H, Sullivan A, Gordon S, White W and Falcone R W, 1993
Sub-picosecond, electromagnetic pulses from intense laser-plasma interaction, Physical Review Letters, Vol.71, No.17, p.2725-8

Hansen J E, 1972
Hartree-Fock calculations for the $4d^9 5s^2 5p^6 4f$ configuration in La IV, Journal of Physics B, Vol.5, p.1096-1100

Hansen J E, Brilly J, Kennedy E T and O'Sullivan G, 1989
Rise and fall of the $4d^{10} \rightarrow 4d^9 4f$ resonance in the Xe isoelectronic sequence, Physical Review Letters, Vol.63, No.18, p.1934-7

Harada T and Kita T, 1980
Mechanically ruled aberration-corrected concave gratings, Applied Optics, Vol.19, No.23, p.3987-93

Hartree D R, 1928
The wave mechanics of an atom with a non-Coulomb central field. Part III: Term values and intensities in series in optical spectra, Proceedings of the Cambridge Philosophical Society, Vol.24, p.426-37

Heimann P, Warwick T, Howells M, McKinney W, Digennaro D, Gee B, Yee D and Kincaid B, 1992
The Advanced Light Source U8 beamline, 20-300eV, Nuclear Instruments and Methods in Physics Research, Vol.A319, p.106-9

Hertel V I, Steger H, deVries J, Weisser B, Menzel C, Kamke B and Kamke W, 1992
Giant plasmon excitation in free C_{60} and C_{70} molecules studied by photoionisation, Physical Review Letters, Vol.68, No.6, 1992

Hirsch J S, Meighan O, Mosnier J-P, van Kampen P, Whitty W, Costello J T, Lewis C L S, MacPhee A G, Hirst G J, Westhall J and Shaikh W, 2000
Vacuum-UV resonant photoabsorption imaging of laser produced plasmas, accepted by Journal of Applied Physics, July 2000

Hoheisel W, Jungmann K, Vollmer M, Weidenauer R and Träger F, 1988
Desorption stimulated by laser-induced surface-plasmon excitation, Vol.60, No.16, p.1649-52

Holst G C, 1996
CCD Arrays, Cameras, and Displays, pg.92, Published by SPIE Optical Engineering Press

Holzapfel W B, 1995
Structural systematics of 4f and 5f elements under pressure, Journal of Alloys and Compounds, Vol.223, p.170-3

Hughes T P, 1975
Plasmas and laser light, Published by Adam Hilger, UK

Irons F E, McWhirter R W P and Peacock N J, 1972
The ion and velocity structure in a laser produced plasma, Journal of Physics B, Vol.5, p.1975-87

Jaeglé P, Jamelot G, Carillon A, Sureau A and Dhez P, 1974
Superradiant line in the soft-X-ray range, Physical Review Letters, Vol.33, No.18, p.1070-3

Jannitti E, Nicolosi P and Tondello G, 1979
Stigmatic observations of laser-produced plasmas with a grazing-incidence spectrograph, Optics Letters, Vol.4, No.6, p.187-9

Jannitti E, Nicolosi P and Tondello G, 1984
Photoionisation and double excitation spectrum of Be^{2+}, Optics Communications, Vol.50, No.4, p.225-30

Jannitti E, Nicolosi P and Tondello G, 1987
An experiment for absorption spectroscopy in the XUV of light ions, Physica Scripta, Vol.36, p.93-8

Johansson B, 1995
Crystal and electronic structure connections between the 4f and 5f transition metals, Journal of Alloys and Compounds, Vol.223, p.211-5

Journal of Alloys and Compounds, 1995
Proceedings of the International Workshop on Actinides at Bühlerhöhe (Black Forest) Germany on July 28-30, 1994, Vol.223, No.2

Käbler W, Meisel G, Rink J and Thompson R C, 1992
Two-step optical excitation for Doppler linewidth reduction and motion study of ions stored in a Paul trap, Journal of Modern Optics, Vol.32, No.2, p.335-47

Kaplan I G, 1997
Giant resonances in atoms, atomic clusters, fullerenes, condensed media, and nuclei, Zeitschrift Für Physik D, Vol.40, p.375-80

Kaplan I G, Mondragón A, and Smirnov Yu. F, 1996
Giant resonances in nuclei, atoms, atomic clusters, and condensed media II, Revista Mexicana de Física, Vol.42, Suplemento 1, p.117-30

Kapteyn H C, Murnane M M, Szoke A, Hawryluk A and Falcone R W, 1990
Enhanced absorption and ASE pedestal suppression in the generation of ultrashort-pulse solid-density plasmas, Ultrafast Phenomena VII, edited by Harris C B, Ippen E P, Mourou G A and Zewail H, Published by Springer, p.122-4

Karpeshin F F, Band I M, Trzhaskowskaya M B and Zon B A, 1992
Study of ^{229}Th through laser-induced resonance internal conversion, Physics Letters B, Vol.282, p.267-70

Karpeshin F F, Band I M, Trzhaskowskaya M B and Listengarten M A, 1996
Optical pumping of ^{229m}Th through NEET as a new effective way of producing nuclear isomers, Physics Letters B, Vol.372, p.1-7

Kelly R L, 1987
Atomic and ionic spectrum lines below 2000 Angstroms: Hydrogen through Krypton, Journal of Physical and Chemical Reference Data, Vol.16, No.1, Parts I & II

Kennedy D J and Manson S T, 1972
Photoionization of the noble gases: cross sections and angular distributions, Physical Review A, Vol.5, No.1, p.227-47

Kennedy E T, Costello J T and Mosnier J-P, 1995
Inner-shell photoionisation studies of atoms, excited atoms and ions with laser-generated plasmas, Proceedings of the 4th US-Mexico Symposium on Atomic and Molecular Physics, Edited by C Cisneros and T J Morgan, Published by World Scientific, p. 406-423

Kennedy E T, Costello J T, Gray A, McGuinness C, Mosnier J-P and van Kampen P, 1999
New dual laser plasma investigations of inner-shell excitations, Journal of Electron Spectroscopy and Related Phenomena, Vol.101-3, p.161-6

Kieffer J C and Chaker M, 1994
X-ray sources based on subpicosecond laser produced plasmas, Journal of X-ray Science and Technology, Vol.4, p.312-22

Kiernan L, 1994
Development of a Multi-Laser, Multi-Channel XUV Spectrometer Facility Based on the Dual Laser Plasma Technique, PhD Thesis, Dublin City University (unpublished)

Kiernan L M, Kennedy E T, Mosnier J-P, Costello J T and Sonntag B F, 1994
First observation of photon-induced triply exited state in atomic lithium, Physical Review Letters, Vol.72, No.15, p.2359-62

Kilkenny J D, Campbell E M, Lindl J D, Logan G B, Meier W R, Perkins L J, Paisner JA, Key M H, Powell H T, McCrory R L and Seka W, 1999
The role of the National Ignition Facility in energy production from inertial fusion, Philosophical Transactions of the Royal Society of London Series A, Vol.357 p.533-53

Kimura I, 1995
Review of co-operative research on the thorium fuel cycle as a promising energy source in the next century, Progress in Nuclear Energy, Vol.29, p.445-52

Kita T, Harada T, Nakano N and Kuroda H, 1983
Mechanically ruled aberration-corrected concave gratings for a flat-field grazing-incidence spectrograph, Applied Optics, Vol.22, No.4, p.512-3

Kjeldsen H, West J B, Folkmann F, Knudsen H and Andersen T, 2000
The absolute photoionization cross section of singly charged magnesium ions in the extreme ultraviolet, Journal of Physics B, Vol.33, No.7, p.1403-14

Kmetec J D, Gordon III C L, Macklin J J, Lemoff B E, Brown G S and Harris S E, 1992
MeV X-ray generation with a femtosecond laser, Physical Review Letters, Vol.68, No.10, p.1527-30

Köble U, Kiernan L, Costello J T, Mosnier J-P and Kennedy E T, 1995
$4f(^1P)$ Giant Dipole Resonance in La^{3+}, Physical Review Letters, Vol.24, No.12, p.2188-91

Köhler S, Albus F, Deißenberger R, Erdmann N, Funk H, Hasse H-U, Herrmann G, Huber G, Klunge H-J, Nunnemann G, Passler G, Rao P M, Riegel J, Trautmann N and Urban F-J, 1995
Determination of the first ionisation potential of actinides by resonance ionisation mass spectroscopy, AIP Conference Proceedings, No.329, p.377-80

Koizumi T, Awaya Y, Gonno M, Itoh Y, Kimura M, Kojima T M, Kravis S, Oura M, Sano M, Sekioka T, Watanabe N, Yamaoka H and Koike F, 1996
4d photoionisation of singly-charged Xe, Ba and Eu ions, Journal of Electron Spectroscopy and Related Phenomena, Vol.79, p.289-92

Koizumi T, Awaya Y, Fujino A, Itoh Y, Kitajima M, Kojima T M, Oura M, Okuma R, Sano M, Sekioka T, Watanabe N and Koike F, 1997
4d photoionisation of multiply charged Xe^{q+} (q=1-3) ions, Physica Scripta, Vol.T73, p.131-2

Korukhov V V and Troshin B I, 1990
Recording of continuous spectra of laser-plasma radiation using a potassium hydrogen phthalate crystal, Optical Spectroscopy (USSR), Vol.68, No.1, P.25-6

Kruer W L, 1991
Intense laser plasma interactions: From Janus to Nova, Physics of Fluids B, Vol.3, No.8, p.2356-66

Kruer W L, 1988
The Physics of Laser Plasma Interactions, Addison-Wesley Publishing Company, p.116

Kucas S and Karazija R, 1998
The location of 4d photoabsorption resonances and the collapse of the 4f radial wavefunction in lanthanides, Physica Scripta, Vol.58, p.220-3

Kyrala G A, Fulton R D and Cobble J A, 1994
Diagnostics of high-brightness short-pulse lasers and the plasmas they generate, Generation, Amplification, and Measurement of Ultrashort Laser Pulses, SPIE, 25-27th January 1994, Los Angeles, California, Vol.2116, p.323-34

Leng Y, Goldhar J, Griem H R and Lee R W, 1995
C VI Lyman line profiles from 10-ps KrF-laser-produced plasmas, Physical Review E, Vol.52, No.4, p.4328-37

Lewis C L S and McGlinchey J, 1985
Quasi-monochromatic, projection radiography of dense laser drive spherical targets, Optics Communications, Vol.53, No.3, p.179-86

L'Huillier A and Balcou Ph, 1993
High-order harmonic generation in rare gases with a 1ps 1053nm laser, Physical Review Letters, Vol.70, No.6, p.774-7

Liberman D A and Zangwill A, 1984
A relativistic program for optical response in atoms using a time-dependent local density approximation, Computer Physics Communications, Vol. 32, p.75-82

Lubrek J and Wendin G, 1996
The Ba 4d-f giant dipole resonance as a probe of the structure of endohedral $Ba@C_n$ metallofullerenes, Chemical Physics Letters, Vol.248, p.147-52

Lucatorto T B, McIlrath T J, Sugar J and Younger S M, 1981
Radical redistribution of the 4d oscillator strength observed in the photoabsorption of the Ba, Ba^+, and Ba^{++} Sequence, Physical Review Letters, Vol.47, No.16, p.1124-8

Lung M and Gremm O, 1998
Perspectives of the thorium fuel cycle, Nuclear Engineering and Design, Vol.180, p.133-46

Mack J E, Stehn J R and Edlén B, 1932
On the concave grating spectrograph especially at large angles of incidence, Journal of the Optical Society of America, Vol.22, p.245-64

Macklin J J, Kmetec J D and Gordon III C L, 1993
High-order harmonic generation using intense femtosecond pulses, Physical Review Letters, Vol.70, No.6, p.766-9

MacPhee A G and Lewis C L S, 1994
CCD imaging from 20eV to 8keV, AIP Conference Proceedings, Vol.332, p.441-5

Madden R P and Codling K, 1965
Two-electron excitation states in helium, The Astrophysical Journal, Vol.141, No.2, p.364-75

Maiman T H, 1960
Stimulated optical radiation in ruby, Nature, Vol.187, p.493-4

Maksimchuk A, Kim M, Workman J, Korn G, Squier J, Du D, Umstadter D, Mourou G and Bouvier M, 1996
Signal averaging x-ray streak camera with picosecond jitter, Review of Scientific Instruments, Vol.67, No.3, p.697-9

Mansfield M W D and Connerade J P, 1976
Observation of 4d→f transitions in europium vapour, Proceedings of the Royal Society A, Vol. 352, p.125-39

Marrs R E, Elliott S R and Knapp D A, 1994
Production and trapping of hydrogenlike and bare uranium ions in an electron beam ion trap, Physical Review Letters, Vol.72, No.26, p.4082-5

Martins M, *private communication*, 2000

Matthew J A D, Netzer F P, Clark C W Morar J F, 1987
Giant 4p-quadrupole resonances in the rare earths, Europhysics Letters, Vol. 4, No.6, p.677-83

Matthews D L, 1996
Possibility of short wavelength X-ray lasers and their applications, X-ray Lasers Conference, 10^{th}–14^{th} of June 1996, Lund, Sweden, Institute of Physics Conference Series, Edited by S Svanberg and C-G Wahlström, No.151, Section 1, p.32-9

Matthews D L, Hagelstein P L, Rosen M D, Eckart M J, Ceglio N M, Hazi A U, Medecki H, MacGowan B J, Trebes J E, Whitten B L, Campbell E M, Hatcher C W, Hawryluk A M, Kauffman R L, Pleasance L D, Rambach G, Scofield J H, Stone G and Weaver T A, 1985
Demonstration of a soft X-ray amplifier, Physical Review Letters, Vol.54, No.2, p.110-3

Matthews D L and Rosen M D, 1988
Soft X-ray lasers, Scientific American, December 1988, p.60-5

McCormack T and O'Sullivan G, 1993
Core-excited transitions in Au I-like Th XII and U XIV, Journal of Physics B, Vol.26, p.L327-32

McGuinness C, *private communication*, 1999

McIlrath T J and Lucatorto T B, 1977
Laser excitation and ionization in a dense Li vapor: observation of the even-parity, core-excited autoionizing states, Physical Review Letters, Vol.38, No.24, p.1390-3

McWhirter R W P, 1965
Plasma diagnostic techniques, Chapter 5: Spectral Intensities, p.201, Edited by R H Huddlestone and S L Leonard, Published by Academic Press Inc.

Meighan O, Gray A, Mosnier J-P, Whitty W, Costello J T, Lewis C L S, MacPhee A, Allott R, Turcu I C E and Lamb A, 1997
Short-pulse, extreme-ultraviolet continuum emission from a table-top laser plasma light source, Applied Physics Letters, Vol.70, No.12, p.1497-9

Meighan O, Dardis L, Kennedy E T, Morgan T J, Mosnier J-P, van Kampen P and Costello J T, 1999
Observation of a 6p-6d giant dipole resonance in the VUV photoabsorption spectrum of a laser-produced thorium plasma, Journal of Physics B, Vol.32, No.13, p.L285-90

Meighan O, Danson C, Dardis L, Lewis C L S, MacPhee A, McGuinness C, O'Rourke R, Shaikh W, Turcu I C E and Costello J T, 2000
Application of a picosecond laser plasma continuum light source to a dual laser plasma photoabsorption experiment, Journal of Physics B, Vol.33, No.6, p.1159-68

Michette A G, Turcu I C E, Schulz M S, Browne M T, Morrison G R, Fluck P, Buckley C J and Foster G F, 1993
Scanning X-ray microscopy using a laser-plasma source, Review of Scientific Instruments, Vol.64, No.4, p.1478-81

Moloney C, 1998
A Study of the Spatial Characteristics of a Laser Plasma Extreme UV Continuum Source for Absorption Spectroscopy, MSc. Thesis, Dublin City University (unpublished)

Mosnier J-P, Bac S, Barchewitz R, Kennedy E T, Collins M and Costello J T, 1996
Measurements of extreme UV yields from Nd:YAG plasmas using a multilayer monochromator, Journal of Electron Spectroscopy and Related Phenomena, Vol.80, p.295-8

Munger C T and Gould H, 1986
Lamb shift in heliumlike uranium (U^{90+}), Physical Review Letters, Vol.57, No.23, p.2927-30

Murnane M M, Kapteyn H C and Falcone R W, 1989a
High-density plasmas produced by ultrafast laser pulses, Physical Review Letters, Vol.62, No.2, p.155-8

Murnane M M, Kapteyn H C and Falcone R W, 1989b
Generation and application of ultrafast x-ray sources, IEEE Journal of Quantum Electronics, Vol.25, No.12, p.2417-22

Murnane M M, Kapteyn H C and Falcone R W, 1990
X-ray streak camera with 2ps response, Applied Physics Letters, Vol.56, No.20, p.1948-50

Murnane M M, Kapteyn H C and Falcone R W, 1991a
Generation of efficient ultrafast laser-plasma x-ray sources, Physics of Fluids B, Vol.3, No.8, p.2409-13

Murnane M M, Kapteyn H C and Rosen M D and Falcone R W, 1991b
Ultrafast X-ray pulses from laser-produced plasmas, Science, Vol.251, p.531-6

Murnane M M, Kapteyn H C, Gordon S P and Falcone R W, 1994
Ultrashort X-ray pulses, Applied Physics B, Vol.58, p.261-6

Murphy N, Costello J T, Kennedy E T, McGuinness C, Mosnier J-P, Weinmann B and O'Sullivan G, 1999
Discrete structure in the 4d photoabsorption spectrum of tellurium and its ions, Journal of Physics B, Vol.32, No.15, p.3905-3922

Nakano N, Kuroda H, Kita T and Harada T, 1984
Development of a flat-field grazing-incidence XUV spectrometer and its application in picosecond XUV spectroscopy, Applied Optics, Vol.23, No.14, p.2386-92

Namioka T, 1961
Theory of the concave grating, Journal of the Optical Society of America, Vol.49, No.5, p.446-60

Nickles P V, Schnuerer M, Kalachnikov M P, Schlegel T and Faenov A Y, 1996
X-ray emission from short-pulse laser plasmas, Optical and Quantum Electronics, Vol.28, p.229-39

Nicolosi P, Jannitti E and Tondello G, 1981
Soft X-ray emission of continua from laser produced plasmas, Applied Physics B, Vol.B26, p.117-24

Nicolosi P, Jannitti E and Tondello G, 1991
A review on experimental studies of the photoabsorption spectra of low Z ions, Journal de Physique IV Colloque C1, Vol.1, p.89-98

Nicolosi P and Villoresi P, 1998
Experimental measurement of the CII L-shell photoabsorption spectrum, Physical Review A, Vol.58, No.6, p.4985-8

Nitsche H, 1995
Synchrotron X-ray absorption spectroscopy: a new tool for actinide and lanthanide speciation in solids and solution, Journal of Alloys and Compounds, Vol.223, p.274-9

Norreys P A, Zhang J, Vairns G, Djaoui A, Dwivedi L, Key M H, Kodama R, Krishnan J, Lewis C L S, Neely D, O'Meill D, Tert G J, Ramsden S A, Rose S J, Tallents G J and Uhomoibhi J, 1993
Measurement of the photo-pump strength of the 3d-5f transitions in the automatically line matched Ni-like Sm photo-pumped X-ray laser, Journal of Physics B, Vol.26, p.3693-9

Offenberger A A and Fedosejevs R, 1989
KrF laser produced plasmas, Laser and Particle Beams, Vol.7, No.3, p.393-403

O'Neill D M, Lewis C L S, Neely D and Davidson S J, 1991
Characterization of a laser-produced plasma using the technique of point-projection absorption spectroscopy, Physical Review A, Vol.44, No.4, p.2641-8

Orth F B, Ueda K, McIlrath T J and Ginter M L, 1986
High-resolution spectra of laser plasma light sources in the normal incidence XUV region, Applied Optics, Vol.25, No.13, p.2215-7

O'Sullivan G, 1983
The origin of line-free XUV continuum emission from laser-produced plasmas of the elements $62 \leq Z \leq 74$, Journal of Physics B, Vol.16, p.3291-3304

O'Sullivan G, Roberts J R, Ott W R, Bridges J M, Pittman T L and Ginter M, 1982
Spectral-irradiance calibration of continuum emitted from rare-earth plasmas, Optics Letters, Vol.7, No.1, p.31-3

O'Sullivan G, Carroll P K, Conway J, Dunne P, Faulkner R, McCormack T, McGuinness C, van Kampen P and Weinmann B, 1994
Extreme ultraviolet continuum emission from laser-generated plasmas and applications to spectroscopy, Optical Engineering, Vol.33, No.12, p.3993-8

O'Sullivan G, McGuinness C, Costello J T, Kennedy E T and Weinmann B, 1996
Trends in 4d-subshell photoabsorption along the iodine isonuclear sequence: I, I^+, *and* I^{2+}, Physical Review A, Vol.53, No.5, p.3211-26

O'Sullivan G, Carroll P K, Dunne P, Faulkner R, McGuinness C and Murphy N, 1999
Supercomplex spectra and continuum emission from rare-earth ions: Sm, a case study, Journal of Physics B, Vol.32, p.1893-1922

Pantelouris M and Connerade J P, 1983
Unexpected evidence that the main 5d→f transition in atomic uranium lies below the 5d threshold, Journal of Physics B, Vol.16, p.L23-8

Pattison C, 1996
Development of a Precision Optical System for High Power Laser Beam Delivery, Final Year Project Thesis, Dublin City University (unpublished)

Pelletier J F, Chaker M and Kieffer J C, 1996
Picosecond soft-X-ray pulses from a high-intensity laser-plasma source, Optics Letters, Vol.21, No.14, p.1040-2

Poletto L, Boscolo A and Tondello G, 1999

Characterisation of a charge-coupled-device detector in the 1100-0.14nm (1-eV to 9-keV) spectral region, Applied Optics, Vol.38, No.1, p.29-36

Radowsky A, 1999
Using thorium in a commercial nuclear fuel cycle: how to do it, Nuclear Engineering International, Vol.44, p.14-16

Radowsky A and Galperin A, 1998
The nonproliferative light water thorium reactor: A new approach to light water reactor core technology, Nuclear Technology, Vol.124, p.215-22

Radtke E-R, 1979a
On the character of the intense 4d-f resonances in atomic La and Tm, Journal of Physics B, Vol.12, No.3, p.L71-5

Radtke E-R, 1979b
Systematic comparisons between the 4d spectra of lanthanide atoms and solids, Journal of Physics B, Vol.12, No.3, p.L77-81

Radziemski L J, Steinhaus D W and Engleman R Jr, 1971
High-resolution atomic-absorption spectra of uranium obtained by the flash-photolysis and flash-discharge techniques, Journal of the Optical Society of America, Vol.61, No.11, p.1538-9

Radziemski L J and Cremers A (Editors), 1989
Laser-induced plasmas and applications, Published by Marcel Dekker Inc. NY.

Ready J F, 1971
Effects of high-power laser radiation, Published by Academic Press Inc.

Rense W A and Violett T, 1959
Method of increasing the speed of a grazing-incidence spectrometer, Journal of the Optical Society of America, Vol.49, No.2, p.139-41

Richter M, Meyer M, Pahler M, Prescher T, Raven E V, Sonntag B and Wetzel H –E, 1989a
Experimental study of atomic 4d giant resonances by photoabsorption and photoelectron spectroscopy: Ba, La and Ce, Physical Review A, Vol.39, No.11, p.5666-75

Richter M, Meyer M, Pahler M, Prescher T, Raven E V, Sonntag B and Wetzel H –E, 1989b
Experimental study of atomic 4d giant resonances by photoabsorption and photoelectron spectroscopy: Sm, Eu and Gd, Physical Review A, Vol.40, No.12, p.7007-19

Rocca J J, 1999
Table-top soft X-ray lasers, Review of Scientific Instruments, Vol.70, No.10, 3799-827

Rocca J J, Shlyaptsev V, Tomasel F G, Cortázar O D, Hartshorn D and Chilla J L A, 1994

Demonstration of a discharge pumped table-top soft X-ray laser, Physical Review Letters, Vol.73, No.16, p.2192-5

Rose-Petruck C, Jimenez R, Guo T, Cavalleri A, Siders C W, Ráksi F, Squier J A, Walker B A, Wilson K R, Barty C P J, 1999
Picosecond-milliångström lattice dynamics measured by ultrafast X-ray diffraction, Nature, Vol.398, 25 March, p.310-2

Rubbia C, 1994a
The energy amplifier, a solid-phase accelerator driven subcritical Th/U^{233} breeder for nuclear energy production with minimal actinide waste, Proceedings of the International Conference on Nuclear Data for Science and Technology, p.1065-71, ORNL

Rubbia C, Rubio J A, Buono S, Carminati F, Fiétier N, Galvez J, Gelès C, Kadi Y, Klapisch R, Mandrillon P, Revol J P and Roche Ch, 1994b
Conceptual design of a fast neutron operated high power energy amplifier, CERN internal report, CERN-AT-95-44 (ET)

Samson J A R, 1967
Techniques of Vacuum Ultraviolet Spectroscopy, Published by John Wiley & Sons Inc.

Schappert G T, Cobble J A, Fulton R D, Kyrala G A, Olson G L and Taylor A J, 1994
X-ray production with subpicosecond laser pulses, AIP Conference Proceedings, Vol.318, p.97-104

Schoenlein R W, Leemans W P, Chin A H, Volfbeyn P, Glover T E, Balling P, Zolotorev M, Kim K-J, Chattopadhyay S and Shank C V, 1996
Femtosecond X-ray pulses at 0.4Å generated by 90° Thomson scattering: A tool for probing the structural dynamics of materials, Science, Vol.274, 11 October, p.236-8

Schweppe J, Belkacem A, Blumenfeld L, Claytor N, Feinburg B, Gould H, Kostroun V E, Levy L, Misawa S, Mowat J R and Prior M H, 1991
Measurement of the lamb shift in lithiumlike uranium (U^{89+}), Physical Review Letters, Vol.66, No.11, p.1434-7

Seaborg G, 1989
Recent research on the heavy transuranium elements, Journal of Nuclear Materials, Vol.166, p.22-35

Seaborg G, 1995
Transuranium elements: the synthetic actinides, Radiochimica Acta, Vol.70/71, p.69-90

Seely J F, Ekberg J O, Brown C M, Feldman U, Behring W E, Reader J and Richardson M C, 1986
Laser-produced spectra and QED effects for Fe-, Co-, Cu- and Zn-like ions of Au, Pb, Bi, Th and U, Physical Review Letters, Vol.57, p.2924-6

Sellmair J and Korschinek G, 1988
The Munich laser ion source, Nuclear Instruments and Methods in Physics Research, Vol.A268, p.473-7

SF code: Optical Constants Grapher Version 2.0, by Mark Thomas, Centre for X-ray Optics, Lawrence Berkeley Laboratory, http://www-cxro.lbl.gov

Shadow ™ is an XUV ray-tracing package developed and licensed by the University of Wisconsin, Madison; see *http://www.xraylith.wisc.edu*

Shaw M, 1996
An Extreme-UV Optical Multichannel Analyser with Resolution Enhancement for Laser Plasma Spectroscopy, M.Sc. Thesis, Dublin City University (unpublished)

Shaw R W, Young J P, Cooper S P and Webb O F, 1999
Spontaneous ultraviolet emission from ^{233}Uranium/^{229}Thorium samples, Physical Review Letters, Vol.82, No.6, p.1109-11

Shepherd R, Booth R, Price D, Bowers M, Swan D, Bonlie J, Young B, Dunn J, White B and Stewart R, 1995
Ultrafast x-ray streak camera for use in ultrashort laser-produced plasma research, Review of Scientific Instruments, Vol.66, No.1, p.719-21

Simanovskii D M, Gladskikh A N, Shmaenok L A and Bobashev S V, 1996
Demonstration of laser induced X-ray generation in an expanding laser produced plasma, Vol.77, No.5, p.849-52

Singh R K and Narayan J, 1990
Pulsed-laser evaporation technique for dispersion of thin films: Physics and theoretical model, Physical Review B, Vol.41, No.13, p.8843-59

Spectra Calc™ (c2.22) is a spectral data processing software package written by Galactic Industries Corporation™, http://www.galactic.com

Spence D E, Kean P N and Sibbett W, 1991
60-fsec pulse generation from a self-mode-locked Ti:sapphire laser, Optics Letters, Vol.16, No.1, p.42-4

Spirlet J-C, 1989
New techniques in the preparation chemistry of transuranium elements, Journal of Nuclear Materials, Vol.166, p.41-7

Stead A D, Page A M and Ford T W, 1995
The prospects for soft x-ray contact microscopy using laser plasmas as an x-ray source, SPIE Vol.2523, p.40-50

Steingruber J, Borgström S, Starczewski T and Litzén U, 1996
Prepulse dependence of X-ray emission from plasmas created by IR femtosecond laser pulses on solids, Journal of Physics B, Vol.29, L75-L81

Strickland D and Mourou G, 1985
Compression of amplified chirped optical pulses, Optics Communications, Vol.56, No.3, p.219-21

Suckewer S, Skinner C H, Milchberg H, Keane C and Voorhees D, 1985

Amplification of stimulated soft X-ray emission in a confined plasma column, Physical Review Letters, Vol.55, No.17, p.1753-56

Sugar J, 1972
Potential barrier effects in photoabsorption. II. Interpretation of photoabsorption resonances in lanthanide metals at the 4d-electron threshold, Physical Review B, Vol.5, No.5, p.1785-92

Sugar J, 1974
Revised ionization energies of the neutral actinides, Journal of Chemical Physics, Vol.60, No.10, p.4103

Svanberg S, L'Huillier A and Wahlström C-G, 1997
Atomic physics using short-wavelength coherent radiation, Nuclear Instruments and Methods in Physics Research A, Vol.398, p.55-64

Tichenor D A, Kubiak G E and Stulen R H, 1995
Extreme ultraviolet lithography for circuit fabrication at 0.1 μm feature size, SPIE Vol.2523, p.23-8

Tondello G, Jannitti E and Malvezzi A M, 1977
Line broadening and self-absorption of BeIV in a laser-produced plasma, Physical Review A, Vol.16, No.4, p.1705-14

Tonner B P, Dunham D, Droubay T, Kikuma J, Denlinger J, Rotenberg E and Warwick A, 1995
The development of electron spectromicroscopy, Journal of Electron Spectroscopy and Related Phenomena, Vol.75, p.309-32

Troyanov M F, Ilyunin V G, Kalashnikov A G, Kuz'minov B D, Nikolaev M N, Raskach F P, Smetanin E Ya and Tsibulya A M, 1998
Some investigations and developments of the thorium fuel cycle, Atomic Energy, Vol.84, No.4, p.225-9

Tsakiris G D, 1990
Applications of a soft x-ray steak camera in laser-plasma interaction studies, SPIE, 19th International Congress on High-Speed Photography and Photonics, Vol.1358, p.174-92

Turcu I C E, Ross I N, Schulz M S, Daido H, Tallents G J, Krishnan J, Dwivedi L and Hening A, 1993
Spatial coherence measurements and X-ray holographic imaging using a laser-generated plasma x-ray source in the water window spectral region, Journal of Applied Physics, Vol.73, No.12, p.8081-7

Turcu I C E, Ross I N, Trenda P, Wharton C W, Meldrum R A, Daido H, Schulz M S, Fluck P, Michette A G, Juna A P, Maldonado J R, Shields H, Tallents G J, Dwivedi L, Krishnan J, Stevens DL, Jenner T J, Batani D and Goodson H, 1994
Picosecond excimer laser-plasma x-ray source for microscopy, biochemistry and lithography, SPIE Proceedings, Vol. 2015, Applications of Laser Plasma Radiation, 14th-16th July 1993, San Diego, California

Umstadter D, Workman J, Maksimchuk A, Liu X, Ellenberger U, Coe J S and Chien C-Y, 1995
Picosecond X-rays from subpicosecond laser-produced hot-dense matter, Journal of Quantitative Spectroscopy and Radiative Transfer, Vol.54, No.1/2, p.401-11

Van Kampen P, *private communication*, 1998

Van Kampen P, Gerth Ch, Martins M, Carroll P K, Hirsch J, Kennedy E T, Meighan O, Mosnier J-P, Zimmermann P and Costello J T, 2000
Photoabsorption and photoion spectroscopy of atomic uranium in the region of 6p and 5d excitations, Physical Review A, Vol.61, No.6, 062706-1 to 7

Van Klinken J, 1998
Energy from thorium?! Reconnoitring a new possibility: FEA, Heavy Ion Physics, Vol.8, p.1-11

Van Wonterghem B and Rentzepis P M, 1990
Characteristics of a Ta photocathode for the generation of picosecond X-ray pulses, Applied Physics Letters, Vol.56, No.11, p.1005-7

Villoresi P and Nicolosi P, 1998
C^{+} and C^{++} ion densities scaling in laser plasmas by ultraviolet photoabsorption spectroscopy, Hyperfine Interactions, Vol.114, p.213-6

Wehenkel C, 1975
Mise au point d'une nouvelle méthode d'analyse quantitative des spectres de pertes d'énergie d'électrons rapides diffusés dans la direction du faisceau incident: application a l'étude des métaux nobles, Le Journal de Physique, Vol.36, p.199-213

Wendin G, 1973
Giant dipole resonance in 4d photoabsorption of atomic barium, Physics Letters, Vol.46A, No.2, p.119-20

Wendin G, 1976
On the character of the $4d^{9}4f\,^{1}P$ resonance in Ba I, Journal of Physics B, Vol.9, No.11, p.L297-302

Wendin G, 1984
Photoionisation of metallic lanthanum, thorium, and uranium in a local-density-based random-phase approximation, Physical Review Letters, Vol.53, No.7, p.724-7

Wendin G and Kerr Del Grande, 1985
On the photoabsorption cross section of uranium metal, Physica Scripta, Vol. 32, p.286-90

Widmann K, Beiersdorfer P, Crespo López-Urrutia J R and Elliott S R, 1997
Spectroscopy at the high-energy electron beam ion trap (SuperEBIT), Hyperfine Interactions, Vol.108, p.73-86

Williams M D, 1973
Ultraviolet spectrum emitted from a laser-produced uranium plasma, Journal of the Optical Society of America, Vol.63, No.3, p.383-4

Wills J M and Eriksson O, 1992
Crystal-structure stabilities and electronic structure for the light actinides Th, Pa, and U, Physical Review B, Vol.45, No.24, p.13879-90

Workman J, Maksimchuk A, Liu X, Ellenberger U, Coe J S, Chien C-Y and Umstadter D, 1995
Control of bright picosecond X-ray emission from intense subpicosecond laser-plasma interactions, Physical Review Letters, Vol.75, No.12, p.2324-27

Workman J, Maksimchuk A, Liu X, Ellenberger U, Coe J S, Chien C-Y and Umstadter D, 1996
Picosecond soft X-ray source from subpicosecond laser-produced plasmas, Journal of the Optical Society of America B, Vol.13, No.1, p.125-31

Wülker C, Theobald W, Schäfer F P and Bakos J S, 1994
Temporal behaviour of X-ray radiation emitted by subpicosecond KrF-laser-heated carbon preplasmas, Physical Review E, Vol.50, No.6, p.4920-5

Yokoya A, Sekiguchi T, Saitoh Y, Okane T, Nakatani T, Shimada T, Kobayashi H, Takao M, Teraoka Y, Hayashi Y, Sasaki S, Miyahara Y, Harami and Sasaki T A, 1998
Soft X-ray beamline specialised for actinides and radioactive materials equipped with a variably polarising undulator, Journal of Synchrotron Radiation, Vol.5, p.10-16

Zangwill A and Soven P, 1980
Density-functional approach to local-field effects in finite systems: Photoabsorption in the rare gases, Physical Review A, Vol.21, No.5, p.1561-72

Zangwill A and Liberman D A, 1984
A non-relativistic program for optical response in atoms using a time-dependent local density approximation, Computer Physics Communications, Vol.32, p.63-73

Zhang J, Key M H, Norreys P A, Tallents G J, Behjat A, Danson C, Demir A, Dwivedi L, Holden M, Holden P B, Lewis C L S, MacPhee A G, Neely D, Pert G J, Ramsden S A, Rose S J, Shao Y F, Thomas O, Walsh F and You Y L, 1995
Demonstration of high gain in a recombination XUV laser at 18.2nm driven by a 20J, 2ps glass laser, Physical Review Letters, Vol.74, No.8, p.1335-8

Zimkina T M, Fomichev V A, Gribovskii S A and Zhukova I I, 1967
Anomalies in the character of the X-ray absorption of rare-earth elements of the lanthanide group, Soviet Physics - Solid State, Vol.9, No.5, p.1128-30

Zon B A and Karpeshin F F, 1990
Acceleration of the decay of ^{235m}U by laser-induced resonant internal conversion, Soviet Physics JETP, Vol.70, No.2, p.224-7

List of Figures and Photographs

List of Tables

Appendix I

The Cowan Code Atomic Structure Calculational Method

Schrödinger's equation for the steady-state of a many-electron system,

$$H\psi_n = E_n\psi_n \tag{AI.1}$$

is the fundamental equation of quantum mechanics. In this equation E_n is the total energy of the system, ψ_n is called the total wavefunction and describes the state of the system and H is the Hamiltonian or Hamiltonian operator.

The Hartree-Fock approach implemented by the Cowan suite of atomic structure codes (Cowan 1981) is a method for obtaining approximate total wavefunctions for many-electron systems. When the Schrödinger equation and Hamiltonian are expressed in spherical polar coordinates, r, θ and ϕ the equation may be solved exactly by the separation of variables method. The resulting wavefunction, factorised into radial and angular parts is written as

$$(r,\theta,\phi) = R_{nl}(r)Y_l^m(\theta,\phi) = \frac{1}{r}P_{nl}(r)Y_l^m(\theta,\phi) \tag{AI.2}$$

where $P_{nl}(r)$ is known as the radial function and $Y_l^m(\theta,\phi)$ is a spherical harmonic. The explicit form of the hydrogenic solutions may be found in most text books on atomic structure.

For a multi-electron atom, the hydrogenic solution is used as a starting point. Hartree (1928) proposed that a wave function for a multi-electron atom be constructed as a simple product of one-electron functions (or orbitals) u_i. Each orbital would take the approximate form of the hydrogenic solution and depend on the co-ordinates of just one electron

$$\psi(1,2,.....,\mathrm{N}) = u_1(1)u_2(2).....u_{\mathrm{N}}(\mathrm{N}) \tag{AI.3}$$

so that

$$|\psi|^2 = |u_1|^2|u_2|^2.....|u_{\mathrm{N}}|^2 \tag{AI.4}$$

By implication any given electron i can be assumed to be moving independently in the field of the nucleus and the remaining N-1 electrons. This is the independent-particle model. The field experienced by electron i due to the other electrons is given by the potential,

$$V_i(r_i) = \sum_{j\neq i}\int\frac{|u_j(r_j)|^2}{r_{ij}}d\tau_j \tag{AI.5}$$

where r_i is the radius vector of the electron from the nucleus. To solve the corresponding time-independent Schrödinger equation, Hartree made the further approximation of replacing $V_i(r_i)$ by its spherical average,

$$V_i(r_i) = \int V_i(r_i)\, d\Omega_i \tag{AI.6}$$

obtaining the resulting set of equations

$$\left(-\frac{1}{2}\nabla_i^2 - \frac{Z}{r_i}\right)u_i + V_i(r_i)u_i = \varepsilon_i u_i \tag{AI.7}$$

for the one-electron functions (or orbitals) u_i. The spherically symmetric nature of the potential leads immediately to the requirement that the angular dependence of u_i is a spherical harmonic.

The basic flaw in Hartree's method is that the wavefunction is not anti-symmetric with respect to the interchange of two co-ordinates sets (i) and (j) thus disobeying the Pauli exclusion principle. This problem was addressed by Fock (1930) by incorporating the spin into new one-electron functions and replacing the simple product function with an anti-symmetrised product. These new one-electron functions are correctly known as spin orbitals

$$\phi_i = u_i\sigma_i = \frac{1}{r}P_{nl}(r)Y_l^{m_l}(\theta,\phi)\sigma_{m_s}(s) \tag{AI.8}$$

where σ represents the spin state. The orthonormality of the spin-orbitals yields

$$\langle \phi_i | \phi_j \rangle = \delta_{ij} \tag{AI.9}$$

for any two orbitals i and j.

A wavefunction which represents a given electronic configuration, and which is anti-symmetric with respect to electron exchange, may be constructed from a linear combination of products of spin-orbitals. The anti-symmetrical function may be written in the form of a determinant

$$\Psi(LS) = \frac{1}{\sqrt{N!}}\begin{vmatrix} \phi_1(1) & \phi_2(1) & \cdots & \phi_N(1) \\ \phi_1(2) & \phi_2(2) & & \phi_N(1) \\ \vdots & & \ddots & \vdots \\ \phi_1(N) & \phi_2(N) & \cdots & \phi_N(N) \end{vmatrix} \tag{AI.10}$$

and is referred to as a determinantal function or a Slater determinant.

As the potential energy $V(r)$ in a multi-electron atom is no longer a simple Coulomb function, exact analytical solutions are no longer possible. The one-electron function, the spin-orbital, differs only from the hydrogenic solution in the radial part $P_{nl}(r)$. Numerical procedures are required for the calculation of the form of $P_{nl}(r)$.

Variational Principle

The variational basis of the Hartree-Fock approach helps to obtain convergent results in many cases, both for the ground state and low lying excited states. The orbitals $\{\phi_i\}$ (or more specifically the radial functions $P_{n_i l_i}$) are determined by requiring that $\langle \Psi | H | \Psi \rangle$ be minimised subject to the condition $\langle \Psi | \Psi \rangle$=1, or, equivalently $\langle \phi_i | \phi_j \rangle = \delta_{ij}$. This is a calculus of variations problem whose solution leads to a set of coupled integro-differential equations,

$$\left(-\frac{1}{2}\nabla_i^2 - \frac{Z}{r_i}\right)u_i(r_i) + \sum_{j\neq i}\left[u_i(r_i)\int \frac{|u_i(r_i)|^2}{r_{ij}}d\tau_j - \delta(m_{s_i}, m_{s_j})u_j(r_i)\int \frac{u_j^*(r_j)u_i(r_j)}{r_{ij}}d\tau_j\right] = \varepsilon_i u_i(r_i) \qquad \text{(AI.11)}$$

This process is known as the Hartree-Fock method and (AI.11) are the Hartree-Fock equations for the wavefunction (AI.10). When these Hartree-Fock equations have been solved to obtain a self-consistent set of radial functions P_{nl}, then these orbitals may be used to obtain the energy of any specified combination of orbitals.

For a complex atom, the energy expression contains many terms. An extremely useful concept is the centre-of-gravity or the 'average energy of the configuration', which is denoted as E_{av} and arises in the Slater-Condon theory of atomic structure. This corresponds to a statistically weighted sum of the energies of all the terms within a configuration

$$E_{av} = \frac{\sum_{levels}(2J+1)E_J}{\sum_{levels}(2J+1)} \qquad \text{(AI.12)}$$

where J is the total angular momentum of a level in a configuration and E_J its energy. A theoretical expression for E_{av} may be obtained and is given by the following equation,

$$E_{av} = \sum_i \frac{1}{2}\int_0^\infty P_{n_i l_i}^*(r)\left[-\frac{d^2}{dr^2} - \frac{2Z}{r} + \frac{l(l+1)}{r^2}\right]P_{n'l}(r)dr$$

$$+\sum_{i>j}\left[\sum_{k=0}^{2l_i}F^k(ij)c^k(l_im_{l_i},l_im_{l_i})c^k(l_jm_{l_j},l_jm_{l_j})-\delta_{m_{s_i}}\delta_{m_{s_j}}\sum_{|l_i-l_j|}^{l_i+l_j}G^k(ij)\left[c^k(l_im_{l_i},l_jm_{l_j})\right]^2\right] \tag{AI.13}$$

The contribution to E_{av} due to the spin-orbit interaction cancels out when all the terms of the configuration are added together as a weighted as in the definition (AI.12). In equation (AI.13), the F^k and G^k terms are special cases of the more general R^k radial integral defined as

$$R^k(ij;tu)=\int_0^\infty\int_0^\infty P_i^*(r)P_j^*(r')\frac{r_<^k}{r_>^{k+1}}P_t(r)P_u(r')drdr' \tag{AI.14}$$

where $r_>$ and $r_<$ are the maximum and minimum of the radial distances r and r' respectively. The symbols i, j, t and u all represent an arbitrary nl combination. The F^k and G^k integrals are defined as $F^K(ij)= R^K(ij;ij)$ and $G^K(ij) = R^K(ij;ji)$ respectively. These radial Coulomb integrals are more commonly referred to as Slater integrals. Finally the coefficients $c^k(lm_l,l'm_{l'})$ are not given here but have been tabulated elsewhere (Condon and Odabasi, 1980). The radial wavefunctions P_{nl} obtained through application of the variational principle in a self-consistent field calculation enable the evaluation of the parameters E_{av}, ζ, F^k, G^k and R^k for a given configuration. ζ is the spin orbit energy integral, and is obtained from the Blume-Watson (Cowan 1981, p.93) formula,

$$H_{so}=\frac{\alpha^2}{2}\frac{1}{r}\frac{dV}{dr}\sum_{i=1}^{N}\bar{l}_i.\bar{s}_i \tag{AI.15}$$

where $V(r)$ is the total field due to the nucleus and core electrons and the summation is taken over outer or valence electrons.

(R)TDLDA Method for Photoionisation Cross Section Calculations

This theoretical method obtains an approximate solution to the Schrödinger wave equation for a many-electron atom using a Local Density Approximation (LDA) whereby the correct many-electron Hamiltonian is replaced with an approximate total energy functional, the variation of which leads to a set of one-electron Schrödinger wave equations (Zangwill & Soven 1980). The TDLDA (Zangwill & Liberman, 1984) and RTDLDA (Liberman & Zangwill, 1984) codes of Zangwill and Liberman introduce time dependency into the Local Density Approximation by accounting for the interaction of electrons in the atomic shell with an external driving photon field of frequency ω.

Both TDLDA and RTDLDA codes have the same structure and numerical techniques except that non-relativistic one electron wavefunctions are replaced by Dirac wavefunctions in the RTDLDA code. The main structure of the TDLDA code is illustrated in the flow diagram in Figure AI.I and is described below.

The user inputs the atomic number Z, the charge state of the atom or ion, the occupation number of each orbital, the spin orientation of each spin-orbital (RTDLDA only) and the subshell binding energies. This information is then used to calculate one electron Kohn Sham wavefunctions ψ_i and their eigenenergies ε_i. This is done by using an approximation to the electronic charge density in order to calculate a potential function. From the potential function one electron wavefunctions are calculated and then used to re-calculate the electronic charge density and this procedure is iterated until self consistency is reached. The code user can change the convergence criteria for both the energy eigenvalues and the potential function.

After self-consistency is reached, the code then simulates the interaction of an external photon field of frequency ω with the electron cloud. The electronic density, $n(\bar{r},\omega)$, changes as a result of the external field, resulting in a change in the Coulomb potential $\partial V_c(\bar{r},\omega)$ and the exchange potential $\partial V_{xc}(\bar{r},\omega)$. An initial estimate of the change in the electronic density $\partial n(\bar{r},\omega)$ is calculated using χ_o, the susceptibility, which describes how strong the system interacts with the external perturbing field. This estimate of

Figure AI.1 Calculational procedure of the TDLDA code

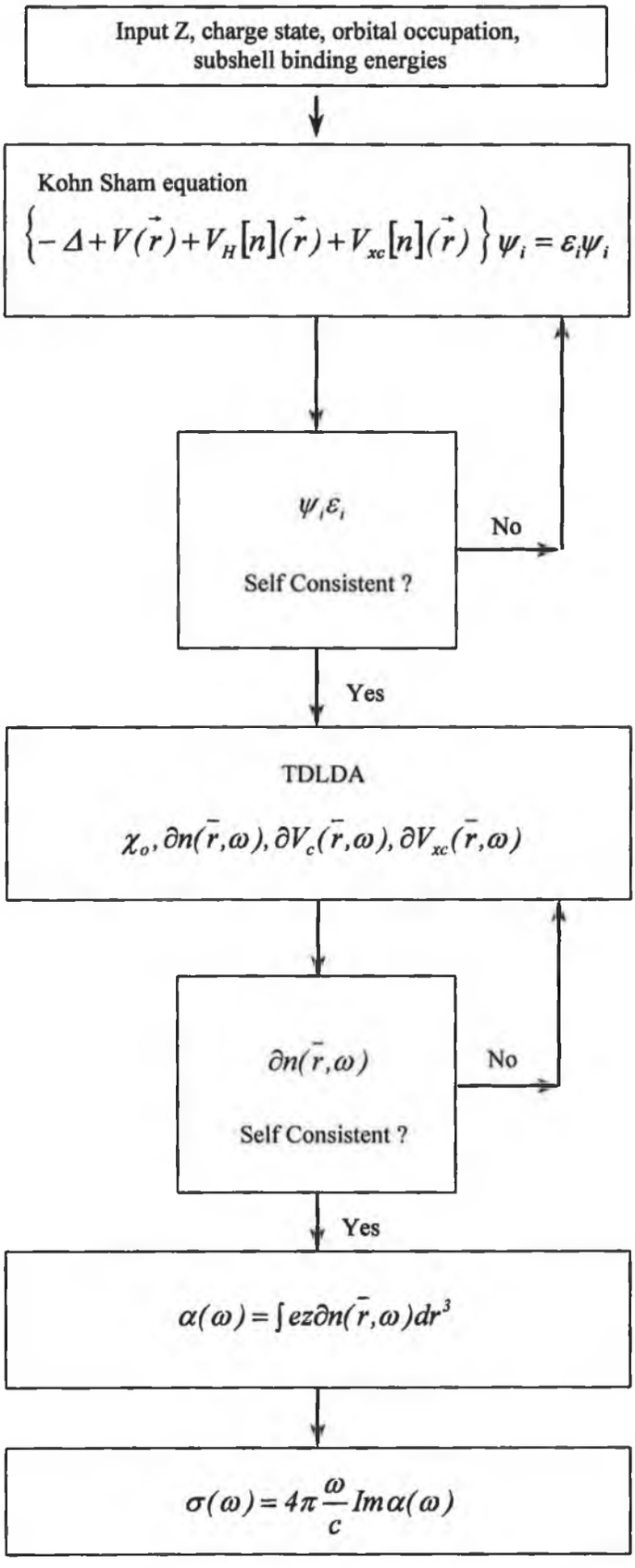

$\partial n(\bar{r},\omega)$ is used to calculate $\partial V_c(\bar{r},\omega)$ and $\partial V_{xc}(\bar{r},\omega)$. These values of $\partial V_c(\bar{r},\omega)$ and $\partial V_{xc}(\bar{r},\omega)$ are then used to re-calculate $\partial n(\bar{r},\omega)$ until self-consistency is reached. $\alpha(\omega)$, the complex dielectric function is then calculated and from this the photoabsorption cross section $\sigma(\omega)$ can be determined.

Appendix II

Year	Researchers / Publication	Atomic/Ionic Species (excitation subshell)	Energy (eV)
1977	**Carroll P K and Kennedy E T** *Doubly excited autoionisation resonances in the absorption spectrum of Li^+ formed in a laser-produced plasma,* PRL Vol.38, No.19, p.1068-71	Li^+ (1s)	62-248
1977	**Kennedy E T and Carroll P K** *Absorption from excited states of Be^+ formed in a laser produced plasma,* Physics Letters Vol.64A, No.1, p.37-8	Be^+ (1s) Be^{+*} (1s)	118-130 118-130
1984	**Jannitti E, Nicolosi P and Tondello G** *An experiment for absorption spectroscopy of ionised species using two laser-produced plasmas,* Physica Vol.124C, p.139-47	B^{2+} (1s) B^{3+} (1s) Be^+ (1s) Be^{2+} (1s)	113-310
1984	**Jannitti E, Nicolosi P and Tondello G** *Photoionisation and double excitation spectrum of Be^{2+},* Opt. Comm. Vol.50, No.4, p.225-30	Be^{2+} (1s)	154-420
1985	**Jannitti E, Mazzoni M, Nicolosi P, Tondello G and Yongchang W**, *Photoabsorption spectrum of Be^+*, J. Opt. Soc. Am. B Vol.2, p.1078-83	Be^+ (2s) Be^{+*} (2p) Be^+, Be^{+*} (1s)	16-18 13-14 118-138
1986	**Carroll P K and Costello J T** *Giant-Dipole-Resonance absorption in atomic thorium by a novel two-laser technique,* PRL Vol.57, No.13, p.1581-3	Th (5d)	80-140
1986	**Jannitti E, Pinzhong F and Tondello G** *The absorption spectrum of BII in the vacuum ultraviolet,* Physica Scripta, Vol.33, p.434-41	B^+ (2s) B^{+*} (2s & 2p)	7-31
1987	**Carroll P K and Costello J T** *The XUV photoabsorption spectrum of uranium vapour,* J. Phys. B. Vol.20, p.L201-5	U (5d)	80-140
1987	**Jannitti E, Nicolosi P and Tondello G** *An experiment for absorption spectroscopy in the XUV of light ions,* Physica Scripta, Vol.36, p.93-8	Be, Be^+, Be^{2+}, Be^{3+} (1s) Be^*, Be^{+*} (1s)	113-310
1987	**Mosnier J-P, Brilly J and Kennedy E T** *Low lying odd parity autoionising states in the 2p-subshell absorption spectrum of AlIII and SiIV,* J. Physique Vol.48 (C9) p.219-22	Al^{2+} (2p) Si^{3+} (2p)	85-95 115-126
1988	**Brilly J, Kennedy E T and Mosnier J-P** *The 2p-subshell absorption spectrum of AlIII,* J. Phys. B Vol.21, No.22, p.3685-93	Al^{2+}, Al^{2+*} (2p)	71-103
1988	**Costello J T, Lynam W G and Carroll P K** *Ultraviolet absorption of refractory elements by a dual laser plasma method,* J. Physique Colloque CI, Vol.49, No.3, p.243-46	Be, Be^+ (1s) B (1s) Si (2p) Sr, Sr^+ (3d)	113-138 191-207 103-124 138-146
1988	**Jannitti E, Nicolosi P and Tondello G** *Photoionisation cross-section measurement of the CV ion,* Phys. Letts. A Vol.131, No.3, p.186-9	C^{4+} (1s)	275-496
1989	**Hansen J E, Brilly J, Kennedy E T and O'Sullivan G,** *Rise and fall of the $4d^{10} \rightarrow 4d^9 4f$ resonance in the Xe isoelectronic sequence,* PRL Vol.63, No.18, p.1934-7	La^{3+} (4d)	120-140

Year	Researchers / Publication	Atomic/Ionic Species (excitation subshell)	Energy (eV)
1990	**Brilly J, Kennedy E T and Mosnier J-P** *2p photoabsorption spectra of valence excited configurations in Al^{2+} and Si^{3+} observed in a dual laser produced plasma experiment,* Physica Scripta Vol.41, p.30-4	Al^{2+*} (2p) Si^{3+*} (2p)	70-80
1990	**Jannitti E, Nicolosi P and Tondello G** *Absorption spectra from 1s inner shell electron of ionised and neutral carbon,* Physica Scripta Vol.41, p.458-63	C, C^+, C^{2+}, C^{2+*}, C^{3+}, C^{3+*}(1s)	275-496
1991	**Costello J T, Kennedy E T, Sonntag B F, Clark C W,** *3p photoabsorption of free and bound Cr, Cr^+, Mn, and Mn^+,* PRA Vol.43, No.3, p.1441-50	Cr, Cr^+ (3p) Mn, Mn^+ (3p)	40-70
1991	**Costello J T, Kennedy E T, Sonntag B F and Cromer C L,** *XUV photoabsorption of laser-generated W and Pt vapours,* J. Phys. B Vol.24, No.24, p.5063-9	W (4f & 5p) Pt (4f & 5p)	30-55 40-90
1992	**Costello J T, Evans D, Hopkins B, Kennedy E T, Kiernan L, Mansfield M W D, Mosnier J-P, Sayyad M H and Sonntag B F,** *The 2p-subshell photoabsorption spectrum of Al^+ in a laser-produced plasma,* J. Phys. B Vol.25, No.23, p.5055-68	Al^+ (2p)	60-250
1992	**Lynam W G, Carroll P K, Costello J T, Evans D and O'Sullivan G,** *The 1s absorption spectrum of neutral and singly ionised boron,* J. Phys. B Vol.25, No.19, p.3963-70	B, B^+ (1s)	188-221
1993	**Dunne P, O'Sullivan G and Ivanov V K,** *Extreme-ultraviolet absorption spectrum of Ga^+,* PRA Vol.48, No.6, p.4358-64	Ga^+ (3p & 3d)	27-250
1993	**Jannitti E, Gaye M, Mazzoni M, Nicolosi P and Villoresi P,** *K-shell photoabsorption spectrum of CII,* PRA Vol.47, No.5, p.4033-41	C^+, C^{+*} (1s)	275-496
1994	**Kiernan L M, Kennedy E T, Mosnier J-P, Costello J T and Sonntag B F,** *First observation of photon-induced triply exited state in atomic lithium,* PRL Vol.72, No.15, p.2359-62	Li (1s) Li^+ (1s)	58-78
1994	**Mosnier J-P, Costello J T, Kennedy E T, Kiernan L and Sayyad M H,** *Even-parity autoionising states in the extreme-ultraviolet photoabsorption spectra of Mg, Al^+, and Si^{2+},* PRA Vol.49, No.2, p.755-61	Mg^* (2p) Al^{+*} (2p) Si^{2+*} (2p)	47-51 68-74 93-101
1995	**Dunne P, O'Sullivan G and Ivanov V K** *The M-shell photoabsorption spectrum of Ge^{2+},* J. Phys. B Vol.28, No.7, p.1241-50	Ge^{2+} (3p & 3d)	27-250
1995	**Jannitti E, Nicolosi P, Villoresi P and Xianping F,** *Measurement of the K-shell photoionisation cross section of CIV through the L-shell photoabsorption spectra,* PRA Vol.51, No.1, p.314-23	C^{3+} (1s) C^{3+} (2s) C^{3+*} (2p)	275-496 50-64 50-64
1995	**Köble U, Costello J T, Mosnier J-P, Kennedy E T and Martins M,** *XUV photoabsorption of laser generated Au vapour,* J. Phys. B Vol.28, No.2, p.181-90	Au, Au^* (5p & 4f)	45-110

Year	Researchers / Publication	Atomic/Ionic Species (excitation subshell)	Energy (eV)
1995	**Köble U, Kiernan L, Costello J T, Mosnier J-P, Kennedy E T, Ivanov V K, Kupchenko V A and Shendrik M S,** *4f (^{1}P) giant dipole resonance in La^{3+}*, PRL Vol.74, No.12, p.2188-91	La^{3+} (4d)	100-140
1995	**McGuinness C, O'Sullivan G, Carroll P K, Audley D and Mansfield M W D,** *3d absorption spectra SrI through SrIV*, PRA Vol.51, No.3, p.2053-62	Sr (3d) Sr^+ (3d) Sr^{2+} (3d) Sr^{3+} (3d)	105-160
1995	**Sayyad M H, Kennedy E T, Kiernan L, Mosnier J-P and Costello J T,** *2p-subshell photoabsorption by Si^{2+} ions in a laser-produced plasma,* J. Phys. B Vol.28, No.9, p.1715-22	Si^{2+} (2p)	105-140
1995	**van Kampen P, Kiernan L, Costello J T, Kennedy E T, van der Mullen J A M and O'Sullivan G,** *The 3p photoabsorption spectra of KII and CaIII,* J. Phys. B Vol.28, No.22, p.4771-9	K^+ (3p) Ca^{2+} (3p)	25-33 44-52
1996	**Cummings A and O'Sullivan G** *Discrete structure in the 3d photoabsorption spectra of neutral, singly ionised and doubly ionised bromine,* PRA Vol.54, No.1, p.323-34	Br, Br^+, Br^{2+} (3d)	60-90
1996	**Mansfield M W D, Costello J T, Kennedy E T, Mosnier J-P, Kiernan L and Köble U,** *Recent observations of giant resonances in atoms and ions-Mo and Mo$^+$,* in *Co-operative effects in many electron systems and their response to external fields,* World Scientific – Proc. of Adriatico Conf.	Mo (4p) Mo^+ (4p)	30-50
1996	**O'Sullivan G, McGuinness C, Costello J T, Kennedy E T and Weinmann B,** *Trends in 4d-subshell photoabsorption along the iodine isonuclear sequence: I, I^+, and I^{2+},* PRA Vol.53, No.5, p.3211-26	I, I^+, I^{2+} (4d)	45-300
1997	**Cummings A and O'Sullivan G,** *Discrete structure in the 4d photoabsorption spectrum of Cs+,* J. Phys. B. Vol.30, No.23, p.5599-5607	Cs^+ (4d)	80-150
1997	**Kiernan L M, Costello J T, Kennedy E T, Mosnier J-P and Sonntag B F,** *Measurement of the XUV photoabsorption spectra of atomic zinc and its ions Zn^{n+}: n=1, 2, and 3 in the region of 3p-subshell excitation,* J. Phys. B Vol.30, No.21, p.4801-12	Zn^+ (3p) Zn^{2+} (3p) Zn^{3+} (3p)	75-120
1997	**van Kampen P, O'Sullivan G, Ivanov V K, Ipatov A N, Costello J T and Kennedy E T,** *Dramatic changes in the 3s autoionisation process at the beginning of the ArI sequence,* PRL Vol.78, No.16, p.3082-5	Ar (3s) K^+ (3s) Ca^{2+} (3s)	26-29 34-48 52-68
1998	**Costello J T, Kennedy E T, Mosnier J-P and Sayyad M H,** *Measurement and analysis of the photoabsorption spectra of laser-produced Al and Si$^+$ in the region of 2p-subshell excitation,* J. Phys. B Vol.31, No.4, p.677-88	Al, Al^* (2p) Si^+, Si^{+*} (2p)	76-82 105-130
1998	**Costello J T, Kennedy E T, Mosnier J-P, Sayyad M H and McGuinness C,** *Extreme-UV photoabsorption spectrum of a laser-produced silicon plasma: evidence for metastable Si$^+$ ions,* J. Phys. B Vol.31, No.13, p.L547-52	Si^+, Si^{+*} (2p)	93-113

Year	Researchers / Publication	Atomic/Ionic Species (excitation subshell)	Energy (eV)
1998	**Nicolosi P and Villoresi P** *Experimental measurement of the CII L-shell photoabsorption spectrum,* PRA Vol.58, No.6, p.4985-8	C^+ (2s & 2p) C^{+*} (2p)	18-33
1998	**O'Reilly F and Dunne P,** *3d photoabsorption in ZnIII and GeV,* J. Phys. B Vol.31, No.4, p.L141-5	Zn^{2+} (3d) Ge^{4+} (3d)	30-100
1998	**O'Reilly F and Dunne P,** *3d photoabsorption in ZnII, GaIII and GeIV,* J. Phys. B Vol.31, No.5, p.1059-68	Zn^+ (3d) Ga^{2+} (3d) Ge^{3+} (3d)	25-100
1998	**van Kampen P and O'Sullivan G,** *Trends in 3p photoabsorption in the ArI isoelectronic sequence: spectra of ScIV and TiV,* J. Phys. B. Vol.31, No.4, p.L135-9	Sc^{3+} (3p) Ti^{4+} (3p)	50-100
1998	**Villoresi P and Nicolosi P** *C^+ and C^{++} ion densities scaling in laser plasmas by ultraviolet photoabsorption spectroscopy,* Hyperfine Interactions Vol.114, p.213-6	C^+, C^{+*} (2p) C^{2+*} (2p)	22-24
1998	**Whitty W, Costello J T, Kennedy E T, Moloney C and Mosnier J-P,** *Absorption spectroscopy of an expanding laser produced lithium plasma in the extreme ultraviolet using the Dual Laser Plasma technique,* Appl. Surf. Sci. Vol.127-9, p.686-91	Li, Li^+ (1s)	70-130
1999	**Chakraborty H S, Gray A, Costello J T, Deshmukh P C, Haque G N, Kennedy E T, Manson S T and Mosnier J-P,** *Anomalous behaviour of the near-threshold photoionization cross section of the neon isoelectronic sequence: A combined experimental and theoretical study,* PRL Vol.83, No.11, p.2151-4	Na^+ (2p) Mg^{2+} (2p) Al^{3+} (2p) Si^{4+} (2p)	45-48 75-81 111-123 143-173
1999	**D'Arcy R, Costello J T, McGuinness C and O'Sullivan G,** *Discrete structure in the 4d photoabsorption spectrum of antimony and its ions,* J. Phys. B Vol.32, No.20, p.4859-76	Sb (4d) Sb^+ (4d) Sb^{2+} (4d) Sb^{3+} (4d)	30-40
1999	**Dunne P, O'Reilly F, O'Sullivan G and Murphy N,** *4d photoabsorption in SnIII,* J. Phys. B Vol.32, No.20, p.L597-602	Sn^{2+} (4d)	25-50
1999	**Kennedy E T, Costello J T, Gray A, McGuinness C, Mosnier J-P and van Kampen P,** *New dual laser plasma investigations of inner-shell excitations,* J. Elec. Spec. & Rel. Phen. Vol.101-3, p.161-6	Ne (2s) Na^+ (2s) Mg^{2+} (2s) Si (2p) Cr^{2+} (3p)	45-49 68-80 95-120 100-130 40-65
1999	**McGuinness C, Martins M, Wernet Ph, Sonntag B F, van Kampen P, Mosnier J-P, Kennedy E T and Costello J T,** *Metastable state contributions to the measured 3p photoabsorption spectrum of Cr^+ ions in a laser-produced plasma,* J. Phys. B Vol.32, No.20, p.L583-91	Cr^+(3p)	35-70
1999	**Meighan O, Dardis L, Kennedy E T, Morgan T J, Mosnier J-P, van Kampen P and Costello J T,** *Observation of a 6p-6d giant dipole resonance in the VUV photoabsorption spectrum of a laser-produced thorium plasma,* J. Phys. B Vol.32, No.13, p.L285-90	Th (6p)	17-32

Year	Researchers / Publication	Atomic/Ionic Species (excitation subshell)	Energy (eV)
1999	**Meighan O, Danson C, Dardis L, Lewis C L S, MacPhee A, McGuinness C, O'Rourke R, Shaikh W, Turcu I C E and Costello J T,** *Application of a picosecond laser plasma continuum light source to a dual laser plasma (DLP) photoabsorption experiment,* J. Phys. B Vol.33, No.6, p.1159-68	Th to Th^{6+} (5d)	80-140
1999	**Murphy N,** *4d photoabsorption in TeV and TeVI,* J. Phys. B Vol.32, No.18, p.L525-9	Te^{4+} (4d) Te^{5+} (4d)	70-102
1999	**Murphy N, Costello J T, Kennedy E T, McGuinness C, Mosnier J-P, Weinmann B and O'Sullivan G,** *Discrete structure in the 4d photoabsorption spectrum of tellurium and its ions,* J. Phys. B Vol.32, No.15, p.3905-22	Te (4d) Te^{+} (4d) Te^{2+} (4d) Te^{3+} (4d)	37-45
2000	**Cummings A, McGuinness C, O'Sullivan G, Costello J T, Mosnier J-P, Kennedy E T,** *Wavefunction collapse with increasing ionisation: 4d photoabsorption of Cs through Cs^{4+},* for submission to Physical Review A	Cs (4d) Cs^{+} (4d) Cs^{2+} (4d) Cs^{3+} (4d) Cs^{4+} (4d)	80-170
2000	**D'Arcy R, Costello J T, Kennedy E T, McGuinness C, Mosnier J-P and O'Sullivan G,** *The evolution of 4d photoabsorption in Sb with increasing ionisation,* J. Phys. B. Vol.33, No.7, p.1383-1401	Sb^{+} (4d) Sb^{2+} (4d) Sb^{3+} (4d) Sb^{4+} (4d)	30-100
2000	**Hirsch J S, Meighan O, Mosnier J-P, van Kampen P, Whitty W, Costello J T, Lewis C L S, MacPhee A G, Hirst G J, Westhall J and Shaikh W,** *Vacuum-UV resonant photoabsorption imaging of laser produced plasmas,* accepted by Journal of Applied Physics, July 2000	Ca (3p) Ca^{+} (3p) Ca^{2+} (3p)	16-35
2000	**van Kampen P, Hirsch J, Mosnier J-P, Kennedy E T, Costello J T, Martins M, Gerth C and Zimmerman P,** *VUV and XUV photoabsorption of laser-produced uranium in the 15 to 150eV region,* PRA, Vol.61, No.6, p.062706-1 to 7	U (6p) U (5d)	15-150

Acknowledgements

I would firstly like to sincerely thank my supervisor Dr. John Costello for his constant support, help and encouragement throughout the entire duration of this project. He was always available to answer questions, to discuss results, to help in the lab and to offer suggestions and advice. I am very grateful for the many opportunities that I have had under his supervision, such as presenting at national and international conferences, working in other research labs and publishing papers. I would also like to thank John and his wife Anne for their hospitality to me and for their friendship.

I would like to thank Prof. Eugene Kennedy and Dr. Jean-Paul Mosnier for all their help and advice over the years.

I would like to thank all the 'lads in the lab' for all the 'laughs in the lab' and also for being such brilliant friends. These are Lee Dardis, Barry Doyle, Andy Gray, John Hirsch, Mohamed Khater, Cormac McGuinness, Alan McKiernan, Chris Moloney, Amy Schneider, Mark Stapleton, Paul van Kampen and William Whitty. Thanks to you all for all your help, encouragement and useful discussions.

A million thanks to my DCU 'amigos' Dr. Deirdre Boilson and Dr. Eilish McLoughlin, who have always been there through thick and thin. I can never thank you enough for all the encouragement, laughs, late nights and weekends, and of course, the trips to Eddie Rockets, the cups of tea and the Pot Noodles! Thanks also to Al Devine, Enda McGlynn, Aisling McEvoy and Samantha Fahy for all the kind words of encouragement and support ... it was really appreciated. Thanks to Des Lavelle for all his help with machining equipment and for the animated political discussions!

I would like to thank Prof. Tom Morgan (Wesleyan University) for his active participation in thorium VUV photoabsorption and emission experiments and for his involvement in the writing of a subsequent publication. I would also like to thank Tom and his wife Janet for their help, encouragement and friendship.

I would like to thank Prof. Ciaran Lewis (QUB) and Dr. Andy MacPhee (QUB and RAL) for their involvement in both experiments performed at RAL and also for many helpful discussions and suggestions. Thanks also to RAL staff, Dr. Colin Danson, Dr. Edmond Turcu, Waseem Shaikh and Sara Huntingdon for their assistance in the lab and also for many useful suggestions.

I would like to thank Dr. Michael Martins and Dr. Cormac McGuinness for calculations that they have performed in order to assist in the interpretation of some of the experimental results presented in this thesis.

A million thanks to my buddy Rowena for her constant help and encouragement and also for so many good times and laughs. Thanks for always being there to listen to me and thanks for being such a brilliant friend.

Thanks also to my buddies Tracy and Kieran. Thank you both for all the encouragement and support, and Kieran thanks for all the help with running codes on the new UNIX system. I would like to thank my buddies Oliver, Cáit, Eamonn, Catherina, Joe and Niamh for all of their encouragement, weekends away and all the good times.

I would like to thank my family a million times over… Thanks to Mam, Dad, Mark and Justin for all your help, unquestioning support and encouragement… I appreciate it so much. Thanks to Justin for the use of his PC 'all day every day'! Thanks also to the Amory's, Mary, Len, Aislinn and Ciara, and the Robinson's, Jim, Judith, David and Martin for all of their support.

The last person I would like to thank is Vincent, my best friend. Thank you for helping me to read and to print this thesis. More importantly, thank you so much for listening to me and for all of your support, encouragement and advice. I appreciate it more than I can ever say.